

N O T I C E

THIS DOCUMENT HAS BEEN REPRODUCED FROM
MICROFICHE. ALTHOUGH IT IS RECOGNIZED THAT
CERTAIN PORTIONS ARE ILLEGIBLE, IT IS BEING RELEASED
IN THE INTEREST OF MAKING AVAILABLE AS MUCH
INFORMATION AS POSSIBLE



Technical Memorandum 80709

Spherical Earth Analysis and Modeling of Lithospheric Gravity and Magnetic Anomalies

**R. R. B. von Frese, W. J. Hinze
and L. W. Bralle**

(NASA-TM-80709) SPHERICAL EARTH ANALYSIS
AND MODELING OF LITHOSPHERIC GRAVITY AND
MAGNETIC ANOMALIES Ph.D. Thesis - Purdue
Univ. (NASA) 180 p HC A09/MF A01 CSCL 08E

N80-30980

Unclas
G3/46 31315

MAY 1980

National Aeronautics and
Space Administration

Goddard Space Flight Center
Greenbelt, Maryland 20771



**SPHERICAL EARTH ANALYSIS AND MODELING OF
LITHOSPHERIC GRAVITY AND MAGNETIC ANOMALIES**

**Ralph R.B. von Frese, William J. Hinze
and Lawrence W. Braile**

**Department of Geosciences
Purdue University
West Lafayette, Indiana 47907**

May, 1980

**Prepared for
GODDARD SPACE FLIGHT CENTER
National Aeronautics and Space Administration
Greenbelt, Maryland 20771
under
NASA Contract No. NAS5-25030**

ACKNOWLEDGEMENTS

The authors wish to acknowledge the contributions of P.L. Bowman, V.W. Chandler, J.S. Koski, and A.J. Luca on previous NASA contracts to Purdue University to develop computer codes and processing techniques for interpretation of satellite elevation potential field data. Special thanks also are due R.A. Langel and the staff of the Geophysics Branch of NASA's Goddard Space Flight Center, and in particular M.A. Mayhew, for many helpful discussions and reviews of this work. However, all claims and results presented in this report are the sole responsibility of the authors.

This report originally was documented as a doctoral dissertation by one of us (R.v.F.) while holding a David Ross Fellowship from Purdue University.

TABLE OF CONTENTS

	Page
LIST OF FIGURES	v
ABSTRACT	xiii
I. INTRODUCTION	1
A. Statement of the Problem	1
B. Objectives	2
II. SPHERICAL EARTH GRAVITY AND MAGNETIC ANOMALY ANALYSIS BY EQUIVALENT POINT SOURCE INVERSION	5
A. Abstract	5
B. Introduction	6
C. The Gravity Point Pole Potential	8
D. The Magnetic Point Dipole Potential	14
E. Combined Gravity and Magnetic Point Source Potentials	19
F. The Inversion Problem	20
G. Examples of Geophysical Processing Applications	26
H. Conclusions	34
I. References	35
III. QUALITATIVE CORRELATION ANALYSIS OF REGIONAL NORTH AMERICAN GRAVITY AND MAGNETIC ANOMALIES	37
A. Abstract	37
B. Introduction	38
C. Data Sources and Preprocessing	41
D. Discussion	51
1. Free-Air Gravity Anomaly Field	51
2. Magnetic Anomaly Field	57
3. Heat Flow Field	59
E. Conclusions	60
F. References	62

	Page
IV. QUANTITATIVE CORRELATION ANALYSIS OF REGIONAL NORTH AMERICAN GRAVITY AND MAGNETIC ANOMALIES	64
A. Abstract.	64
B. Introduction	65
C. Quantitative Correlation Procedure	68
D. Data Sets and Processing	71
1. Gravity Anomaly Maps	71
2. Magnetic Anomaly Maps	78
E. Quantitative Correlation Results and Discussion	84
1. Correlation Analysis (I-5)	84
2. Correlation Analysis (II-5)	91
3. Correlation Analysis (III-3)	97
F. Conclusions	111
G. References	113
V. SPHERICAL EARTH GRAVITY AND MAGNETIC ANOMALY MODELING BY GAUSS-LEGENDRE QUADRATURE INTEGRATION	115
A. Abstract	115
B. Introduction	115
C. Description of the Method	116
D. Illustration of the Method	124
E. Conclusions	136
F. References	137
VI. GRAVITY AND MAGNETIC ANOMALY MODELING OF MISSISSIPPI EMBAYMENT CRUSTAL STRUCTURE AT SATELLITE ELEVATIONS	139
A. Abstract	139
B. Introduction	139
C. Model Description	140
D. Results and Discussion	144
E. Conclusions	152
F. References	153
VII. SUMMARY AND CONCLUSIONS	155
BIBLIOGRAPHY	160

LIST OF FIGURES

Figure		Page
II.1	Gravity and magnetic anomaly analysis in spherical coordinates by equivalent point source inversion (see text for details).	10
II.2	Geometry of the magnetic polarization contrast vector, $\Delta \vec{j}$, at the point (r_1, θ_1, ϕ_1) in terms of the orthonormal spherical basis vectors \hat{e}_r , \hat{e}_θ , and \hat{e}_ϕ . In the absence of remanence, the polarization of the point dipole at (r_1, θ_1, ϕ_1) is induced only and $\Delta \vec{j} = \Delta k * \vec{F}_1$, where Δk = volume magnetic susceptibility and \vec{F}_1 is the geomagnetic field vector with inclination and declination I_1 and D_1 , respectively.	15
II.3	A) Stereographic equal-area polar (SEAP) projection of smoothed 1° -averaged free-air gravity anomaly data for the United States, Mexico and Central America. Amplitude range (AR) of the data set is 41 to -53 mgal and the amplitude mean (AM) is -0.61 mgal. Contour interval (CI) is 10 mgal and the reference elevation (Z) of the observations is 0.0 km. B) Equivalent point source (EPS) approximation of smoothed 1° -averaged free-air gravity anomalies	27
II.4	A) Relative geoidal anomalies derived from equivalent point source inversion of smoothed 1° -averaged free-air gravity anomalies. B) Equivalent point source approximation of smoothed 1° -averaged free-air gravity anomalies upward continued to 450 km elevation	29
II.5	A) Equivalent point source approximation of the first radial derivative of smoothed 1° -averaged free-air gravity anomalies. B) Equivalent point source approximation of the radial Laplacian component of smoothed 1° -averaged free-air gravity anomalies. At 450 km elevation the radial Laplacian component is nearly identical to the second radial derivative of the gravity anomalies	30

Figure		Page
II.6	A) Multielevation POGO satellite magnetometer data reduced to a common elevation of 450 km by equivalent prism source inversion according to the procedures of Mayhew (1979). B) Equivalent source approximation of the total magnetic intensity anomaly data differentially reduced to the radial pole. The normalization amplitude (N) assumed for the radially polarizing field was 60,000 gammas.	32
II.7	Total magnetic intensity anomaly comparisons (after Mayhew (1979)) illustrating the fit between arbitrarily selected tracks of POGO satellite magnetic measurements (dots) and the corresponding equivalent source values (crosses). The solid line in each comparison corresponds to the elevation of the POGO satellite magnetometer data.	33
III.1	Stereographic equal-area polar (SEAP) projection of free-air gravity anomaly data for North America. Amplitude range (AR) of the data set is 185 to -285 mgal and the amplitude mean (AM) is -7.63 mgal. Contour interval (CI) is 10 mgal and reference elevation (Z) of the observations is 0.0 km.	42
III.2	Wavelength characteristics of low-pass, high-cut filter used to process gravity anomaly and topographic data of North America.	43
III.3	High-cut ($\lambda \leq 8^\circ$) filtered free-air gravity anomaly data for North America.	44
III.4	High-cut filtered free-air gravity anomaly data for North America resampled at 2° intervals.	45
III.5	Spherical equivalent source field approximation of resampled free-air gravity anomaly data for North America.	46
III.6	Spherical equivalent source field approximation of resampled free-air gravity anomaly data for North America upward continued to 450 km elevation	47

Figure		Page
III.7	Total magnetic intensity anomaly data for North America derived from POGO satellite magnetometer observations reduced to a uniform elevation of 450 km by the equivalent prism source inversion procedures described by Mayhew (1979).	49
III.8	Spherical equivalent source field approximation of total magnetic intensity anomaly data for North America differentially reduced to radial polarization. The normalizing amplitude (AMP) assumed for the radially polarizing induction field was 60,000 gammas.	50
III.9	Heat flow (Chapman and Pollack, (1975)), geological provinces and selected structures of North America	52
III.10	1°-averaged topographic elevations for North America.	55
III.11	High-cut ($\lambda \leq 8^\circ$) filtered 1°-averaged topographic elevations for North America	56
III.12	Seismically determined crustal thickness map (Warren and Healy, 1973) for the conterminous United States	58
IV.1	Stereographic equal-area polar (SEAP) projection of high-cut ($\lambda \leq 8^\circ$) filtered 1°-averaged free-air gravity anomaly data for North America. Amplitude range (AR) of data set is 40 to -62 mgal and the amplitude mean (AM) is -7.87 mgal. Contour interval (CI) is 10 mgal and reference elevation (Z) of the observations is 0.0 km.	72
IV.2	Spherical equivalent source field approximation of free-air gravity anomaly data for North America.	73
IV.3	Spherical equivalent source field approximation of free-air gravity anomaly data for North America upward continued to 450 km elevation	75
IV.4	Spherical equivalent source field approximation of first order radial derivative of free-air gravity anomaly data for North America.	76

Figure		Page
IV.5	Spherical equivalent source field approximation of second order radial derivative of free-air gravity anomaly data for North America.	77
IV.6	Spherical equivalent source field approximation of radially polarized total magnetic intensity anomaly data for North America. The radial pole reduction was achieved using a normalized polarizing amplitude (AMP) of 60,000 gamma.	79
IV.7	Spherical equivalent source field approximation of high-cut ($\lambda \leq 12^\circ$) filtered radially polarized total magnetic intensity anomaly data for North America.	81
IV.8	Spherical equivalent source field approximation of the first order radial derivative of radially polarized total magnetic intensity anomaly data for North America.	82
IV.9	Spherical equivalent source field approximation of the high-cut ($\lambda \leq 8^\circ$) filtered first order radial derivative of radially polarized total magnetic intensity anomaly data for North America.	83
IV.10	Positive (0.0 to 1.0) correlation coefficients derived from correlation analysis (I-5).	86
IV.11	Negative (-1.0 to 0.0) correlation coefficients derived from correlation analysis (I-5).	87
IV.12	Histogram of correlation coefficients derived from correlation analysis (I-5).	88
IV.13	Slope ($\Delta j/\Delta m$) coefficients derived from correlation analysis (I-5).	89
IV.14	Intercept coefficients derived from correlation analysis (I-5).	90
IV.15	Positive (0.0 to 1.0) correlation coefficients derived from correlation analysis (II-5).	92
IV.16	Negative (-1.0 to 0.0) correlation coefficients derived from correlation analysis (II-5).	93

Figure		Page
IV.17	Histogram of correlation coefficients derived from correlation analysis (II-5)	94
IV.18	Slope ($\Delta j/\Delta m$) coefficients derived from correlation analysis (II-5)	95
IV.19	Intercept coefficients derived from correlation analysis (II-5).	96
IV.20	Selected correlations at 450 km elevation between the radial first order radially polarized magnetic anomaly derivatives and the radial second order free-air gravity anomaly derivatives for North America	98
IV.21	Positive (0.0 to 1.0) correlation coef- ficients derived from correlation analysis (III-3)	99
IV.22	Negative (-1.0 to 0.0) correlation co- efficients derived from correlation analysis (III-3)	100
IV.23	Histogram of correlation coefficients derived from correlation analysis (III-3).	101
IV.24	Slope ($\Delta j/\Delta m$) coefficients derived from correlation analysis (III-3).	102
IV.25	Intercept coefficients derived from correlation analysis (III-3)	103
IV.26	High-cut ($\lambda \leq 8^\circ$) filtered positive (0.0 to 1.0) correlation coefficients derived from correlation analysis (III-3).	105
IV.27	High-cut ($\lambda \leq 8^\circ$) filtered negative (-1.0 to 0.0) correlation coefficients derived from correlation analysis (III-3).	106
IV.28	High-cut ($\lambda \leq 8^\circ$) filtered slope ($\Delta j/\Delta m$) coefficients derived from correlation analysis (III-3)	107
IV.29	High-cut ($\lambda \leq 8^\circ$) filtered intercept coefficients derived from correlation analysis (III-3)	108

Figure		Page
IV.30	Gravity and magnetic anomaly correspondence at satellite elevations along 37° N latitude between 238° E and 284° E longitude. A) First radial free-air gravity derivatives (dotted profile) and radially polarized magnetic anomalies from Figures IV.4 and 6, respectively. B) Second radial free-air gravity derivatives (dotted profile) and smoothed first radially polarized magnetic anomaly derivatives from Figures IV.5 and 9, respectively. C) Unfiltered and high-cut filtered (dotted profile) correlation coefficients from correlation analysis (III-3). D) Unfiltered and high-cut filtered (dotted profile) slope values from Figures IV.24 and 28, respectively	110
V.1	Gravity and magnetic anomaly modeling in spherical coordinates of a geologic body with arbitrary shape and physical properties by Gauss-Legendre quadrature integration (see text for details)	117
V.2	Gravity anomaly comparisons for a spherical prism.	125
V.3	Magnetic anomaly comparisons for a spherical prism.	127
V.4	Magnetic anomaly comparisons for a spherical prism where the Gauss-Legendre quadrature solution (B) is developed from interpolated limits of integration	128
V.5	Vertical (A) and horizontal (B) vector magnetic anomaly components for a spherical prism.	129
V.6	Remanent magnetic anomaly comparisons for a spherical prism.	131
V.7	A) SEAP projection of crustal thickness anomaly model geometry adapted from Warren and Healy (1973). The model is referenced to a body point grid which gives latitude, longitude, and top and bottom radial coordinates for the 9 points of the model's surface envelope used to interpolate the variable volume limits of integration. The shape of the thickened crust (10 km) is indicated by the 50 km depth contour on which the grid is superimposed.	

Figure		Page
	B) SEAP projection of the gravity anomaly for the crustal thickness model calculated at 450 km elevation by Gauss-Legendre quadrature integration	133
V.8	A) SEAP projection of total magnetic intensity anomaly for the crustal thickness model computed in the IGRF-1965 updated to 1968 by Gauss-Legendre quadrature integration. B) SEAP projection of reduced to the pole magnetic anomaly for the crustal thickness model by Gauss-Legendre quadrature integration using a normalized polarizing amplitude of 60,000 gamma.	134
V.9	Relative precision of the gravity anomaly (A) and total magnetic intensity anomaly (B) calculations is essentially unchanged at 450 km elevation by a 93.75% reduction in the number of Gauss-Legendre nodes.	135
VI.1	Index map of the Mississippi Embayment (shaded contour) region where G is the gravity profile studied by Ervin and McGinnis (1975), R is the seismic refraction line studied by McCamy and Meyer (1966), and S is the surface wave propagation path studied by Austin and Keller (1979). The lateral subsurface boundary of the model generalized in Figure VI.2.C for this study also is indicated.	141
VI.2	Mississippi Embayment density models adapted from A) Ervin and McGinnis (1975) and B) Austin and Keller (1979). C) The density contrast model generalized for this study from Austin and Keller (1979). Body #2 with magnetization contrast -0.0024 emu/cm^3 also was used to model POGO satellite magnetometer data over the Embayment. D) The gravity data of Cordell (1977) used to develop the lateral subsurface configuration outlined in Figure VI.1 of the density contrast model generalized in C	142
VI.3	Mississippi Embayment satellite-level comparisons between Gauss-Legendre quadrature modeled gravity and magnetic anomalies and upward continued 1° -averaged free-air gravity and reduced to the pole POGO satellite magnetic anomaly data. Each anomaly field is plotted on a stereographic equal-area polar projection	145

Figure		Page
VI.4	Mississippi Embayment satellite-level profile comparisons between Gauss-Legendre quadrature modeled gravity anomaly and observed upward continued 1° -averaged free-air gravity anomaly data along 35°N latitude. The shaded region indicates the location of the generalized Mississippi Embayment crustal model along the profile.	146
VI.5	Mississippi Embayment satellite-level profile comparisons between Gauss-Legendre quadrature modeled gravity anomaly and observed upward continued 1° -averaged free-air gravity anomaly data along 37°N latitude. The shaded region indicates the location of the generalized Mississippi Embayment crustal model along the profile.	147
VI.6	Mississippi Embayment satellite-level profile comparisons between Gauss-Legendre quadrature modeled magnetic anomaly and high-pass ($\lambda \leq 10^\circ$) filtered reduced to the pole POGO satellite observed magnetic anomaly data along 35°N latitude. The shaded region indicates the location of the generalized Mississippi Embayment crustal model along the profile.	150
VI.7	Mississippi Embayment satellite-level profile comparisons between Gauss-Legendre quadrature modeled magnetic anomaly and high-pass ($\lambda \leq 10^\circ$) filtered reduced to the pole POGO satellite observed magnetic anomaly data along 37°N latitude. The shaded region indicates the location of the generalized Mississippi Embayment crustal model along the profile.	151

ABSTRACT

To facilitate geologic interpretation of satellite elevation potential field data, analysis techniques are developed and verified in the spherical domain that are commensurate with conventional flat earth methods of potential field interpretation.

A powerful approach to the spherical earth problem relates potential field anomalies to a distribution of equivalent point sources by least squares matrix inversion. Linear transformations of the equivalent source field lead to corresponding geoidal anomalies, pseudo-anomalies, vector anomaly components, spatial derivatives, continuations, and differential magnetic pole reductions.

Correlation of gravity and magnetic anomalies combined with other geological and geophysical data is useful for enhancing the quality and uniqueness of the geological interpretation of potential anomaly fields. Equivalent point source inversion is used to investigate qualitative visual spatial correlations of surface free-air gravity and POGO satellite magnetic anomalies and regional heat flow and tectonic data for North America and adjacent marine areas. A more quantitative analysis of the regional potential field anomaly correlations at satellite elevations also is considered utilizing Poisson's theorem in a moving-window linear regression analysis between suitable derivatives of the anomalous gravity and magnetic potentials.

An inverse relationship is observed qualitatively and quantitatively between long-wavelength gravity and magnetic anomalies over continental terrane. Regional correlations of negative gravity and positive magnetic anomalies characterize areas of large relative crustal thickness and magnetization as exemplified by a prominent magnetic high which corresponds to a gravity minima trend extending from the Anadarko Basin to the Cincinnati Arch. Negative magnetic and positive gravity anomalies characterize thinner crust and regions of higher heat flow such

as the Cordillera of North and Central America and the Yellowstone geothermal region. Over oceanic areas gravity and magnetic anomalies show limited correlation.

The capacity to model potential field anomalies is essential to verifying and detailing the lithospheric interpretation of these data. Gauss-Legendre quadrature integration is used to develop a versatile procedure for numerically modeling anomalous gravity and magnetic potentials and their spatial derivatives on a spherical earth due to a geologic body of arbitrary shape and physical properties. The procedure is well suited for satellite potential field modeling because the accuracy and efficiency improves with increasing distance between source and observation points.

The spherical earth modeling procedure is used to investigate Mississippi Embayment crustal structure synthesized from published surface wave dispersion, seismic refraction and Bouguer gravity anomaly studies of the region. Modeled gravity and magnetic anomaly comparisons with upward continued free-air gravity and reduced to the pole POGO satellite magnetic anomalies of the area support the failed-rift (aulacogen) hypothesis for the origin of the Mississippi Embayment. These results indicate that an aulacogen at satellite elevations is characterized by observable positive gravity and negative magnetic anomalies derived primarily from a high-density rift component of non-magnetic lower crustal material.

The procedures and results of this investigation provide a comprehensive approach to the lithospheric analysis of potential field anomalies in the spherical domain and, hence, have widespread application in the analysis and design of satellite gravity and magnetic surveys for geological investigation.

I. INTRODUCTION

A. Statement of the Problem

The theory of plate tectonics has revolutionized the geosciences by explaining paleo and contemporary geodynamics, as well as providing new insight into the processes which lead to mineral and petroleum deposits and unifying much of our geological knowledge into a coherent principle. The origin and much of the development of this concept has been based largely upon regional surveys and observations made in remote areas of the earth. The plate tectonics concept was triggered in fact by regional magnetic surveys of the ocean basins and earthquake epicenter and foci locations in areas generally remote from the scientific centers of the world.

Today we have entered a period where technological developments offer the promise of another quantum jump in our knowledge of the earth. This technological development, satellite observations, already has had a tremendous impact upon surface-derived spectral information through the ERTS and LANDSAT programs. Now these observations are being turned toward the study of the subsurface and in particular the earth's lithosphere.

Satellite observations have three principal advantages for the measurement of potential fields that are related to lithospheric variations. First, data can be obtained from the entire earth - no region is too remote for observation - and patterns difficult to measure and perceive in surface or near-surface data are delineated by the broad data coverage. Second, satellite observations form a consistent data set free from non-uniformity caused by problems such as secular variations in force fields and differences between continental and oceanic observations. Lastly, force fields observed from satellites, such as

magnetic fields, are potential fields whose intensity is strongly dependent on the source to sensor distance. Thus, satellite-elevation observations are largely free from the near-surface geologic sources which tend to mask or distort the signatures of deep, broad lithospheric variations.

Of course, these advantages are negated in many applications because of the loss of resolving power with increased source to sensor distance. However, this is not necessarily the case for applications related to defining lithospheric provinces. On the contrary, the integration of the field expression of multiple sources permits the characterization of attributes of geologically significant lithospheric regions measured in hundreds or even thousands of kilometers. These zones identified and characterized on a global basis should provide useful information for deciphering earth history including paleo and contemporary geodynamics, delineation of segments of the lithosphere into resource provinces, and for numerical modeling of lithospheric processes.

The realization of the importance of these observations has led to increased availability of highly accurate data for analysis. However, commensurate advances in procedures to analyze and interpret these data for lithologic information have not kept pace and are unavailable generally. The overall objective of this investigation is aimed toward rectifying this problem which currently limits the utility of satellite potential field data in lithospheric studies.

B. Objectives

Geologic interpretation of conventional low-level or ground-based gravity and magnetic survey data relies on a sophisticated arsenal of procedures to analyze the anomalies in the Cartesian plane. Conventional applications of procedures such as continuation, differentiation, magnetic reduction to the pole, etc., involve simplifying assumptions which generally do not hold over large areas of a spherical earth that also exhibit considerable variations of geomagnetic field amplitude, declination and

inclination. Accordingly, attempts to directly adapt these procedures for analysis of regional-scale survey data registered in degrees of latitude and longitude are problematic and difficult to accomplish.

An alternative approach is described and demonstrated in section II whereby many of the objectives of conventional processing technology can be achieved accurately and efficiently for gravity and magnetic anomalies registered in spherical coordinates. The procedure involves relating the potential anomaly field to a spherical distribution of equivalent point sources by least squares matrix inversion. The processing objective then can be computed in spherical coordinates directly from the equivalent point source distribution.

However, the geologic interpretation of gravity and magnetic anomaly data, even when suitably processed, often leads to ambiguous results because of interfering anomalies, inadequate anomaly resolution and the multiplicity of equivalent anomaly sources. An important and time-honored technique for reducing this ambiguity is to analyze the correlations between the potential field anomalies along with other classes of geophysical data. Gravity and magnetic data are particularly suited for correlation analysis because anomalies in gravity and magnetic fields often are related genetically, although it is clear that the lack of anomaly correlation also can provide significant information for the geologic interpretation of these data.

In section III, equivalent point source inversion is used to prepare long-wavelength gravity and magnetic anomaly fields over North America and adjacent oceanic regions for visual spatial correlation with each other and regional heat flow and tectonic data. POGO satellite magnetic anomalies are differentially reduced to the pole so that the data uniformly reflect source magnetization characteristics. Surface free-air gravity anomaly values also are upward continued to satellite elevations for comparison with the magnetic data and the long-wavelength, low order and degree spherical harmonic representation of heat flow.

A more quantitative approach to the correlation of these potential field anomalies is investigated in section IV. Here, Poisson's theorem is used in a moving-window linear regression analysis performed between

suitable derivatives of the anomalous gravity and magnetic potentials which are developed from equivalent point source inversion processing. The regression parameters generated by moving-window Poisson's analysis are useful for establishing patterns of correlation and non-correlation between the potential field anomalies. For spatially correlating gravity and magnetic anomalies these results include an initial estimate of the ratio of physical property contrasts for the inferred source to facilitate further investigation and modeling.

Modeling provides critical data for effective survey design and serves as an efficient approach for verifying and detailing anomaly interpretation. A technique is described and demonstrated in section V which utilizes Gauss-Legendre quadrature integration to numerically model gravity and magnetic anomalies in spherical coordinates due to a geologic source with arbitrary shape and physical properties. This procedure is used in section VI to model satellite-elevation gravity and magnetic signatures of the crustal structure of the Mississippi Embayment for comparison with the POGO satellite magnetic data and upward continued free-air gravity anomalies.

In general, sections II through VI attempt to describe and verify techniques for generalized processing (e.g., differentiation, continuation, regridding, etc.), correlation analysis and modeling of potential field anomalies in the spherical domain that are commensurate with geophysical procedures of potential field interpretation enjoying widespread acceptance in conventional flat earth applications. These sections are documented so that they are individually complete and, hence, each section can be considered on an independent basis. However, because the spherical earth procedures are demonstrated principally by analyses of POGO satellite magnetic and surface free-air gravity anomaly data for North America, this documentation style includes some unavoidable repetition regarding the description of these data sets.

Finally, in section VII the results of this investigation are reviewed in the context of utilizing satellite potential field measurements for lithospheric analysis.

II. SPHERICAL EARTH GRAVITY AND MAGNETIC ANOMALY ANALYSIS BY EQUIVALENT POINT SOURCE INVERSION

A. Abstract

Artificial, earth-orbiting satellites are making increasingly available consistent, regional-scale potential field data which offer the promise of greatly enhancing our understanding of the structure, dynamics and geological history of the earth's crust and upper mantle. To realize this promise, procedures are required for lithospheric analysis of gravity and magnetic anomalies registered in spherical coordinates. An efficient and powerful approach to the spherical earth problem is to relate regional potential field anomalies to a spherical distribution of equivalent point sources by least squares matrix inversion. Simple linear transformations of the corresponding equivalent point source field yield a number of geophysically interesting quantities for the potential field anomalies because the anomalous potential and its spatial derivatives of all orders are linearly related. For gravity anomalies, for example, equivalent point source inversion can be used to compute corresponding geoidal deflections, anomaly continuations, vector anomaly components and derivatives at any point in source-free space. Similarly, for magnetic anomalies equivalent point source inversion can give least squares estimates at any point in source-free space of the vector anomaly components, anomaly continuations and spatial derivatives, as well as the magnetic anomalies differentially reduced to the pole. Pseudo-potential field anomalies also are available from equivalent point source inversion. A number of examples using 1° -averaged surface free-air gravity anomalies and POGO satellite magnetometer data for the United States, Mexico and Central America illustrate the capabilities of the method.

B. Introduction

Regional-scale anomalies of the earth's magnetic and gravity fields provide important constraints for refining the basic model of plate tectonics and understanding intra-plate dynamics. These anomalies, especially when combined with other geophysical and geological data, may be anticipated to yield much information concerning regional physical property variations that are important for determining the structure, dynamics and geological history of the earth's crust and upper mantle. The realization of the importance of these observations has led to increased availability of highly accurate regional-scale potential field data for analysis. Commensurate advances in data analysis for lithospheric interpretation, however, have not kept pace and generally are unavailable.

Regional gravity and magnetic surveys represent spherically composited data for areas ranging in size from a few degrees to complete global coverage by satellite measurements. Typical processing objectives include data regridding, continuation, differentiation, and other wavelength filtering operations. For regional magnetic surveys it also is desirable from the standpoint of lithospheric interpretation to reduce the data for the variable geomagnetic field effects of inclination, declination and intensity.

Spherical surface harmonic functions are a natural representation for spherically registered gravity and magnetic anomaly fields. In general, spherical harmonics also are well suited for accomplishing the processing objectives described above because these operations involve only modifications of the geometric variables of the anomalies. However, the problem of representing potential field measurements over a spherical domain with an orthonormal set of spherical harmonic functions in general is a formidable task of computation (e.g., Kaula, 1967), especially when it is desired to retain for analysis higher order and degree terms involving wavelengths of the order of a few hundred kilometers or less.

When potential field anomalies are spherically registered at constant elevation, Fourier transform methods yield a simpler

numerical representation of the data which is suitable for strike-sensitive and wavelength filtering. These filters are applicable because the frequency response of the potential field anomaly is invariant for any uniform orthogonal translation of the degree-coordinates of the anomaly over the spherical domain. As an example, low-pass filtering a set of 1° -averaged free-air gravity anomalies can be useful to help eliminate topographic mass contributions, where it is noted that topographic mass effects tend to be minimized when free-air gravity anomalies are averaged over areas of the order 3° and larger (Woollard, 1962; Strange and Woollard, 1964).

Fourier transform methods applied in the spherical domain to discriminate anomaly source characteristics, however, normally necessitate regridding of the data to a Cartesian plane. The regridding procedure with all its attendant problems is required in such cases because the Fourier frequency characterization of an anomaly is variant for spherical translations of the anomaly source. Continuation and differentiation by Fourier transform methods also require Cartesian reregistration of the data to avoid distortions due to a Nyquist degree-wavelength which is variable in terms of the linear radial dimension of these operations.

Another approach to spherical earth processing is to invert potential field anomalies on a spherical distribution of equivalent point sources. In contrast to processing by spherical harmonics or Fourier transform methods, equivalent point source inversion yields numerically efficient representations of potential field anomalies to any desired degree of wavelength resolution which can be directly processed in the spherical domain.

In principle, equivalent point source inversion takes advantage of the ambiguity of source physical properties and distributions which is a feature inherent to all potential field anomalies. Every potential field observation, for example, represents the integrated effect of sources which may be characterized with equal facility by an infinite number of combinations of source physical properties and geometric parameters (e.g., Ramsey, 1940; Kellogg, 1954). The objective, then, is to relate a set of spherically registered potential field measurements to a distribution of equivalent sources with numerical properties which are amenable to spherical earth processing objectives.

Especially convenient from a numerical standpoint are equivalent point sources because the characteristics of their gravity and magnetic potentials are simplest to describe mathematically. As will be demonstrated, the point source potential and all its geophysically interesting derivatives can always be expressed as the product of an appropriate physical property value and a purely geometrical point source function which describes the inverse distance between source and observation points. By specifying the geometrical distribution of the equivalent point sources, the problem reduces to one of determining a set of physical property values by matrix inversion techniques such that the potential field anomalies due to the equivalent point source distribution approximate the observed anomalies to a specified precision. Thus, once a suitable set of physical property values has been found, the equivalent source field representation of the observed anomalies is calculated by summing at each observation point the anomaly effect due to each of the equivalent point sources. To obtain an equivalent source field representation of the continuation, differentiation, etc. of the observed anomalies to the same degree of precision as reflected in the original approximation, the summation procedure is simply repeated using the appropriate geometrical point source function.

To further illustrate the mechanism and versatility of equivalent point source inversion, it is desirable to develop explicitly the properties of gravity point poles and magnetic point dipoles which facilitate analyses of potential field anomalies in the spherical domain for subsurface information that are analogous to conventional flat earth methods of geophysical interpretation.

C. The Gravity Point Pole Potential

The gravity point pole is defined as a source of negligible diameter when compared to the distance between the source and observation points. Its scalar gravitational potential $GP(R)$ at a point with spherical coordinates (r, θ, ϕ) located a distance \vec{R} from the source point (r_1, θ_1, ϕ_1) is given by

$$GP(R) = \frac{G \Delta m}{|\vec{r} - \vec{r}_1|} = \frac{G \Delta m}{R}, \quad \text{where} \quad (II-1)$$

G = universal gravitational constant ($=6.67 \cdot 10^{-8} \text{ cm}^3/(\text{gm} \cdot \text{sec}^2)$),

Δm = mass contrast of the point pole,

$$R = |\vec{r} - \vec{r}_1| = (r^2 + r_1^2 - 2rr_1 \cos \delta)^{1/2}, \quad (II-2)$$

\vec{r} = radius vector directed from observation point (r, θ, ϕ) to earth's center,

\vec{r}_1 = radius vector directed from source point (r_1, θ_1, ϕ_1) to earth's center,

δ = angle between \vec{r} and \vec{r}_1 at the observation point (r, θ, ϕ) , such that $\cos \delta = \cos \theta \cos \theta_1 + \sin \theta \sin \theta_1 \cos(\phi - \phi_1)$,

θ, θ_1 = co-latitude coordinates of observation and source points, respectively, and

ϕ, ϕ_1 = longitude coordinates of observation and source points, respectively.

The geometric characteristics of the point source potential are illustrated in Figure II.1.

Because of the dependence of the potential on the inverse of the distance R , the derivatives of the point pole potential $GP(R)$ are linearly related by the relationship

$$\frac{\partial^n}{\partial R^n} \left(\frac{1}{R^k} \right) = \frac{(-1)^n}{R^{k+n}} \cdot \frac{(k+n-1)!}{(k-1)!}. \quad (II-3)$$

This result provides a useful function for considering derivatives of the potential.

Now, the vector gravitational force field $GF(\vec{R})$ at the distance \vec{R} is given in spherical coordinates by the negative gradient of the scalar point pole potential as

$$GF(\vec{R}) = -\vec{\nabla}(GP(R)) = -\frac{\partial}{\partial R} \{ GP(R) \} \vec{\nabla} R = \left\{ -G \frac{\partial}{\partial R} \left(\frac{1}{R} \right) \vec{\nabla} R \right\} \Delta m, \quad \text{where}$$

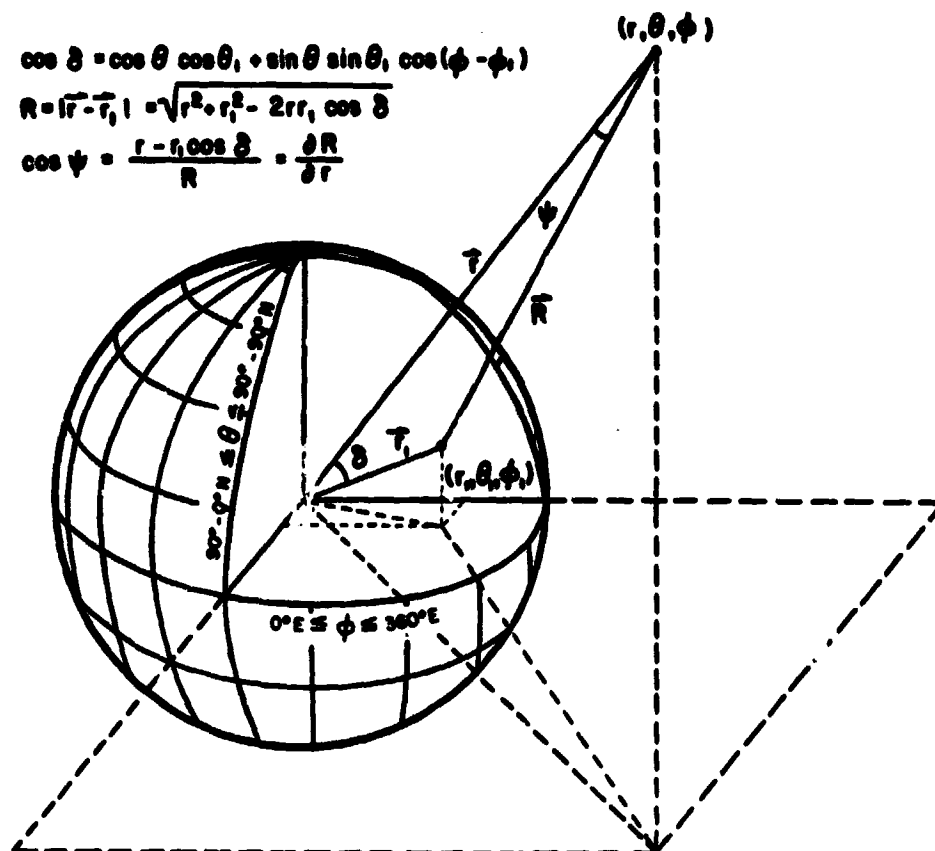
the gradient of R is

$$\vec{\nabla} R = \frac{\partial R}{\partial r} \hat{e}_r + \frac{1}{r} \frac{\partial R}{\partial \theta} \hat{e}_\theta + \frac{1}{r \sin \theta} \frac{\partial R}{\partial \phi} \hat{e}_\phi, \quad \text{such that}$$

$$\frac{\partial R}{\partial r} = \frac{r - r_1 \cos \delta}{R} = \frac{\lambda}{R}, \quad (II-4)$$

GEOMETRY OF EQUIVALENT POINT SOURCE INVERSION

$$\begin{aligned}\cos \delta &= \cos \theta \cos \theta_1 + \sin \theta \sin \theta_1 \cos(\phi - \phi_1) \\ R &= |\vec{r} - \vec{r}_1| = \sqrt{r^2 + r_1^2 - 2rr_1 \cos \delta} \\ \cos \psi &= \frac{r - r_1 \cos \delta}{R} = \frac{\partial R}{\partial r}\end{aligned}$$



GRAVITY ANOMALY

$$\begin{aligned}\Delta g &= \left[-G \frac{\partial}{\partial R} \left(\frac{1}{R} \right) \frac{\partial R}{\partial r} \right] = \Delta m \\ &= q_{np}(R) = \Delta \pi_p\end{aligned}$$

MAGNETIC ANOMALY

$$\begin{aligned}\Delta T &= \left[-\vec{u} \cdot \vec{\nabla} \left\{ \vec{u} \cdot \vec{\nabla} \left(\frac{1}{R} \right) \right\} \right] = \Delta i \\ &= q_{np}(R) = \Delta \pi_p\end{aligned}$$

THE INVERSION PROBLEM

For a set of n -observations (OBS) and a set of p -point source geometric functions (Q) find a set of p -physical property values (ΔX) such that

$$Q(r, \theta, \phi, r_1, \theta_1, \phi_1) = \Delta X = \text{OBS}(r, \theta, \phi)$$

Figure II.1 Gravity and magnetic anomaly analysis in spherical coordinates by equivalent point source inversion (see text for details).

$$\frac{1}{r} \frac{\partial R}{\partial \theta} = \frac{r_1 (\sin \theta \cos \theta_1 - \cos \theta \sin \theta_1 \cos(\phi - \phi_1))}{R} = \frac{B}{R} \quad (\text{II-5})$$

$$\frac{1}{r \sin \theta} \frac{\partial R}{\partial \phi} = \frac{r_1 \sin \theta_1 \cos(\phi - \phi_1)}{R} = \frac{C}{R}, \quad \text{and} \quad (\text{II-6})$$

\hat{e}_r , \hat{e}_θ and \hat{e}_ϕ are the spherically orthogonal basis vectors. Accordingly, the gravitational force field at (r, θ, ϕ) is given by

$$\vec{F}(\vec{R}) = \left\{ -G \frac{\partial}{\partial R} \left(\frac{1}{R} \right) \left(\frac{A}{R} \hat{e}_r + \frac{B}{R} \hat{e}_\theta + \frac{C}{R} \hat{e}_\phi \right) \right\} \Delta m, \quad (\text{II-7})$$

where the radial scalar component is

$$\Delta g = \left\{ -G \frac{\partial}{\partial R} \left(\frac{1}{R} \right) * \frac{\partial R}{\partial r} \right\} \Delta m = \left\{ \frac{G * A}{R^3} \right\} \Delta m, \quad (\text{II-8})$$

the horizontal θ -co-latitude scalar component is

$$\left\{ -G \frac{\partial}{\partial R} \left(\frac{1}{R} \right) * \left(\frac{1}{r} \frac{\partial R}{\partial \theta} \right) \right\} \Delta m = \left\{ \frac{G * B}{R^3} \right\} \Delta m, \quad \text{and} \quad (\text{II-9})$$

the horizontal ϕ -longitude scalar component is

$$\left\{ -G \frac{\partial}{\partial R} \left(\frac{1}{R} \right) * \left(\frac{1}{r \sin \theta} \frac{\partial R}{\partial \phi} \right) \right\} \Delta m = \left\{ \frac{G * C}{R^3} \right\} \Delta m. \quad (\text{II-10})$$

Also, because

$$\left\{ \frac{\partial GP(R)}{\partial R} \right\}^2 = \left\{ \frac{\partial GP(R)}{\partial R} \right\}^2 * \left\{ \left(\frac{\partial R}{\partial r} \right)^2 + \left(\frac{1}{r} \frac{\partial R}{\partial \theta} \right)^2 + \left(\frac{1}{r \sin \theta} \frac{\partial R}{\partial \phi} \right)^2 \right\},$$

the total horizontal component of the gravitational force field (II-7) can be expressed in terms of the radial component (II-8) as

$$\frac{\partial GP(R)}{\partial R} \left\{ \left(\frac{1}{r} \frac{\partial R}{\partial \theta} \right)^2 + \left(\frac{1}{r \sin \theta} \frac{\partial R}{\partial \phi} \right)^2 \right\} = \Delta g \left\{ \left(\frac{R}{A} \right)^2 - 1 \right\}. \quad (\text{II-11})$$

In relating a set of gravity observations to equation (II-7), it is important to recognize the distinction between the total gravity anomaly and the gravity effect due to local geologic mass variations. In geophysical practice, the quantity which is considered is the anomalous perturbation of the radial component of the earth's geocentric gravitational field. The use of this quantity, which commonly is called the gravity effect, Δg , for lithospheric analysis assumes the gravity anomaly due to geological mass variations is so small that perturbations of the earth's gravity field in any direction other than the normal are negligible. Thus, when relating an observed gravity anomaly value

to the gravitational force field of a point pole, the objective is to express the observed gravity effect as the radial component of equation (II-7) which is given by equation (II-8).

For lithospheric interpretation, it frequently is desirable to analyze the spatial derivatives of the gravity anomalies. Differentiation of a set of regional-scale gravity observations, for example, can help identify the higher frequency crustal components of the anomaly field. The derivatives also provide useful information for modeling the geometric characteristics of anomalous sources.

To obtain equivalent source field representations of the spatial derivatives for a set of gravity observations it is necessary to develop the spatial derivatives of the gravity effect of the gravity point pole. The first order derivative components of the point pole gravity effect can be calculated from the negative gradient as

$$\begin{aligned} -\vec{\nabla}(\Delta g) &= -G \left\{ \vec{\nabla} \left(\frac{A}{R^3} \right) \right\} \Delta m = -G \left\{ A \vec{\nabla} \left(\frac{1}{R^3} \right) + \left(\frac{1}{R^3} \right) \vec{\nabla} A \right\} \Delta m \\ &= \left\{ -G \left(A \frac{\partial}{\partial R} \left(\frac{1}{R^3} \right) + \left(\frac{1}{R^3} \right) \frac{\partial A}{\partial R} \right) \vec{R} \right\} \Delta m, \end{aligned} \quad (\text{II-12})$$

where the components of $\vec{\nabla} R$ are given by equations (II-4, 5 and 6). Now, to evaluate $(\partial A / \partial R)$ note that $(\partial A / \partial r) = (\partial A / \partial R) (\partial R / \partial r) = 1$ and, hence,

$$(\partial A / \partial R) = R/A. \quad (\text{II-13})$$

Accordingly, equation (II-12) becomes

$$-\vec{\nabla}(\Delta g) = \left\{ -G \left(\frac{1}{R^2 A} - \frac{3A}{R^4} \right) + \left(\frac{A}{R} \hat{e}_r + \frac{B}{R} \hat{e}_\theta + \frac{C}{R} \hat{e}_\phi \right) \right\} \Delta m,$$

where the scalar first radial derivative of Δg is given by

$$\frac{-\partial \Delta g}{\partial r} = \left\{ -G \left(\frac{1}{R^3} - \frac{3A^2}{R^5} \right) \right\} \Delta m, \quad (\text{II-14})$$

the scalar first horizontal θ -co-latitude derivative of Δg is derived from

$$-\frac{1}{r} \frac{\partial \Delta g}{\partial \theta} = \left\{ -G \left(\frac{B}{R^3 A} - \frac{3AB}{R^5} \right) \right\} \Delta m, \quad (\text{II-15})$$

and the first horizontal ϕ -longitudinal derivative of Δg is obtained from

$$\frac{-1}{r \sin \theta} \frac{\partial \Delta g}{\partial \phi} = \left\{ -G \left(\frac{C}{R^3} - \frac{3AC}{R^5} \right) \right\} \Delta m. \quad (\text{II-16})$$

Also, by the same argument which led to the development of equation (II-11) it can be shown that the total horizontal gradient of Δg may be expressed in terms of its radial derivative according to the relation

$$\frac{\partial \Delta g}{\partial R} \left\{ \left(\frac{1}{r} \frac{\partial R}{\partial \theta} \right)^2 + \left(\frac{1}{r \sin \theta} \frac{\partial R}{\partial \phi} \right)^2 \right\} = \frac{\partial \Delta g}{\partial r} \left\{ \left(\frac{R}{A} \right)^2 - 1 \right\}. \quad (\text{II-17})$$

Another useful tool for lithospheric interpretation is the Laplacian which, in terms of the gravity effect of the point pole, is given by

$$\begin{aligned} \nabla^2 (\Delta g) &= \frac{1}{r^2} \frac{\partial}{\partial r} \left(r^2 \frac{\partial \Delta g}{\partial r} \right) + \frac{1}{r^2 \sin \theta} \frac{\partial}{\partial \theta} \left(\sin \theta \frac{\partial \Delta g}{\partial \theta} \right) + \frac{1}{r^2 \sin^2 \theta} \frac{\partial^2 \Delta g}{\partial \phi^2} \\ &= \left\{ \frac{\partial^2 \Delta g}{\partial r^2} + \frac{2}{r} \frac{\partial \Delta g}{\partial r} \right\} + \left\{ \frac{1}{r^2} \frac{\partial^2 \Delta g}{\partial \theta^2} + \frac{1}{r^2} \cot \theta \frac{\partial \Delta g}{\partial \theta} \right\} + \left\{ \frac{1}{r^2 \sin^2 \theta} \frac{\partial^2 \Delta g}{\partial \phi^2} \right\}. \end{aligned}$$

Now, $\nabla^2 (\Delta g) = 0$ because Δg is a potential function and, hence,

$$-\left\{ \frac{\partial^2 \Delta g}{\partial r^2} + \frac{2}{r} \frac{\partial \Delta g}{\partial r} \right\} = \frac{1}{r^2} \left\{ \frac{\partial^2 \Delta g}{\partial \theta^2} + \cot \theta \frac{\partial \Delta g}{\partial \theta} + \frac{1}{\sin^2 \theta} \frac{\partial^2 \Delta g}{\partial \phi^2} \right\}, \quad (\text{II-18})$$

where $(\partial \Delta g / \partial r)$ is evaluated in (II-14) and the second radial derivative is given by

$$\frac{\partial^2 \Delta g}{\partial r^2} = \frac{\partial}{\partial R} \left\{ \frac{\partial \Delta g}{\partial r} \right\} \frac{\partial R}{\partial r} = G \left\{ \frac{15A^3}{R^7} - \frac{9A}{R^5} \right\} \Delta m. \quad (\text{II-19})$$

Equation (II-18) relates the horizontal gravity anomaly curvature to the radial curvature which is the Laplacian component normally computed for analysis. Because of the dependence of the Laplacian on first and second order derivatives it is especially sensitive to higher frequency anomalies. Hence, relating a set of regional scale gravity observations to the radial Laplacian component given by (II-18) can be useful for studying the shallower crustal anomaly components of the data. Also, the zero contour of equation (II-18) can be used to roughly delineate the lateral extent of the anomaly source because the edges of the source are approximated by the inflection points of the anomaly which correspond to zero curvature. From the sign convention used in equation (II-18) it is obvious that the zero contour

which delineates regions of positive or negative radial Laplacian values outlines, respectively, regions of positively or negatively contrasting densities.

In consideration of the foregoing derivations it is clear that the results of this section are linearly related by geometry through equation (II-3). Hence, once a set of gravity observations has been suitably related to a distribution of point poles according to equation (II-8), then all the variables necessary for evaluating the gravitational potential, anomaly vector components and spatial derivatives, as well as the continuation of any of these quantities, also have been determined for the observation set.

D. The Magnetic Point Dipole Potential

The magnetic point dipole is defined as a dipole of negligible length when compared to the distance between the dipolar source and observation points. Its scalar magnetic potential $MP(R)$ evaluated at the observation point (r, θ, ϕ) located a distance \vec{R} from the source point (r_1, θ_1, ϕ_1) is given by

$$MP(R) = \Delta \vec{j} \cdot \vec{\nabla}_1 \left(\frac{1}{R} \right) = -\Delta \vec{j} \cdot \vec{\nabla} \left(\frac{1}{R} \right), \quad \text{where} \quad (II-20)$$

$\vec{\nabla}_1$ = the gradient operator in source point coordinates such that $\vec{\nabla}_1 \left(\frac{1}{R} \right) = -\vec{\nabla} \left(\frac{1}{R} \right)$ in observation point coordinates,

R = given in (II-2), and

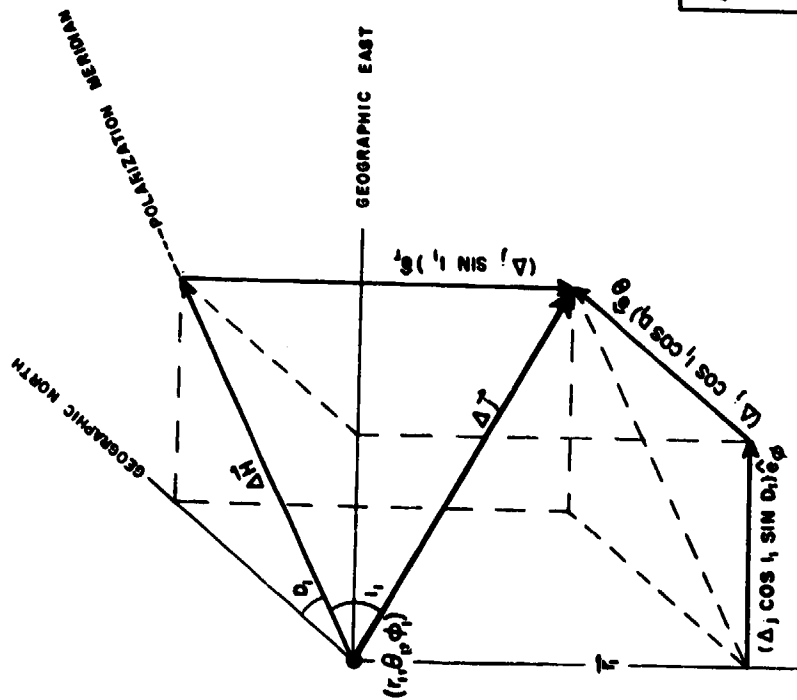
$\Delta \vec{j}$ = the magnetic polarization contrast vector of the source point.

The relationships between source point and observation point geometry are illustrated in Figure II.1.

As shown in Figure II.2, the polarization contrast vector may be expressed in terms of its inclination, I_1 , and declination, D_1 , and the spherically orthonormal basis vectors of the source point as

$$\Delta \vec{j} = \Delta j * \vec{u}_1 = \Delta j * \{ (\sin I_1) \hat{e}_r + (\cos I_1 \cos D_1) \hat{e}_\theta + (\cos I_1 \sin D_1) \hat{e}_\phi \}, \quad (II-21)$$

where \vec{u}_1 = the unit polarization field vector. Here, it should be noted that if polarization is induced only, then the polarization contrast is given by



SCALAR MAGNETIC POLARIZATION ELEMENTS

$\Delta H = \Delta j \cos \theta_1$	(HORIZONTAL COMPONENT)
$\Delta j(r_1) = \Delta j \sin \theta_1$	(RADIAL COMPONENT)
$\Delta H \tan \theta_1$	
$\Delta j(\theta) = \Delta H \cos \theta_1$	(LATITUDE COMPONENT)
$\Delta j(\phi) = \Delta H \sin \theta_1$	(LONGITUDE COMPONENT)
$\Delta H^2 = \Delta j(\theta)^2 + \Delta j(\phi)^2$	
$\Delta j^2 = \Delta j(\theta)^2 + \Delta j(\phi)^2 + \Delta j(r_1)^2$	
$\Delta H^2 = \Delta j(\theta)^2 + \Delta j(\phi)^2$	

MAGNETIC POLARIZATION VECTOR

$$\begin{aligned} \Delta \vec{j} = \Delta j \vec{u}_1 &= \Delta j \left[(\sin \theta_1) \hat{e}_r + (\cos \theta_1 \cos \phi_1) \hat{e}_\theta + (\cos \theta_1 \sin \phi_1) \hat{e}_\phi \right] \\ &= \Delta \vec{j}(r_1) + \Delta \vec{j}(\theta) + \Delta \vec{j}(\phi) \end{aligned}$$

Figure II.2 Geometry of the magnetic polarization contrast vector, $\Delta \vec{j}$, at the point (r_1, θ_1, ϕ_1) in terms of the orthonormal spherical basis vectors \hat{e}_r , \hat{e}_θ , and \hat{e}_ϕ . In the absence of remanence, the polarization of the point dipole at (r_1, θ_1, ϕ_1) is induced only and $\Delta \vec{j} = \Delta k \vec{F}_1$, where $\Delta k =$ volume magnetic susceptibility and \vec{F}_1 is the geomagnetic field vector with inclination and declination I_1 and D_1 , respectively.

$$\Delta \vec{j} = \Delta k * \vec{F}_1, \quad \text{where} \quad (\text{II-22})$$

Δk = the magnetic susceptibility contrast, and

\vec{F}_1 = the geomagnetic field vector at the source point such that

$$\vec{F}_1 = F_1 * \vec{u}_1.$$

According to equations (II-21) and (II-4, 5 and 6) the magnetic scalar potential of a point dipole reduces to

$$\begin{aligned} MP(R) &= -\Delta j \cdot \vec{\nabla} \left(\frac{1}{R} \right) = \{ -\vec{u}_1 \cdot \vec{\nabla} \left(\frac{1}{R} \right) \} \Delta j \\ &= \left\{ - \frac{\partial}{\partial R} \left(\frac{1}{R} \right) * \vec{u}_1 \cdot \vec{\nabla}_R \right\} \Delta j \\ &= \frac{\Delta j}{R^2} * \left\{ \sin I_1 \left(\frac{\partial R}{\partial r} \right) + \cos I_1 \cos D_1 \left(\frac{1}{r} \frac{\partial R}{\partial \theta} \right) + \cos I_1 \sin D_1 \left(\frac{1}{r \sin \theta} \frac{\partial R}{\partial \phi} \right) \right\} \\ &= \frac{\Delta j}{R^3} * \{ \sin I_1 (A) + \cos I_1 \cos D_1 (B) + \cos I_1 \sin D_1 (C) \} \\ &= \frac{\Delta j}{R^3} * E. \end{aligned} \quad (\text{II-23})$$

Now, the vector magnetic force field, $MF(\vec{R})$, at distance \vec{R} due to the point dipole scalar potential is given by

$$\begin{aligned} MF(\vec{R}) &= -\vec{\nabla}(MP(R)) = - \left\{ \vec{\nabla} \left(\frac{1}{R^3} \right) * E + \frac{1}{R^3} * \vec{\nabla} E \right\} \Delta j \\ &= - \left\{ \frac{\partial}{\partial R} \left(\frac{1}{R^3} \right) \vec{\nabla}_R * E + \frac{1}{R^3} \left(\frac{\partial E}{\partial R} \right) \vec{\nabla}_R \right\} \Delta j \\ &= MF(r) \hat{e}_r + MF(\theta) \hat{e}_\theta + MF(\phi) \hat{e}_\phi, \quad \text{where} \end{aligned} \quad (\text{II-24})$$

$$MF(r) = \left\{ \frac{-A}{R^4} * J \right\} \Delta j, \quad MF(\theta) = \left\{ \frac{-B}{R^4} * J \right\} \Delta j, \quad MF(\phi) = \left\{ \frac{-C}{R^4} * J \right\} \Delta j, \quad \text{and}$$

$$\begin{aligned} J &= \left(\frac{R}{A} - \frac{3A}{R} \right) \sin I_1 + \left(\frac{R r_1 \cos \delta}{B} - \frac{3B}{R} \right) \cos I_1 \cos D_1 + \\ &\quad \left(\frac{R r_1 \sin \theta \cos(\phi - \phi_1)}{C} - \frac{3C}{R} \right) \cos I_1 \sin D_1. \end{aligned}$$

Equation (II-24) is useful for representing vector magnetic anomaly data. However, most magnetic data taken for geophysical applications represent scalar total anomaly intensity measurements which contain no information to discriminate the vector components. For geophysical

interpretation, then, the assumption is made that the magnetic anomaly due to geological magnetization variations is so small that perturbations of the geomagnetic field in any direction other than its direction are negligible. Kontis and Young (1964) have shown this assumption to be reasonably valid for anomalies with amplitudes less than about 10,000 gamma* in the earth's magnetic field. Hence, for geophysical interpretation purposes, a total magnetic anomaly measurement is taken to represent a perturbation of the geomagnetic field along its direction at the point of measurement.

Thus, to represent a set of total intensity measurements in terms of the magnetic field of point dipoles it is necessary to compute equation (II-24) in the direction of the geomagnetic field at the observation points. This can be achieved by taking the vector dot product between equation (II-24) and the unit geomagnetic field vector, \vec{u} , at the observation point. Accordingly, the total magnetic anomaly, ΔT , at \vec{R} due to the point dipole is

$$\Delta T = \vec{u} \cdot \nabla (\vec{R}) = \{ -\vec{u} \cdot \nabla (\vec{u}_1 \cdot \nabla (\frac{1}{R})) \} \Delta j$$

$$= MF(r) \sin I + MF(\theta) \cos I \cos D + MF(\phi) \cos I \sin D, \quad (II-25)$$

where I and D are the inclination and declination, respectively, of the geomagnetic field at the observation point. In the application of equation (II-25) geomagnetic field models such as the IGRF-1965 (Cain et al., 1967) commonly are used to obtain pertinent values of (I_1, D_1, F_1) at the source point and (I, D) at the observation point.

Consideration of equation (II-25) in its expanded form suggests that the derivation of derivatives for total anomaly fields is likely to yield fairly complicated algebraic expressions. Fortunately, these expressions can be considerably simplified by reducing the data to the pole which in effect is an adjustment of the anomalies to what they would be if radially (vertically) polarized by a magnetic field of uniform intensity. In conventional applications the spatial scale of the magnetic survey is small enough that a single value of geomagnetic field inclination, declination and amplitude may be assumed for the pole reduction. Over regional-scale areas, however, magnetic anomalies must be differentially reduced to the pole for values of geomagnetic inclination, declination and amplitude which are variable at all source and observation point locations.

*) 1 gamma = 1 nanoTesla, nT

For total magnetic anomaly observations referenced to a distribution of equivalent point dipoles according to equation (II-25), differential reduction to radial polarization is readily achieved by setting $I=I_1=90^\circ$, $D=D_1=0^\circ$ and using the normalized polarization $\Delta j'$ given by $\Delta j' = \Delta j(N/F_1)$ where N is the desired polarizing amplitude. Accordingly, equation (II-25) reduced to the pole leads to a considerably simplified radial polarization anomaly $\Delta T(N)$ given by

$$\Delta T(N) = - \left\{ \frac{1}{R^3} - \frac{3A^2}{R^5} \right\} \Delta j'. \quad (\text{II-26})$$

An assumption which is implicit in the application of (II-26) is, of course, that the magnetic anomalies contain no appreciable component of remanence. When this condition holds, equation (II-26) can be used to adjust the magnetic observations so that they uniformly reflect anomaly source characteristics of geometry and magnetization. Because of this considerable practical significance to geophysical interpretation, the radially polarized anomaly, $\Delta T(N)$, in general is more suitable for derivative analysis than the total field anomaly, ΔT .

The first order spatial derivatives of a set of vertically polarized magnetic anomalies may be obtained from the negative gradient of (II-26) which is

$$-\vec{\nabla}(\Delta T(N)) = \vec{\nabla} \left\{ \frac{1}{R^3} - \frac{3A^2}{R^5} \right\} \Delta j' = \vec{\nabla} R \left\{ \frac{9}{R^4} - \frac{15A^2}{R^6} \right\} \Delta j',$$

where the scalar first radial derivative of $\Delta T(N)$ is given by

$$-\frac{\partial \Delta T(N)}{\partial r} = \left\{ \frac{15A^3}{R^7} - \frac{9A}{R^5} \right\} \Delta j', \quad (\text{II-27})$$

the scalar first horizontal θ -gradient component of $\Delta T(N)$ is

$$-\frac{1}{r} \frac{\partial \Delta T(N)}{\partial \theta} = \left\{ \frac{15A^2 B}{R^7} - \frac{9B}{R^5} \right\} \Delta j', \quad (\text{II-28})$$

and the scalar first horizontal ϕ -gradient component of $\Delta T(N)$ is

$$-\frac{1}{r \sin \theta} \frac{\partial \Delta T(N)}{\partial \phi} = \left\{ \frac{15A^2 C}{R^7} - \frac{9C}{R^5} \right\} \Delta j'. \quad (\text{II-29})$$

Also, because $\Delta T(N)$ is a potential function its Laplacian is zero, so that the radial Laplacian component of $\Delta T(N)$ may be equated with the horizontal component according to the relation

$$- \left\{ \frac{\partial^2 \Delta T(N)}{\partial r^2} + \frac{1}{r} \frac{\partial \Delta T(N)}{\partial r} \right\} = \quad (\text{II-30})$$

$$\frac{1}{r^2} \left\{ \frac{\partial^2 \Delta T(N)}{\partial \theta^2} + \cot \theta \frac{\partial \Delta T(N)}{\partial \theta} + \frac{1}{\sin^2 \theta} \frac{\partial^2 \Delta T(N)}{\partial \phi^2} \right\},$$

where the second derivative of $\Delta T(N)$ is given by

$$\frac{\partial^2 \Delta T(N)}{\partial r^2} = \left\{ \frac{109A^4}{R^9} - \frac{90A^2}{R^7} + \frac{9}{R^5} \right\} \Delta j'. \quad (\text{II-31})$$

E. Combined Gravity and Magnetic Point Source Potentials

For a point mass which also is magnetized, the observation-to-source point geometry is invariant so that the magnetic and gravitational potentials of the point source can be compared directly. Consideration of equations (II-14 and 26), for example, shows that for a common point source the gravity effect and radially polarized magnetic anomaly are related by

$$\begin{aligned} \Delta T(N) &= \frac{\Delta j'}{G \Delta m} * \frac{\partial \Delta g}{\partial r} \\ &= \frac{\Delta j'}{G \Delta m} * \Delta g \left\{ \frac{1}{A} - \frac{3A}{R^2} \right\}. \end{aligned} \quad (\text{II-32})$$

When the magnetic anomaly is calculated directly from the gravity potential as in equation (II-32), the result commonly is called the pseudo-magnetic anomaly. The corresponding pseudo-gravity anomaly, on the other hand, is given by

$$\Delta g = \frac{G \Delta m}{\Delta j'} * \Delta T(N) \left\{ \frac{A R^2}{R^2 - 3A^2} \right\}. \quad (\text{II-33})$$

Pseudo-potential field calculations facilitate enhanced geologic interpretation of gravity and magnetic anomalies. The procedure, for example, is to relate an observed gravity anomaly to a set of point masses, Δm , by one of the least squares matrix inversion techniques described in the next section. Comparing an estimate for the bulk magnetization contrast-to-density contrast ratio of the anomalous body to the equivalent point masses, Δm , gives corresponding equivalent point magnetizations, $\Delta j'$, which can be used to calculate the pseudo-magnetic anomaly from

equation (II-32) or, even more simply, from equation (II-26). A similar procedure can be used to develop from an observed magnetic anomaly the corresponding pseudo-gravity anomaly using equations (II-33 or 8). If the pseudo-potential field anomalies are similar to the observed potential field anomalies, common source structure can be inferred for both magnetic and gravity anomalies, thus, minimizing the ambiguity inherent to the analysis of each of the anomalies by itself. Of course, dissimilarity between pseudo and observed anomalies also can lead to valid inferences regarding source lithology and structure.

Equations (II-32 and 33) are special consequences of a more general result noted by Poisson (1826) as a theorem which describes the relationship between the gravitational and magnetic potentials of any uniformly dense and magnetized body. In its geophysical context Poisson's theorem states that at an observation point the resultant magnetic anomaly is related to the first derivative of the gravity anomaly taken in the direction of magnetization by the magnetization contrast-to-density contrast ratio of the body. By equation (II-3) it is clear that Poisson's theorem also can be extended to relate the n -th magnetic anomaly derivative to the appropriate $(n+1)$ -th gravity anomaly derivative. Equations (II-19 and 27), for example, combine to relate the second order radial gravity anomaly derivative to the radially polarized first order magnetic anomaly derivative for a common point source. In general, then, Poisson's theorem provides an important quantitative basis for comparing gravity and magnetic anomalies and, hence, for minimizing the ambiguity associated with the lithologic interpretation of these potential fields.

F. The Inversion Problem

As described previously, the measured potential field anomaly at any observation point is the summation at the observation point of the potential field effects due to each of the anomalous sources. Because of source ambiguity of potential fields it is clear that distributions of point sources exist for any measured anomaly such that the integrated anomalous effect of the point sources represents with equivalent facility the observed integrated effect of the true sources. The current objective, then, is directed toward resolving the problem of obtaining

for a given set of observed potential field anomalies, a distribution of equivalent point sources suitable for processing purposes.

The effort begins from a consideration of equations (II-8 and 25) which relate equivalent point sources to measured anomalies of the earth's radial gravity field or total magnetic intensity field, respectively. Both of these equations may be generalized as shown in Figure II.1, so that the incremental anomaly effect due to the p-th point source at the n-th observation point is given by $q_{np}(R) \cdot \Delta x_p$, where $q_{np}(R)$ is the geometric point source function and Δx_p is the appropriate physical property value. Accordingly, the relationship between a set of n-observations ($obs_1, obs_2, \dots, obs_n$) and a set of p-point sources can be expressed by the system of linear equations

$$\begin{aligned} q_{11} \Delta x_1 + q_{12} \Delta x_2 + \dots + q_{1p} \Delta x_p &= obs_1 \\ q_{21} \Delta x_1 + q_{22} \Delta x_2 + \dots + q_{2p} \Delta x_p &= obs_2 \\ \cdot &\cdot \\ \cdot &\cdot \\ \cdot &\cdot \\ q_{n1} \Delta x_1 + q_{n2} \Delta x_2 + \dots + q_{np} \Delta x_p &= obs_n \end{aligned}$$

In matrix notation the linear system is more conveniently described by

$$Q \cdot \Delta X = OBS, \quad (II-34)$$

where Q is an (n-row by p-col) matrix with elements given by the geometric point source functions ($q_{np}(R)$), ΔX is a (p by 1) column matrix containing the physical property values (Δx), and OBS is an (n by 1) column matrix of the anomaly observations (obs_n).

Now, the geometric variables of the observation points are known, so that the complete determination of the elements of Q can be made by simply specifying the geometric distribution of the equivalent point sources. Hence, by pre-determining the equivalent point source locations equation (II-34) can be solved for a set of physical property values ΔX by a number of well known matrix inversion techniques.

For example, when $p = n$, Q is a square matrix and the exact solution given by

$$\Delta X = Q^{-1} \cdot OBS \quad (II-35)$$

can be obtained by well documented numerical methods (e.g., Carnahan, 1969) if Q is not near-singular. Theoretically, Q has singular values only if the source point and observation point are specified at the same location, in which case the classical singularity of potential fields arises and the inversion effort is rendered meaningless. In practice, however, care must be taken to insure that the elements of Q are not made near-singular with respect to the working precision of the computer by improper scaling practice. An extreme example of bad scaling procedure is to specify source point locations so close to the observation point locations that the significant figures of the difference in their spatial location is in meters, whereas all other spatial variables of the Q elements have significant figures given in hundreds or thousands of kilometers. In such instances, the computer's ability to distinguish the spatial difference in source and observation point locations from its representation of zero may be so impaired that the resultant Q matrix can be considered singular within the computer's working precision. On the other hand, good scaling strategy as suggested by the example requires that all variables of any physical dimension of the problem be computed with roughly equivalent precision. With respect to the applications considered in this paper, experience has shown that proper scaling of the Q matrix in general is not difficult to achieve.

The solution given by (II-35) normally requires $p^2 = n^2$ machine storage locations for determining Q^{-1} . Hence, because of the large number of anomaly observations usually being considered, the exact solution often is impractical to compute even when the problem is suitably scaled. In most applications, then, computer storage constraints require that problem (II-34) be set up so that the number (p) of equivalent point sources is substantially less than the number (n) of observations.

When $p < n$, the solution to the overconstrained system of equation (II-34) is given by

$$\Delta X = (Q^T Q)^{-1} * Q^T * \text{OBS.} \quad (\text{II-36})$$

This solution is well known in the literature of numerical methods as a least squares solution in the sense that it minimizes the Euclidean vector norm of the residual, $|\text{OBS} - Q \cdot \Delta X|^2$. Assuming the problem is properly scaled so that Q is not near-singular, procedures for obtaining (II-36) fall generally into two basic categories depending on how the values of the solution vector are to be used in subsequent analysis.

For processing purposes such as continuation, differentiation, etc., the solution ΔX merely represents a set of weighting coefficients which operate on suitably modified geometric point source functions to achieve a least squares approximation of the processed observations. The physical reality of the property values contained in ΔX are of limited consequence to these processing objectives and all that is required, simply, is a set of property values which provide a least squares fit between the observed anomalies and equivalent point source anomalies. To obtain this type of solution, numerous methods are available in the general literature for application.

The Choleski decomposition algorithm (Lawson and Hanson, 1974), for example, can be recommended when it is desired to minimize machine computation time because the method yields a least squares solution set of weighting coefficients without the necessity of directly computing the product matrix $Q^T Q$ or its inverse. Choleski factorization is applicable when Q is properly scaled because the product matrix $Q^T Q$ is positive definite with Q as its Choleski factor. The application of Choleski decomposition requires at least (p^2) storage allocations and, hence, the algorithm may not be optimal when machine storage is the primary constraint.

Machine storage requirements can be reduced to roughly $(p(p + 1)/2)$ allocations when the inverse $(Q^T Q)^{-1}$ is used to determine the solution. Because the product matrix $Q^T Q$ is symmetric, its inverse may be determined using only those values contained in either the upper or lower triangular half of the product matrix. In general, then, the product matrix $Q^T Q$ can be operated on in "packed" form where, for instance, the columns of the upper triangle of the product matrix are stored sequentially in a singly-dimensioned array of length $(p(p + 1)/2)$. Hence,

to determine the solution (II-36) only about one half of the entries of the product matrix need to be calculated to yield the inverse $(Q^T Q)^{-1}$. Although slower than the Choleski decomposition algorithm, the procedure minimizes machine storage requirements for determining the least squares solution vector ΔX .

The second major solution category occurs when it is desired to constrain the values of the solution vector ΔX for subsequent analysis. This situation arises, for example, when physically realistic property values are required for modeling volume elements of the crust or some other geologic feature of the earth. Constrained solutions to equation (II-34) can be achieved by the eigenvalue-eigenvector matrix decomposition analysis suggested by Lanczos (1961).

Accordingly, the eigenvalue-eigenvector decomposition of Q is given by $Q = U \cdot S \cdot V^T$ to yield the solution vector

$$\Delta X = (V \cdot S^{-1} \cdot U^T) \cdot \text{OBS.} \quad (\text{II-37})$$

Here, U and V are orthogonal matrices with columns which are the eigenvectors associated with the columns and rows of Q , respectively, and S is a diagonal matrix with elements which are the eigenvalues, λ , of Q . The eigenvalues and eigenvectors are obtained from the square symmetric product matrix $Q^T Q$ and the inverse S^{-1} is a diagonal matrix of eigenvalue inverses, $1/\lambda$. Jackson (1972) has shown that the Lanczos solution (II-37) is a least squares solution for the overconstrained system (i.e., $p < n$) and, hence, is identical to the conventional solution (II-36) when Q is not near-singular. In contrast to conventional algorithms such as Choleski decomposition or packed form solutions, however, numerical procedures for obtaining the Lanczos solution require substantially greater machine computation time and storage of at least $(p^2 + p(p + 1)/2)$ allocations.

The main advantage of the Lanczos solution is that eigenvalues contained in S can be manipulated to constrain the values of the solution vector ΔX without altering its least squares property. Eliminating eigenvalues found near each end of the eigenvalue spectrum, for example, minimizes the occurrence of extreme property values in the least squares solution vector that may be difficult to rationalize physically. An

example of a more sophisticated procedure is presented by Vigneressé (1978) for tapering the eigenvalue spectrum to obtain a solution which is constrained to lie within a restricted range of density contrasts in an application to gravity interpretation.

The Lanczos procedure also provides a generalized least squares solution for the case where Q is near-singular and, hence, where the conventional techniques are not applicable. Here, near-singularities of Q correspond to small eigenvalues which can be eliminated from the problem by comparing the eigenvalues to an acceptable threshold value. The surviving eigenvalues and associated eigenvectors are then combined as in (II-37) to obtain a generalized solution which is a least squares fit of the observed anomalies. Bowman et al., (1979) present a fuller discussion of the procedure as applied to equivalent point source processing and some applications to gravity and magnetic anomaly inversion.

Finally, the problem of specifying the geometric distribution of equivalent point sources for purposes of efficient inversion must be considered. In practice, machine computation time and storage requirements frequently dictate the source distribution characteristics for inversion. As discussed by Bowman et al., (1979), these requirements can be minimized by the strategic assignment of a point source to each feature of the observed data that is to be modeled. Here, the geometric characteristics of the strategic source distribution can be specified according to well known rules relating the depth and wavelength characteristics of point sources (e.g., Nettleton, 1942; Smellie, 1956).

Another numerically convenient approach which is more automatic in its application, is to perform the inversion on a spherical grid of point sources at constant depth. For this application, the initial depth of the source grid should be on the order of the source grid spacing (e.g., Dampney, 1969; Ku, 1977). In practice, the source grid density of unknowns generally is specified according to available computer resources, so that adjustments of the equivalent source field to more precisely reflect wavelength characteristics of the observed data normally reduce to straightforward adjustments of the source grid depth.

It also should be noted that edge effects frequently are observed in radial continuations of the equivalent source field when the lateral dimensions of the source grid are roughly coincident with the observation grid. This result reflects the decreased energy density associated with point sources located near the edges of the distribution that tends to be emphasized by continuation. Edge effects are particularly troublesome when the observed data set is so large that processing has to be accomplished via subsets at one elevation which must be rejoined at a new elevation. Experience has shown, however, that edge effects can be minimized by including in the inversion a peripheral ring of observed data which extends laterally beyond the source grid a distance roughly equal to or greater than the radial distance between the source grid and the desired elevation of continuation.

G. Examples of Geophysical Processing Applications

To illustrate the equivalent point source inversion technique and its processing capabilities, regional gravity and magnetic anomaly data obtained from NASA-GSFC for the United States, Mexico and Central America are considered. Accordingly, Figure II.3.A shows a stereographic equal-area polar (SEAP) projection of smoothed 1° -averaged free-air gravity anomalies observed for the region $(239.5-280.5)^\circ\text{E}$ longitude and $(9.5-50.5)^\circ\text{N}$ latitude. The observation grid consists of $(42,42)$ -values at 1° spacing where the relative elevation (Z) of the observations is 0.0 km. The amplitude range (AR) of the observations is between 41 mgal and -53 mgal and the amplitude mean (AM) is -0.61 mgal.

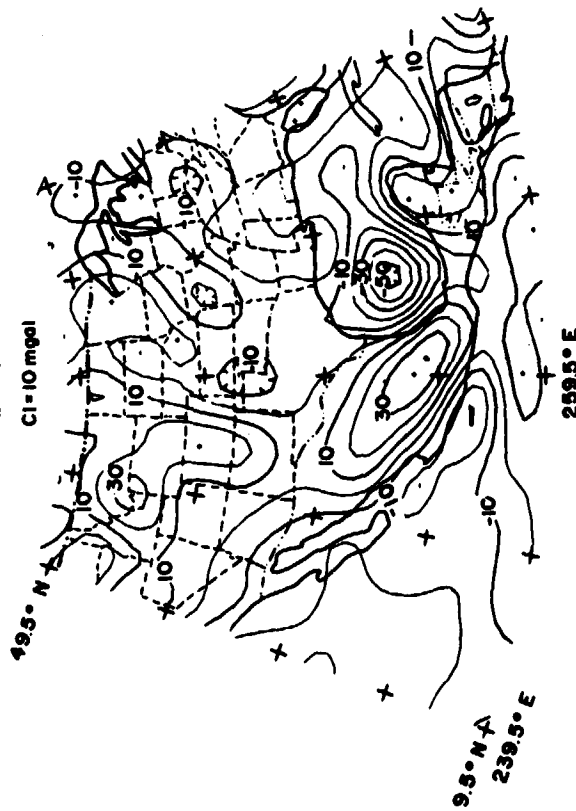
The least squares representation of the observations by equivalent point source inversion is given in Figure II.3.B. Here, the observations are inverted on a source grid of $(15,15)$ -values to obtain the least squares solution vector of density contrasts given by equation (II-36). The point source grid spans the region $(240-280)^\circ\text{E}$, $(10-50)^\circ\text{N}$ at a depth of 400 km below the relative elevation of the observation grid. The point sources are uniformly spaced at 2.857° intervals over the source grid. As shown by a consideration of the amplitude means of Figures II.3.A and 3.B, the mean error of the least squares fit of the observed gravity data is negligible.

ORIGINAL $<1^{\circ}>$ FA GRAVITY ANOMALIES

AR = (41, -53) mgal AM = -0.61 mgal

Z = 0.0 km

CI = 10 mgal



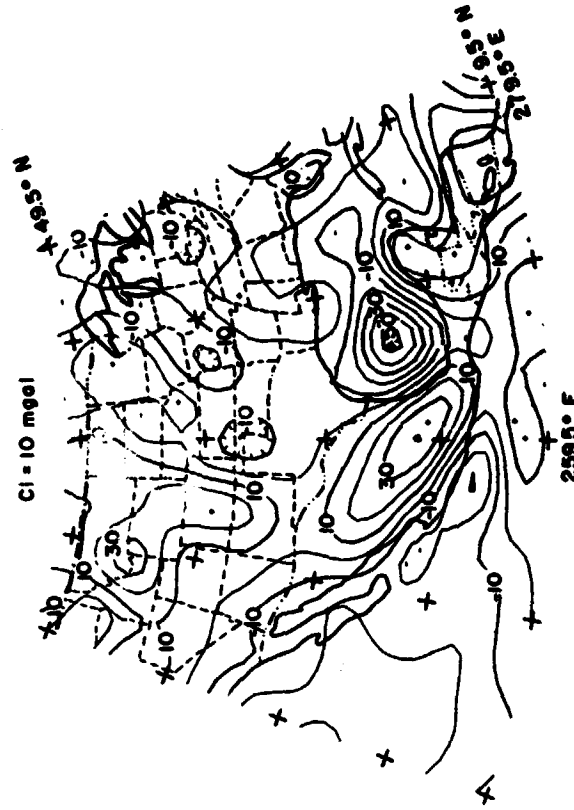
***** A *****

EPS $<1^{\circ}>$ FA GRAVITY ANOMALIES

AR = (40, -52) mgal AM = -0.60 mgal

Z = 0.0 km

CI = 10 mgal



***** B *****

Figure II.3 A) Stereographic equal-area polar (SEAP) projection of smoothed 1° -averaged free-air gravity anomaly data for the United States, Mexico and Central America. Amplitude range (AR) of the data set is 41 to -53 mgal and the amplitude mean (AM) is -0.61 mgal. Contour interval (CI) is 10 mgal and the reference elevation (Z) of the observations is 0.0 km. B) Equivalent point source (EPS) approximation of smoothed 1° -averaged free-air gravity anomalies.

An obvious by-product of the inversion is a least squares density model for the observed gravity anomalies. By Brun's formula (Heiskanen and Moritz, 1967), if the anomalous potential of the model is known, then the geoid height anomaly due to the anomalous mass is given by the ratio of anomalous potential to normal gravity ($\approx 9.8 \text{ m/sec}^2$). A least squares estimate of the gravitational potential of the observed anomalies can be readily computed by integrating at each observation point the potentials due to each of the source points according to equation (II-1). Hence, by dividing this result by the normal acceleration of gravity a least squares approximation of the geoidal anomalies can be obtained. Accordingly, Figure II.4.A illustrates a least squares representation of the geoidal deflections due to the mass anomalies responsible for the observed free-air gravity anomaly data of Figure II.3.A. The geoidal deflections given in Figure II.4.A are accurate on a relative basis. However, when compared to global-scale geoids, these anomalies must be adjusted by a nearly constant value that reflects the broad-scale geoidal deflection due to long-wavelength variations of the gravitational potential which are too large to be adequately sampled by the restricted spatial coverage considered in this illustration.

Another processing example is given in Figure II.4.B where the results of the inversion are used to obtain a least squares representation of the observed gravity anomalies upward continued to a typical satellite elevation. In this application, the gravity effect of the equivalent point sources was recomputed at 450 km elevation using equation (II-8). Further processing applications are shown in Figures II.5.A and 5.B where the inversion results are used to obtain least squares representations at 450 km elevation of the radial first derivative and Laplacian component of the observed gravity data according to equations (II-14 and 18), respectively. At 450 km elevation, it turns out that the radial Laplacian is nearly identical to the second radial derivative field of the gravity anomalies. Note also, that the anomalies given in Figures II.4.A, 4.B, 5.A and 5.B all have now been reregistered to integral degree nodes of the spherical grid spanning the region (240-280) $^{\circ}$ E, (10-50) $^{\circ}$ N at 1 $^{\circ}$ -station intervals.

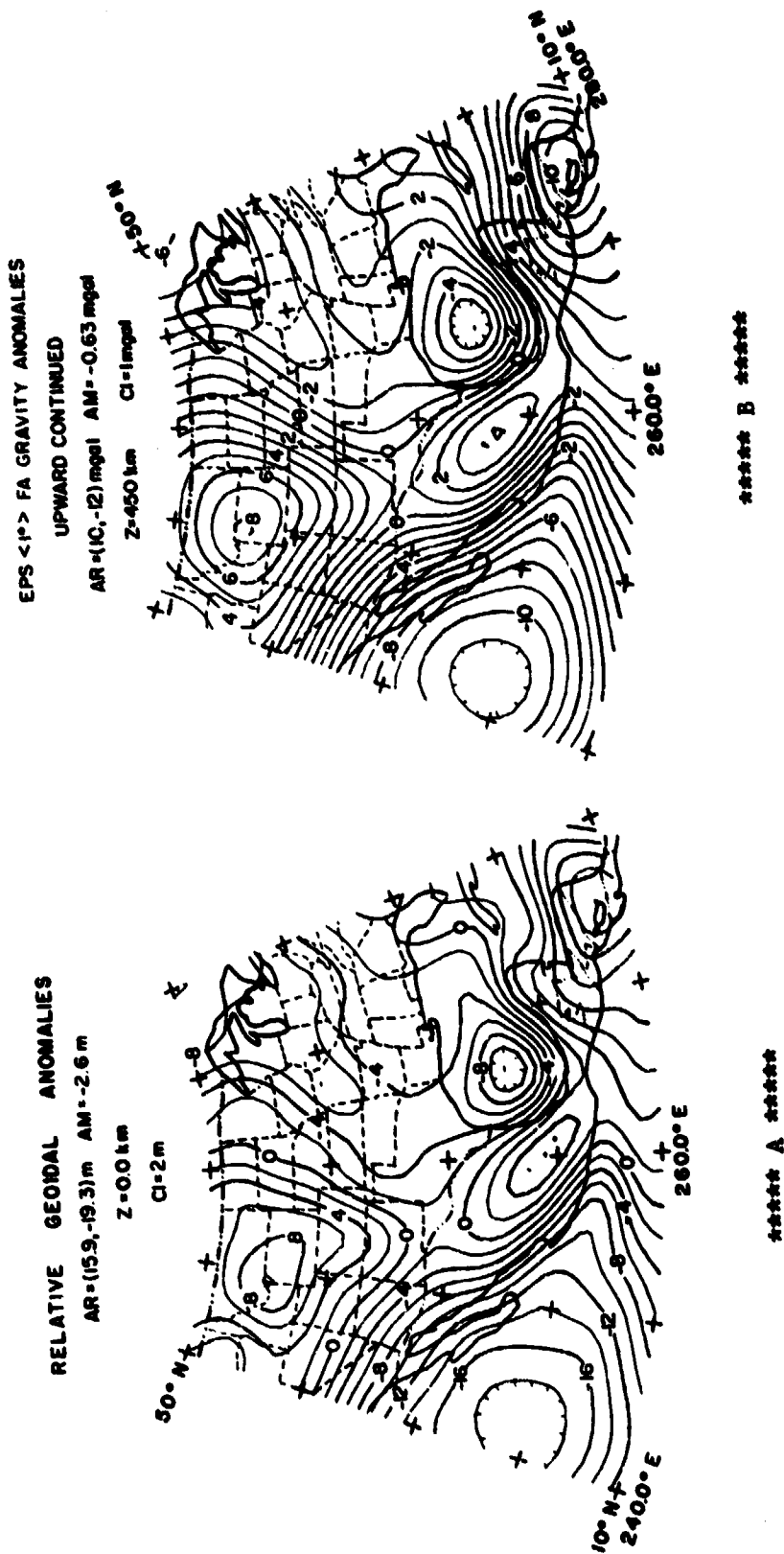


Figure II.4 A) Relative geoidal anomalies derived from equivalent point source inversion of smoothed 1° -averaged free-air gravity anomalies. B) Equivalent point source approximation of smoothed 1° -averaged free-air gravity anomalies upward continued to 450 km elevation.

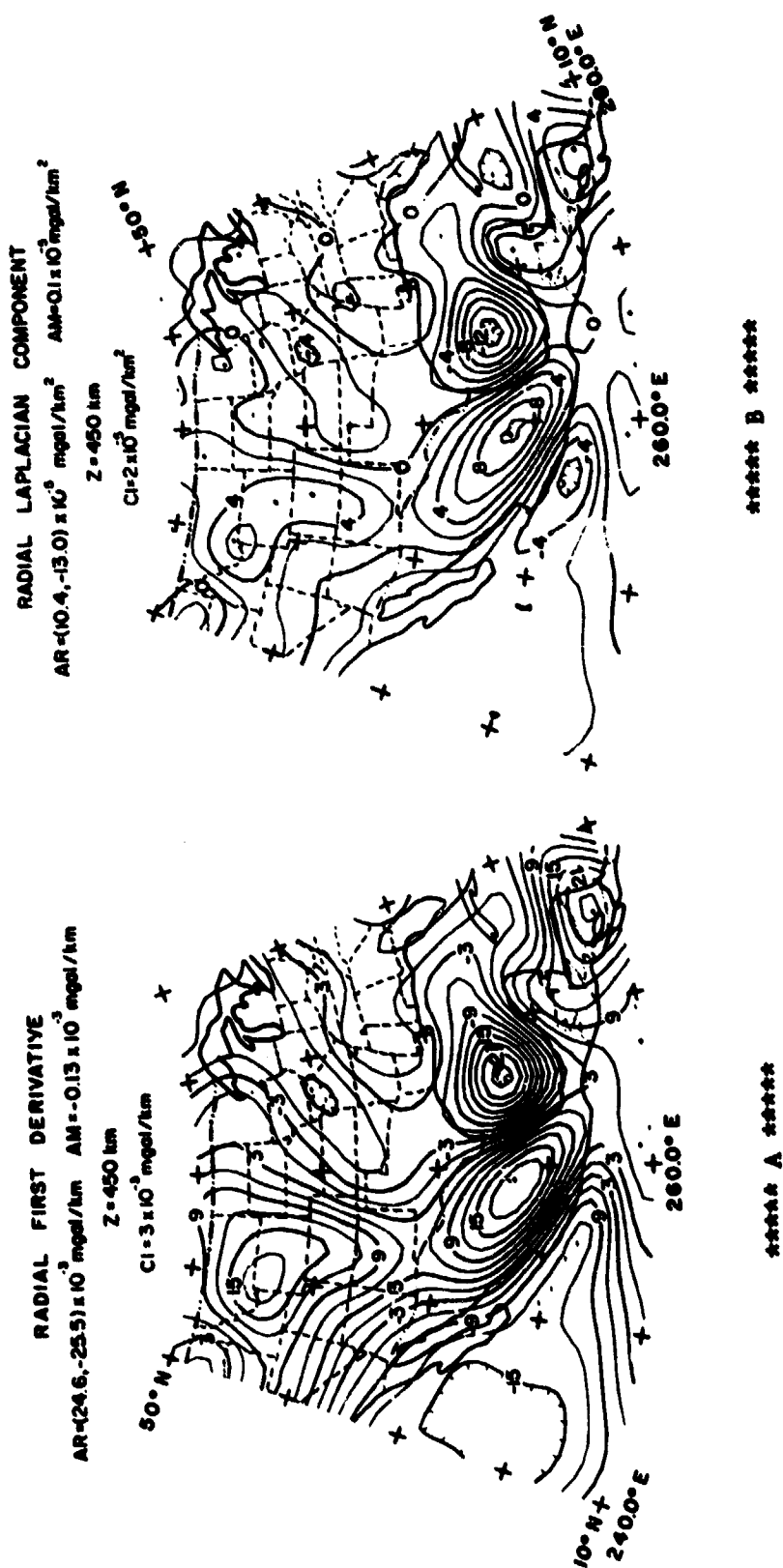


Figure II.5 A) Equivalent point source approximation of the first radial derivative of smoothed 1° -averaged free-air gravity anomalies. B) Equivalent point source approximation of the radial Laplacian component of smoothed 1° -averaged free-air gravity anomalies. At 450 km elevation, the radial Laplacian component is nearly identical to the second radial derivative of the gravity anomalies.

In Figure II.6.A, an equivalent source dipole field representation of POGO satellite magnetometer observations conducted during 1968 is presented. The magnetic data were reduced in profile form according to the procedures described by Mayhew (1979) to yield 4271 anomaly values from 345 satellite tracks ranging in elevation between 240 km and 700 km over the study area. To reduce the total magnetic anomalies to a common elevation the profile data were inverted on a spherical grid of (15,15) spherical prisms* to obtain the least squares solution vector of dipole moments given in (II-36). The equivalent prism source grid was located at the surface of the earth and uniformly spanned the region (240-280)[°]E, (10-50)[°]N at 2.857[°] intervals. The dipoles were oriented along the main geomagnetic field directions given by the IGRF-1965 updated to 1968. The fit of the equivalent source field to the observed profile data is to 1 gamma standard deviation. Examples illustrating the general degree of this fit for an arbitrary selection of profiles between 10[°]N and 50[°]N are given in Figure II.7. Recomputing the equivalent source field at 450 km elevation using equation (II-25) modified to include spherical prismatic volumes gives the least squares representation shown in Figure II.6.A of variable elevation satellite magnetic anomaly data reduced to a common elevation of 450 km.

Assuming that the magnetization is predominantly by induction, the variable influence of the geomagnetic field on the total magnetic intensity anomalies recorded in Figure II.6.A can be eliminated by differentially reducing the data to vertical polarization. This result is achieved by recomputing the equivalent source field using equation (II-26) modified for spherical prisms. Accordingly, Figure II.6.B illustrates the least squares representation of the total magnetic anomaly data of Figure II.6.A differentially reduced to the pole using a normalized polarizing amplitude (N) of 60,000 gamma.

*) To convert the spherical prismatic dipolar moment formulation of Mayhew (1979) to point dipole moments, it is necessary only to multiply the prismatic moments by the spherical volumes of the corresponding prisms.

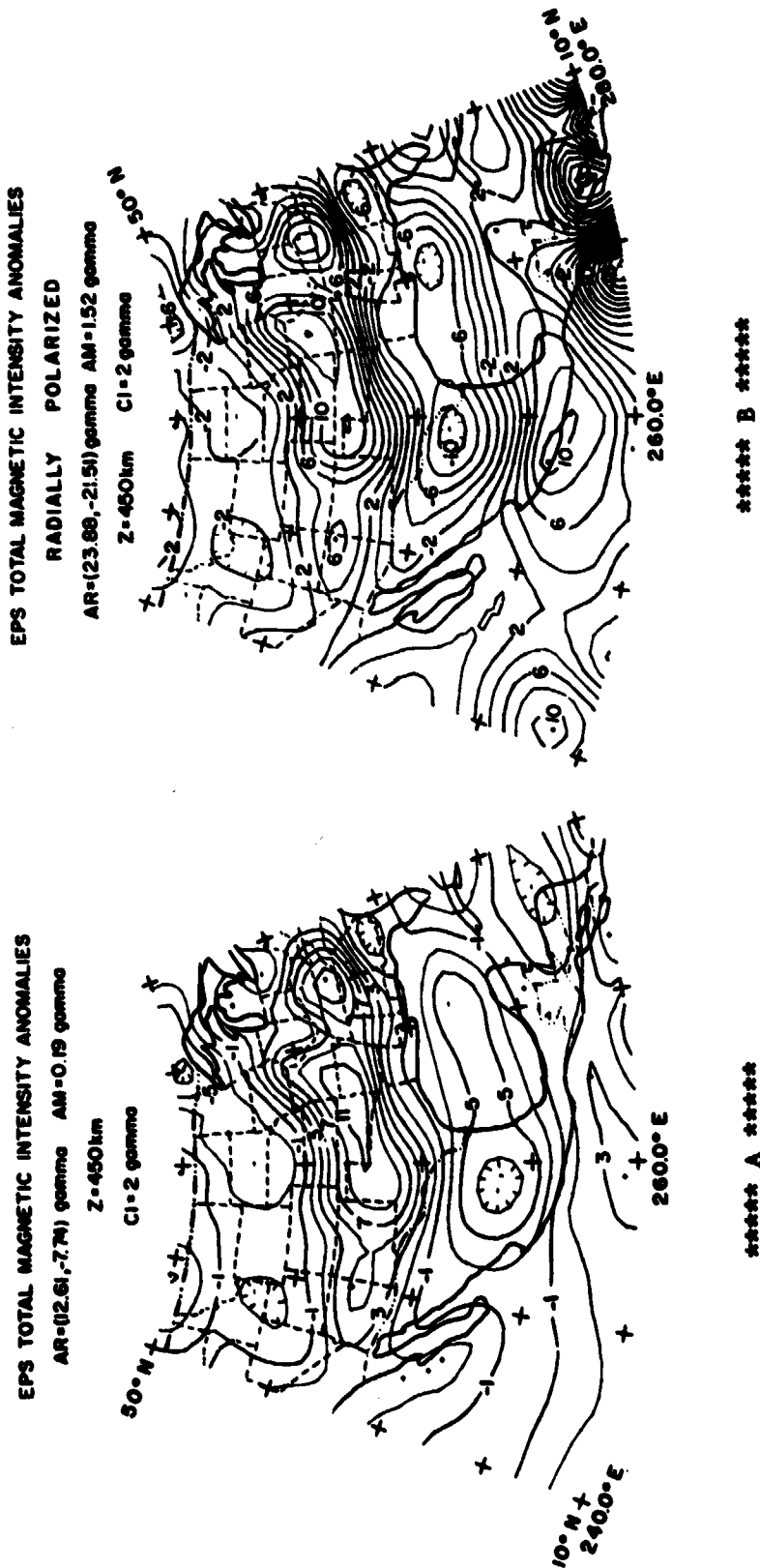


Figure II.6 A) Multielevation POGO satellite magnetometer data reduced to a common elevation of 450 km by equivalent prism source inversion according to the procedures of Mayhew (1979). B) Equivalent source approximation of the total magnetic intensity anomaly data differentially reduced to the radial pole. The normalization amplitude (N) assumed for the radially polarizing field was 60,000 gammas.

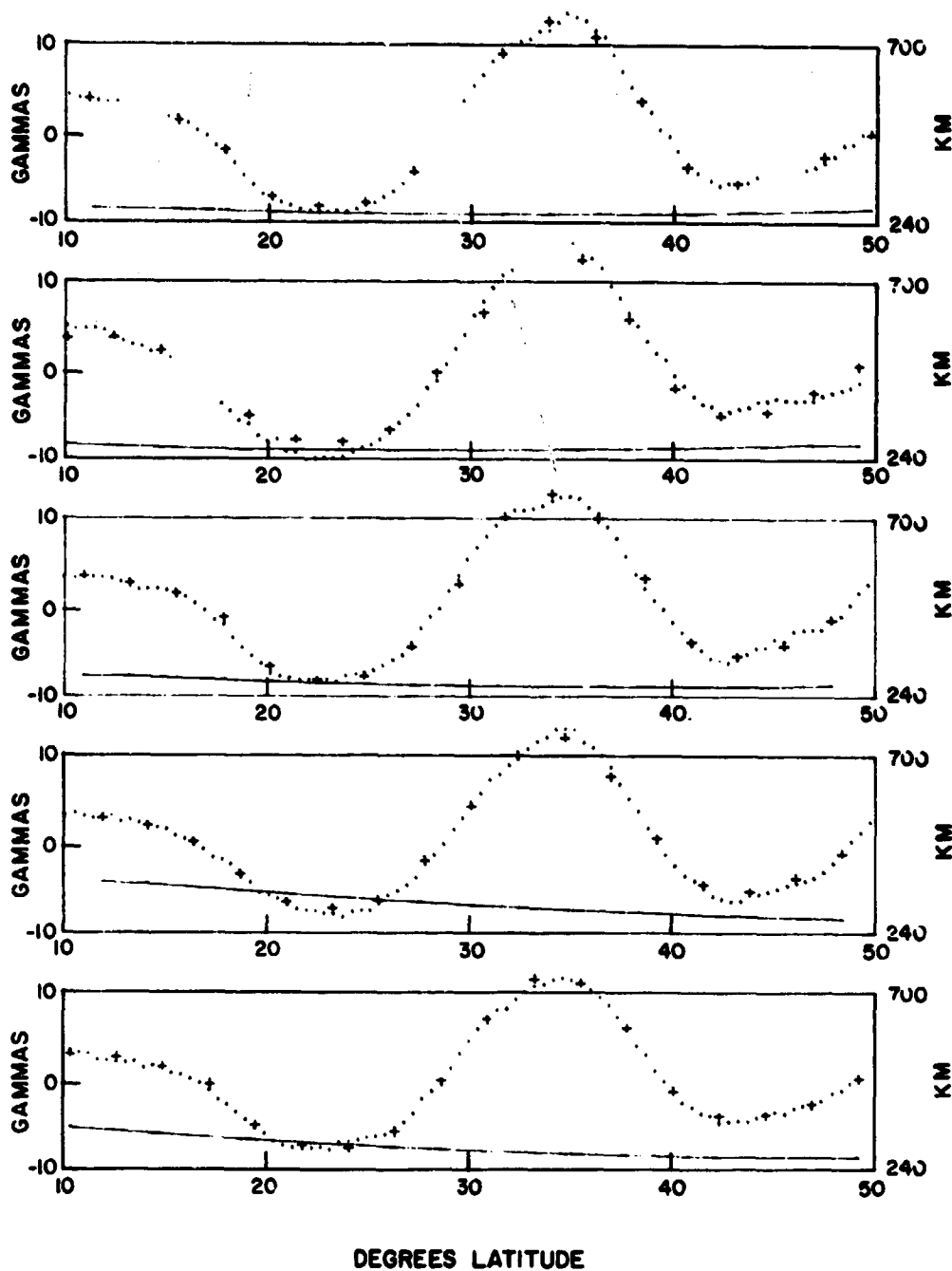


Figure II.7 Total magnetic intensity anomaly comparisons (after Mayhew (1979)) illustrating the fit between arbitrarily selected tracks of POGO satellite magnetic measurements (dots) and the corresponding equivalent source values (crosses). The solid line in each comparison corresponds to the elevation of the POGO satellite magnetometer data.

A comparison of Figures II.6.A and 6.B shows that anomalies in the southern portion of the radially polarized map generally are shifted differentially from 3° to as much as 5° to the north. Larger amplitudes also are observed for these anomalies because of the positive difference between the scalar intensities of the radially polarizing field and the IGRF-1965 updated to 1968 at low latitudes. Northern amplitudes, on the other hand, show only slight relative alterations which include principally northward displacements that rarely exceed 1° or 2° . The behavior of the radially polarized data, then, is consistent with that anticipated for the conventional pole reduction.

In consideration of the foregoing examples it is clear that once a set of potential field anomalies have been related to a set of equivalent point sources by least squares matrix inversion, then a number of geophysically interesting characteristics of the observed data also are known with equivalent least squares precision. In general, these characteristics include the associated potentials, vector anomaly components and spatial derivatives, as well as continuations of these elements.

H. Conclusions

Equivalent point source inversion is an efficient and versatile approach to spherical earth processing of regional potential field anomalies. The procedure is to relate observed anomalies to a set of equivalent point sources by a system of linear equations. By pre-determining the locations of the point sources, the problem simplifies to solving the linear equation system for a solution vector of physical property values. In practice, the system of equations normally is overconstrained in the sense that the number of point source physical property values of the solution is less than the number of observed anomaly values. From the general literature of numerical methods, however, several well-known matrix inversion methods are available to obtain the solution vector such that the resultant equivalent source field is a least squares representation of the observed data.

The anomalous potential and its spatial derivatives of all orders are linearly related so that when an equivalent point source least squares representation for any one of these elements has been determined, representations with equivalent least squares precision also are available for the rest of the elements by simple linear transformations. This result has great practical significance because considerable geophysical information is related to the anomalous potential and its spatial derivatives. From the least squares inversion of observed gravity anomalies, for example, geoidal anomalies, vector anomaly components and derivatives at any point in source-free space also may be computed with equivalent least squares precision. Similarly, the results of equivalent point source inversion of observed magnetic anomalies can be used to obtain least squares representations at any point in source-free space of the vector anomaly components, differential pole reductions and spatial derivatives. Pseudo-potential field calculations also can be readily performed using the equivalent point source inversion formulation.

In consideration of these results, it is concluded that equivalent point source inversion represents a powerful and efficient method for spherical earth processing of regional-scale gravity and magnetic anomalies. Accordingly, the method has widespread application in the analysis and design of regional-scale gravity and magnetic surveys for lithospheric investigation.

I. References

- Bowman, P.L., L.W. Braile, V.W. Chandler, W.J. Hinze, A.J. Luca and R.R.B. von Frese, Magnetic and gravity anomaly correlation and its application to satellite data, NASA-GSFC TM79702, 1979.
- Cain, T.C., S.J. Hendricks, R.A. Langel, W.V. Hudson, A proposed model for the International Geomagnetic Reference Field-1965, J. Geomag. Geoelectr., 19, 335-355, 1967.
- Carnahan, B., Applied Numerical Methods, J. Wiley and Sons, Inc. New York, 1969.
- Dampney, C.N.G., The equivalent source technique, Geophysics, 34, 39-53, 1969.
- Heiskanen, W.A., and H. Moritz, Physical Geodesy, W.H. Freeman and Co., San Francisco, 1967.

- Jackson, D.D., Interpretation of inaccurate, insufficient and inconsistent data, *Geophys. J.R. Astro. Soc.*, 28, 97-109, 1972.
- Kaula, W.M., Theory of statistical analysis of data distributed over a sphere, *Reviews of Geophysics*, 5, 83-107, 1967.
- Kellogg, O.D., *Foundations of Potential Theory*, Dover Publications, Inc., New York, 1953.
- Kontis, A.L. and G.A. Young, Approximation of residual total-magnetic intensity anomalies, *Geophysics*, 29, 623-627, 1964.
- Ku, C.C., A direct computation of gravity and magnetic anomalies caused by 2- and 3-dimensional bodies of arbitrary shape and arbitrary magnetic polarization by equivalent point method and a simplified cubic spline, *Geophysics*, 42, 610-622, 1977.
- Lanczos, C., 1961, *Linear Differential Operators*, D. Van Nostrand Co., London, 1961.
- Lawson, C.L. and R.J. Hanson, *Solving Least Squares Problems*, Prentice-Hall, Inc., New Jersey, 1974.
- Mayhew, M.A., Inversion of satellite magnetic anomaly data, *J. Geophys.*, 45, 119-128, 1979.
- Nettleton, L.L., Gravity and magnetic calculations, *Geophysics*, 7, 293-310, 1942.
- Poisson, S.D., Memoire sur la theorie du magnetisme, *Memories de l'Academie royale des sciences de l'Institut de France*, 247-348, 1826.
- Ramsey, A.S., *An Introduction to the Theory of Newtonian Attraction*, Cambridge Univ. Press, New York, 1940.
- Smellie, D.W., Elementary approximations in aeromagnetic interpretation, *Geophysics*, 21, 1021-1040, 1956.
- Strange, W.E. and G.P. Woollard, The use of geologic and geophysical parameters in the evaluation, interpolation and prediction of gravity, *Hawaii Inst. of Geophys.*, Doc. HIG-64-17, 1964.
- Vigneresse, J.L., Damped and constrained least squares method with application to gravity interpretation, *J. Geophys.*, 45, 17-28, 1978.
- Woollard, G.P., The relationship of gravity anomalies to surface elevation, crustal structure and geology, *Univ. of Wis. Geophys. Polar Res. Center. Res. Rept. SER. 62-9*, 1962.

III. QUALITATIVE CORRELATION ANALYSIS OF REGIONAL NORTH AMERICAN GRAVITY AND MAGNETIC ANOMALIES

A. Abstract

Regional free-air gravity anomalies of North America and adjacent oceanic areas mapped by low-pass filtering and upward continuing to 450 km elevation are compared to 450 km elevation POGO satellite magnetic anomalies differentially reduced to the pole, published 12th degree spherical harmonic representation of heat flow, and regional geologic information. In general, gravity anomalies of the continental areas parallel the prevailing north-south structural trends, while the predominant oceanic anomalies strike east-west. The oceanic areas are more negative than the continental area except for the minimum over the Hudson Bay region. Free-air anomalies upward continued to 450 km elevation tend to correlate with the regional heat flow pattern. The positive free-air gravity anomaly associated with the Cordillera corresponds to regional high heat flow values and the negative anomaly over Hudson Bay is correlative with a heat flow minimum. In addition, the generally negative anomalies of the oceanic areas correlate with low heat flow values. Comparison of gravity and satellite magnetic anomalies indicates little correlation over oceanic areas, although the oceanic areas have a more subdued anomaly pattern in both data sets. Over the continent, several prominent free-air gravity anomalies have an inverse correspondence to magnetic anomalies. Magnetic anomalies in contrast to gravity anomalies show limited correlation to the heat flow pattern. It is concluded that combined interpretation of the three geophysical data sets can decrease the ambiguity of the interpretation process because of the different parameters mapped and the variable range of the depth of the anomalous sources.

B. Introduction

Long-wavelength geophysical anomalies covering several degrees of surface area have long been of interest in studying the megatectonic features of the earth. However, their potential usefulness has been hindered by limited areal coverage and the inherent ambiguity in their interpretation. Recently, these problems have been alleviated somewhat by improved compositing and processing of data covering both continents and oceans and the availability of multi-data sets which when used in combined analysis tend to decrease possible alternative interpretations. Accordingly, regionally correlatable free-air gravity anomaly, differentially reduced to the pole satellite magnetic anomaly and regional heat flow maps of North and Central America and adjacent oceanic areas are presented and the correlation and potential significance of selected anomalies are discussed.

Free-air gravity anomalies reflect differences in the mass per unit surface area of the subjacent earth which are calculated by comparing observed gravity with theoretical gravity values based on planetary (latitude) and elevation effects. Thus, free-air anomalies correspond to the combined gravity effect of topography and deeper geologic mass variations which may be difficult to separate for purposes of interpretation. This problem is compounded because major elevation variations occur as an effect of tectonism which is also the primary cause of geologic mass variations. Nonetheless, free-air anomalies sometimes are preferred to Bouguer anomalies for regional tectonic studies because the Bouguer topographic mass reduction eliminates the effect of large segments of mass that are involved in tectonism.

When averaged over regional-scale areas, free-air anomalies are reduced in amplitude and tend toward a zero value, suggesting the mass per unit surface area down to some level in the earth is approximately equal when considering large surface elements (Woollard, 1962). This is strong direct support for the hypothesis of isostasy. Empirical evidence suggests that areas on the order of 3° and larger generally tend to be characterized by free-air anomalies that approach

zero (Woollard, 1962; Strange and Woollard, 1964), although the size of a specific area will be a function of local strength characteristics. Thus, regional scale variations of free-air gravity anomaly values on the order of 3° or larger frequently are considered to reflect isostatic variations within the earth's crust and mantle. Averaged positive free-air anomalies correspond to regions of mass excess or crustal loading, whereas negative anomalies correlate with regions of mass deficiency and, hence, the anomalies indicate the degree of isostatic equilibrium.

A number of mechanisms have been postulated which may cause mass variations within the earth. These include density variations in the mantle due to convection, relatively static compositional or petrological variations, and the delayed response of the earth to loading phenomena such as glaciation, de-glaciation, erosion and sediment deposition. In general, free-air gravity anomalies by themselves cannot be used to distinguish the causative mechanism due to the interpretational ambiguity inherent to potential fields. However, when combined with other geophysical and geological data, regional-scale free-air gravity anomalies may yield information concerning regional mass variations that are important to understanding the structure, dynamics and geological history of the earth's crust and upper mantle. Accordingly, regional anomalies in magnetics and heat flow also are presented and correlated with gravity anomalies to facilitate their interpretation.

The correlation between these data sets is complicated because of the dissimilarity in causative characteristics and range of depth of origin. The relationship between rock properties which cause magnetic and gravity anomalies, for example, often is complex, non-linear and non-universal. Nonetheless, the correlation of these anomalies derived from continental crystalline crust is a standard approach to geological and geophysical interpretation (Hinze *et al.*, 1975). This is a consequence of the general correspondence between densities and magnetizations of specific crystalline lithologies (Nettleton and Elkins, 1944). However, there are many exceptions to the generalities because magnetic minerals are a minor constituent of rocks and are subject to alteration to non-magnetic forms and the

effects of strong remanent magnetization. Similarly, heat flow will be reflected in temperatures that, in turn, alter the density of rocks by thermal expansion or contraction and control at least in part the effects of mineral alteration. Furthermore, heat flow and associated temperatures will control rock magnetization through the Curie temperature of ferrimagnetic minerals which is the temperature above which geologically significant magnetizations are eliminated. Thus, the three physical characteristics, density, magnetization and temperature may be related within the crystalline crust of the continents, but they are subject to numerous complicating variations.

The difference in source depth range further complicates the correlation of force fields, although this can be turned to the advantage of geologic interpretation. Gravity anomalies may originate from the surface to deep within the mantle or even the core, but the source of magnetic anomalies is limited by the depth of the Curie isotherm ($\approx 575^{\circ}\text{C}$) which may be as deep as 70 km, but generally is at a depth of ≈ 40 km. For source depth of heat flow, Pollack and Chapman (1977) have found that within continental regions 40% of the mean heat flux is derived from radiogenic sources within about the upper ≈ 8 km of the crust. The remainder is obtained from radiogenic contributions of the lower crust and upper mantle and a deeper portion that enters the base of the lithosphere which varies in thickness from roughly 50 to 300 km. Thus, magnetic anomalies are limited to sources within the crust and uppermost mantle while gravity anomalies and variable surface heat flux have origins which may reach several hundred kilometers or more into the mantle.

In general, then, correlation of these data sets, either direct or inverse, or even the lack of correlation can be useful in limiting the possible geologic interpretation of specific anomalies. Accordingly, the data sets provide different, but inter-related evidence which, when combined with surface geologic information, can help to clarify the tectonic history of North America.

C. Data Sources and Preprocessing

To investigate the regional wavelength features of North America's free-air gravity anomaly field, a data set of 1° -averaged surface values based on the GRS-1967 and IGSN-1971 was obtained from NASA's Goddard Space Flight Center for the region $(214.5-307.5)^\circ\text{E}$ longitude and $(4.5-58.5)^\circ\text{N}$ latitude. The observed data set consisted of 5170 values (= 94 cols, 55 rows) at 1° intervals of which approximately 600 were unassigned. Nearly all of the unassigned values were restricted to the regions $(214.5-242.5)^\circ\text{E}$, $(4.5-27.5)^\circ\text{N}$ and $(242.5-272.5)^\circ\text{E}$, $(4.5-14.5)^\circ\text{N}$ which are located in the Pacific Ocean of the southwest portion of the data set. In order to extend coverage to these regions, the missing values were interpolated from the surrounding observations. The contoured stereographic equal-area polar (SEAP) projection in Figure III.1 illustrates the resultant data set with an amplitude range (AR) from 185 to -285 mgal and amplitude mean (AM) of -7.63 mgal.

To minimize the effects of local topography as well as to enhance the longer wavelength characteristics of the data which are important at satellite elevations, the gravity data were subjected to a low-pass filter that strongly attenuated anomalies of wavelengths less than 8° . The wavelength characteristics of the high-cut filter are illustrated in Figure III.2 and the filtered gravity anomalies are presented in Figure III.3. Classically, unshaded anomalies (10 to -10 mgal) in Figure III.3 correspond to regions of approximate isostatic equilibrium.

A further consideration in the design of the adopted filter was to obtain low-pass filtered anomalies which could be adequately resampled at 2° intervals to optimize available computer resources for subsequent inversion processing. Accordingly, the smoothed gravity anomalies were resampled at 2° intervals to yield the set of (46,27) anomaly values for the region $(216-306)^\circ\text{E}$, $(6-58)^\circ\text{N}$ illustrated in Figure III.4.

To effectively project the gravity anomalies to the satellite elevations of the magnetic anomalies, the resampled data were inverted on a spherical grid of (19,14) equivalent point gravity poles. The

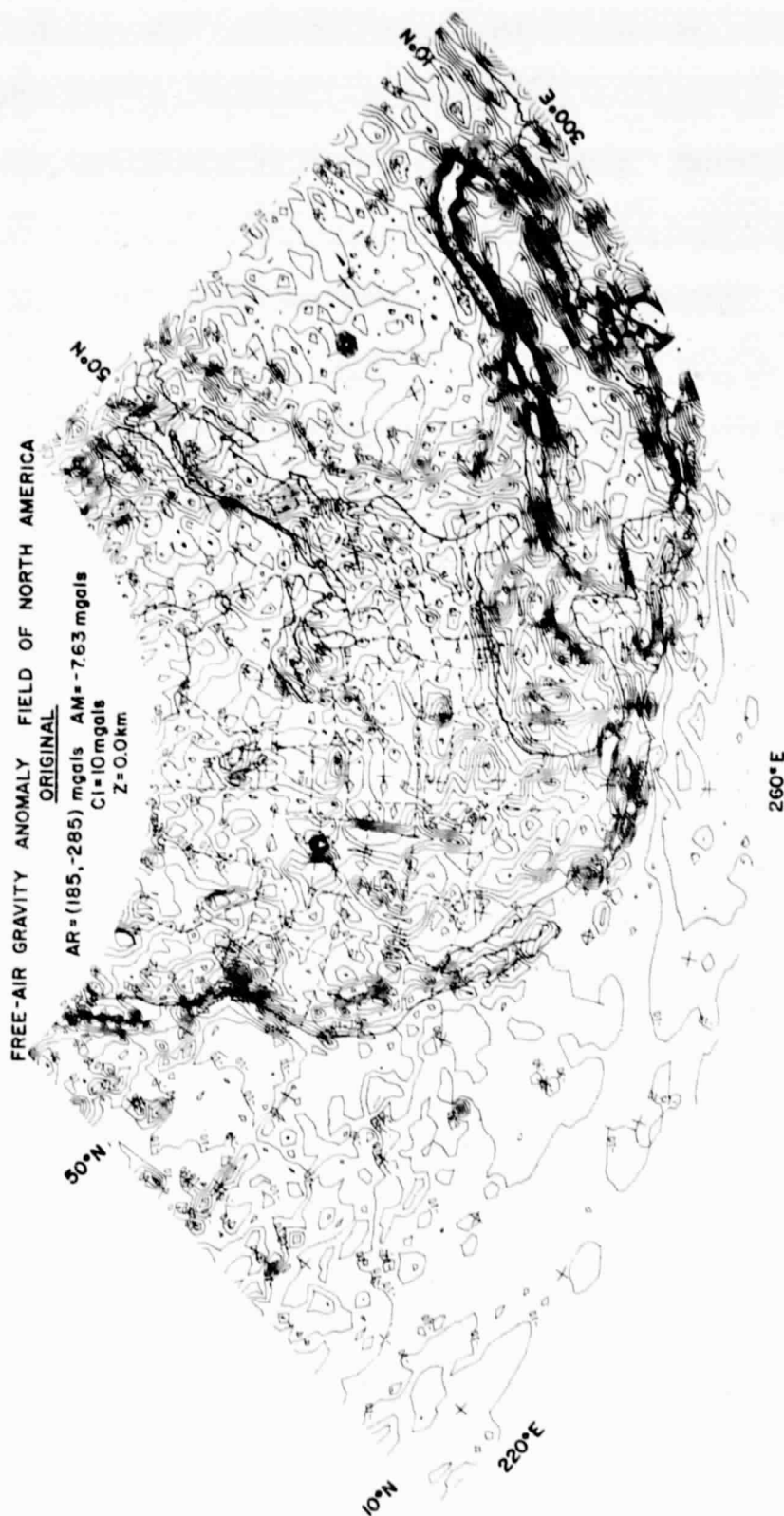


Figure III.1 Stereographic equal-area polar (SEAP) projection of free-air gravity anomaly data for North America. Amplitude range (AR) of the data set is 185 to -285 mgal and the amplitude mean (AM) is -7.63 mgal. Contour interval (CI) is 10 mgal and reference elevation (Z) of the observations is 0.0 km.

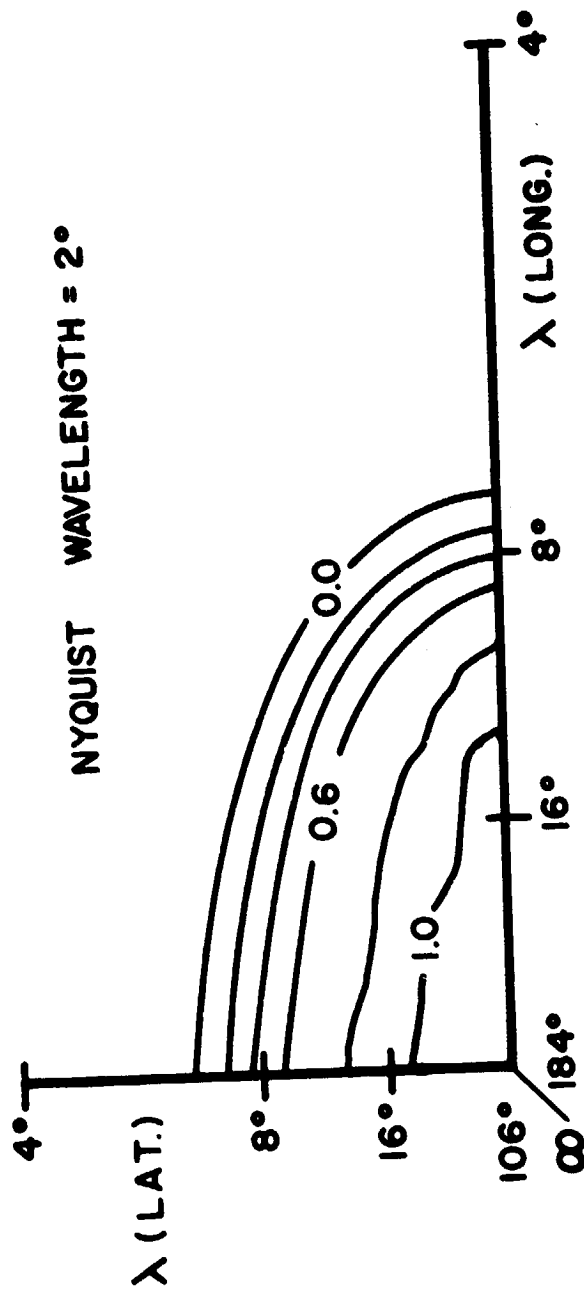


Figure III.2 Wavelength characteristics of low-pass, high-cut filter used to process gravity anomaly and topographic data of North America.

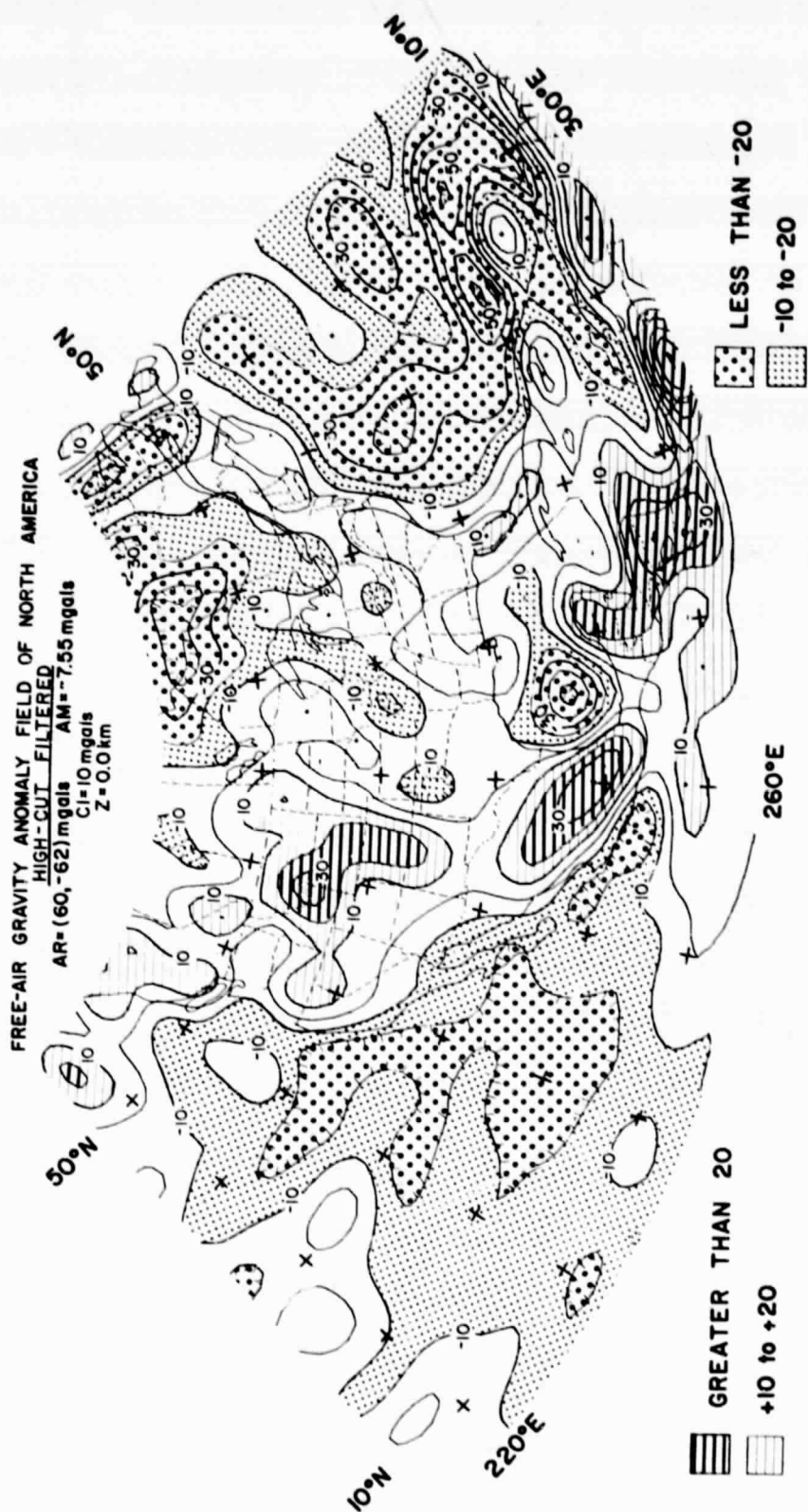


Figure III.3 High-cut ($\lambda \leq 8^\circ$) filtered free-air gravity anomaly data for North America.

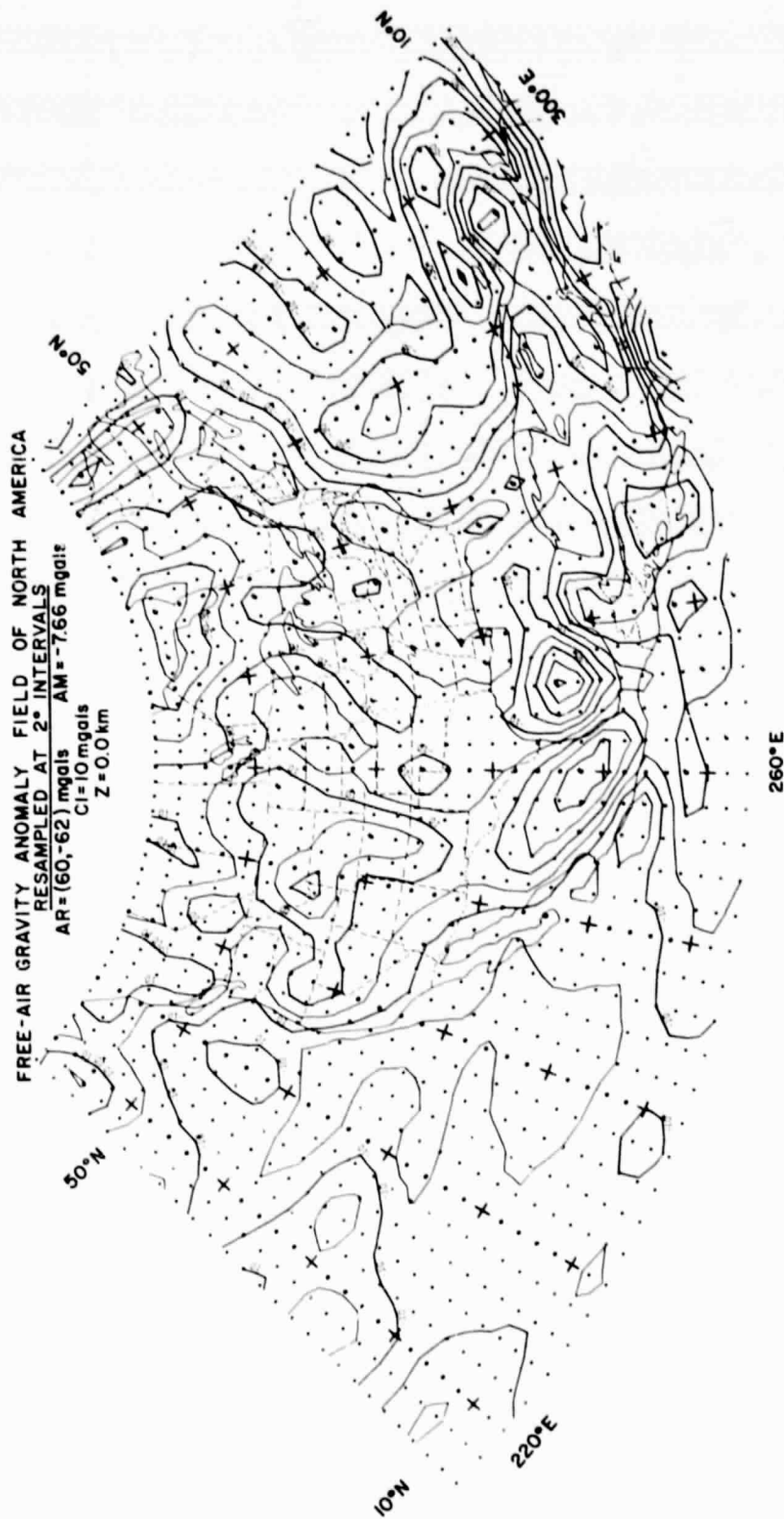


Figure III.4 High-cut filtered free-air gravity anomaly data for North America resampled at 2° intervals.

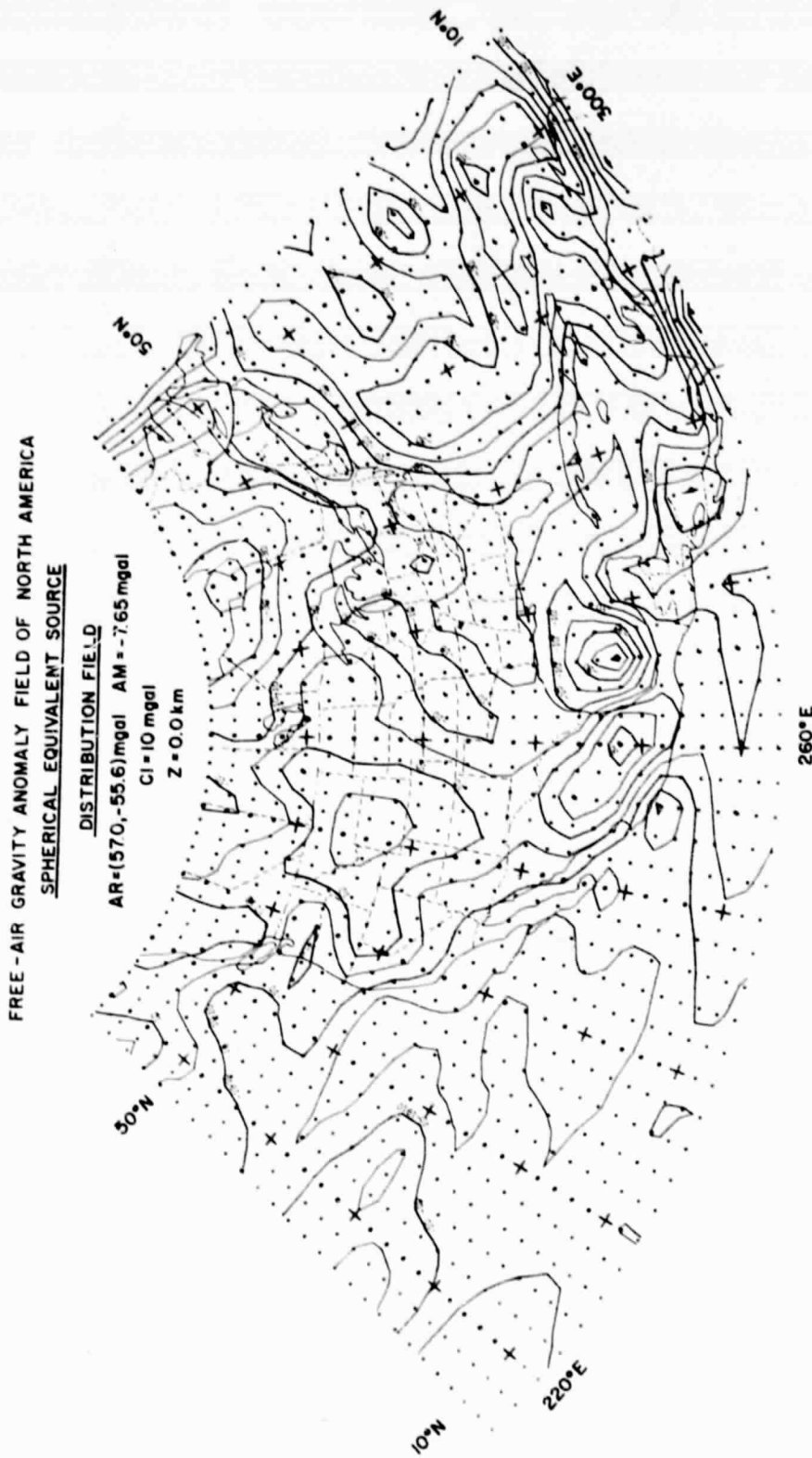


Figure IJL.5 Spherical equivalent source field approximation of resampled free-air gravity anomaly data for North America.

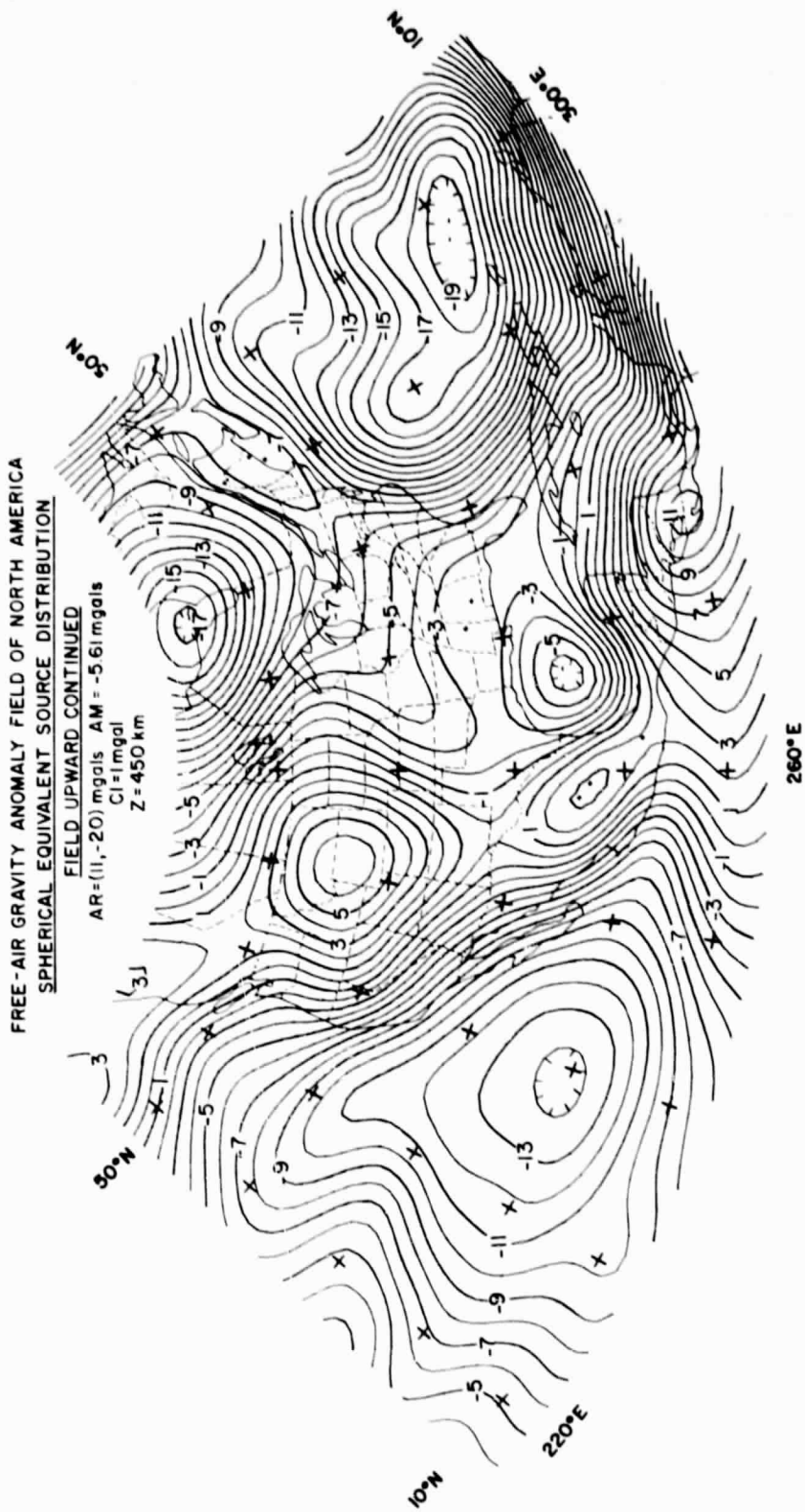
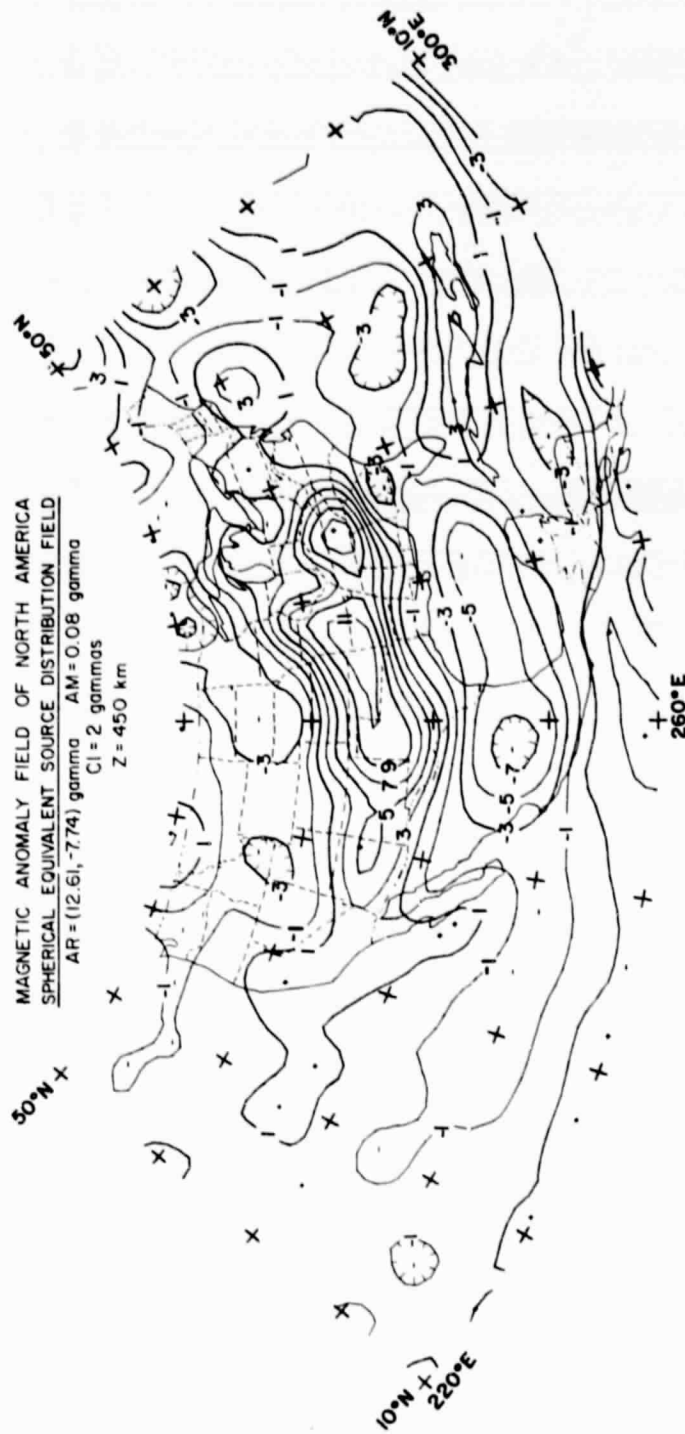


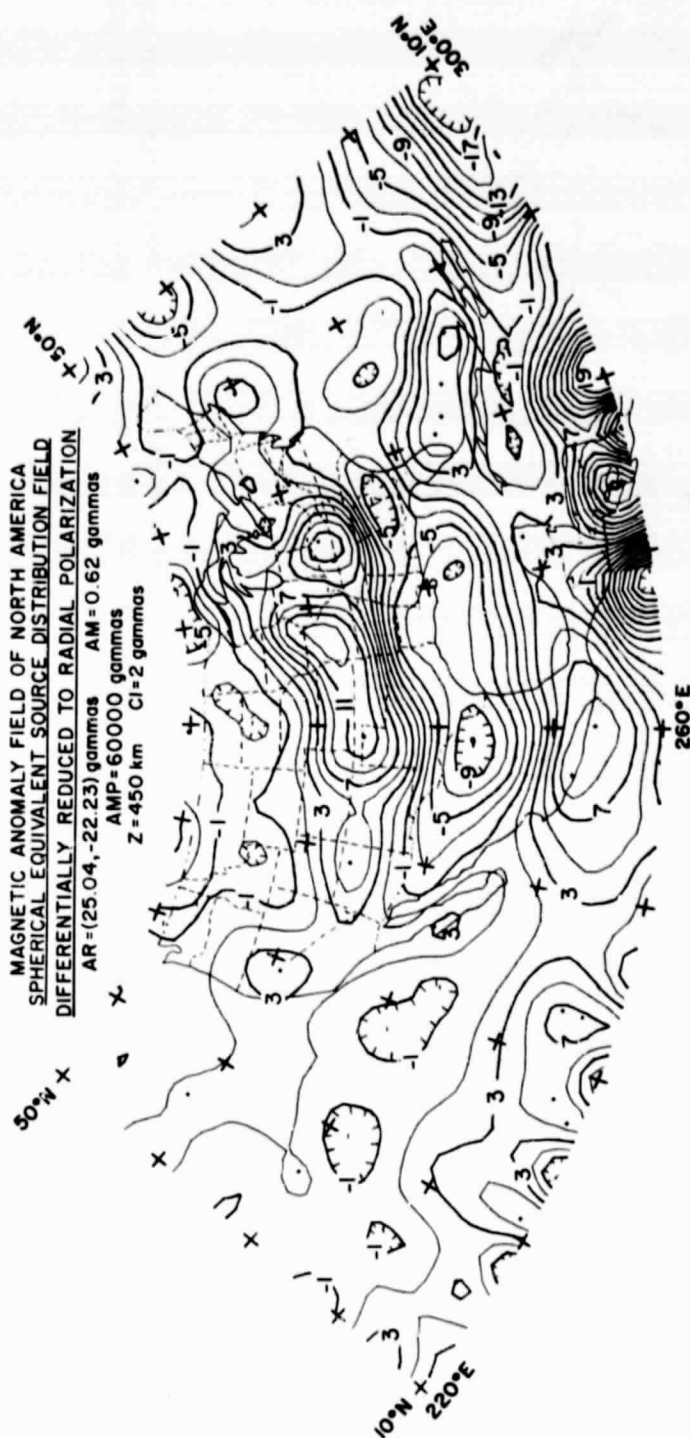
Figure III.6 Spherical equivalent source field approximation of resampled free-air gravity anomaly data for North America upward continued to 450 km elevation.

equivalent source grid was located at a depth of 400 km below the relative elevation of the observation grid and spanned the region $(216-306)^{\circ}\text{E}$, $(6-58)^{\circ}\text{N}$. The station spacing of the source grid was 5° in longitude and 4° in latitude. The resultant equivalent source field approximation of the resampled data is given in Figure III.5. The field of the equivalent point source model was calculated at 450 km elevation above sea level in Figure III.6 to provide an estimate of the upward continued gravity anomalies for comparison with the satellite magnetic anomaly data.

POGO satellite magnetometer observations obtained during 1968 were processed using the procedures described by Mayhew (1979) to yield a magnetic anomaly map of North America at 450 km elevation. Briefly, data processing consisted of removal of the POGO 13th degree geomagnetic field from the original orbital profiled data. Next, data profiles were selected in the elevation range (240-700) km and a least squares quadratic function was fitted to the profiles and removed to account for DS variation arising from ring current flow in the magnetosphere during storm time. An inversion then was performed on a spherical surface grid of prismatic dipolar moments which were oriented in the local direction of the IGRF-1965 updated to 1968. The field of these dipolar moments was recomputed at 450 km elevation in the local direction of the IGRF-1965 updated to 1968 over the region $(220-300)^{\circ}\text{E}$, $(10-50)^{\circ}\text{N}$ to obtain the total magnetic intensity anomaly map for North America given in Figure III.7.

Assuming that the anomalies are derived primarily by induction in the earth's present geomagnetic field, the magnetic map was differentially reduced to radial (vertical) polarization to remove distortions incorporated in the data by variable inclination, declination and amplitude effects of the geomagnetic field. Differential reduction to the pole was achieved by recomputing the field of the equivalent sources assuming a normalizing induction field with an amplitude equal to 60,000 gammas and oriented radially at both source and observation grids. The differentially reduced to the pole magnetic anomaly map for North America is shown in Figure III.8.





Finally, the regional heat flow map for the study area (Chapman and Pollack, 1975) is shown in Figure III.9 for comparison. This map is a smoothed, degree 12 spherical harmonic representation of observed heat flow which is supplemented in areas without observations by geologically predicted heat flow values. Major physiographic provinces and selected structures also are generalized for North America and adjacent marine areas in Figure III.9.

D. Discussion

Comparing Figures III.3, 6, 8 and 9 shows a number of interesting associations which are outlined below. The possible geological significance of these correlations also are considered.

1. Free-Air Gravity Anomaly Field

Although free-air anomalies near zero are generally considered indicative of isostatic equilibrium, it should be noted that care must be exercised with this interpretation because the averaged free-air gravity anomaly of the data set is approximately -7 mgal. This is reflected in the negative geoidal deflection over North America (Chapman and Talwani, 1979) and suggests a mass deficiency over the entire study area. Therefore, all observations regarding the isostatic state of selected portions of the study area should be considered on a relative basis.

A study of the low-pass filtered surface free-air gravity anomalies (Figure III.3) shows the continents characterized by near zero or local positive anomalies, whereas negative anomalies predominate in the oceanic regions. The major exception is the broad negative (-40 mgal) anomaly centered over Hudson Bay which has been interpreted to reflect incomplete isostatic adjustment of the crust following Pleistocene de-glaciation (Innes, et al., 1968), although this explanation has been questioned (Jeffreys, 1975).

In general, the Pacific Ocean is gravitationally more quiet than the Atlantic Ocean. The anomaly values in the Pacific Ocean increase to the west with increasing age of the oceanic crust, thus, suggesting a possible direct relationship between age and mass. However, oceanic ridge areas (e.g., the East Pacific and Juan deFuca

GEOLOGICAL PROVINCES AND SELECTED
STRUCTURES OF NORTH AMERICA
CHAPMAN AND POLLACK'S (1975) HEAT FLOW MAP

CI = 10 mWm⁻²

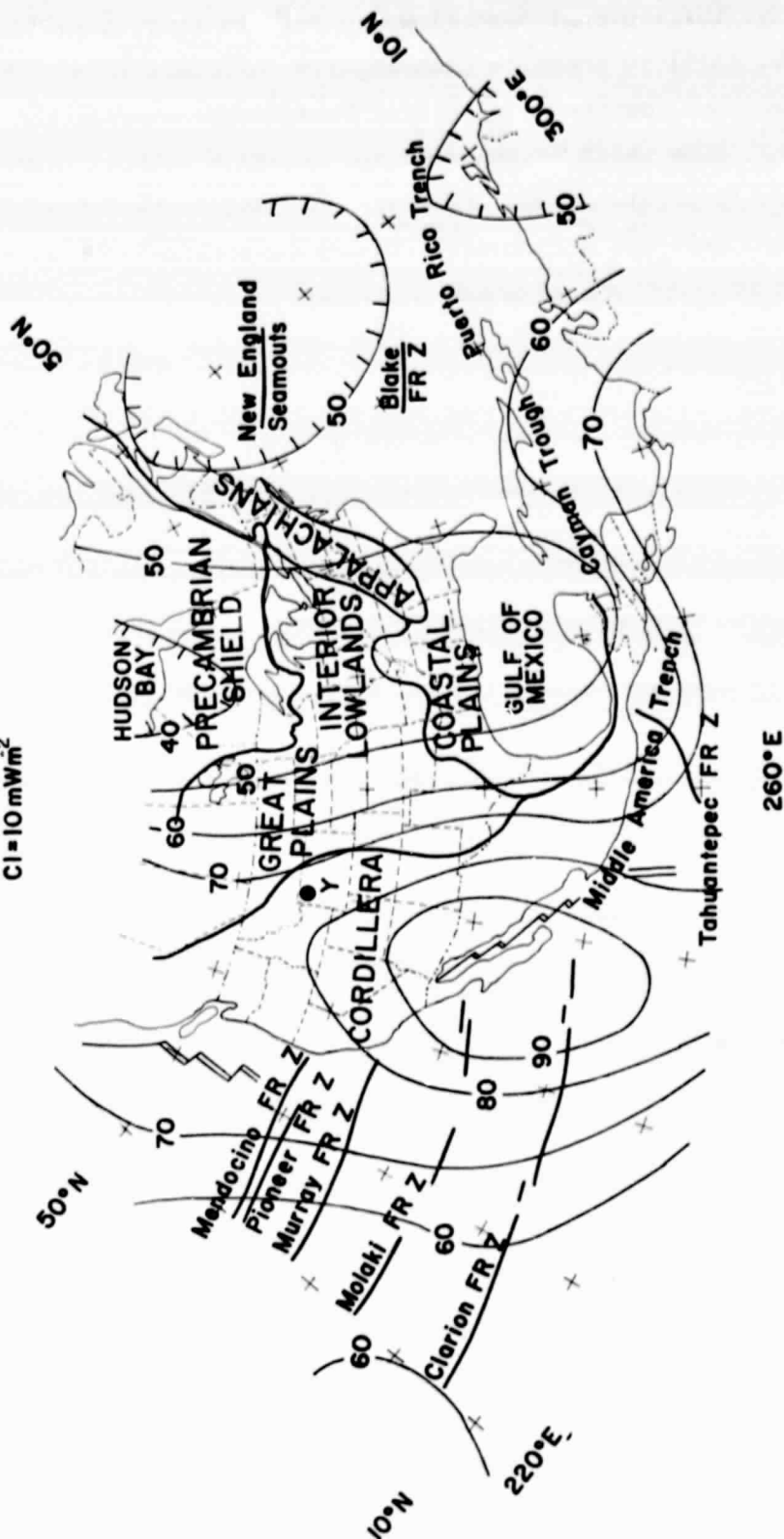


Figure III.9 Heat flow (Chapman and Pollack, (1975)), geological provinces and selected structures of North America.

Ridges) of the Pacific are characterized by relative positive anomalies. In contrast, the western Atlantic along the eastern seaboard, despite its age and relative tectonic stability, is a broad negative gravity anomaly. Talwani and Le Pichon (1969) have postulated lateral inhomogeneities in the upper mantle to explain this anomaly, although it is closely related to a deep oceanic plain.

The largest variations of the entire free-air gravity data set are the negative (-60 mgal) anomalies associated with the Puerto Rico Trench. A common interpretation for these large negative free-air anomalies, which frequently are observed over oceanic trenches (e.g., Vening Meinesz, 1964; Worzel, 1976), is that the earth's crust is being subducted resulting in a mass deficiency. The Sigsbee Deep of the western portion of the Gulf of Mexico also is characterized by a large negative (-50 mgal) free-air gravity anomaly. This is an unusually large amplitude minimum for the observed bathymetry and, thus, raises questions regarding the nature of the crust beneath the Gulf of Mexico.

Both oceans are characterized by pronounced east-west striking anomalies which contrast sharply to structurally compatible, general north-south orientations of the continental anomalies. Off the west coast of California and the Baja Peninsula, the east-west trending arms of the broad Pacific low (-20 mgal) show a particularly interesting correspondence to a number of major fracture zones. For instance, the northern-most west striking arm of this negative anomaly is closely bounded on the north by the Mendocino-Pioneer fracture zones and to the south by the Murray fracture zone.

Within the continent, the Appalachians are associated with a weakly positive, free-air gravity anomaly which continues south across Florida and Cuba. The Mississippi Embayment also is affiliated with a weakly positive north-south trending linear anomaly. The mass excess of the Mississippi Embayment and Delta probably is due in part to an anomalously dense crust that may be a relic of the Mississippi Embayment aulacogen (Ervin and McGinnis, 1975) and not simply the added mass of the sediments.

Within the eastern U.S., east of the Cordillera, the relationship between gravity anomalies and cratonic basins and uplifts is

inconsistent and poorly defined. The Ocala Uplift, for instance, is a relative positive anomaly while the Cincinnati Arch and Sioux Uplift are negative. The Anadarko Basin is associated with a negative anomaly in contrast to the Michigan, Illinois, Williston and Alberta Basins which are all characterized by relative positive free-air gravity anomalies.

In general, positive gravity anomalies characterize the Cordillera of North and Central America. Maxima are located over the geothermal region of the Yellowstone area, the southern Rocky Mountains, the central plateau of Mexico, much of Central America south of Mexico and northern South America. Most of these areas are regional elevation highs, although the relationships are much too complex for the maxima to be explained simply by the excess topographic mass. A few examples illustrate this point with reference to Figures III.10 and 11 which show, respectively, the 1° -averaged topography of the study region and topographic variations high-cut filtered for wavelengths roughly smaller than 8° using the filter of Figure III.2. The Yellowstone and southern Rocky Mountain areas are topographic highs, but a topographic high over the Idaho Batholith area which is larger than the Yellowstone area is not a maximum. The maximum over central Mexico is related to a high plateau area, but is confined within higher mountainous belts. It is bordered on the north by the Cross Range Province which terminates the Basin and Range Province and on the south by the east-west Neovolcanic Province. In contrast, a maximum gravity anomaly occurs over the relatively low-lying Yucatan Peninsula. In southeast Mexico, the Cordillera gravity maxima are separated by a minimum which projects onto the northern extension of the Tehuantepec Fracture Zone.

The Coast Range of the U.S. and the Basin and Range Province of the U.S. and northern Mexico are generally free of gravity anomalies suggesting that they are approximately in isostatic equilibrium. However, the Basin and Range Province grades into a Volcanic Rift Province in northeastern California and southern Oregon and Idaho (Hamilton and Myers, 1966) which is a gravity maximum. This maximum appears to be related to a mass excess which is related to Mesozoic crustal thinning and Cenozoic rifting and volcanism. This contrasts with the relative gravity minimum over the Columbia River Plateau basalts of Washington and adjacent states.

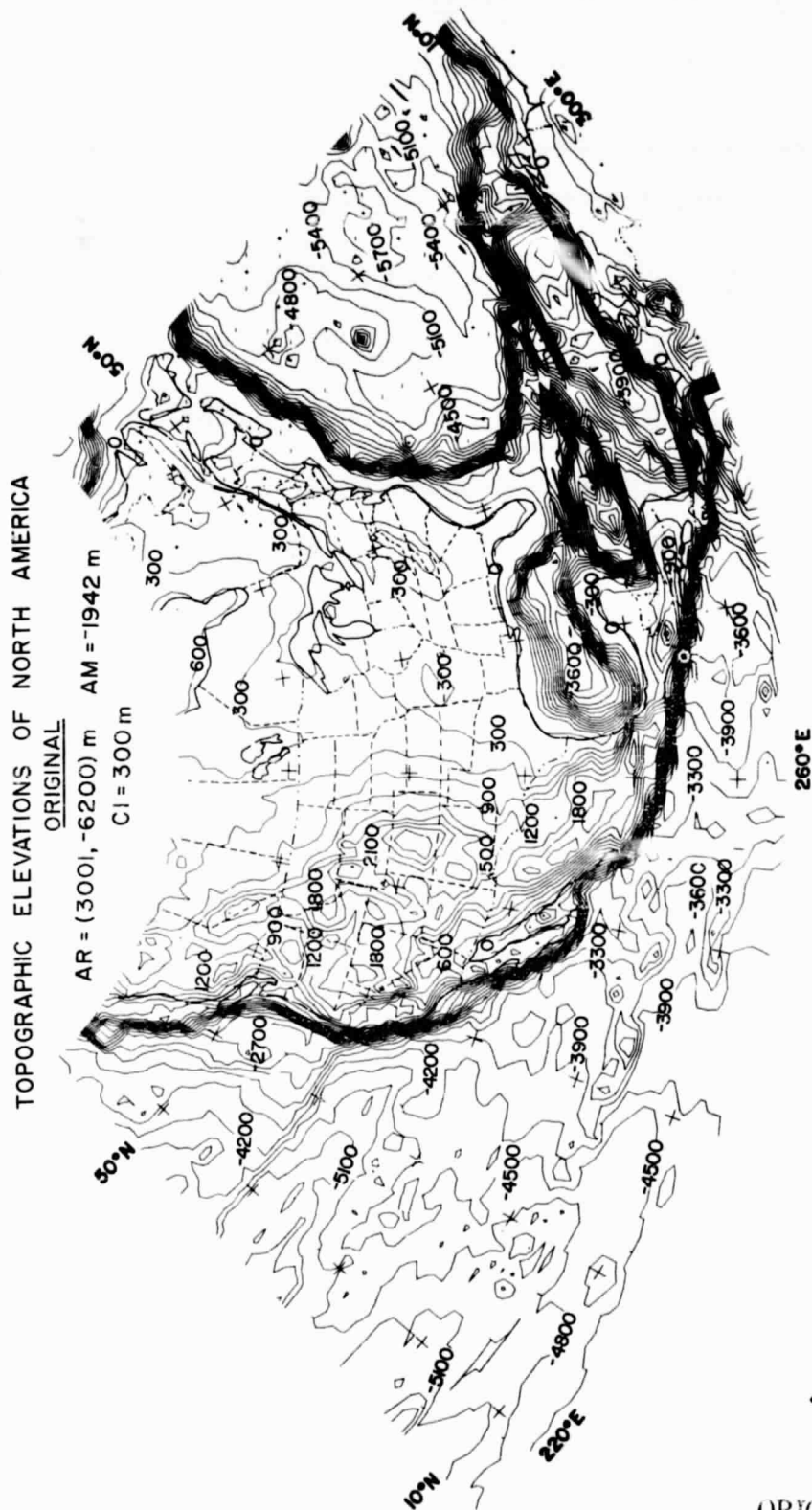


Figure III.10 1°-averaged topographic elevations for North America.

ORIGINAL PAGE IS
OF POOR QUALITY

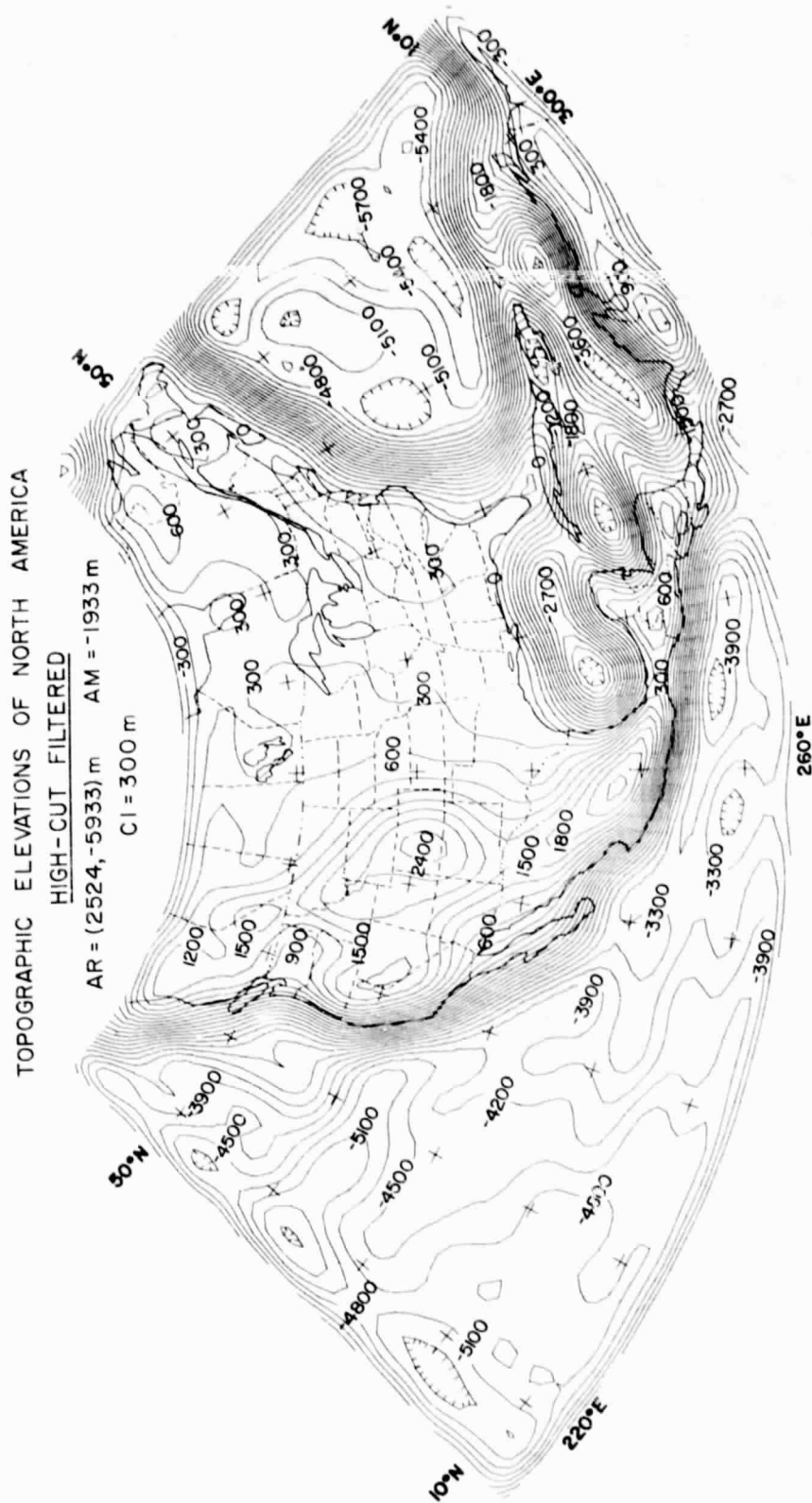


Figure III.11 High-cut ($\lambda \leq 8^\circ$) filtered 1° -averaged topographic elevations for North America.

A study of Figure III.6 shows that the major anomalies are still represented, although much of the anomaly detail has been lost in upward continuing the free-air gravity field to 450 km. The positive anomalies affiliated with the Cordilleran System of the U.S., southern Mexico and Central America have survived the upward continuation process, but with this exception the anomaly field is dominated by the negative anomalies centered over the Puerto Rico Trench, Hudson Bay, the Gulf of Mexico and the Pacific Plate.

2. Magnetic Anomaly Field

The most obvious feature of the radially polarized magnetic anomaly map of Figure III.8 is a prominent east-west high across the midcontinent which is breached by a negative anomaly in the Mississippi Embayment region (Mayhew, 1976; 1977). The closures of this magnetic high correspond to a trend of free-air gravity anomaly minima which extends from the Anadarko Basin of the eastern panhandle of Texas to the tri-state area of Indiana, Ohio and Kentucky (Figures III.3 and 6). It is interesting to note that these areas of increased magnetic anomalies and decreased gravity anomalies also are shown by seismic evidence to be areas of thicker crust (Warren and Healy, 1973) as illustrated in Figure III.12. Accordingly, the combination of negative gravity and positive magnetic anomalies can be interpreted to reflect displacement by anomalously thick crustal material of the denser and less magnetic material of the mantle.

To the west, the large transcontinental magnetic high appears to overprint a northwest trend of negative magnetic anomalies which corresponds to the Cordillera and affiliated positive free-air gravity anomalies. Here the inverse correlation of gravity and magnetic anomalies may be related to increased heat flow from beneath the lithosphere which is likely to deflect the Curie isotherm to a shallower depth, thus, producing a region of relative net negative magnetization. Similarly, a negative magnetic closure over eastern Idaho which corresponds to a prominent positive free-air gravity anomaly, is interpreted as due to a lower net crustal magnetization related to a thinner magnetic crust over the path of the Yellowstone hot spot.

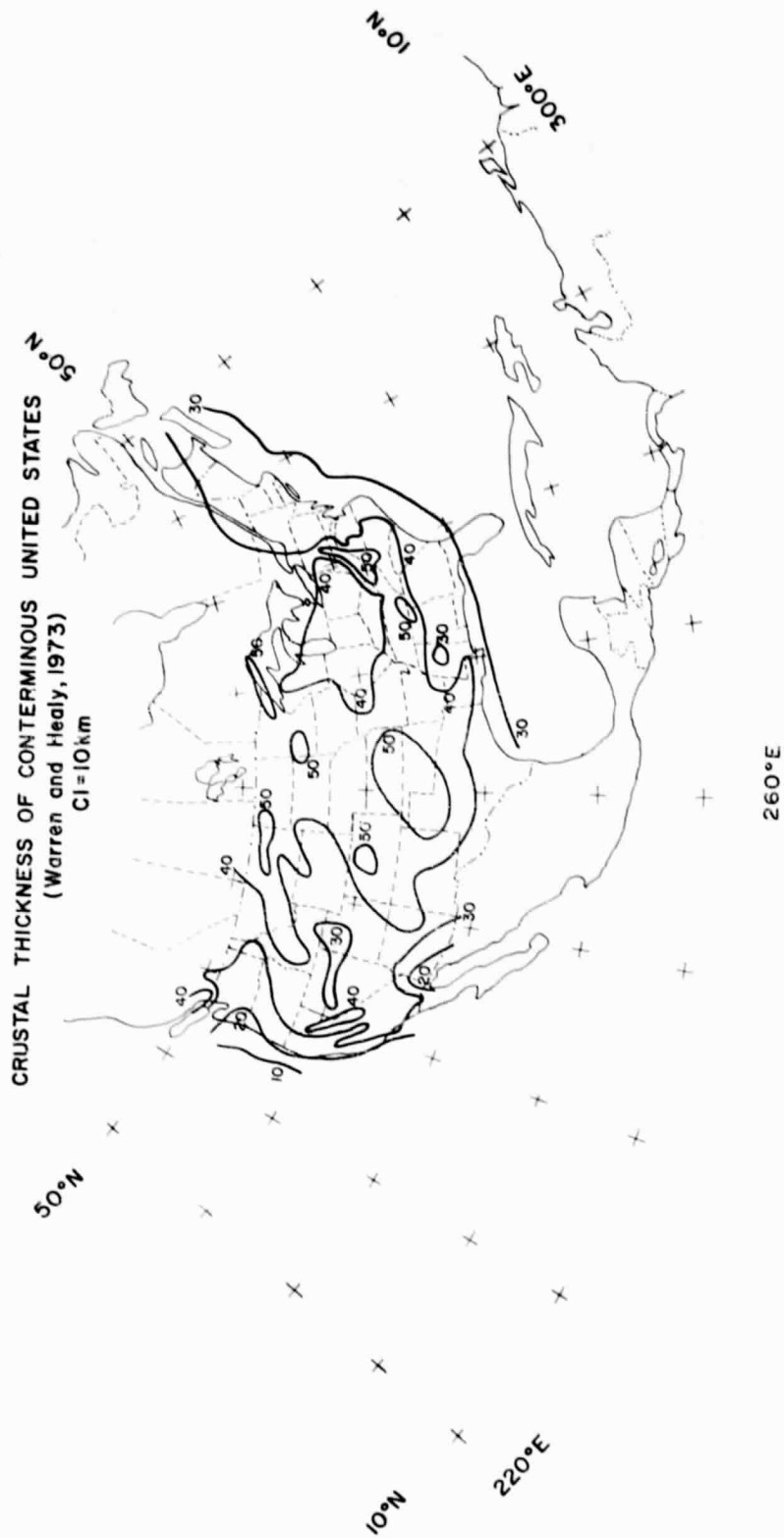


Figure III.12 Seismically determined crustal thickness map (Warren and Healy, 1973) for the conterminous United States.

Other prominent features of Figure III.8 include the magnetic high over the Antilles-Bahamas Platform which extends to southern Florida and the broad negative magnetic anomaly that projects along the Gulf Coast of the U.S. from Louisiana westward across Mexico. The eastern component of the negative anomaly appears to correspond with the southern terminus of the weakly positive free-air gravity anomaly of the Mississippi Embayment, whereas the western component roughly correlates with a large positive gravity feature of the Cordillera.

The magnetic anomalies of the western third of the continent (i.e., the Cordillera) are relatively subdued in contrast to the characteristics of the eastern two-thirds of the continent. The western portion has relatively broad strong positive gravity anomalies and a regional heat flow maximum (Figure III.9) with a shallower Curie isotherm. Thus, the subdued magnetic anomaly pattern appears to be the result of a relatively thin and laterally homogeneous magnetic crust.

In general, the correlation of magnetic and gravity anomalies over continental regions may be restricted because the gravity data contain long-wavelength effects of deep crustal or upper mantle sources which are too deep to be magnetic anomaly sources as a result of regimes where the temperature exceeds the Curie point of magnetite. The contrasting north-south gravity trends and east-west magnetic trends over North America may be evidence of this effect. The correlation of anomalies also may be hindered by remanent magnetization effects which are at a large angle to the present field or may even be reversed. Finally, correlations may be limited by anomaly sources with inconsistent density and magnetization distributions. However, even this information from restricted gravity and magnetic correlations can be useful as a guide to delineating and modeling sources by pointing out, for instance, remanent magnetization effects and possible depths of anomaly sources.

3. Heat Flow Field

Other than the previously noted correlation of the high heat flow region of western U.S. (Figure III.9) with a subdued magnetic anomaly pattern (Figure III.8), there is no general correlation of the two maps. However, in a regional sense, the direct correlation

of the heat flow map with the upward continued gravity anomaly map (Figure III.6) is rather striking. This supports the suggestion that regional gravity and heat flow anomalies may have a deeper source than magnetic anomalies and, thus, may be more prone to correlation. The positive gravity anomalies of the Cordillera correlate with anomalously high heat flow values ($>60 \text{ mWm}^{-2}$), but the axis of the heat flow high lies west of the axis of the gravity anomaly. This is believed to be the result of the very broad wavelength of the heat flow high (12th degree spherical harmonic) which has superimposed the effect of the heat flow high of the magmatic region of western North America with the heat flow maxima associated with the Gorda and Juan deFuca Oceanic Ridges off the northwest coast of the U.S. In general, the negative gravity anomalies of the oceans correlate with low heat flow values, although an exception occurs for the observed heat flow maximum centered over the Baja Peninsula (Chapman and Pollack, 1975) which correlates with negative gravity anomaly values. The negative gravity anomalies of Hudson Bay and the western Atlantic Ocean also are correlative with relative heat flow minima.

E. Conclusions

Regional continental free-air gravity anomalies of North America parallel prevailing north-south structural trends, while the anomalies of the adjacent oceanic areas are more negative and subdued and strike roughly east-west. The mean free-air anomaly of the area is approximately -7 mgal suggesting a broad general mass deficiency which is reflected in negative geoidal deflections. Western North America and much of Central America are characterized by broad positive free-air gravity anomalies in contrast to more areally-limited maxima and minima of the eastern portion of the continent. Hudson Bay and western Gulf of Mexico are marked negative anomalies. Some regional gravity anomalies are related to surface elevation or bathymetry, but the number of exceptions are sufficient to suggest that the sources of the anomalies are largely deeper geologic mass variations. This is substantiated by the correlation of several regional gravity and magnetic

anomalies, although there are exceptions which may have different explanations. However, it appears that several gravity anomalies are derived from beneath the magnetic crust.

The magnetic anomaly map shows a more complex pattern with positive anomalies over the continents and Antilles-Bahamas Platform as compared to generally negative anomalies for the oceans. The entire area has an unexplained east-west striking bias to the magnetic anomalies. The general relationship between gravity and magnetic anomalies over the continents is inverse. Regions of large relative crustal thickness in particular appear to be characterized by negative free-air gravity and positive magnetic anomalies. Negative magnetic and positive gravity anomalies, on the other hand, may be related to regions of increased heat flow.

Free-air gravity anomalies upward continued to 450 km directly correlate with a 12th degree spherical harmonic representation of the heat flow, but little correlation is observed between specific magnetic anomalies and this heat flow pattern. Nevertheless, high heat flow areas tend to have a subdued magnetic pattern as a result of the lower net crustal magnetization associated with shallow Curie isotherm regions.

These broad conclusions suggest that combined interpretation of long-wavelength gravity, magnetic, and heat flow anomalies can significantly decrease the ambiguity of the interpretation process because these anomalies map not only different parameters, but their potential sources tend to cover different depth ranges within the earth. In general, gravity anomalies and heat flow are derived from both crustal and sub-crustal sources, while magnetic anomalies have principally crustal sources. Therefore, the mapping of long-wavelength magnetic anomalies provides a valuable complementary set of data to gravity and heat flow anomalies for the investigation of megatectonic features of the continents and oceans.

F. References

- Bowman, P.L., L.W. Braile, V.W. Chandler, W.J. Hinze, A.J. Luca, and R.R.B. von Frese, Magnetic and gravity anomaly correlation and its application to satellite data, NASA-GSFC TM79702, 1979.
- Chapman, D.S., and H.N. Pollack, Global heat flow: A new look, Earth and Planetary Science Lt., 28, 23-32, 1975.
- Chapman, M.E., and M. Talwani, Comparison of gravimetric geoids with Geos 3 altimetric geoid, Jour. Geophy. Res., 84, 3803-3816, 1979.
- Ervin, C.P. and L.B. McGinnis, Reelfoot rift: Reactivated precursor to the Mississippi Embayment, Geol. Soc. Am. Bull., 86, 1287-1295, 1975.
- Hamilton, W., and W.B. Myers, Cenozoic tectonics of the western United States, Rev. Geophysics, 4, 509-549, 1966.
- Hinze, W.J., L.W. Braile, V.W. Chandler, and F.E. Mazzella, Combined magnetic and gravity analysis, U.S.G.S. Final Rpt., NASA Contract No. S-500 29A Modification No. 8, 1975.
- Innes, M.J.S., A.K. Goodacre, A.A. Weston, and J.R. Weber, Gravity and isostasy in the Hudson Bay region, Science, History and Hudson Bay, 2, 703-728, 1968.
- Jefferys, H., The Fenno-Scandian uplift, Roy. Geol. Soc. Lond., 131, 323-325, 1975.
- Mayhew, M.A., Magnetic anomaly map of North America south of 50°N from POGO data, GSFC-NASA Doc. X-922-76-201, 1976.
- Mayhew, M.A., Large scale variations in crustal magnetization in central U.S. based on satellite data, EOS Trans., AGU, 59, 228, 1977.
- Mayhew, M.A., Inversion of satellite magnetic anomaly data, J. Geophys., 45, 119-128, 1979.
- Nettleton, L.L., and T.A. Elkins, Association of magnetic and density contrasts with igneous rock classifications, Geophysics, 9, 60-78, 1944.
- Pollack, H.N., and D.S. Chapman, On the regional variation of heat flow, geotherms, and lithospheric thickness, Tectonophysics, 38, 279-296, 1977.
- Strange, W.E., and G.P. Woollard, The use of geologic and geophysical parameters in the evaluation, interpolation, and prediction of gravity, Hawaii Inst. of Geophys., Doc. HIG-64-17, 1964.

- Talwani, M., and X. LePichon, Gravity field over the Atlantic Ocean; in Hart, P.J., ed., The Earth's Crust and Upper Mantle, Am. Geophys. Union Geophys. Mon., 13, 341-351, 1969.
- Vening Meinesz, F.A., Developments in Solid Earth Geophysics-1-The Earth's Crust and Mantle, Elsevier, New York, 1964.
- Warren, D.H. and J.H. Healy, Structure of the crust in the conterminous United States, Tectonophysics, 20, 203-213, 1973.
- Woollard, G.P., The relation of gravity anomalies to surface elevation, crustal structure and geology, Univ. Wis. Geophys. Polar Res. Center Res. Rep. SER. 62-9, 1962.
- Worzel, J.L., Gravity investigations of the subduction zone; in Sutton, G.H., M.H. Manghnani, and R. Moberly, eds., The Geophysics of the Pacific Ocean Basin and its Margin, Am. Geophys. Union Geophys. Mon., 19, 1-15, 1976.

IV. QUANTITATIVE CORRELATION ANALYSIS OF REGIONAL NORTH AMERICAN GRAVITY AND MAGNETIC ANOMALIES

A. Abstract

To quantitatively investigate the regional correlations of gravity and magnetic anomalies over North America, Poisson's theorem is used in a moving-window linear regression analysis performed between suitable derivatives of the anomalous potential fields at 450 km elevation. The results of moving-window Poisson's analysis are useful for establishing patterns of anomaly correlation and provide initial physical property constraints to facilitate further investigation of correlating anomalies. The statistical correlation of regional gravity and magnetic anomalies over continental terrane is predominantly inverse. In particular, regions of large relative crustal thickness are associated with negative gravity and positive magnetic anomalies, as well as exceptionally large magnetization* ($\approx 1.8 \times 10^{-2} \text{ emu/cm}^3$). This characterization is exemplified by a prominent east-west magnetic high across the midcontinent which corresponds to a trend of gravity maxima that extends from western Texas to the Cincinnati Arch. Negative magnetic and positive gravity anomalies, on the other hand, are related to thinner crust and regions of higher heat flow. Typical examples include the Cordillera of North and Central America and the Yellowstone geothermal region. Over oceanic areas regional anomaly correlations are poorly developed probably because of decreased crustal magnetization. Statistically, however, these regions are characterized primarily by direct gravity and magnetic anomaly correspondences.

*) $1 \text{ emu/cm}^3 = 1 \text{ oersted} = (10^3/4\pi) \text{ A/m}$

B. Introduction

The utility of long-wavelength gravity anomalies, covering several degrees of surface area, for geologic analysis has been recognized for many years. More recently magnetic anomalies which have significant energy in wavelengths of several hundred kilometers or more have been identified as originating from within the earth's crust and perhaps the uppermost mantle (Alldredge et al., 1963). The geological interpretation of these regional anomalies is hindered by the effect of anomaly superposition and the source ambiguity which is inherent to the analysis of potential fields. A common approach to minimizing these interpretational limitations, especially in continental terrane, is to evaluate the correlation between anomalous gravity and magnetic potentials.

The basis of correlation analysis is the hypothesis, commonly validated in continental areas, that variations in lithology and physical properties of the crystalline crust are reflected in both their bulk mineralogy, which controls rock density and, thus, gravity anomalies, and their minor mineral content, specifically magnetite, which is the primary cause of magnetic anomalies. Consideration of the general magnetic and density properties of the crust and upper mantle and the geologic causes of their variations suggests that correlation between long-wavelength magnetic and gravity anomalies, both direct and inverse, are anticipated, but not on a universal basis. Seismic and other geophysical and geologic evidence shows that the lithosphere is marked by vertical variations, principally by the Moho which separates the crust and mantle and by a much more poorly defined and less consistent boundary between the upper and lower crust. Increasing evidence points to lateral variations in the petrophysical and chemical attributes of these so called "layers." The vertical and lateral variations plus temperature perturbations are all potential sources of gravity and magnetic anomalies.

Geophysical and geologic evidence clearly indicates that the density of the crust increases from a mean value of approximately 2.7 gm/cm^3 at the surface to roughly the 2.9 to 3.0 gm/cm^3 range at the base of the crust where there is a sharp increase to roughly 3.3 gm/cm^3 in the upper mantle. The magnetic properties of these layers are much less precisely known, but generally the lower crust is believed to have a

magnetization of roughly 5×10^{-3} emu/cm³ made up equally of induced and viscous remanent magnetization, which is several orders of magnitude greater than the mean magnetization of the upper crust. Wasilewski et al., (1979) present a strong case for a non-ferrimagnetic upper mantle. As a result for a constant thickness crust, we anticipate a direct correlation between gravity and magnetic anomalies as the thickness of the layers of the crust change. In contrast, if the upper crust is relatively constant in thickness and the depth to the Moho is accommodated by varying the thickness of the lower crust, an inverse relationship is anticipated between gravity and magnetic anomalies.

Intra-layer lithologic variations caused by plutonic differentiates and regional and local metamorphism and alteration are known to be common in the upper crust and are almost certainly present on a widespread scale in the lower crust and upper mantle. Where ground-truth is available from direct observation of the upper crust, gravity and magnetic anomalies from these variations often are correlatable. There are many exceptions, and even these are geologically informative, but in the main both the density and magnetization increase as the plutonic and metamorphic rocks become more mafic. Thus, we anticipate that lithologic variations within the lower crust will produce correlative anomalies. In fact, the correlation generally should be better from lower crustal rocks because slower cooling of the mafic rocks at depth will lead to increased exsolution of magnetite from the essentially non-magnetic components of the titanomagnetite series, thus, increasing the magnetization of the denser mafic rocks. Furthermore, remanent magnetization which so commonly complicates the correlation of upper crustal rocks, particularly the eruptive rocks, will be decreased in lower crustal rocks by the higher ambient temperatures and the increased age of the rocks. Thus, in general, intra-layer lithologic variations of the lower crust will yield directly correlative gravity and magnetic anomalies, although the correlations will not be universal or always direct.

Finally, temperature variations, both regional and local within the crust, will affect the correlation of gravity and magnetic anomalies.

Although the density of rocks will vary with temperature as a function of the volume coefficient of thermal expansion, the effect is minimal when considering the profound effect that temperature has upon magnetic properties. Magnetic susceptibility will be increased over certain temperature ranges and remanent magnetization will be decreased and viscous magnetization in the direction of the earth's magnetic field will be increased as temperature increases. However, the critical temperature is the Curie temperature, above which ferrimagnetic minerals are transformed into the essentially non-magnetic, paramagnetic form. Thus, increased temperatures which reach the Curie point range of ferrimagnetic minerals within the lower crust (500° - 550°C) will decrease the thickness of this highly magnetic layer. The decreased magnetic anomaly will have an inverse relationship to the free-air gravity anomaly because regionally higher temperatures are associated with geodynamic processes which produce a thinned crust and an inflated elevation which may not be isostatically compensated. Both of these conditions will lead to an increase in mass and a relative positive free-air gravity anomaly correlating with a negative magnetic anomaly.

Correlation of anomalies generally has been accomplished by subjective visual correlation of anomalies over regional areas. To decrease the subjectivity of the correlation techniques it is desirable to utilize a more quantitative approach, preferably a method based upon Poisson's theorem which theoretically relates magnetic and gravity anomalies from a common source.

One such method is given by Chandler et al., (1980) which employs Poisson's theorem in a moving-window linear regression analysis that traverses across multiple source gravity and magnetic data sets to quantitatively identify regions of spatially coincident anomalies. For regions of high correlation, the method also gives initial estimates of the physical property contrast ratios for the inferred sources. To investigate its applicability to the study of regional-scale potential field data, moving-window Poisson's analysis was performed between a number of gravity and magnetic anomaly maps prepared at satellite elevations for North America and its marine environs south of 50°N latitude.

C. Quantitative Correlation Procedure

Poisson's theorem relates at an observation point the magnetic potential of a uniformly dense and magnetized body to the first derivative component of the gravity potential taken in the direction of magnetization by the ratio of the body's magnetization-to-density properties. Accordingly, Poisson's theorem can be extended to equate the total magnetic intensity anomaly reduced to normal (radial) polarization, $\Delta T(N)$, and the first radial derivative of the gravity anomaly, $\partial \Delta g / \partial r$ by the relation

$$\Delta T(N) = \frac{\Delta j}{G \cdot \Delta m} * \frac{\partial \Delta g}{\partial r}, \quad \text{where} \quad (\text{IV-1})$$

Δg = gravity anomaly,

Δm = density contrast of the source,

G = universal gravitational constant, and

Δj = magnetization contrast of the source.

Equation (IV-1) shows that the property contrast ratio ($\Delta j / \Delta m$) for a single anomalous source can be obtained at a common observation point from its gravity and total magnetic field anomalies by calculating the radial gravity derivative and reducing the magnetic anomaly to radial polarization.

For regional-scale, complex data sets containing interfering anomalies due to multiple sources, spatial segments may occur where the anomaly of a particular source is dominant. The approximate Poisson's relationship in such instances is given by the linear equation

$$\Delta T(N) = A + \frac{\Delta j}{G \cdot \Delta m} * \frac{\partial \Delta g}{\partial r}, \quad (\text{IV-2})$$

where the intercept A reflects the anomaly base level within the spatial segment considered, and the slope ($\Delta j / \Delta m$) is a weighted average for the interfering sources that is most heavily weighted towards the dominant source.

The concept of Poisson's analysis restricted to limited segments of a complex anomaly has been used successfully by Lyubimov and

Lyubimov (1968), Wilson (1970), and Chandler et al., (1980). For combined analysis of multiple source gravity and magnetic data sets, Chandler et al., (1980) utilize the generalized Poisson's relationship (IV-2) in a moving-window linear regression analysis. The procedure is to center a window of specified size on each node of a uniform grid to which the appropriate gravity and magnetic data have been registered. Within the window, a least-squares linear regression is performed between the spatially coincident data where the radial gravity derivative serves arbitrarily as the independent regression variable. For each window position, the regression yields 1) a correlation coefficient that is indicative of the linear fit of the data within the window, 2) a slope ($\Delta g/\Delta m$) coefficient, and 3) an intercept coefficient (A) which gives the anomaly base level for the data within the window. The regression parameters are assigned to the central grid node of the window position. The window is shifted next one grid position and the regression analysis repeated. This procedure is continued until the entire data space has been subjected to moving-window Poisson's analysis.

The size of the operational window chosen for a given application must be large enough that a minimum number of data points are involved to achieve a credible linear regression, yet small enough to resolve the anomalies of interest from the interference of neighboring anomalies. Currently, no quantitative method is evident for making this choice. However, Chandler et al., (1980) have obtained useful results with windows that include at least 5 data points and are between 0.5 and 1.0 times the half-width of the primary anomalies of interest.

The behavior of the linear regression coefficients can be useful in establishing patterns of correlation between gravity and magnetic anomalies. The most significant linear regression exhibits correlation coefficients approaching either 1.0 or -1.0 which reflect, respectively, either direct (+) or inverse (-) correspondence between gravity and magnetic anomalies. Variations of the intercept parameter (A) reflect base level changes due to regional anomalies and the effects of localized anomaly interference.

For a particular window position, the slope of the regression line gives an estimate of $(\Delta j/\Delta m)$ for the dominant anomaly source. However, this ratio is not uniquely definitive of the anomaly source lithology because $(\Delta j/\Delta m)$ is a function of the physical properties of both the source and country rock. Also, different combinations of Δj and Δm will give the same source ratio. The estimated slope value $(\Delta j/\Delta m)$ can serve, however, as an initial constraint for facilitating further interpretation.

Due to anomaly interference, variations of the slope values across multiple source data sets reflect both geologically significant and erroneous $(\Delta j/\Delta m)$ estimates. There is no quantitative criteria for discriminating geologically significant slope values. However, Chandler *et al.*, (1980) recommend emphasis on slope values corresponding to the high-gradient limbs and peaks of spatially well matched gravity and magnetic anomalies which generally are characterized by higher correlation coefficients and zones of spatially stable regression parameters. Particular emphasis should be placed on anomaly gradients because slight shifts of anomaly peaks will cause a marked decrease in the correlation over the peaks, but will not cause a marked change over the high-gradient areas. The dominance of a particular anomaly source is reflected in the spatial stability of the regression parameters. Spatial instability of these parameters generally characterizes transition zones between the dominance of adjacent anomalies. In such instances, the regression coefficients, particularly the intercept values, can exhibit marked local fluctuations.

Spatial differentiation of equation (IV-2) shows that the moving-window Poisson's analysis readily can be extended to investigate correlations of the n -th magnetic spatial derivative anomaly field and the $(n+1)$ -th gravity spatial derivative anomaly field. Spatial differentiation tends to emphasize the near-surface, higher frequency components of potential field anomalies. This can be important to regional correlation analysis of satellite gravity and magnetic anomalies because spatial differentiation will minimize the interfering effects of gravity sources located deeper than the depth of the Curie isotherm which effectively defines the maximum depth extent for magnetic anomaly sources.

Suitable wavelength filtering in general can enhance the geologic significance of the results of moving-window Poisson's analysis by enhancing the spectral compatibility of gravity and magnetic anomaly data which contain the effects of common sources. Chandler *et al.*, (1980) present a number of examples which illustrate the utility of wavelength filtering for moving-window Poisson's analysis.

D. Data Sets and Processing

To implement moving-window Poisson's analysis pertinent gravity anomaly derivatives and radially polarized magnetic anomalies and derivatives must be computed over a common observation grid. These processing procedures and the characteristics of the resultant data sets are considered below.

1. Gravity Anomaly Maps

The gravity maps used in this investigation all are derived from the smoothed, 1° -averaged surface free-air gravity anomalies illustrated in the contoured stereographic equal-area polar (SEAP) projection of Figure IV.1. As described by Bowman *et al.*, (1979), the smoothed gravity anomaly map was obtained by high-cut filtering anomalies with wavelengths less than about 8° from a data set of 1° -averaged values provided by NASA-GSFC. The data set in Figure IV.1 consists of (82,42) values uniformly spanning the region $(219.5-300.5)^\circ\text{E}$, $(9.5-50.5)^\circ\text{N}$ at 1° intervals. The amplitude range (AR) of the data set is between 40 mgal and -62 mgal and the amplitude mean (AM) is -7.87 mgal.

In general, the continent is characterized by relatively positive anomalies which trend roughly NS along the prevalent geological strike of the region. The Appalachian and Ouachita Mountain Systems exhibit a slightly positive free-air gravity anomaly which continues south across Florida and Cuba. The Mississippi Embayment also is characterized by a weakly positive anomaly. The Cordilleran System is delineated by a well defined trend of positive free-air anomalies which attain maxima of roughly 30 mgal over Mexico and the Yellowstone geothermal region.

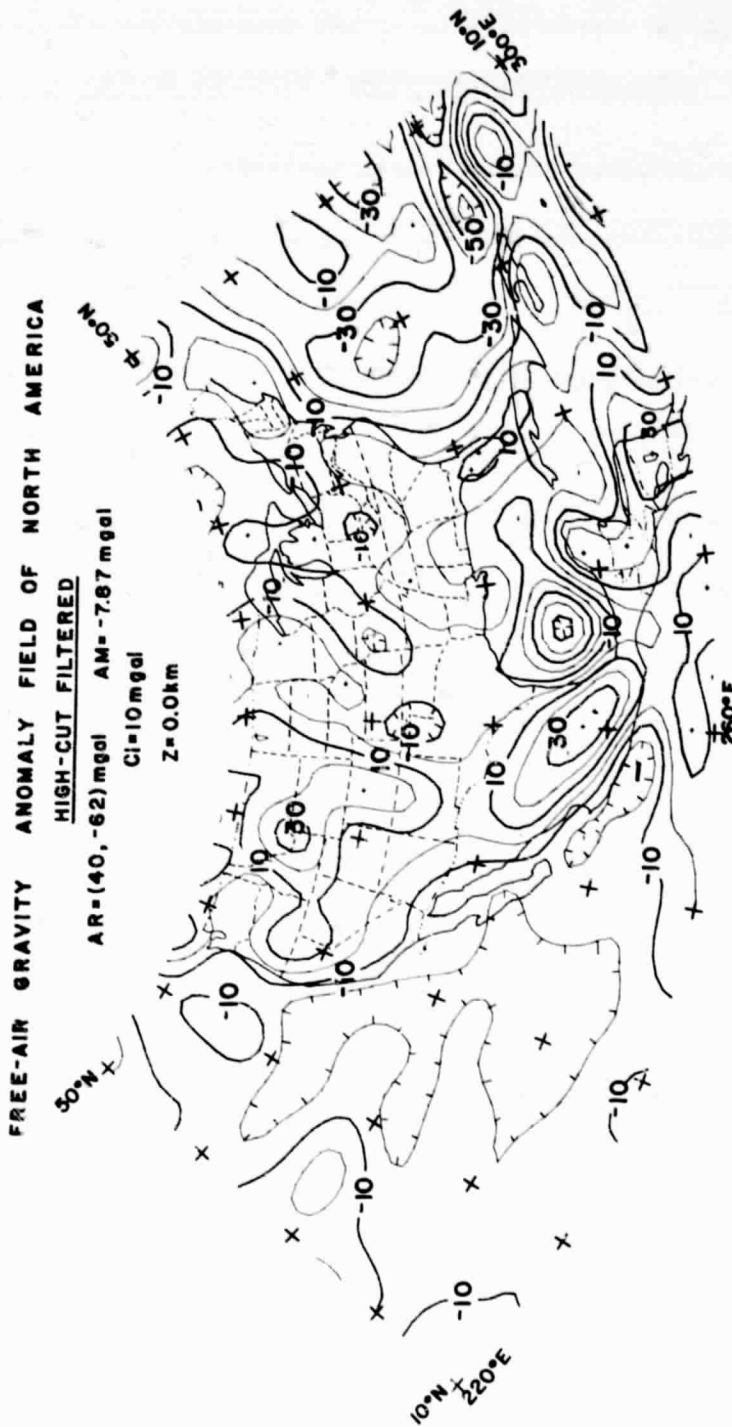


Figure IV.1 Stereographic equal-area polar (SEAP) projection of high-cut ($\lambda \leq 8^\circ$) filtered 1° -averaged free-air gravity anomaly data for North America. Amplitude range (AR) of data set is 40 to -62 mgal and the amplitude mean (AM) is -7.87 mgal. Contour interval (CI) is 10 mgal and reference elevation (Z) of the observations is 0.0 km.

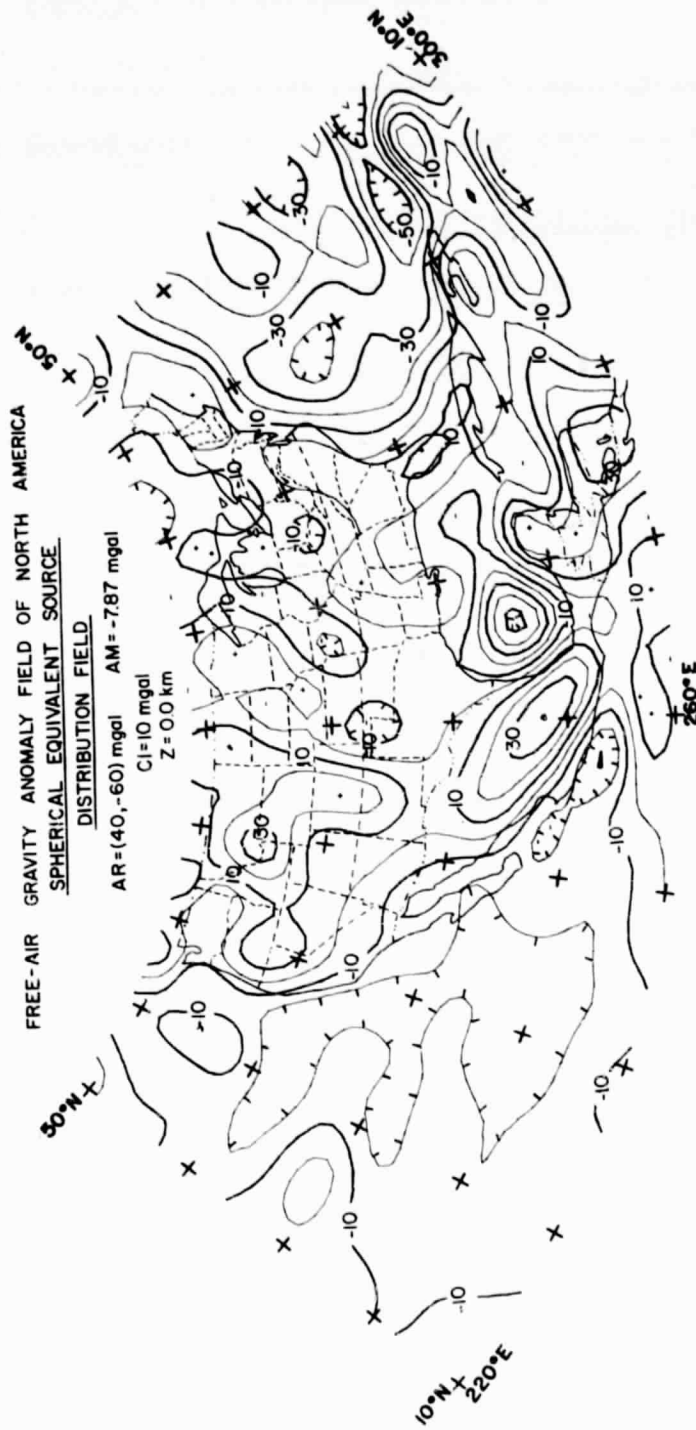


Figure IV.2 Spherical equivalent source field approximation of free-air gravity anomaly data for North America.

By contrast, oceanic anomalies are generally negative and trend EW along major fracture zones and trench systems. A number of fracture zones are well delineated by the EW striking components of the broad Pacific low (-20 mgal) off the west coast of California and the Baja Peninsula. The largest variations of the entire data set are the negative (-60 mgal) anomalies associated with the Puerto Rico Trench. The Gulf of Mexico also is characterized by a prominent negative (-50 mgal) free-air gravity anomaly.

To project the smoothed free-air gravity anomalies to satellite elevations for comparison with POGO satellite magnetic anomalies, the data of Figure IV.1 were related by least squares matrix inversion to a spherical grid of 435 gravity point poles. The grid of equivalent point sources was located at a depth of 400 km below the earth's surface and uniformly spanned the region $(220-300)^{\circ}\text{E}$, $(10-50)^{\circ}\text{N}$ at a station interval of 2.857° . Computing the gravity effect of the point sources over the observation grid of Figure IV.1 gives the equivalent source approximation of the smoothed free-air gravity anomaly field shown in Figure IV.2. A comparison of the amplitude means for the gravity anomaly maps of Figures IV.1 and 2 shows that the equivalent point source approximation fits the original data with negligible error.

To upward continue the smoothed free-air gravity anomalies to satellite elevations the equivalent point source field was computed next at 450 km elevation as shown in Figure IV.3. Here the upward continued data set consists of (81,41) values computed at integral degree nodes of the spherical grid uniformly spanning the region $(220-300)^{\circ}\text{E}$, $(10-50)^{\circ}\text{N}$ at a station interval of 1° . Besides the obvious loss of resolution, Figure IV.3 shows that the only positive anomalies surviving upward continuation are affiliated with the Cordilleran System of the U.S., Mexico and Central America. Otherwise, the upward continued data are dominated by negative anomalies associated with the Puerto Rico Trench, the Gulf of Mexico, and the Pacific Plate.

In Figure IV.4, the first order radial derivative of the free-air gravity anomaly field at 450 km elevation is computed from the equivalent point source distribution for quantitative correlation via Poisson's theorem with satellite magnetic anomaly data reduced to the pole. The first radial derivative data provide enhanced resolution

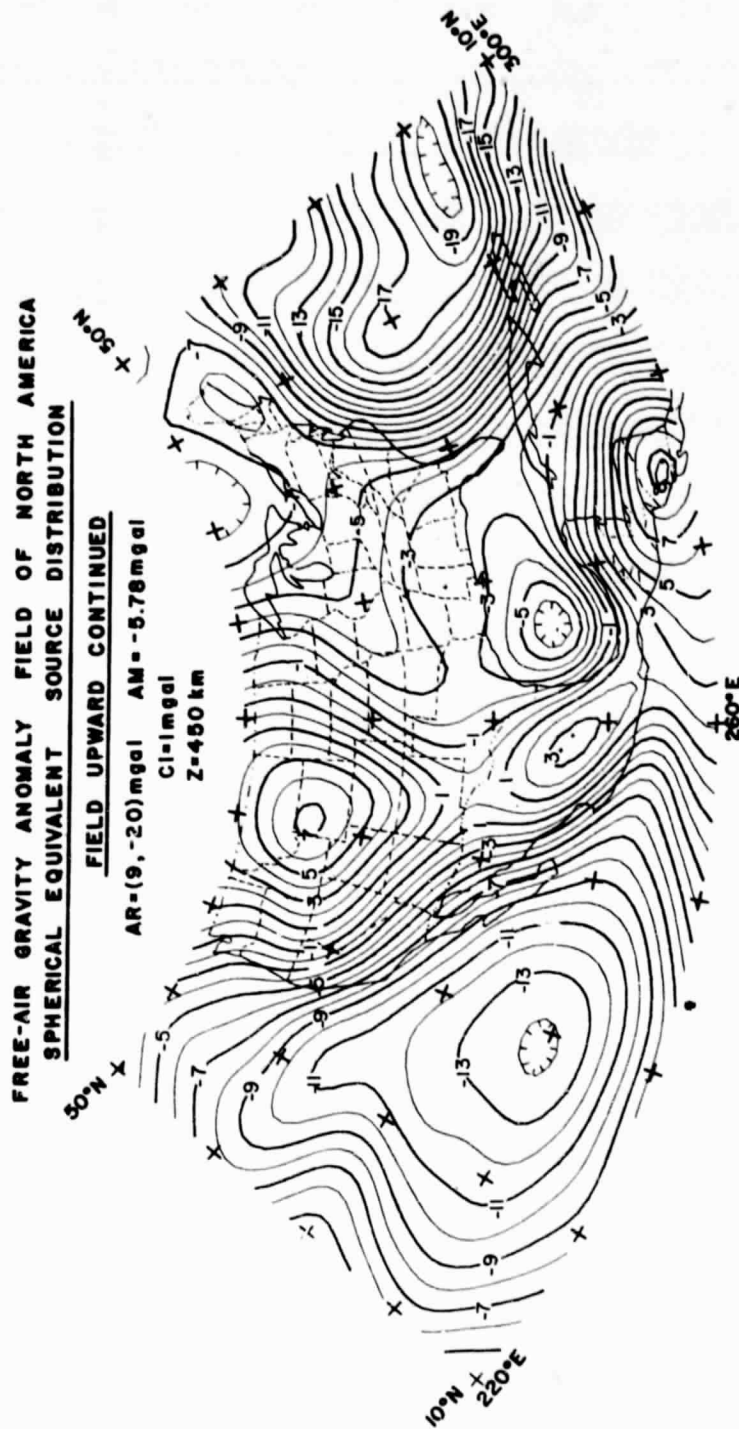


Figure IV.3 Spherical equivalent source field approximation of free-air gravity anomaly data for North America upward continued to 450 km elevation.

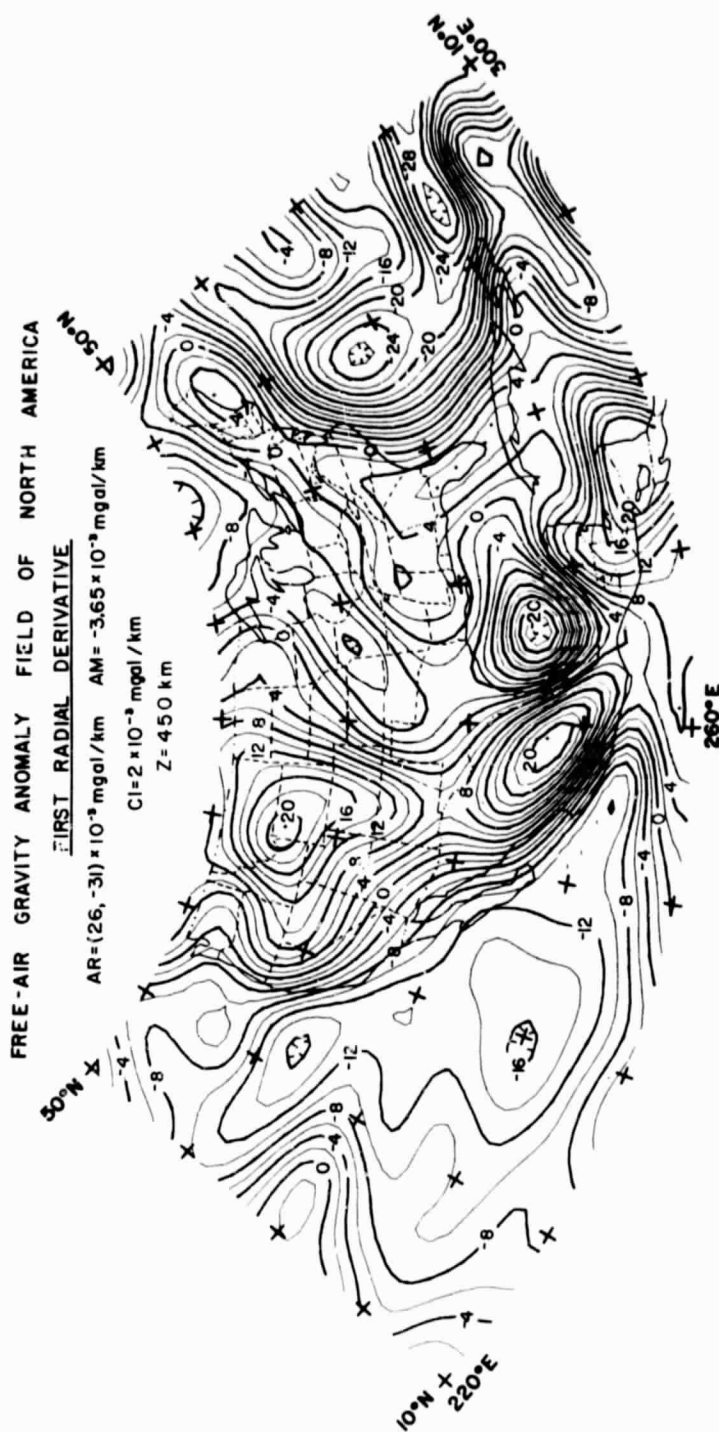


Figure IV.4 Spherical equivalent source field approximation of first order radial derivative of free-air gravity anomaly data for North America.

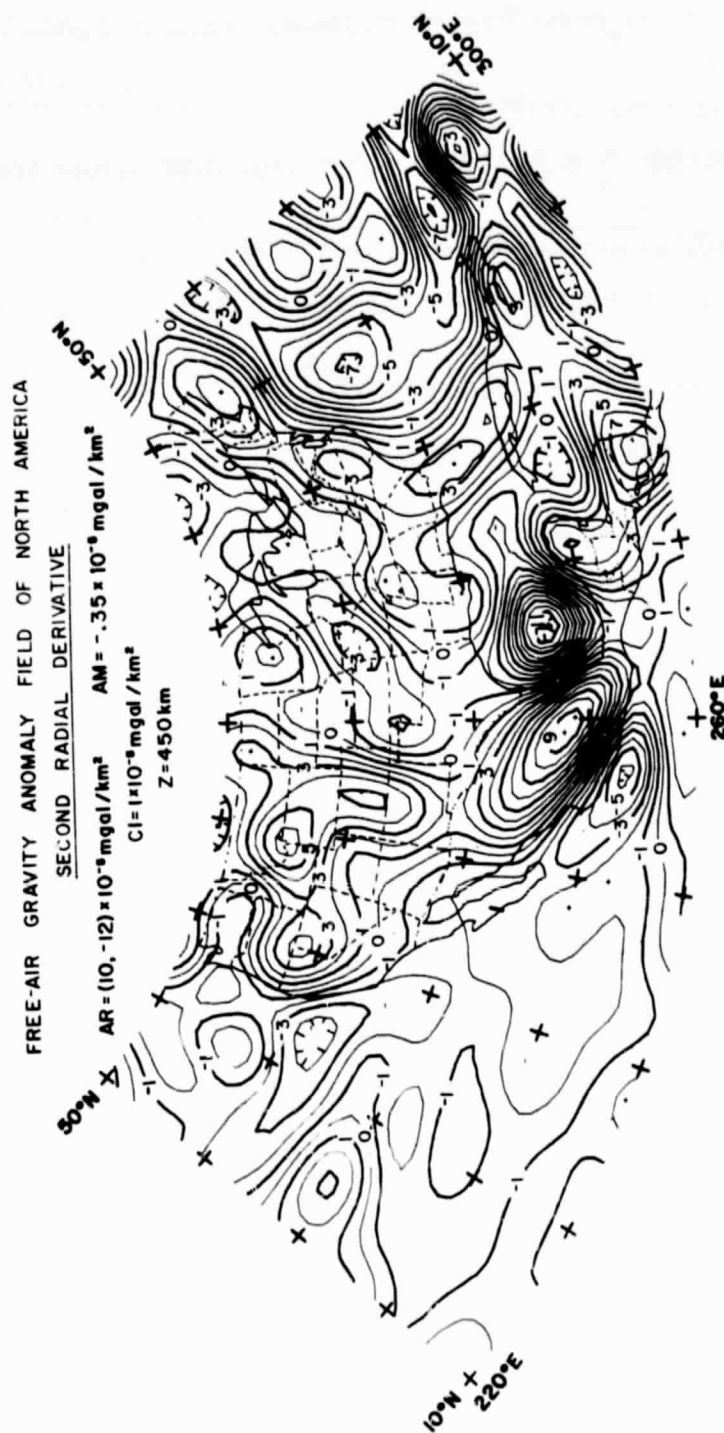


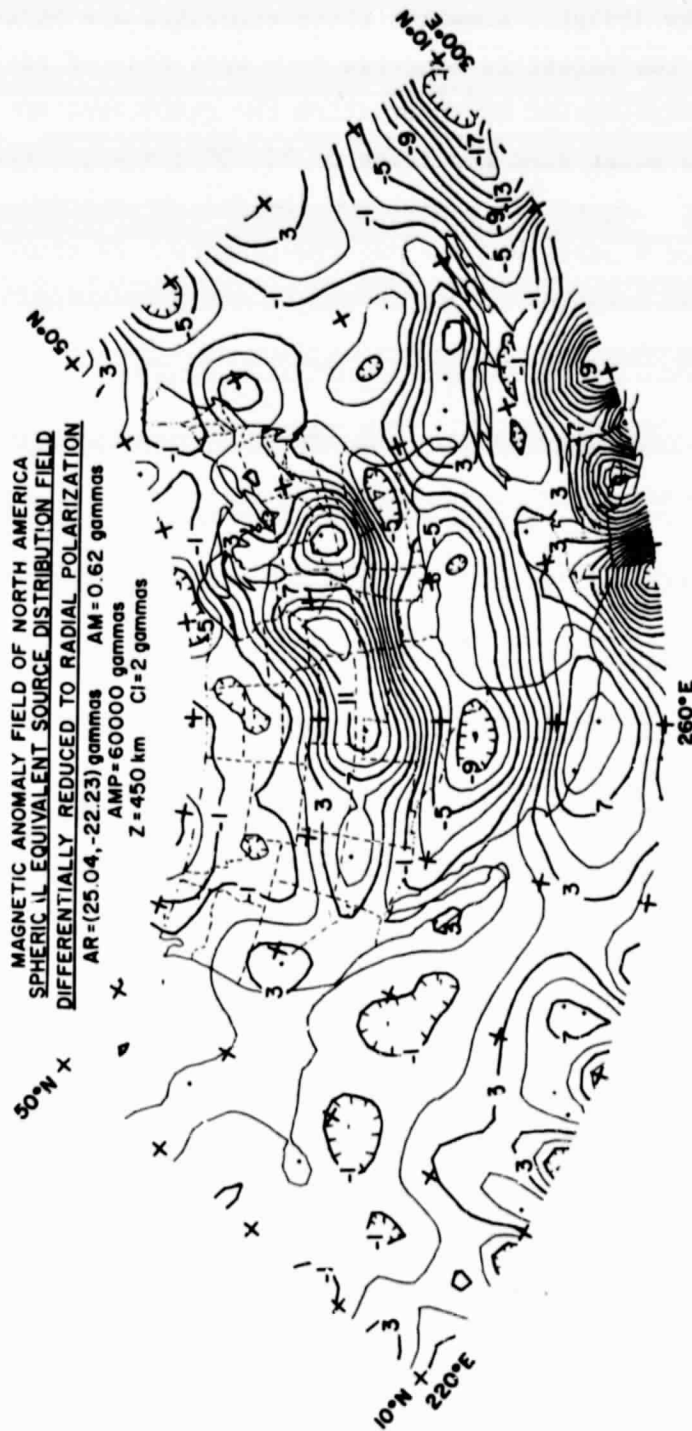
Figure IV.5 Spherical equivalent source field approximation of second order radial derivative of free-air gravity anomaly data for North America.

of the higher frequency components of the upward continued gravity anomaly field. The Cordilleran System is characterized by a distinct positive zone of first order radial gradients which is flanked on the west by the broad negative zone of the Pacific Plate. To the east a well-defined zone of negative radial first derivative anomalies is evident which extends from the Great Lakes region SW across the mid-continent and terminates abruptly over the Gulf of Mexico as a large amplitude negative anomaly. Weakly positive first order gradients are affiliated with the Appalachian Mountain System which project SE across Florida and Cuba. The Atlantic is characterized by a broad zone of negative first order radial derivative anomalies with minimum values over the Puerto Rico Trench.

The second radial derivative of the upward continued gravity anomalies is shown in Figure IV.5 as derived from the equivalent point source distribution for comparison by a straightforward extension of Poisson's theorem with the first radial derivative of the satellite magnetic anomaly data reduced to the pole. The second derivative data provide further enhancement of the higher frequency (crustal ?) components of the upward continued gravity anomaly field. The spectral characteristics of the second derivative field are very similar to the characteristics of the surface free-air gravity anomalies of Figure IV.1 which have been low-pass filtered for wavelengths of the order of 9° and larger. Accordingly, the second derivative anomalies show many of the associations previously noted for the smoothed 1° -averaged surface free-air gravity anomalies of Figure IV.1. In addition, the second radial derivative map of Figure IV.5 shows a distinct arcuate banding of alternating positive and negative long-wavelength anomalies which extends westward across the Atlantic Ocean onto the eastern seaboard of the U.S. This arcuate banding of anomalies appears to project even further westward, although the pattern is disrupted frequently across the continental U.S.

2. Magnetic Anomaly Maps

POGO-1968 satellite magnetometer observations reduced to the pole at 450 km elevation are mapped in Figure IV.6. This map was prepared



by least squares matrix inversion of multielevation satellite magnetic profiles on an equivalent source distribution of spherical prismatic dipolar moments in the IGRF-1965 updated to 1968 according to the procedures described by Mayhew (1979). Assuming these anomalies are derived primarily by induction, the satellite magnetic data were reduced differentially to radial polarization by recomputing the equivalent source fields using a uniformly polarizing amplitude of 60,000 gamma and normal geomagnetic field inclination at all source and observation points.

The main features of Figure IV.6 include the prominent EW transcontinental high which is breached in the region of the Mississippi Embayment. To the west, this high appears to overprint a NW trend of lows that corresponds to the Cordilleran System. The larger amplitudes of the transcontinental positive magnetic anomaly also correspond to a well-defined trend of gravity lows that extends from the Anadarko Basin of the eastern panhandle of Texas to the tri-state region of Indiana, Ohio and Kentucky (see Figures IV.1 and 5). This trend of gravity lows also characterizes a region of enhanced crustal thickness according to seismic evidence (Warren and Healy, 1973).

Additional features of the radially polarized magnetic data of Figure IV.6 include the high over the Antilles-Bahamas Platform and the prominent magnetic low along the northern Gulf of Mexico which extends westward into Mexico. The magnetic relief of the Atlantic Ocean is considerable in comparison to the Pacific Ocean which appears as a region of relatively subdued magnetic character.

Continental magnetic anomalies exhibit pronounced EW trends in contrast to the NS trends of the gravity anomaly field. This result is an apparent manifestation of the longer wavelength components of the satellite magnetic data which are illustrated in Figure IV.7. To construct Figure IV.7, the radially polarized data of Figure IV.6 were high-cut filtered for wavelengths smaller than about 12° . The resultant map shows that major sources of positive long-wavelength magnetic anomalies include the previously discussed transcontinental region, the Antilles-Bahamas Platform and the southeastern coast of Mexico along the Middle America Trench. Negative long-wavelength magnetic anomalies characterize northern Mexico and the northwestern third of the U.S. where the western component of the latter anomaly is centered over the Yellowstone geothermal region.

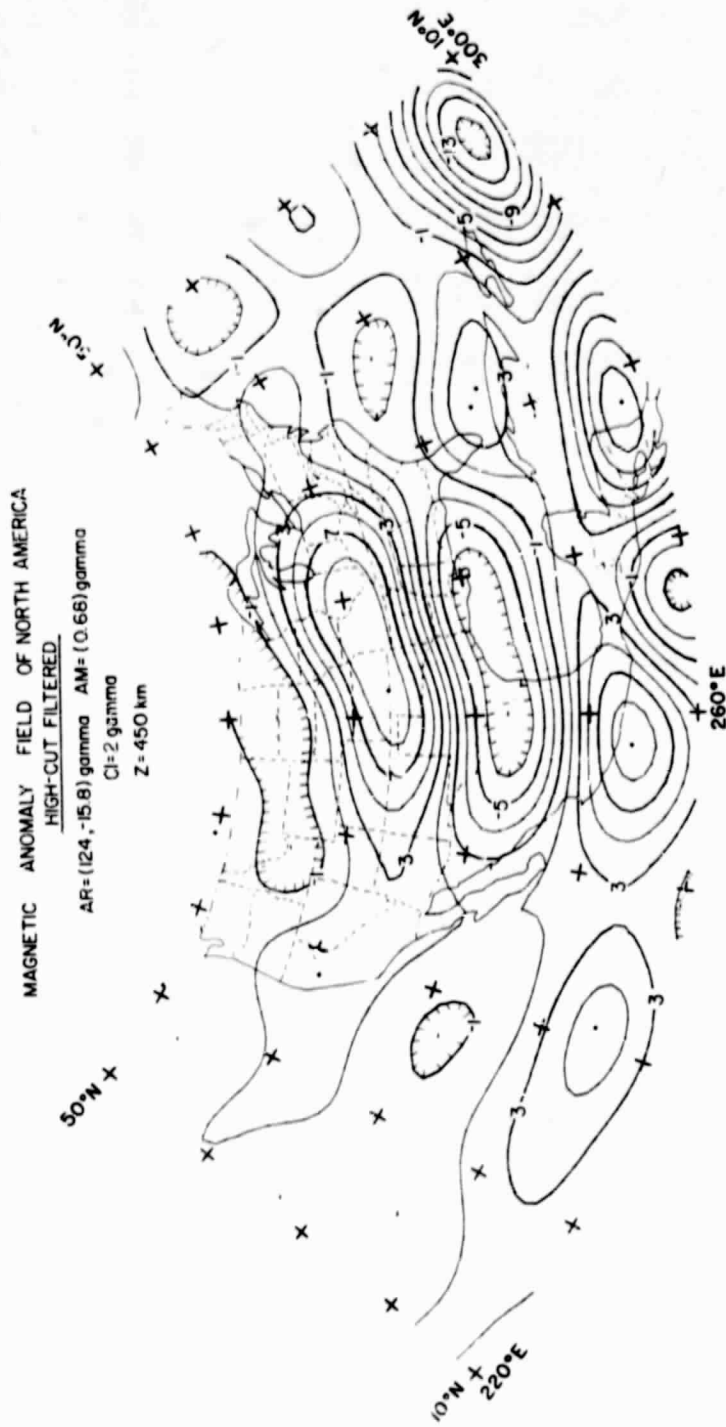


Figure IV.7 Spherical equivalent source field approximation of high-cut ($\lambda \leq 12^\circ$) filtered radially polarized total magnetic intensity anomaly data for North America.

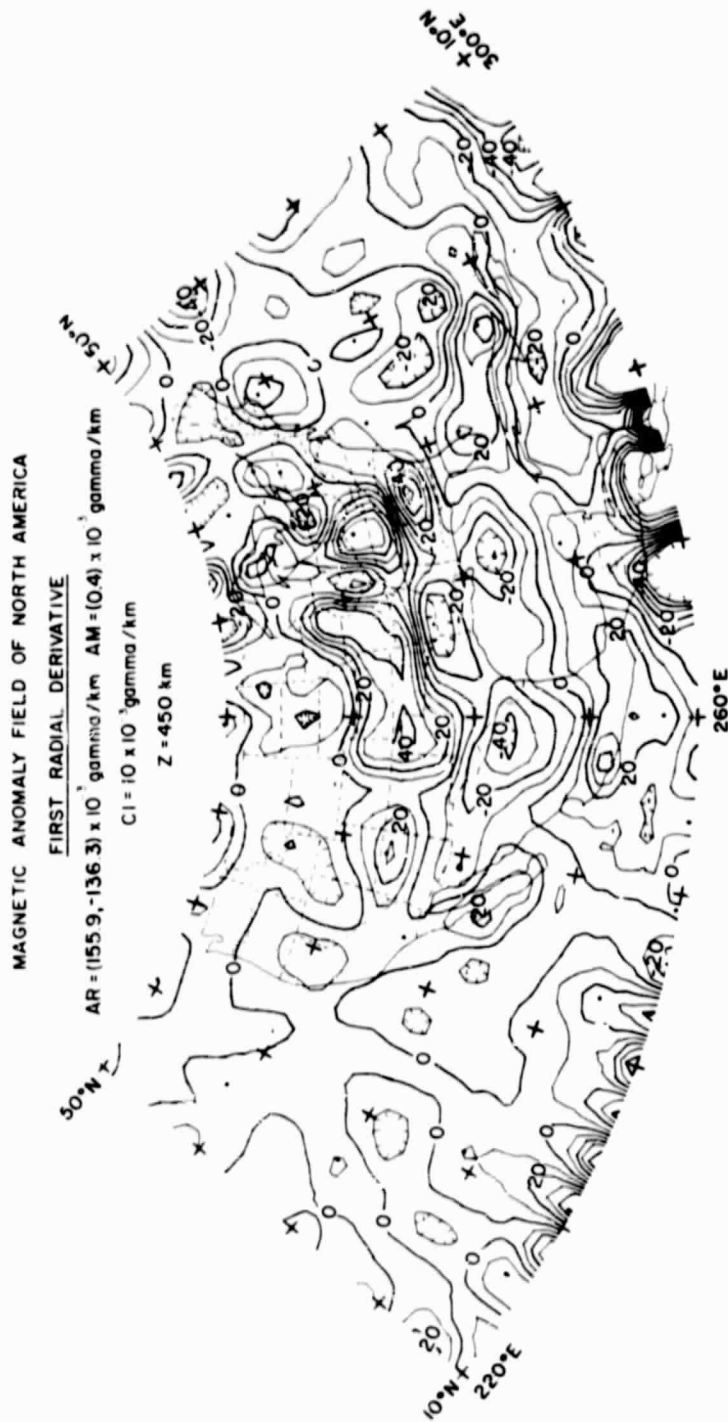


Figure IV.8 Spherical equivalent source field approximation of the first radial derivative of radially polarized total magnetic intensity anomaly data for North America.

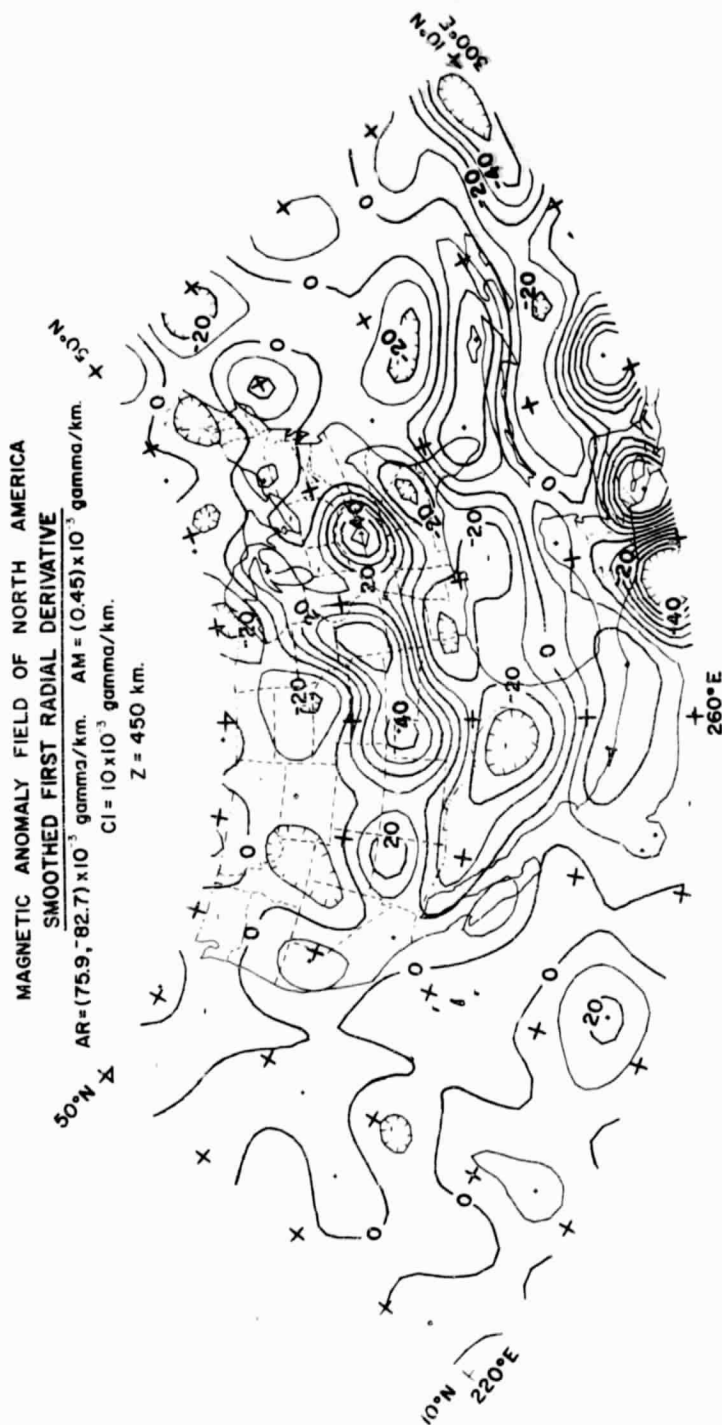


Figure IV.9 Spherical equivalent source field approximation of the high-cut ($\lambda \leq 8^\circ$) filtered first order radial derivative of radially polarized total magnetic intensity anomaly data for North America.

For comparison with the second derivative map (Figure IV.5) of the upward continued gravity anomalies, the first order radial derivative of the radially polarized magnetic anomaly field as shown in Figure IV.8 is computed from the equivalent source field. To make the first derivative magnetic anomalies more compatible spectrally with the second derivative gravity anomalies, and thereby more amenable to correlation analysis via Poisson's theorem, the data of Figure IV.8 were high-cut filtered for anomaly wavelengths smaller than about 8° . The resultant smoothed first order radial derivative magnetic anomalies are illustrated in Figure IV.9.

The magnetic derivative maps provide an increased resolution of the previously mentioned anomalies. In addition, more subdued anomaly trends become apparent. For example, a series of negative anomalies is observed to extend along the continental side of the eastern seaboard of the U.S. to Georgia where the trend turns westward along the southern margin of the U.S. and then across northern Mexico to the Gulf of California. On the oceanic side of the eastern U.S. seaboard, a trend of positive derivative anomalies is evident which projects from the Baltimore Canyon area southward until it intersects the positive anomalies of the Antilles-Bahamas Platform. Further eastward across the Atlantic Ocean, an arcuate pattern of banded negative and positive anomalies begins to emerge which shows a direct correspondence to the previously discussed gravity anomaly pattern of the Atlantic. The Pacific coast of North America by contrast generally is characterized by a trend of positive first order magnetic derivative anomalies.

E. Quantitative Correlation Results and Discussion

To investigate quantitative regional correlations of satellite-elevation gravity and magnetic anomalies over North America, moving-window Poisson's analysis was performed on the data sets described in the previous section. The results of these correlation analyses and their potential geological significance are outlined below.

1. Correlation Analysis (I-5)

Correlation analysis (I-5) was performed between the first radial gravity derivative map of Figure IV.4 and the radially polarized magnetic

anomaly map of Figure IV.6 using a 5×5 data point ($=4^\circ \times 4^\circ$) operational window. The positive and negative correlation coefficients derived from the moving-window Poisson's analysis are plotted separately in Figures IV.10 and 11, respectively. These correlation coefficients graphically characterize the oceans by direct correspondences of gravity and magnetic anomalies, whereas the continental correlations are predominantly inverse.

A histogram of the correlation coefficients is given in Figure IV.12 where the oceanic and continental anomaly correspondences are reflected as two distinct peaks of relatively high statistical correlation. Roughly 32% of the correlation coefficients have absolute values greater than or equal to ± 0.7 , thus, indicating that a significant portion of the gravity and magnetic anomalies exhibit strong statistical correlation.

An analysis of the correlation coefficient patterns in Figures IV.10 and 11 shows that broad-scale regions of high correlation coefficients generally are associated with anomaly gradients. Correlations of anomaly peaks normally exhibit slight phase shifts of as much as a degree or two and, hence, tend to be characterized by fluctuating correlation coefficients. The slope and intercept coefficients as shown in Figures IV.13 and 14, respectively, also have much the same pattern as the correlation coefficients. These results suggest that the regression parameters generally are more sensitive to phase shifts of the anomaly peaks than to phase shifts of the gradients.

Accordingly, it is difficult to make broad geological generalizations from these regression parameters except on an anomaly-by-anomaly basis. As an example, consider the previously discussed trans-continental region of negative gravity and positive magnetic anomalies. Much of this region is characterized by relatively stable intercept values and correlation coefficients which range between -0.6 to -0.8 . The corresponding distribution of slope values, which gives an initial constraint on the physical properties of the possible source for subsequent interpretation, is roughly equal to $-0.06 \text{ oersted} \cdot \text{cm}^3/\text{gm}$. If the source of this gravity low and magnetic high corresponds to a thickened crust as suggested by previous arguments and seismic evidence

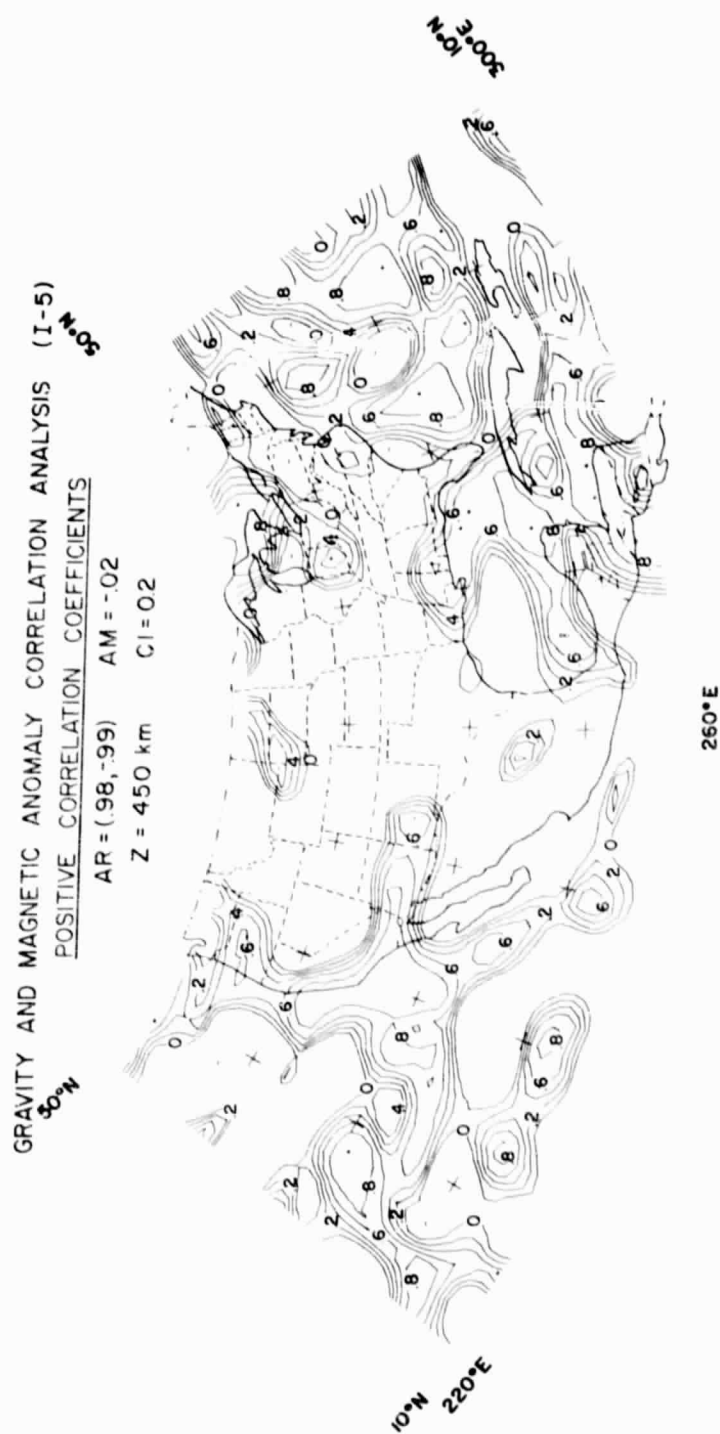


Figure IV.10 Positive (0.0 to 1.0) correlation coefficients derived from correlation analysis (I-5).

ORIGINAL PAGE IS
OF POOR QUALITY

GRAVITY AND MAGNETIC ANOMALY CORRELATION ANALYSIS (I-5)
NEGATIVE CORRELATION COEFFICIENTS

AR = (.98, .99) AM = .02
Z = 450 km CI = 0.2

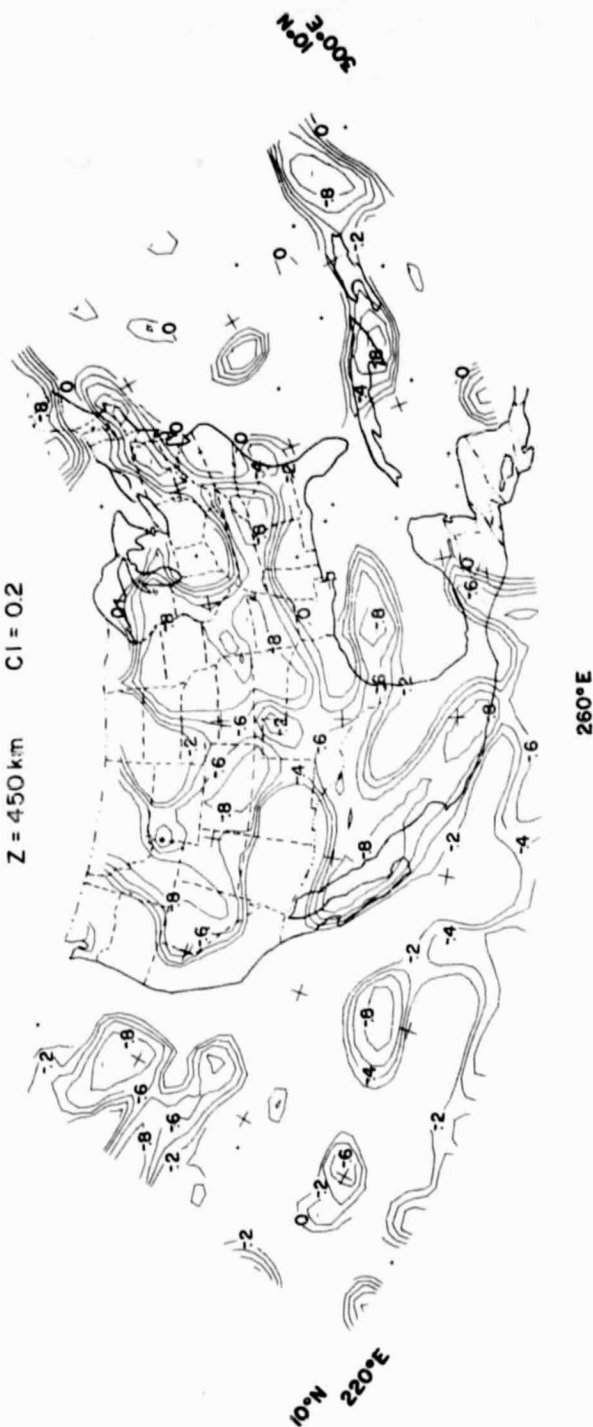


Figure IV.11 Negative (-1.0 to 0.0) correlation coefficients derived from correlation analysis (I-5).

GRAVITY AND MAGNETIC ANOMALY
CORRELATION ANALYSIS (I-5)
CORRELATION COEFFICIENTS
Z = 450 km

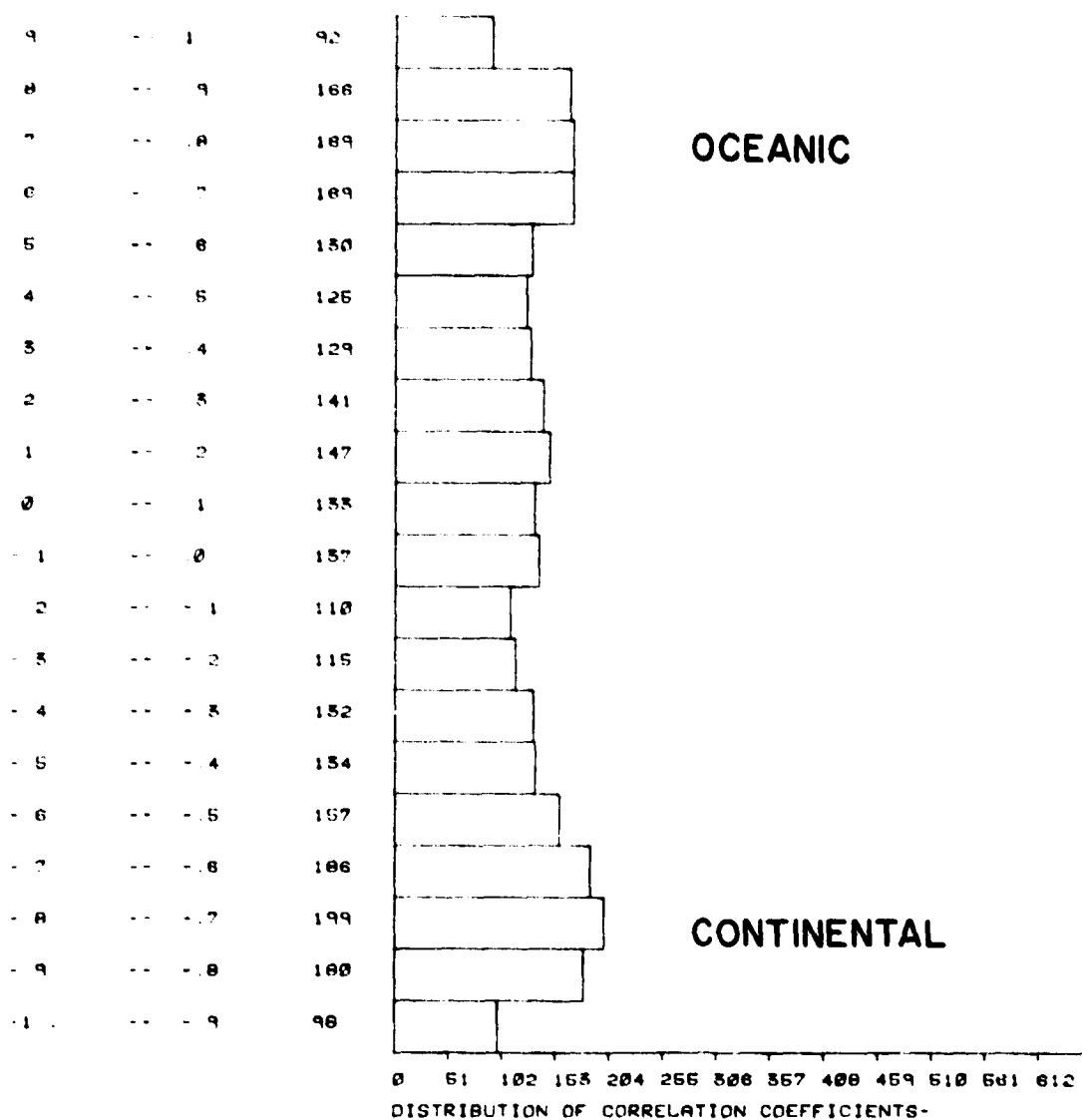


Figure IV.12 Histogram of correlation coefficients derived from correlation analysis (I-5).

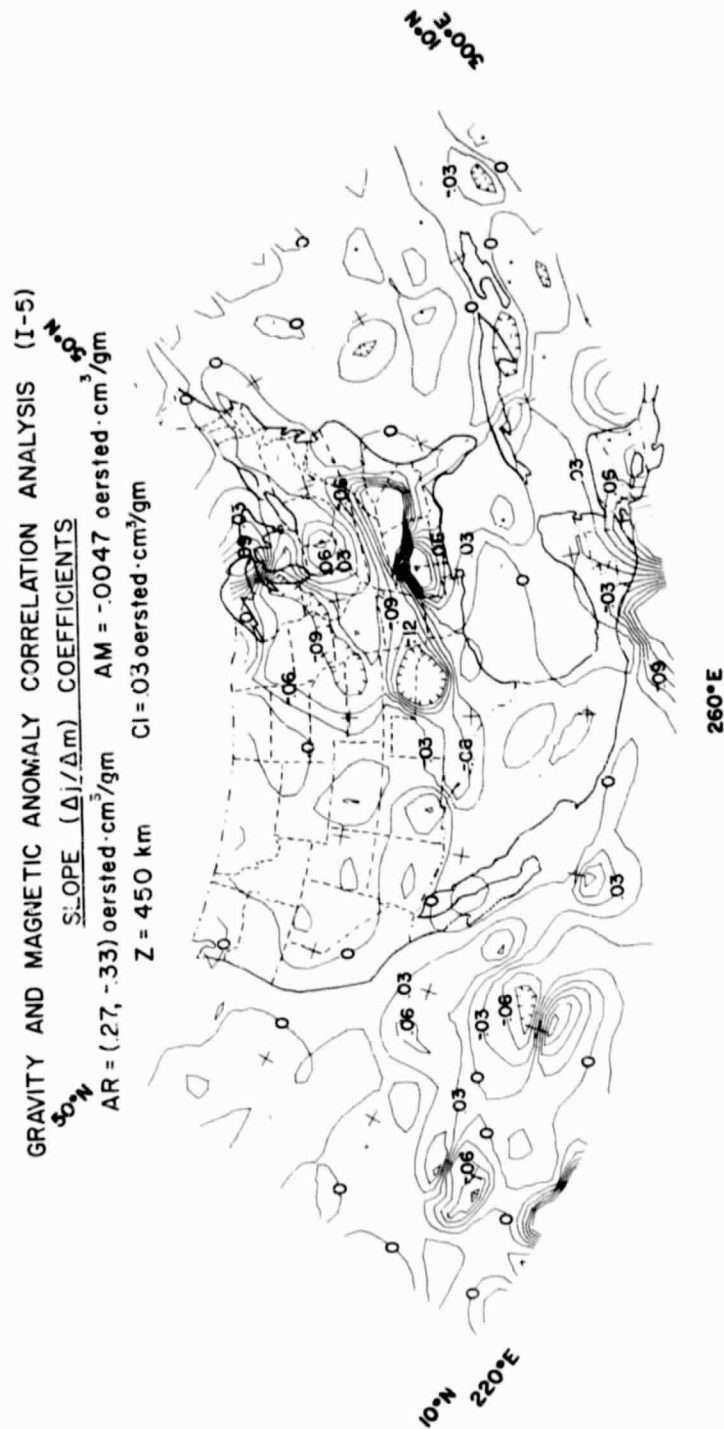


Figure IV.13 Slope ($\Delta j/\Delta m$) coefficients derived from correlation analysis (I-5).

GRAVITY AND MAGNETIC ANOMALY CORRELATION ANALYSIS (I-5)

INTERCEPT COEFFICIENTS

AR = (34.7, -45.0) gamma AM = 1.2 gamma

Z = 450 km CI = 3.0 gamma

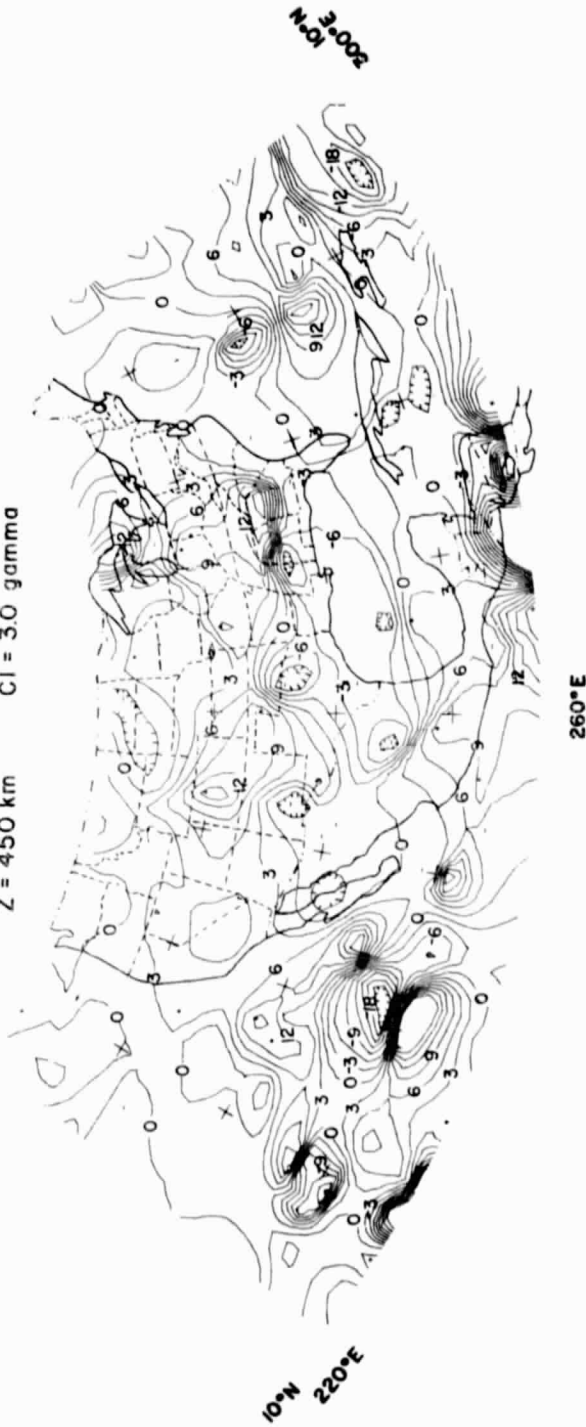


Figure IV.14 Intercept coefficients derived from correlation analysis (I-5).

(Warren and Healy, 1973), and the density contrast at the base of the crust is -0.3 gm/cm^3 , then this slope value indicates a magnetic polarization for the source of roughly $1.8 \times 10^{-2} \text{ emu/cm}^3$. This polarization value suggests source magnetization that is several orders of magnitude greater than the value $\approx 5 \times 10^{-3} \text{ emu/cm}^3$ commonly accepted for the lower crust (Hall, 1974; Shuey et al., 1973).

2. Correlation Analysis (II-5)

Correlation analysis (II-5) was performed between the second radial gravity derivative map of Figure IV.5 and the first radial magnetic derivative anomalies of Figure IV.8 using a 5×5 data point moving-window. This analysis should emphasize correspondences between nearer surface, crustal anomalies because both data sets are radial derivative maps.

Positive and negative correlation coefficients derived from this analysis are plotted separately in Figures IV.15 and 16, respectively. Again, these coefficients statistically characterize prevailing inverse and direct anomaly correspondences, respectively, for continental and oceanic regions. The histogram of the correlation coefficients given in Figure IV.17 shows two broad peaks for the continental and oceanic anomaly correlations. Approximately 23% of the anomaly correlations exhibit correlation coefficients with absolute magnitude greater than or equal to ± 0.7 . However, inspection of Figures IV.5 and 8 shows that a greater number of spatial correlations of anomalies appear evident than for the data sets considered in the previously described analysis. Hence, the decrease in the number of high correlations with respect to the results of analysis (I-5) suggests that the $4^\circ \times 4^\circ$ window may be too large to effectively resolve many of the higher frequency derivative anomaly correlations.

Correlation coefficient fluctuations are similar to those observed for the slope and intercept values as shown in Figures IV.18 and 19. However, broad-scale variations of these coefficients generally correspond to anomaly gradients which make geologically significant generalizations unclear except on an individual anomaly basis. The results for the transcontinental anomaly correspondences are essentially the same as those obtained from the previous analysis.

GRAVITY AND MAGNETIC ANOMALY CORRELATION ANALYSIS (II-5)

POSITIVE CORRELATION COEFFICIENTS

AR = (.96, -.97) AM = .005

Z = 450 km CI = 0.2

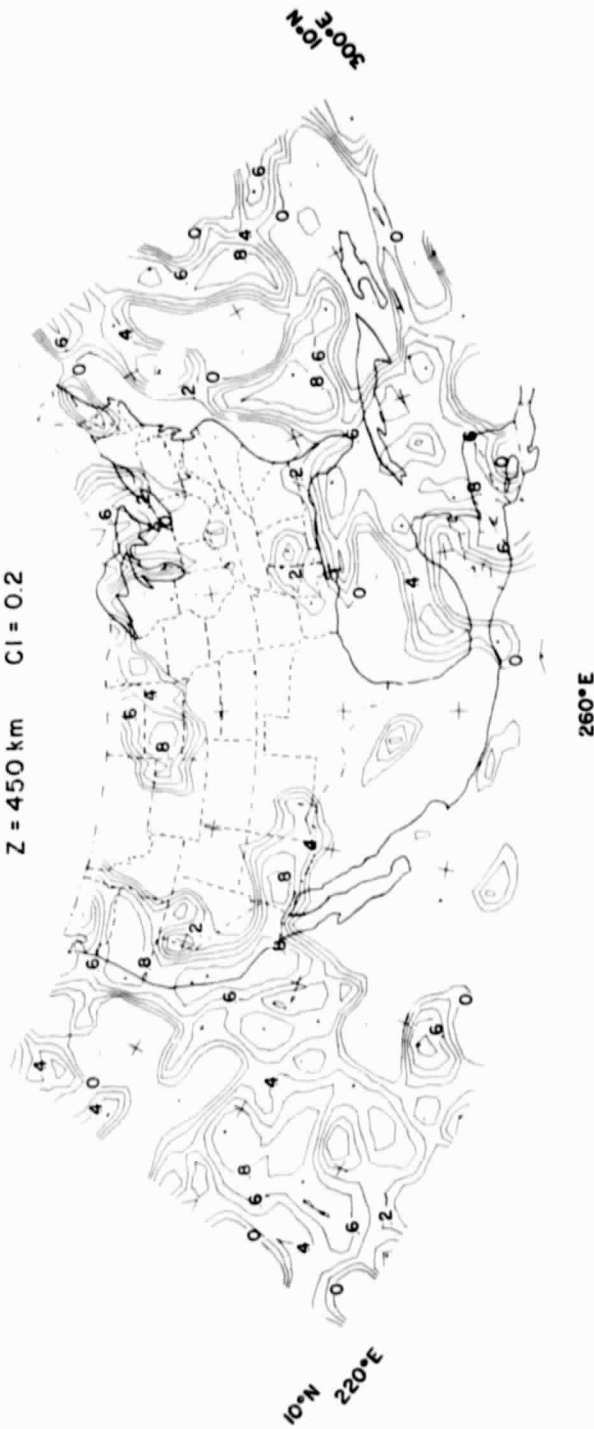


Figure IV.15 Positive (0.0 to 1.0) correlation coefficients derived from correlation analysis (II-5).

GRAVITY AND MAGNETIC ANOMALY CORRELATION ANALYSIS (II-5)
 NEGATIVE CORRELATION COEFFICIENTS

AR = (.96, -.97) AM = .005
 Z = 450 km CI = 0.2

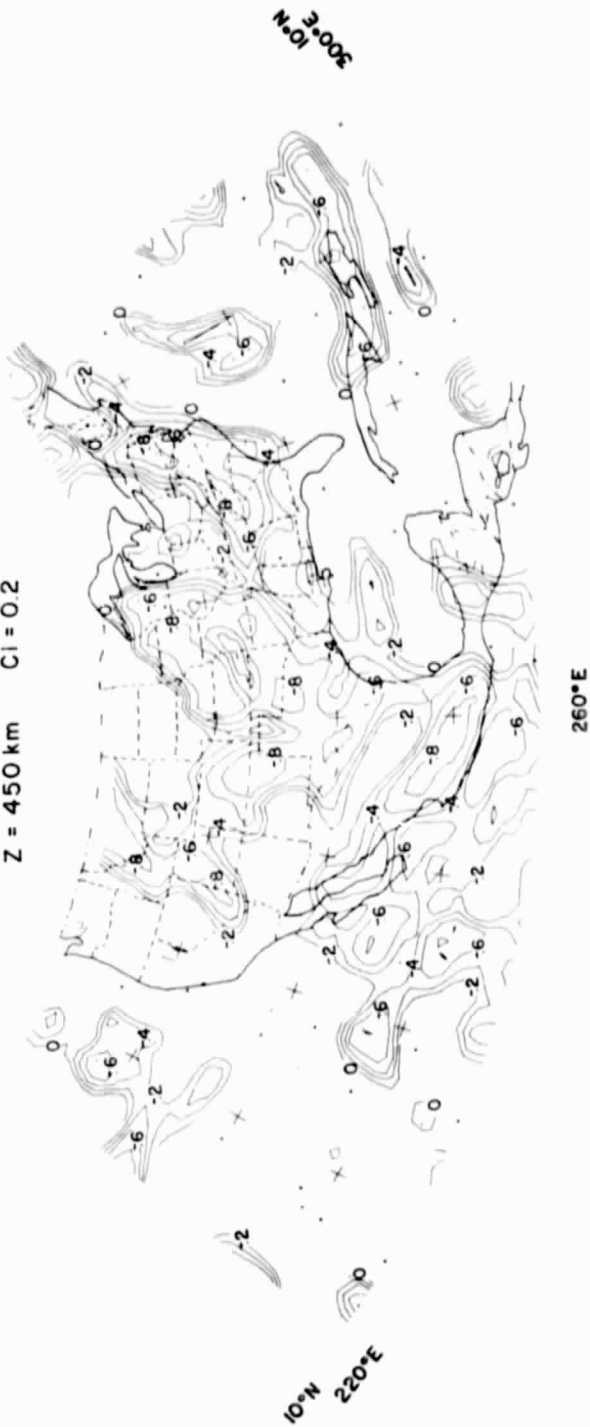


Figure IV.16 Negative (-1.0 to 0.0) correlation coefficients derived from correlation analysis (II-5).

ORIGINAL PAGE IS
 OF POOR QUALITY

**GRAVITY AND MAGNETIC ANOMALY
CORRELATION ANALYSIS (II-5)
CORRELATION COEFFICIENTS**

Z = 450 km

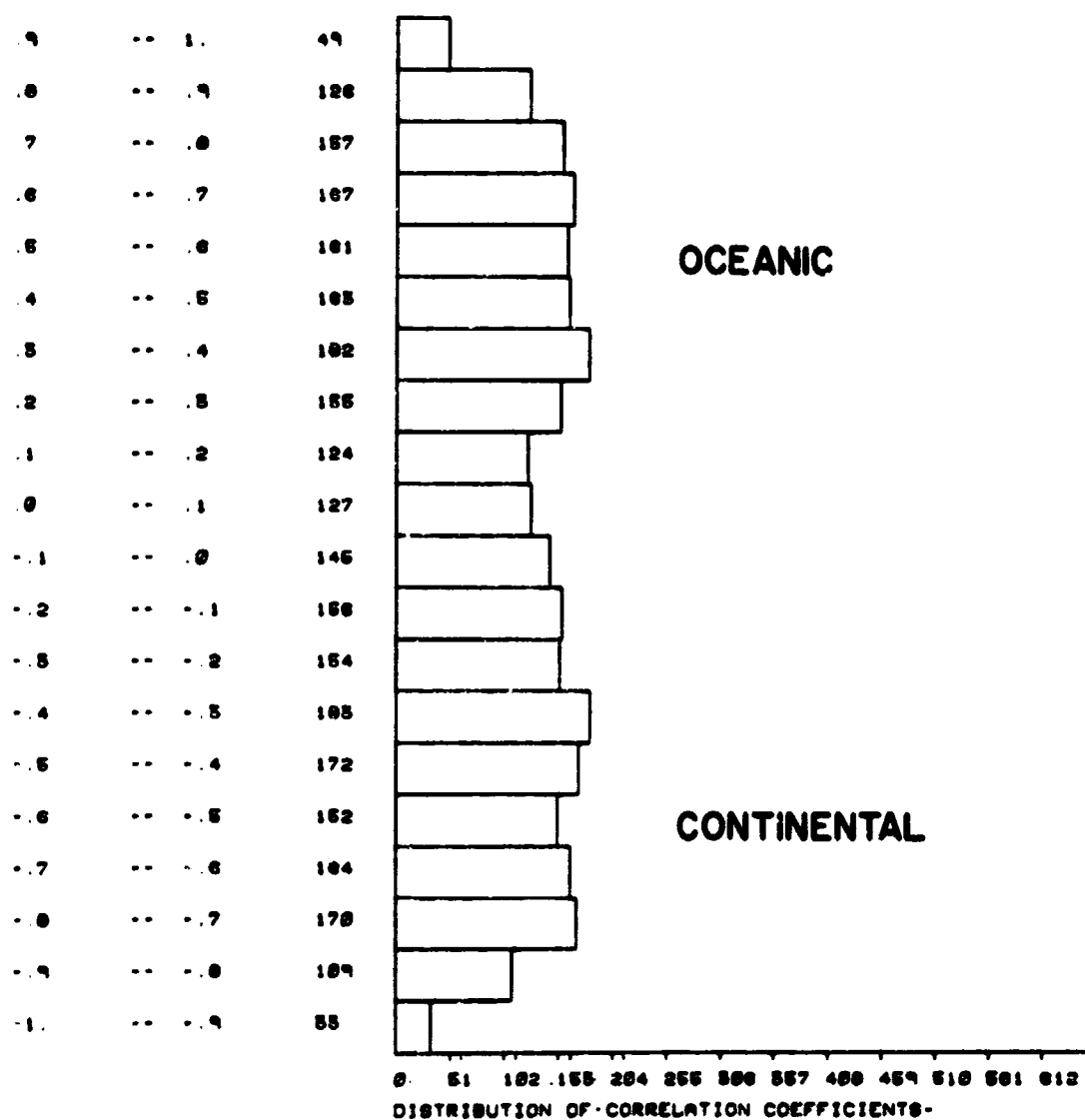


Figure IV.17 Histogram of correlation coefficients derived from correlation analysis (II-5).

GRAVITY AND MAGNETIC ANOMALY CORRELATION ANALYSIS (II-5)

$\Delta j / \Delta m$
 SLOPE $(\Delta j / \Delta m)$ COEFFICIENTS
 AR = (27, -25) oersted \cdot cm³/gm AM = -0029 oersted \cdot cm³/gm
 Z = 450 km CI = .03 oersted \cdot cm³/gm

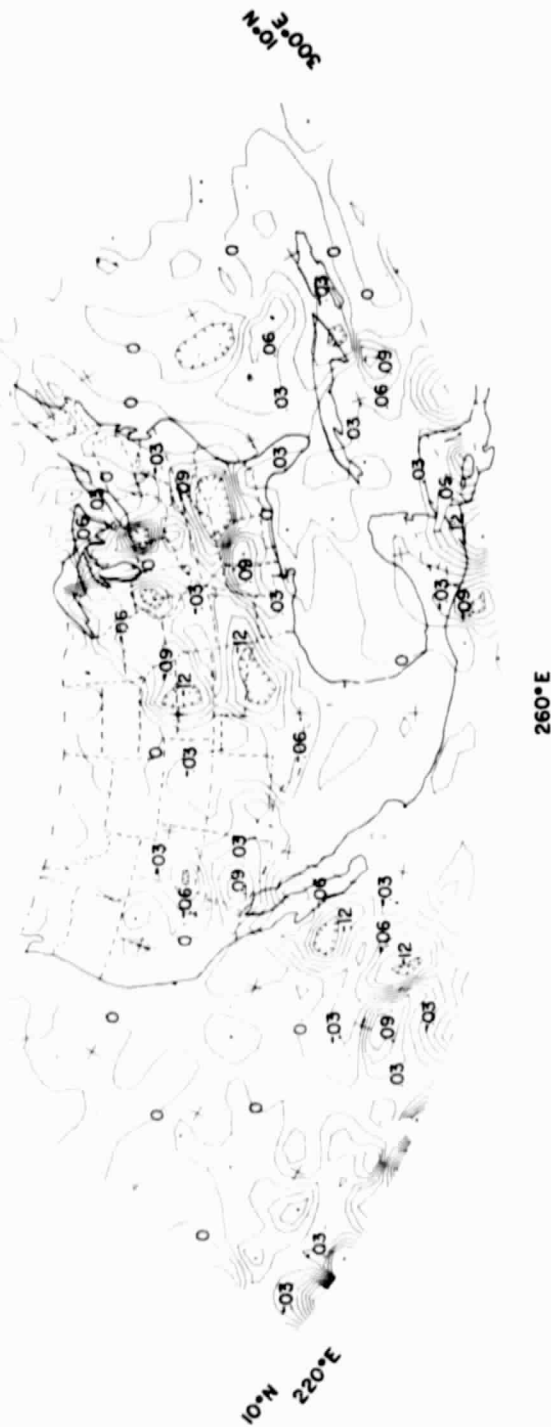


Figure IV.18 Slope $(\Delta j / \Delta m)$ coefficients derived from correlation analysis (II-5).

GRAVITY AND MAGNETIC ANOMALY CORRELATION ANALYSIS (II-5)

INTERCEPT COEFFICIENTS

$$AR = (128.3; 85.3) \times 10^3 \text{ gamma/km} \quad AM = 0.79 \times 10^3 \text{ gamma/km}$$

$$Z = 450 \text{ km} \quad CI = 10 \times 10^3 \text{ gamma/km}$$

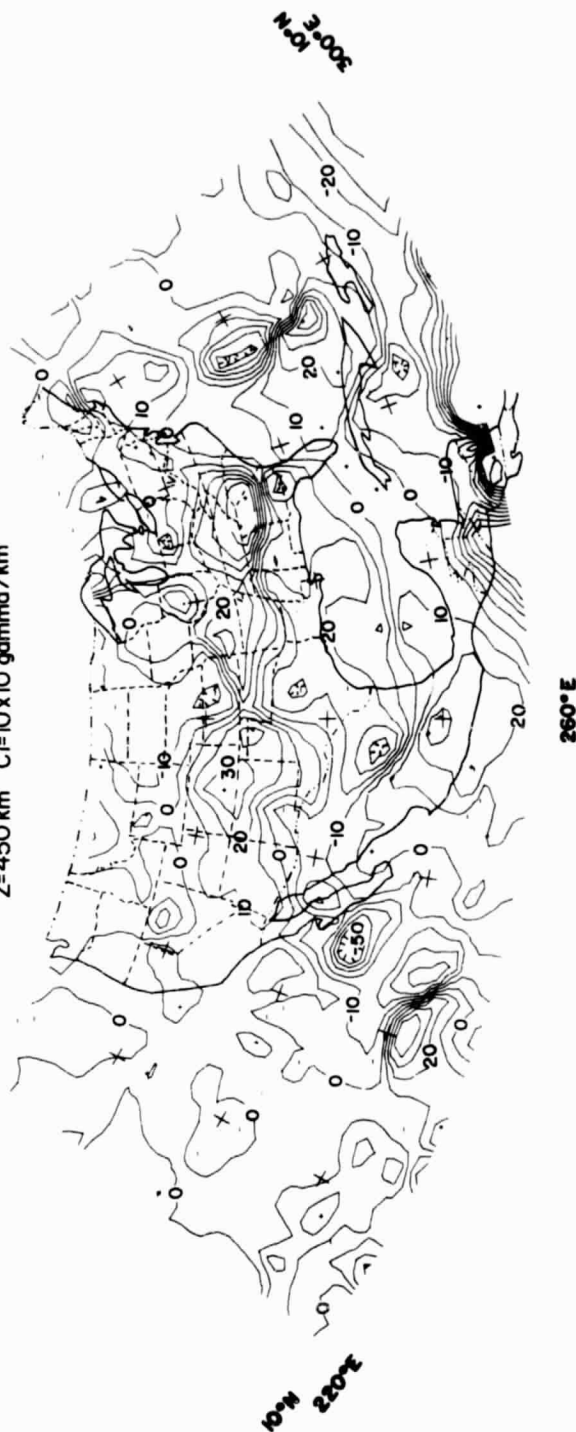


Figure IV.19 Intercept coefficients derived from correlation analysis (II-5).

3. Correlation Analysis (III-3)

Correlation analysis (III-3) using a 3×3 point ($= 2^\circ \times 2^\circ$) moving window was performed between the second radial gravity derivative map of Figure IV.5 and the first radial magnetic derivative anomalies of Figure IV.9 low-pass filtered for wavelengths roughly 8° and larger. The data sets considered here should be more spectrally compatible than those used in the previous analysis because the second radial gravity derivative map exhibits similar wavelength characteristics to the surface data of Figure IV.1 which has been high-cut filtered for wavelengths roughly smaller than 8° . Also, the smaller operational window can be expected to better resolve the higher frequency correlations of the derivative anomalies.

A number of the derivative anomaly correlations are shown in Figure IV.20 where selected second derivative gravity anomalies (heavy contours) are plotted on the smoothed magnetic anomaly derivative map. The spatial coincidence of the anomalies in Figure IV.20 clearly demonstrates the continental area as a region characterized basically by two types of inversely correlating gravity and magnetic anomalies. One type of inverse correspondence is exemplified by the positive gravity anomalies which are associated with breaches of the transcontinental magnetic high by the Cordillera and the northern Mississippi Embayment. The Yellowstone area also is characterized by well-defined positive gravity and negative magnetic anomalies. The second type of continental anomaly correspondence is illustrated by the trend of negative gravity and positive magnetic anomalies which extends from the Anadarko Basin to the tri-state region of Indiana, Ohio and Kentucky. Oceanic anomaly correspondences are less clear, although direct anomaly correlations generally appear to characterize the Gulf of Mexico, Caribbean and Atlantic Ocean regions of the eastern third of the study area.

These generalizations, again, are supported statistically by the distributions of positive and negative correlation coefficients derived from analysis (III-3) which are mapped in Figures IV.21 and 22, respectively. The histogram of the correlation coefficients illustrated in Figure IV.23 shows the continental and oceanic anomalies exhibit relatively strong statistical correspondences. Roughly 41% of the

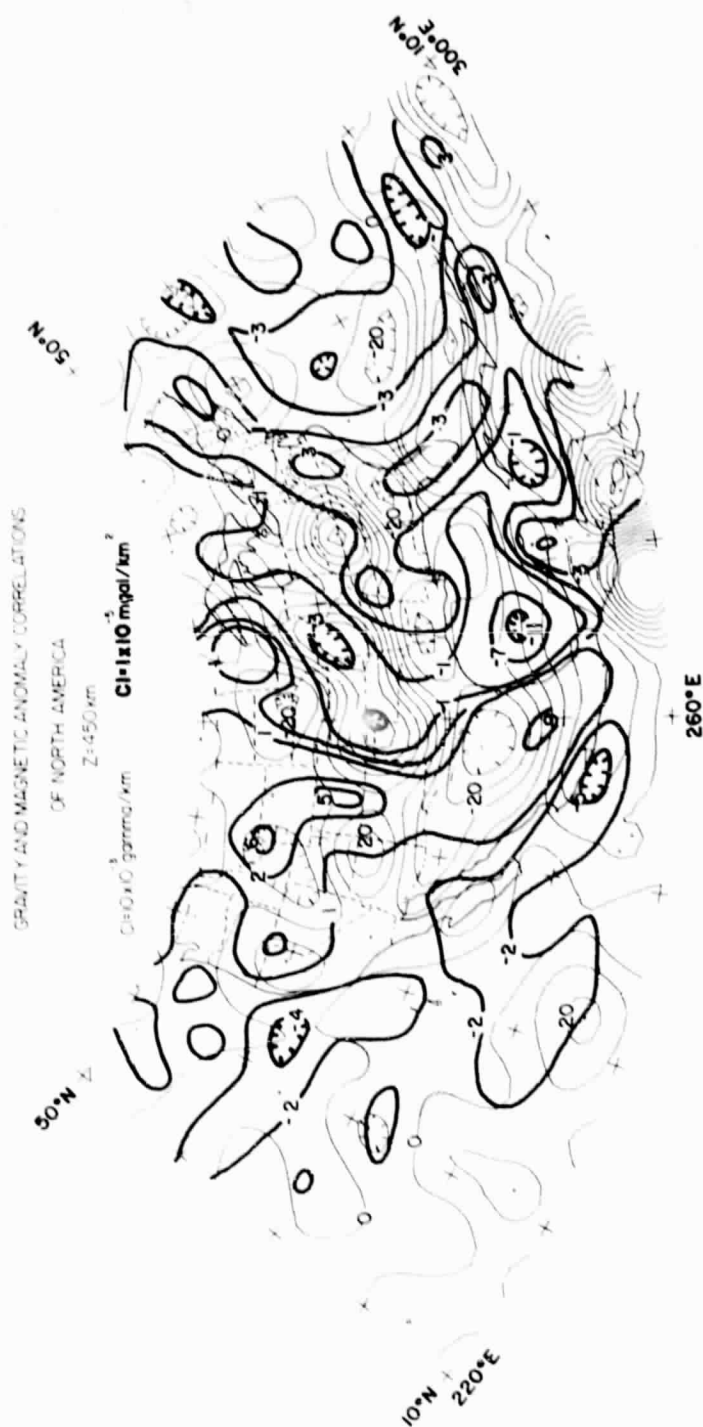


Figure IV.20 Selected correlations at 450 km elevation between the radial first order radially polarized magnetic anomaly derivatives and the radial second order free-air gravity anomaly derivatives for North America.

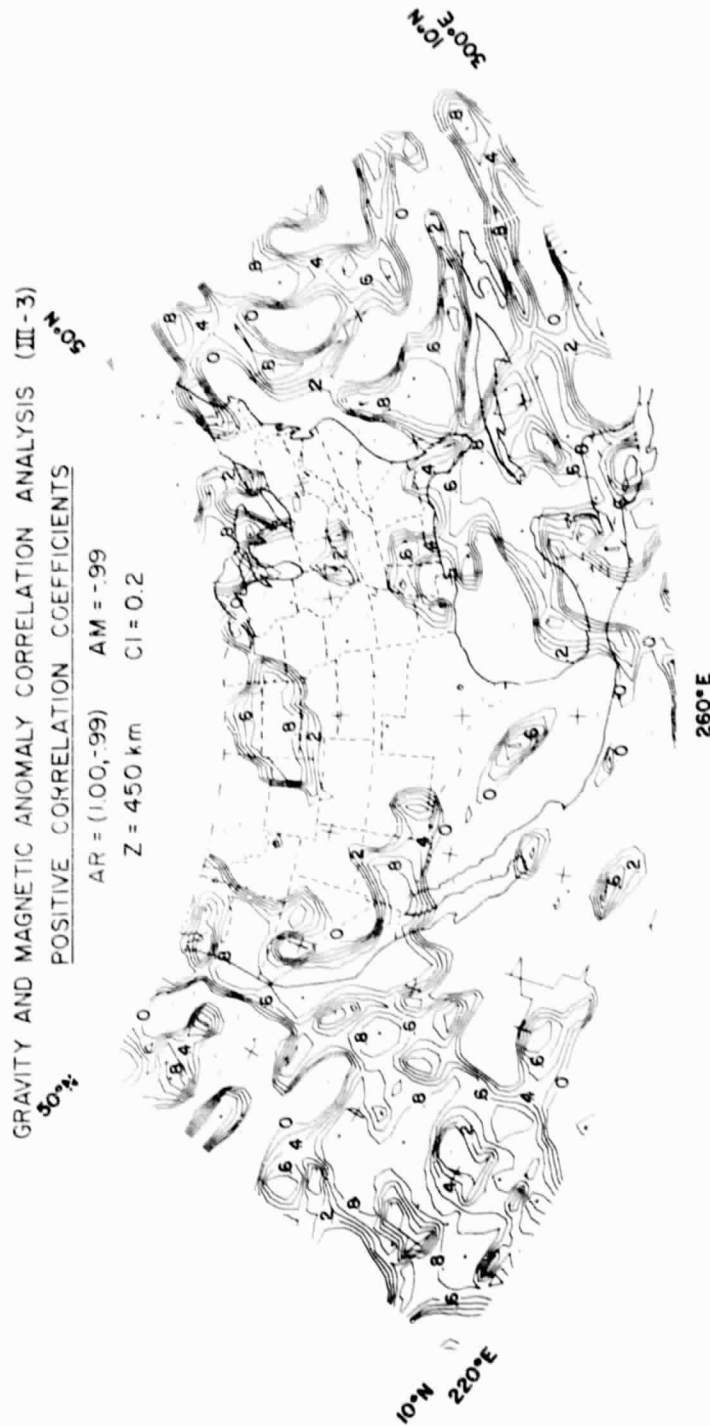


Figure IV.21 Positive (0.0 to 1.0) correlation coefficients derived from correlation analysis (III-3).

ORIGINAL PAGE IS
OF POOR QUALITY

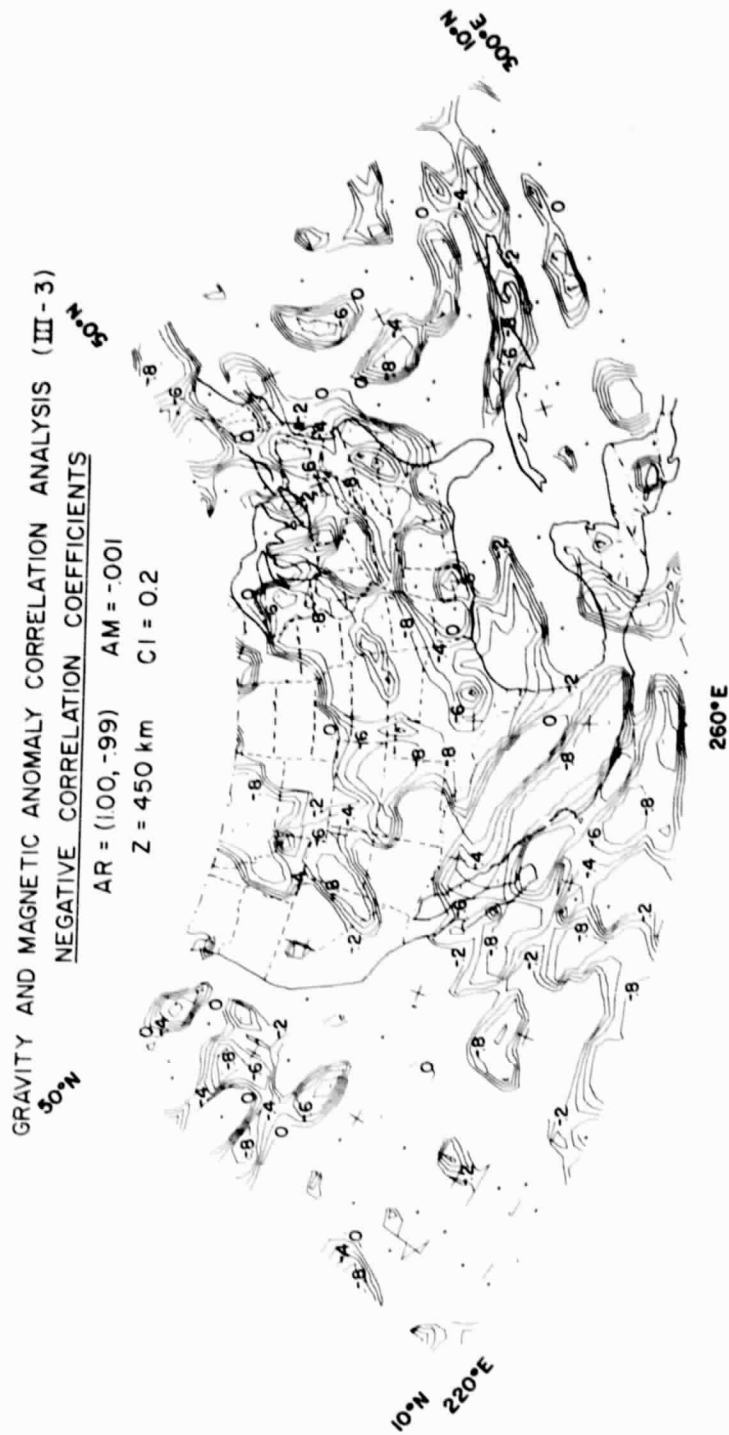


Figure IV.22 Negative (-1.0 to 0.0) correlation coefficients derived from correlation analysis (III-3).

**GRAVITY AND MAGNETIC ANOMALY
CORRELATION ANALYSIS (III-3)
CORRELATION COEFFICIENTS**

Z = 450 km

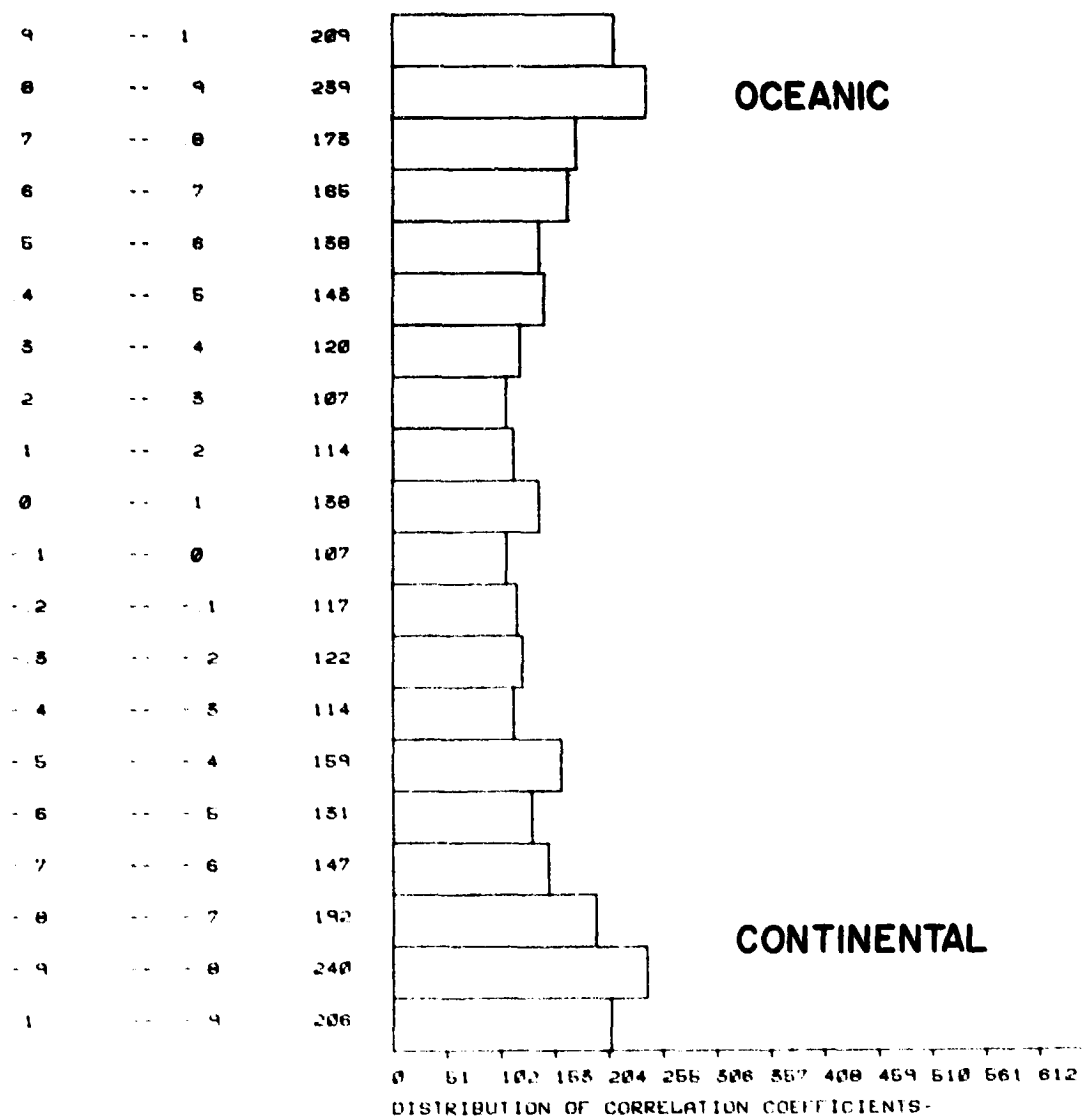


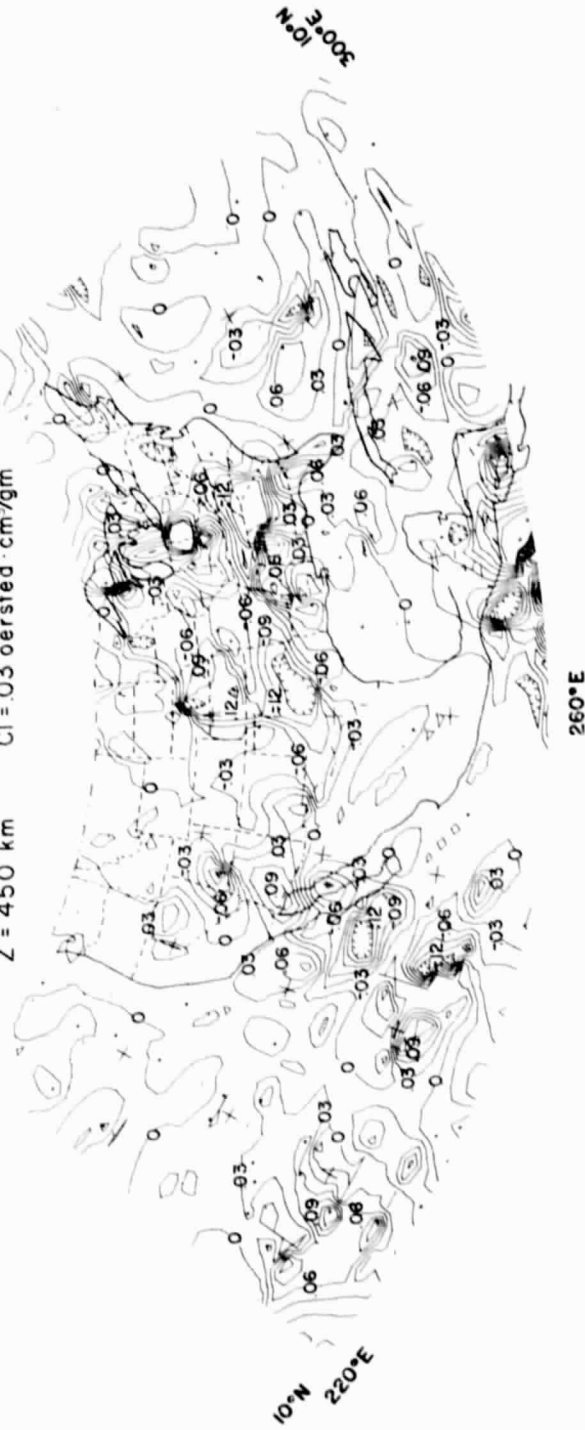
Figure IV.23 Histogram of correlation coefficients derived from correlation analysis (III-3).

GRAVITY AND MAGNETIC ANOMALY CORRELATION ANALYSIS (III-3)

50°N
SLOPE ($\Delta j / \Delta m$) COEFFICIENTS

AR = (.27, -.43) oersted \cdot cm³/gm AM = -.0024 oersted \cdot cm³/gm

Z = 450 km CI = .03 oersted \cdot cm³/gm



GRAVITY AND MAGNETIC ANOMALY CORRELATION ANALYSIS (III-3)

INTERCEPT COEFFICIENTS
 $AR = (215.4, -127.1) \times 10^3 \text{ gamma/km}$ $AM = .28 \times 10^3 \text{ gamma/km}$

$Z = 450 \text{ km}$ $CI = 10.0 \text{ gamma}$

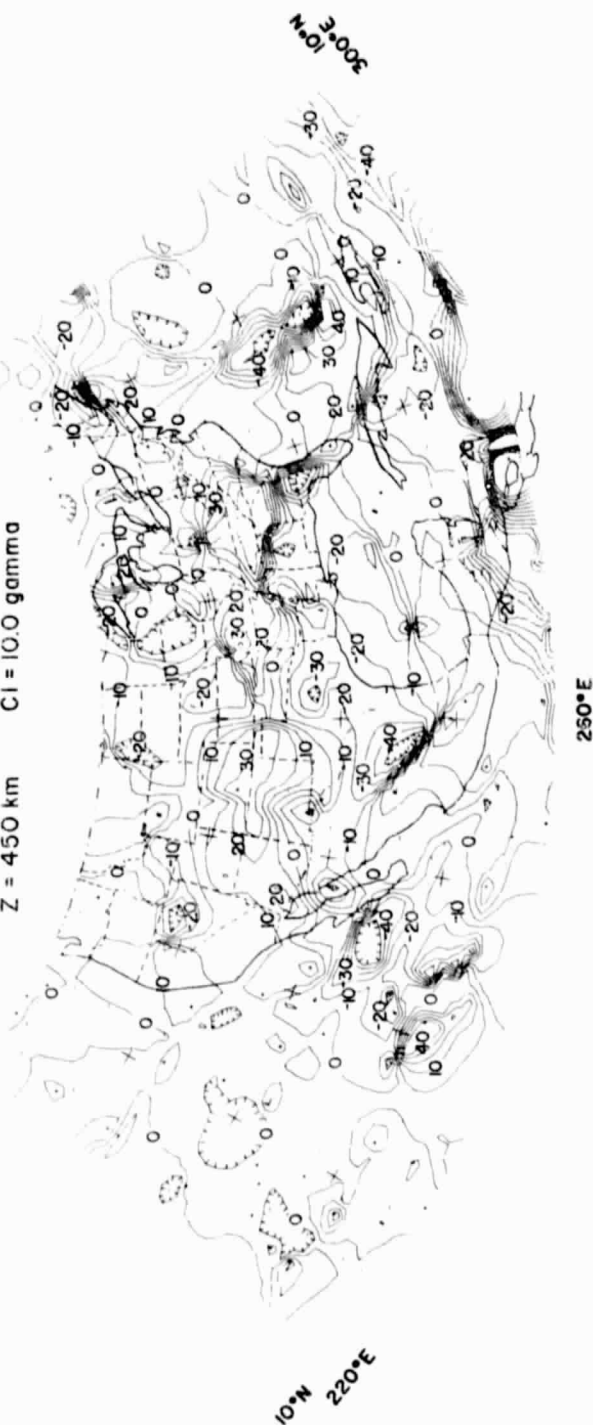


Figure IV.25 Intercept coefficients derived from correlation analysis (III-3).

derivative anomalies show correlation coefficients of absolute magnitude greater than or equal to ± 0.7 . The increased number of relatively strong correlations reflects both the decreased size of the operational window and the enhanced spectral compatibility of the data sets.

Fluctuations of the correlation coefficients tend to emphasize the slight phase shifts of the correlating anomaly peaks that are evident in Figure IV.20. This behavior also is illustrated by the slope and intercept values which are plotted in Figures IV.24 and 25, respectively. Hence, despite the increased number of high statistical correlations, the relationship between the regression parameters and potential field anomalies remains essentially complex and must be considered on an individual anomaly basis.

In the complicated behavior of the regression coefficients, however, continental inverse anomaly correlations tend to be characterized in a fairly uniform manner. Gravity lows corresponding to the peaks of the transcontinental magnetic high all continue to exhibit correlation coefficients of -0.8 to -0.6 and slope values of the order of -0.06 oersted*cm³/gm. Gravity maxima corresponding to magnetic lows, on the other hand, as observed for the Yellowstone area and the breaches of the transcontinental magnetic high by the Cordillera and the northern Mississippi Embayment tend to all be characterized by correlation coefficients up to -0.8 and slope values ranging between zero and -0.03 oersted*cm³/gm.

To investigate the possibility that the regression parameters contain significant long-wavelength information, the correlation, slope and intercept coefficients of analysis (III-3) were low-pass filtered for wavelengths roughly greater than 8° . Positive and negative low-pass filtered correlation coefficients are given in Figures IV.26 and 27, respectively, whereas the smoothed slope and intercept coefficients are illustrated, respectively, in Figures IV.28 and 29. The regression parameters all exhibit similar fluctuating behavior which generally emphasizes the slight spatial disparity between correlating anomaly peaks. However, these variations are considerably simplified by the smoothing process and, hence, facilitate a more generalized interpretation of the correlating gravity and magnetic anomalies than the previously discussed results.

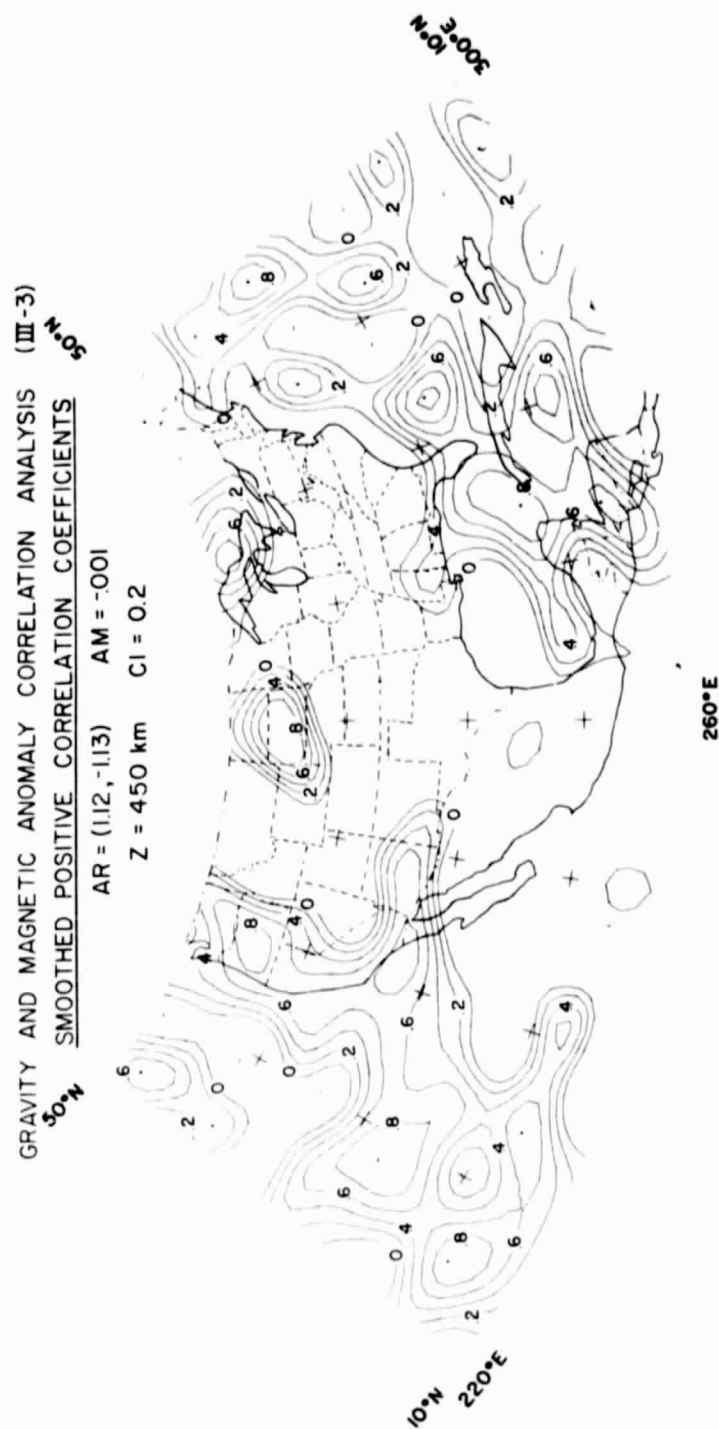


Figure IV.26 High-cut ($\lambda \leq 8^\circ$) filtered positive (0.0 to 1.0) correlation coefficients derived from correlation analysis (III-3).

GRAVITY AND MAGNETIC ANOMALY CORRELATION ANALYSIS (III-3)
 SMOOTHED NEGATIVE CORRELATION COEFFICIENTS

AR = (112, -113) AM = -0.001
 Z = 450 km CI = 0.2

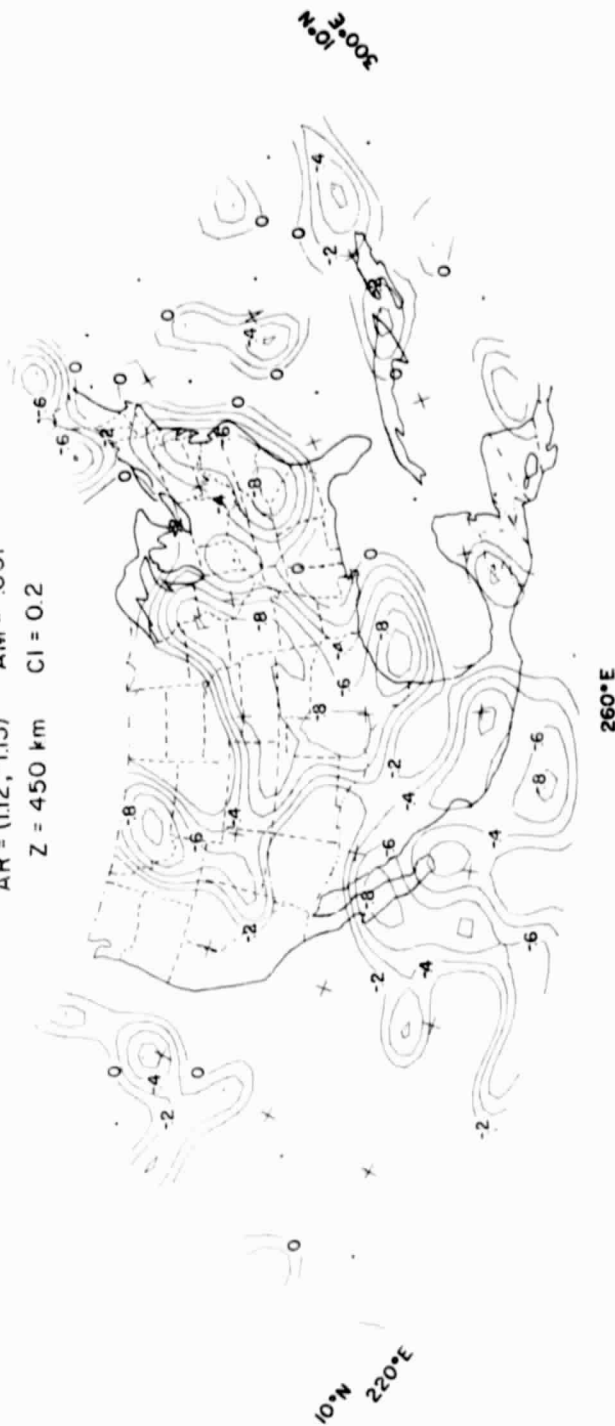


Figure IV.27 High-cut ($\lambda \leq 8^\circ$) filtered negative (-1.0 to 0.0) correlation coefficients derived from correlation analysis (III-3).

GRAVITY AND MAGNETIC ANOMALY CORRELATION ANALYSIS (III-3)

SMOOTHED SLOPE ($\Delta j / \Delta m$) COEFFICIENTS

AR = (.13, -.17) oersted cm^3/gm AM = -.0024 oersted cm^3/gm

Z = 450 km CI = .03 oersted cm^3/gm



Figure IV.28 High-cut ($\lambda \leq 8^\circ$) filtered slope ($\Delta j / \Delta m$) coefficients derived from correlation analysis (III-3).

GRAVITY AND MAGNETIC ANOMALY CORRELATION ANALYSIS (III-3)

SMOOTHED INTERCEPT COEFFICIENTS

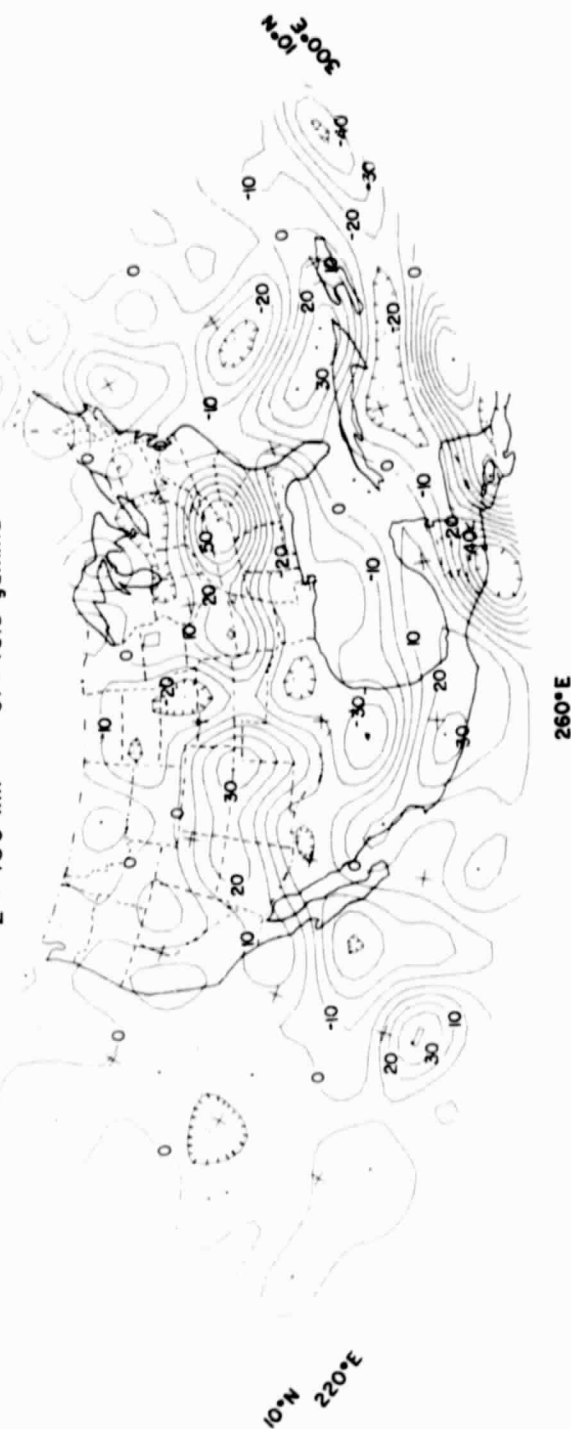
 $AR = (66.8, -68.8) \times 10^{-3} \text{ gamma/km}$
 $AM = 32 \text{ g} \times 10^{-3} \text{ gamma/km}$
 $Z = 450 \text{ km}$
 $CI = 100 \text{ gamma}$


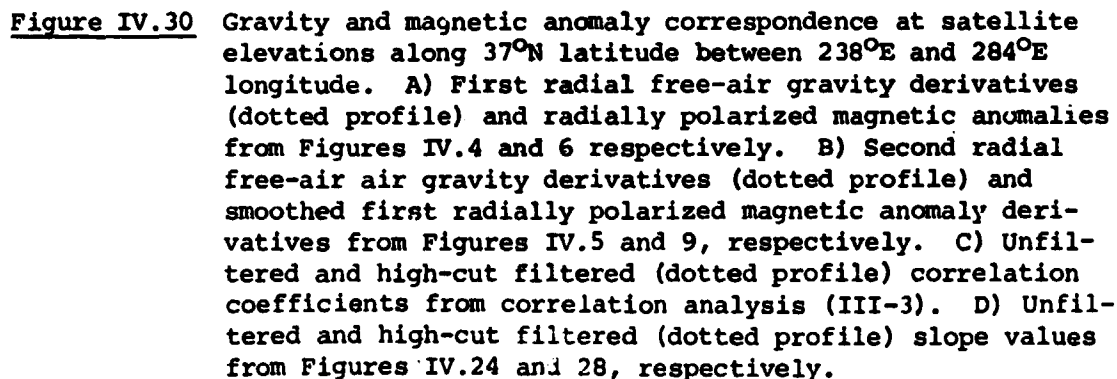
Figure IV.29 High-cut ($\lambda \leq 8^\circ$) filtered intercept coefficients derived from correlation analysis (III-3).

ORIGINAL PAGE IS
OF POOR QUALITY

For example, oceanic regions are broadly characterized by small slope values in contrast to the continents. In consideration of the large magnetizations previously inferred for major portions of the continent, this result perhaps reflects decreased polarization of the oceanic crust relative to continental crust because of the marked effect of temperature and time on the remanent magnetization properties of crustal extrusive rocks. The smoothed regression parameters also indicate more readily than in previous examples the uniform relationship between continental inverse anomaly correlations and the regression coefficients. The transcontinental positive magnetic peaks, for example, which correspond inversely with gravity lows are uniformly characterized in the slope map of Figure IV.28 by $(\Delta j/\Delta m)$ values ranging between -0.06 and -0.09 oersted \cdot cm³/gm.

The general characteristics of continental inverse gravity and magnetic anomaly correlations are further exemplified by the results for the profile along 37°N between 238°E and 284°E illustrated in Figure IV.30. The top set of profiles (Figure IV.30.A) shows the first radial derivative gravity data (dotted profile) and radially polarized magnetic data taken from Figures IV.4 and 6, respectively, along the 37°N parallel of latitude. The next set of profiles (Figure IV.30.B) corresponds to the second radial gravity derivative data (dotted profile) and smoothed first radial derivative magnetic anomalies along 37°N taken from Figures IV.5 and 9, respectively. The third profile set (Figure IV.30.C) gives both low-pass filtered (dotted profile) and unfiltered correlation coefficients corresponding to analysis (III-3), and the final set of profiles (Figure IV.30.D) shows the slope values along 37°N extracted from Figures IV.24 and 28 (dotted profile).

These profiles clearly demonstrate the strong inverse correlation of regional gravity and magnetic anomalies that generally typifies North America. For the anomalies east of 270°E which are related to the gravity minima and magnetic highs discussed previously, the large $(\Delta j/\Delta m)$ values suggest crustal magnetization which is appreciably higher than indicated by conventional arguments, so that the magnetic high may be due to an intra-layer magnetic polarization variation.



The Mississippi Embayment is associated with a well-defined gravity maximum and magnetic minimum. As described in section VI, seismic and surface gravity data indicate that the crustal structure of the Embayment consists of essentially four components. The major gravity source for the Embayment, however, corresponds to a portion of the lower crust with density contrast equal to 0.20 gm/cm^3 . This particular feature also can account for the POGO satellite magnetic data of the region if a polarization contrast equal to -0.0024 emu/cm^3 is assumed. The resultant physical property contrast ratio ($= -0.012 \text{ oersted*cm}^3/\text{gm}$) of the major gravity and magnetic source inferred for the Embayment compares very favorably with the slope value ($= -0.011 \text{ oersted*cm}^3/\text{gm}$) given in Figure IV.30.D.

An especially broad band distribution of relatively strong inverse correlations is evident between the Mississippi Embayment and the Colorado Plateau. Uniform apparent ($\Delta j/\Delta m$) values roughly equal to $-0.037 \text{ oersted*cm}^3/\text{gm}$ tend to characterize this region, except for the marked local fluctuation in the vicinity of the 1° phase shift between the gravity anomaly peak at 259°E and the magnetic anomaly peak at 260°E .

The pronounced gravity maximum and magnetic low over the eastern margin of the Colorado Plateau probably reflects the increased heat flow and decreased crustal thickness of the region (Keller *et al.*, 1979). Crustal thickening and lower heat flow over the Plateau result in a substantial decrease of gravity anomalies and slightly enhanced magnetics. However, west of the Plateau the effect of high heat flow and complicated tectonic styles yields an overall deterioration of anomaly correlations that is reflected in the general behavior of the correlation coefficients for this region.

F. Conclusions

Anomaly correlations as well as non-correlations provide useful information for the geologic interpretation of anomalous gravity and magnetic sources within the subsurface. To quantitatively assess patterns of anomaly correlation for multiple source data sets, Poisson's

theorem can be used to perform a regression analysis on appropriate gravity and magnetic anomaly data within a window that traverses the data sets. The regression parameters derived from this moving-window Poisson's analysis include 1) correlation coefficients which provide a statistical measure of the coincidence and uniformity of the anomaly sources, 2) slope coefficients ($\Delta g/\Delta m$) which provide initial constraints on source physical properties to facilitate subsequent modeling for more detailed interpretation, and 3) intercept coefficients which reflect base level changes due to interfering anomalies.

To investigate quantitative regional correlations of long-wavelength gravity and magnetic anomalies over North America and adjacent marine areas a number of data sets were prepared at 450 km elevation which satisfy the theoretical considerations of Poisson's theorem in regions of common potential field sources. These data sets indicate the general relationship between gravity and magnetic anomalies over the continent is inverse. Regions of large relative crustal thickness such as the midcontinent appear to be characterized by negative gravity and positive magnetic anomalies at satellite elevations. Accordingly, this continental type of inverse anomaly correlation may reflect displacement of denser and less magnetic mantle material by an anomalously thick crust. However, the magnetic maxima probably also reflect an increase in the magnetic polarization of the crust in these areas. Negative magnetic and positive gravity anomaly correlations, on the other hand, as exemplified by the Yellowstone geothermal region may be related to regions of increased heat flow where the Curie point isotherm is likely to be deflected to shallower depths to yield anomalous sources of net negative magnetization.

The distinct inverse characterization of continental gravity and magnetic anomaly correlations is supported statistically by the application of moving-window Poisson's analysis to the regional data sets. These results indicate that satellite elevation gravity and magnetic anomalies derived from continental crust demonstrate remarkable regional correlations that are useful in decreasing the ambiguity of lithologic and structural interpretation.

Oceanic regions tend to exhibit overall poor anomaly correlations perhaps as a result of decreased crustal magnetization. Statistically, however, oceanic anomalies appear to be characterized by generally positive correlations which probably are best exemplified by the anomalies of the Caribbean, eastern Gulf of Mexico and the Atlantic Ocean.

Poisson's moving-window regression analysis has been shown in this investigation to be particularly sensitive to phase shifts of anomaly peaks which complicates the interpretation of the quantitative correlations. Hence, in the application of this method it is desirable to obtain a high degree of spectral compatibility between the data sets to be correlated. This objective perhaps can be best achieved by simply filtering one of the data sets in the frequency domain using the spectral characteristics of the other data set as the filter.

A number of reasons can be suggested which may account for the apparent phase shifting of anomaly peaks. Geologically significant mechanisms include sources with appreciable moments of remanent magnetization, sources with inhomogeneous properties of magnetization or density, and the differential response in time of magnetic and density properties to dynamic heat sources. Data reduction and processing problems also may lead to inadequate definition of anomalies. In the magnetic data set, however, this situation will soon be alleviated by the availability of scalar and vector magnetic anomaly data from the current Magsat program (Langel, 1979) which should provide higher resolution data to upgrade the quantitative correlation analysis of regional North American gravity and magnetic anomalies.

G. References

- Allredge, L.R., G.D. Van Voorhis and T.M. Davis, A magnetic profile around the world, *Jour. Geophy. Res.*, 68, 3679-3692, 1963.
- Bowman, P.L., L.W. Braile, V.W. Chandler, W.J. Hinze, A.J. Luca and R.R.B. von Frese, Magnetic and gravity anomaly correlation and its application to satellite data, NASA-GSFC TM79702, 1979.
- Chandler, V.W., J.S. Koski, W.J. Hinze and L.W. Braile, Combined analysis of multi-source gravity and magnetic anomaly data sets, *Geophysics* (in press), 1980.
- Hall, D.H., Long-wavelength aeromagnetic anomalies and deep crustal magnetization in Manitoba and Northwestern Ontario, Canada, *Pageoph.*, 40, 403-430, 1974.

Keller, G.R., L.W. Braile and P. Morgan, Crustal structure, geophysical models and contemporary tectonism of the Colorado Plateau, *Tectonophysics*, 61, 131-147, 1979.

Langel, R.A., Near-earth satellite magnetic field measurements: A prelude to Magsat, EOS (Am. Geophys. Union Trans.), 60, 667-668, 1979.

Lyubimov, A.A. and G.A. Lyubimov, The use of Poisson's ratio for geologic interpretation of gravity and magnetic anomaly analogs, *Razvedka i Okhrana Nedr*, 34, 38-42, 1968.

Mayhew, M.A., Inversion of satellite magnetic anomaly data, *J. Geophys.*, 45, 119-128, 1979.

Shuey, R.T., D.K. Schellinger, E.H. Johnson and L.B. Alley, Aero-magnetics and the transition between the Colorado Plateau and the Basin and Range Provinces, *Geology*, 1, 107-110, 1973.

Warren, D.H. and J.H. Healy, Structure of the crust in the conterminous United States, *Tectonophysics*, 20, 203-213, 1973.

Wasilewski, P.J., H.H. Thomas and M.A. Mayhew, The Moho as a magnetic boundary, NASA-GSFC TM80245, 1979.

V. SPHERICAL EARTH GRAVITY AND MAGNETIC ANOMALY MODELING BY GAUSS-LEGENDRE QUADRATURE INTEGRATION

A. Abstract

Increasing interest in the geologic significance of long-wave-length geophysical anomalies has focused attention on spherical gravity and magnetic modeling. Gauss-Legendre quadrature integration provides an especially powerful approach to the spherical earth modeling problem. A procedure has been developed using this numerical integration scheme for calculating the anomalous potential of gravity and magnetic fields and their spatial derivatives on a spherical earth for an arbitrary body represented by an equivalent point source distribution of gravity poles or magnetic dipoles. The distribution of equivalent point sources is determined directly from the coordinate limits of the source volume. Variable integration limits for an arbitrarily shaped body are derived from interpolation of points which approximate the body's surface envelope. The versatility of the method is enhanced by the ability to treat physical property variations within the source volume and to consider variable magnetic fields over the source and observation surface. The method is particularly well suited for satellite gravity and magnetic anomaly modeling because the accuracy and efficiency of the application improves with increasing distance between source and observation point. A number of examples verify and illustrate the capabilities of the technique.

B. Introduction

Computation of theoretical anomalous gravity and magnetic fields due to geologic models is an important element in interpreting potential field data and designing surveys. For regional gravity and magnetic surveys measured in degrees of latitude and longitude, procedures are required which model directly in spherical coordinates potential field anomalies due to large-scale, arbitrarily shaped sources with variable density or magnetization characteristics.

In a review of computer modeling techniques, Bhattacharyya (1978) presents methods that in principle are suitable for spherical earth modeling of regional features. These procedures generally are based on approximations of the anomalous source as a group of prisms or polygonal laminae, the effects of which are evaluated and summed at each observation point to yield the total anomaly. However, for typical spherical earth modeling applications, the bookkeeping problem involved with subdividing the large-scale source into simple forms to reflect arbitrary characteristics of geometry and physical properties commonly is formidable.

A simple and more efficient procedure is to represent quadratures of the source volume by equivalent point sources according to the well known technique of Gaussian quadrature integration. In principle, the appropriate geometric distribution of equivalent point sources can be determined directly from the coordinate limits of the source volume, so that an accurate estimate of the source affiliated anomaly is obtained by evaluating and summing at each observation point the differential anomaly values due to each point source of the equivalent source distribution.

Gaussian quadrature is a time-honored technique for numerical integration that has been well studied in the general literature of numerical methods (e.g., Carnahan, 1969). Potential field modeling by Gauss-Legendre quadrature was used by Ku (1977) to evaluate gravity and magnetic anomalies in Cartesian coordinates due to bodies of arbitrary shape and magnetic polarization. In this discussion, the method is extended to spherical coordinates and the general problem of sources with arbitrary shape and variable density and magnetization properties.

C. Description of the Method

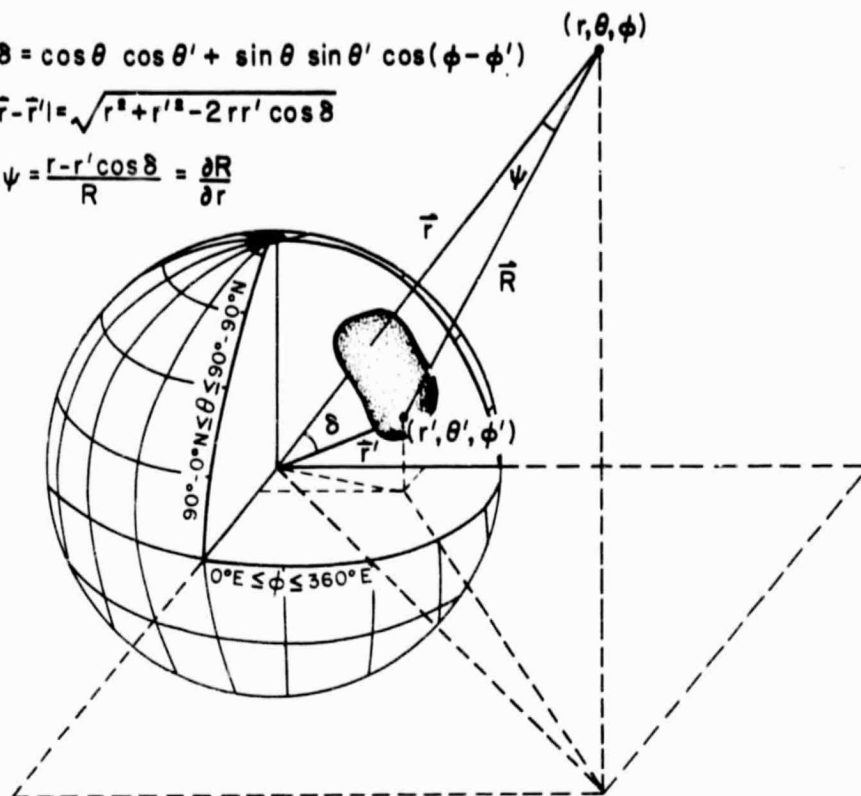
As illustrated in Figure V.1 which outlines the main results of this section, it is convenient for gravity and magnetic modeling problems to consider the anomalous body as being composed of a source volume distribution of gravity point poles or magnetic point dipoles, respectively. Hence, to estimate the anomalous gravity or magnetic field at some observation point, it is necessary to evaluate and sum the anomaly values due to each of these point sources at the observation point.

GRAVITY AND MAGNETIC MODELING BY GAUSS-LEGENDRE QUADRATURE

$$\cos \delta = \cos \theta \cos \theta' + \sin \theta \sin \theta' \cos(\phi - \phi')$$

$$R = |\vec{r} - \vec{r}'| = \sqrt{r^2 + r'^2 - 2rr' \cos \delta}$$

$$\cos \psi = \frac{r - r' \cos \delta}{R} = \frac{\partial R}{\partial r}$$



GRAVITY ANOMALY

$$\Delta g = \left[-G \frac{\partial}{\partial R} \left(\frac{1}{R} \right) \frac{\partial R}{\partial r} \right] * \Delta m$$

MAGNETIC ANOMALY

$$\Delta T = \left[-\vec{u} \cdot \vec{\nabla} \left\{ \vec{u}' \cdot \vec{\nabla}' \left(\frac{1}{R} \right) \right\} \right] * \Delta j$$

$$\left[\int_{\phi'_a}^{\phi'_b} \int_{\theta'_a}^{\theta'_b} \int_{r'_a}^{r'_b} (q(r', \theta', \phi') * \Delta x) dr' d\theta' d\phi' \right]$$

GENERALIZED ANOMALY

$$\int_{\phi'_a}^{\phi'_b} \int_{\theta'_a}^{\theta'_b} \int_{r'_a}^{r'_b} (q(r', \theta', \phi') * \Delta x) dr' d\theta' d\phi'$$

$$\left(\frac{\phi'_{kb} - \phi'_{ka}}{2} \right) \sum_{k=1}^{nk} \left\{ \left(\frac{\theta'_{jb} - \theta'_{ja}}{2} \right) \sum_{j=1}^{nj} \left[\left(\frac{r'_{ib} - r'_{ia}}{2} \right) \sum_{i=1}^{ni} (q(r'_i, \theta'_j, \phi'_k) * \Delta x) A_i \right] A_j \right\} A_k$$

Figure V.1 Gravity and magnetic anomaly modeling in spherical coordinates of a geologic body with arbitrary shape and physical properties by Gauss-Legendre quadrature integration (see text for details).

In particular, the radial anomaly, Δg , due to a gravity point pole referenced to a geocentric coordinate system as shown in Figure V.1 is given by

$$\Delta g = \left\{ -G \frac{\partial}{\partial R} \left(\frac{1}{R} \right) \frac{\partial R}{\partial r} \right\} \Delta m, \quad \text{where} \quad (V-1)$$

G = universal gravitational constant ($=6.67 \times 10^{-8} \text{ cm}^3 / (\text{gm} \cdot \text{sec}^2)$),

R = distance from observation point (r, θ, ϕ) to source point (r', θ', ϕ') ,

r, r' = radial distances from earth's center to the observation point and source point, respectively,

θ, θ' = co-latitude coordinates of observation and source points, respectively,

ϕ, ϕ' = longitude coordinates of observation and source points, respectively, and

Δm = mass contrast of the point pole.

For a magnetic point dipole, on the other hand, the total magnetic intensity anomaly, ΔT , is given by

$$\Delta T = \left\{ -\vec{u} \cdot \vec{\nabla} \left(\vec{u}' \cdot \vec{\nabla}' \left(\frac{1}{R} \right) \right) \right\} \Delta j, \quad \text{where} \quad (V-2)$$

$\vec{\nabla}, \vec{\nabla}'$ = gradient operators in observation point and source point coordinates, respectively,

Δj = magnetization contrast of the point dipole, and

\vec{u}, \vec{u}' = unit geomagnetic field vectors at the observation point and source point, respectively.

Conventionally, the unit vectors \vec{u} and \vec{u}' are expressed in terms of geomagnetic field inclination (I, I') and declination (D, D'). Also, when the point dipole polarization is by induction

$$\Delta j = \Delta k \cdot F', \quad \text{where} \quad (V-3)$$

Δk = magnetic susceptibility contrast of the point dipole, and

F' = scalar geomagnetic field intensity at the source point.

Hence, in regional-scale applications of equation (V-2) geomagnetic field models such as the IGRF-1965 (Cain et al., 1967) normally are used to obtain pertinent values of (I', D', F') at the source point and (I, D) at the observation point.

Consideration of equations (V-1) and (V-2) shows that the incremental gravity and magnetic anomaly values due to a point source located a distance R from the observation point can be generalized according to the relation

$$q(R) \Delta x, \quad \text{where} \quad (V-4)$$

$q(R)$ = the geometrical point source function which essentially describes the inverse distance between the observation point and source point, and

Δx = the appropriate physical property contrast of the point source. Hence, to determine the total potential field anomaly it is necessary to evaluate at each observation point (r, θ, ϕ) the volume integral given by

$$\int_a^{\phi'_b} \int_a^{\theta'_b} \int_a^{r'_b} (q(r, \theta, \phi; r', \theta', \phi') \Delta x) dr' d\theta' d\phi', \quad (V-5)$$

where the primed variables refer to the coordinates of the anomalous body such that

ϕ'_a, ϕ'_b = lower and upper longitude limits of the source volume,

θ'_a, θ'_b = lower and upper co-latitude limits of the source volume, and

r'_a, r'_b = lower and upper radial limits of the source volume.

Consider, now, the numerical evaluation of the innermost integral in equation (V-5). Most numerical integration techniques involve the use of interpolation polynomials to approximate the integrand according to a summation formula of the general type given by

$$\int_a^{r'_b} (q(r') \Delta x) dr' \approx \sum_{i=1}^{n_i} A_i q(r'_i) \Delta x, \quad (V-6)$$

where the n_i values A_i are the weights to be given to the n_i functional values $(q(r'_i) \Delta x)$ evaluated at the interpolation coordinates, r'_i . Conventional integration formulae such as Simpson's rule or the trapezoidal rule assume equal spacing of the arguments r'_i which is generally appropriate when dealing with an integrand that is not well known analytically. However, as shown in equations (V-1) and (V-2) the integrand being considered here involves a familiar analytic function which may be computed for any argument to great precision. In such instances, Gaussian quadrature formulae can be developed to yield selected values of interpolation r'_i and coefficients A_i so that the sum in equation (V-6) gives the integral exactly when $(q(r') \Delta x)$ is a polynomial of degree $2n_i$ or less (e.g., Carnahan, 1969).

In general, it may be shown that the Gaussian coefficients A_i can be obtained from a polynomial of order n_i which is orthogonal over the interval of integration such that the n_i points of interpolation

r'_i are the zeros of the polynomial. Families of orthogonal polynomials which commonly are used to develop Gaussian quadrature formulae include Legendre, Laguerre, Chebyshev and Hermite polynomials. However, in this discussion only Legendre polynomials are considered which is the prototype of the Gaussian method.

Legendre polynomials $P_{n_i}(\bar{r}')$ of order n_i which are orthogonal over the interval $-1 \leq \bar{r}' \leq 1$ are given by

$$P_{n_i}(\bar{r}') = \left(\frac{1}{2^{n_i} n_i!} \right) \left(\frac{d^{n_i}}{d\bar{r}'^{n_i}} (\bar{r}'^2 - 1)^{n_i} \right), \text{ where } P_0(\bar{r}') = 1. \quad (V-7)$$

Accordingly, the standard Gauss-Legendre quadrature over the interval $(-1, 1)$ is given by

$$\int_{-1}^1 (q(\bar{r}') * \Delta x) d\bar{r}' = \sum_{i=1}^{n_i} A_i * q(\bar{r}'_i) * \Delta x, \quad (V-8)$$

where the interpolation points \bar{r}'_i at which the integrand is evaluated are the zeros of equation (V-7) and the Gaussian coefficients are

$$A_i = \frac{2(1 - \bar{r}'_i{}^2)}{n_i^2 \{P_{n_i-1}(\bar{r}'_i)\}^2}. \quad (V-9)$$

Now for arbitrary limits of integration such as indicated in equation (V-6) it is necessary to map the standard interval $-1 \leq \bar{r}'_i \leq 1$ into the interval of integration $r'_a \leq r'_i \leq r'_b$ according to the transformation

$$r'_i = \frac{\bar{r}'_i (r'_b - r'_a) + (r'_b + r'_a)}{2}. \quad (V-10)$$

Accordingly, the integral in equation (V-6) can be approximated as

$$\begin{aligned} \int_{r'_a}^{r'_b} (q(r') * \Delta x) dr' &= \frac{(r'_b - r'_a)}{2} \int_{-1}^1 \left(q\left(\frac{\bar{r}'_i (r'_b - r'_a) + (r'_b + r'_a)}{2}\right) * \Delta x \right) d\bar{r}' \\ &= \frac{(r'_b - r'_a)}{2} \sum_{i=1}^{n_i} A_i * q(r'_i) * \Delta x. \end{aligned} \quad (V-11)$$

Extending this procedure to volume integrals is straightforward. Thus, the Gauss-Legendre formula for the general evaluation of equation (V-5) is given by

$$\oint_a^{\phi'_b} \oint_a^{\theta'_b} \int_a^{r'_b} (q(r', \theta', \phi') \Delta x) dr' d\theta' d\phi' = \quad (V-12)$$

$$\left(\frac{\phi'_{kb} - \phi'_{ka}}{2} \right) \sum_{k=1}^{nk} \left(\frac{\theta'_{jb} - \theta'_{ja}}{2} \right) \sum_{j=1}^{nj} \left(\frac{r'_{ib} - r'_{ia}}{2} \right) \sum_{i=1}^{ni} (q(r'_i, \theta'_j, \phi'_k) \Delta x) A_i A_j A_k$$

where

$$r'_i = 0.5 \{ \bar{r}'_i (r'_{ib} - r'_{ia}) + r'_{ib} + r'_{ia} \},$$

$$\theta'_j = 0.5 \{ \bar{\theta}'_j (\theta'_{jb} - \theta'_{ja}) + \theta'_{jb} + \theta'_{ja} \},$$

$$\phi'_k = 0.5 \{ \bar{\phi}'_k (\phi'_{kb} - \phi'_{ka}) + \phi'_{kb} + \phi'_{ka} \},$$

$\bar{r}'_i, \bar{\theta}'_j, \bar{\phi}'_k$ = coordinates of the subdivision in the limits of integration from -1 to 1 which correspond to zero nodes of equation (V-7),

A_i, A_j, A_k = Gauss-Legendre quadrature coefficients given by equation (V-9),

ϕ'_{ka}, ϕ'_{kb} = lower and upper volume limits of the body in the k-th coordinate of longitude,

$\theta'_{ja}, \theta'_{jb}$ = lower and upper volume limits of the body in the j-th coordinate of co-latitude, and

r'_{ia}, r'_{ib} = lower and upper volume limits of the body in the i-th radial coordinate.

The quadrature formula given in equation (V-12) shows that gravity and magnetic anomalies can be accurately computed by summing at each observation point the anomalous effect of $nk \cdot nj \cdot ni$ equivalent point sources located at source point coordinates $(r'_i, \theta'_j, \phi'_k)$, where each of the differential point source anomalies is appropriately weighted by Gauss-Legendre quadrature coefficients and the volume coordinate limits of the anomalous body being modeled. This result is well suited for machine computation where the input consists principally of values of the integrand for selected source points $(r'_i, \theta'_j, \phi'_k)$, affiliated subdivision coordinates $(\bar{r}'_i, \bar{\theta}'_j, \bar{\phi}'_k)$ and coefficients (A_i, A_j, A_k) , and the volume coordinate limits of the body for each dimension of every source point coordinate $(r'_i, \theta'_j, \phi'_k)$.

The selected values of the integrand for gravity or magnetic modeling purposes are readily obtained from equations (V-1) or (V-2), respectively. Also, the Legendre subdivision coordinates of the interval (-1,1) and associated Gaussian coefficients may be computed directly from equations (V-7) and (V-9), respectively; although, it generally is found to be more machine efficient to input these values from tables

using an algorithm such as described by Carnahan (1969). Values which are applicable for such algorithms are tabulated to 30 digit precision for orders $n = 2$ to 512 by Stroud and Secrest (1966). However, for most regional lithospheric modeling applications experience suggests subdivision coordinates and associated coefficients to 10 digit precision for orders up to $n = 16$ normally are sufficient.

For a uniformly dimensioned body such as a prism, the integration limits for the evaluation of equation (V-12) are easy to specify. In this case, for example, $(\phi'_{ka}, \phi'_{kb}) = (\phi'_a, \phi'_b)$, $(\theta'_{ja}, \theta'_{jb}) = (\theta'_a, \theta'_b)$ and $(r'_{ia}, r'_{ib}) = (r'_a, r'_b)$. However, for the more general case of a body with arbitrary shape the integration limits are known in one dimension only so that the problem of determining the integration limits in the remaining two dimensions for each equivalent point source coordinate must be considered.

Procedures can be developed to efficiently handle this problem, such as the method described by Ku (1977) where a modified cubic spline function is used to interpolate the desired integration limits from a set of body point coordinates which provide a rough approximation of the surface envelope of the body. Typically, the procedure is to specify, for example, the longitudinal limits of integration of the body to obtain the n_k Gauss-Legendre nodes ϕ'_k as described above. Interpolations of the body point coordinates are performed next to determine the maximum and minimum latitude coordinates of the body for each longitude coordinate ϕ'_k . These values of course provide the latitude limits of integration for evaluating the n_j nodes θ'_j . Similarly, the radial coordinates of the body points are interpolated at each horizontal coordinate (ϕ'_k, θ'_j) to yield appropriate radial limits of integration from which the n_i nodes r'_i can be determined. Procedures such as this are readily adapted for efficient machine processing so that the integration limits of arbitrarily shaped bodies can be determined accurately for evaluation of the quadrature formula given in equation (V-12).

The quadrature formula in general has considerable versatility in modeling applications because anomalous gravity and magnetic potentials and their respective spatial derivatives of any order are all linearly related. Hence, to model the radial derivative of the

potential field anomaly due to an arbitrary source, for example, it is necessary simply to exchange $q(R)$ for $\partial q(R)/\partial r$ in equation (V-12). Additional geophysically interesting quantities which can be modeled from simple linear transformations of the integrand of equation (V-12) include the anomalous potential, vector anomaly components and the spatial derivatives of any order. Relative geoidal anomalies can be modeled as well by computing the anomalous gravitational potential of the body at the surface of the earth and dividing it by normal gravity according to Brun's formula (Heiskanen and Moritz, 1967).

Bodies with variable physical property contrast also are accommodated readily by the quadrature solution. To emphasize the fact that Δx can be expressed as a function of source position (i.e., $\Delta x = \Delta x(r', \theta', \phi')$) when necessary, the generalized point source anomaly ($q(R) \cdot \Delta x$) has been carried intact throughout the foregoing developments. Conventional modeling procedures normally assume bodies with uniform physical properties so that each property variation must be modeled as a separate body. To model the total magnetic intensity anomaly due to a regional source subject to regional variations of geomagnetic field induction by the well known method of Talwani (1965), for example, requires that the source be subdivided into blocks wherein the geomagnetic field polarization is uniform. Each block in turn must be subdivided into a group of approximating polygonal laminae to insure accuracy of the numerical integration which evaluates the anomaly. By contrast, the Gauss-Legendre quadrature approach is to simply polarize each point dipole in the quadrature formula according to the polarization characteristics of an acceptable numerical model of the geomagnetic field (e.g., the IGRF-1965 by Cain et al., 1967)). This example also illustrates the technique for modeling bodies with remanent magnetization by quadrature formulation. Here, the magnetization of the point dipoles is achieved using a polarization field that represents the vector sum of induced and remanent magnetic polarizations.

Finally, considerable computational flexibility is available for the practical implementation of the quadrature formulation. Ku (1977) noted the tradeoffs which occur in applications of the method between efficient computation and the accuracy of the solution. A large number of Gauss-Legendre nodes insures a very accurate quadrature solution, although the same degree of accuracy often can be achieved

by a substantially smaller number of equivalent point sources. In fact, the accuracy of the solution remains essentially unchanged for different numbers of nodes as long as the node spacing is smaller than the distance to the observation point. Hence, the minimum number of nodes to specify in a given application should be such that the distance to the observation point is greater than the node spacing. In general, then, the accuracy of the quadrature formulation can readily be controlled by adjusting the number of Gauss-Legendre nodes relative to the elevation of the observation point.

D. Illustration of the Method

A computer program is described in von Frese et al., (1980) which was developed for regional lithospheric gravity and magnetic modeling applications by Gauss-Legendre quadrature. The program was used to construct the examples of this section which illustrate some of the capabilities of the method.

To demonstrate and verify the method for regional scale modeling applications, gravity and magnetic anomalies due to a three-dimensional spherical prism were modeled on a spatial scale small enough that the results could be compared readily with conventional modeling techniques in Cartesian coordinates. In Figure V.2, for example, a comparison of gravity anomalies is given due to a 6.67 km thick prism with density contrast 0.25 gm/cm^3 . The observation grid consists of (16,16) stations uniformly spanning the region $(273-274)^\circ\text{E}$, $(40-41)^\circ\text{N}$ at an elevation (Z) of 6.67 km above the top of the prism.

The well known method of Talwani and Ewing (1960) was used to calculate the gravity effect of the prismatic model as shown in Figure V.2.A. The gravity anomaly was determined by evaluating and summing at each observation point the gravity anomalies due to 11 horizontal polygonal laminae used to approximate the prism. As shown in Figure V.2.A, the resultant anomaly has an amplitude range (AR) between 36.0 mgal and 0.3 mgal and an amplitude mean (AM) of 5.4 mgal. The anomaly was computed and contoured in Cartesian coordinates assuming $1^\circ = 100 \text{ km}$. This assumption distorts slightly the true geometry of a spherical prism in this $1^\circ \times 1^\circ$ region in northwestern Indiana where 1° in longitude and latitude is more nearly equal to 88 km and 112 km, respectively.

PRISMATIC MODEL GRAVITY ANOMALY FIELDS

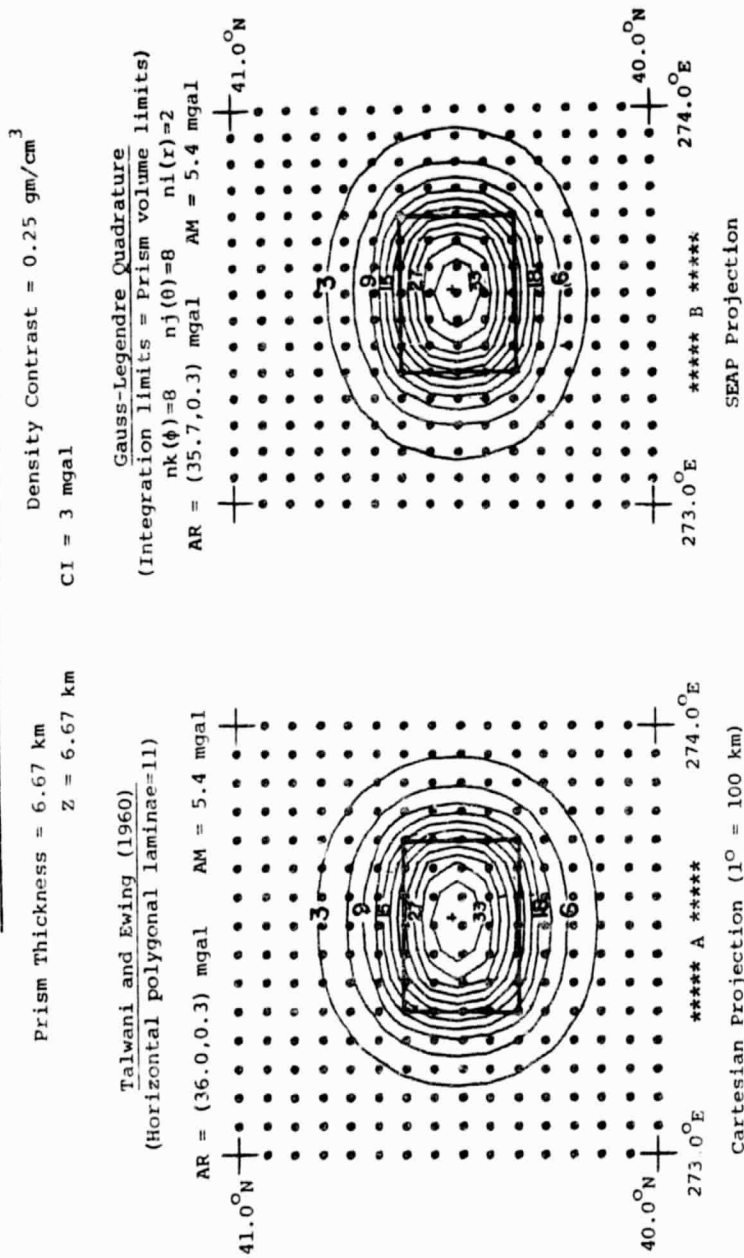


Figure V.2 Gravity anomaly comparisons for a spherical prism.

In Figure V.2.B, the gravity anomaly of the spherical prism computed by Gauss-Legendre quadrature integration is contoured on a stereographic equal-area polar (SEAP) projection. In this case, the gravity anomaly was calculated in spherical coordinates by evaluating at each observation point an $n_k \cdot n_j \cdot n_i = 8 \cdot 8 \cdot 2 = 128$ point quadrature formula where the integration limits were specified directly from the spherical coordinate limits of the prism volume. The results shown in Figure V.2 indicate the two methods agree very well with respect to the relatively small spatial scale under consideration. The slight disparity between the results probably is due to geometric distortion introduced by the use of Cartesian coordinates for calculation of the spherical prism anomaly.

A comparison of magnetic anomaly fields is illustrated in Figure V.3 for the prism model with volume magnetic susceptibility contrast* equal to 0.0005 emu/cm^3 and uniform polarizing intensity $F' = 60,000$ gamma, inclination $I' = 75^\circ$ and declination $D' = 0^\circ$. Over the observation grid, uniform geomagnetic field attitude characteristics of inclination, $I = 75^\circ$ and declination $D = 0^\circ$ also are assumed. The total magnetic intensity anomaly of the spherical prism calculated in Cartesian coordinates according to the method of Talwani (1965) is shown in Figure V.3.A. The resultant anomaly corresponds well with the magnetic anomaly calculated in spherical coordinates by Gauss-Legendre quadrature in Figure V.3.B. This correspondence also holds for the exact closed form solution for the magnetic anomaly of the prism in Cartesian coordinates given by Andreasen and Zietz (1969) which is illustrated in Figure V.4.A.

Figure V.4.B illustrates the magnetic anomaly calculated by Gauss-Legendre quadrature integration using the algorithm described previously to interpolate the limits of integration from a set of points which sample the surface envelope coordinates of an arbitrarily shaped body. Here, the set of body points used in the algorithm comprise the longitude, latitude, and top and bottom radial coordinates of the prism for each node of the observation grid that overlies the boundary or interior of the prism. The actual interpolation was performed using the "mean slope" cubic spline function described by Ku (1977). The excellent agreement between Figures V.4.B and V.3.B shows that the algorithm can be used to obtain interpolated integration limits for arbitrarily shaped bodies with sufficient precision to insure accurate anomaly determinations.

*) $1 \text{ emu/cm}^3 = 1 \cdot 4\pi$

PRISMATIC MODEL TOTAL MAGNETIC ANOMALY FIELDS

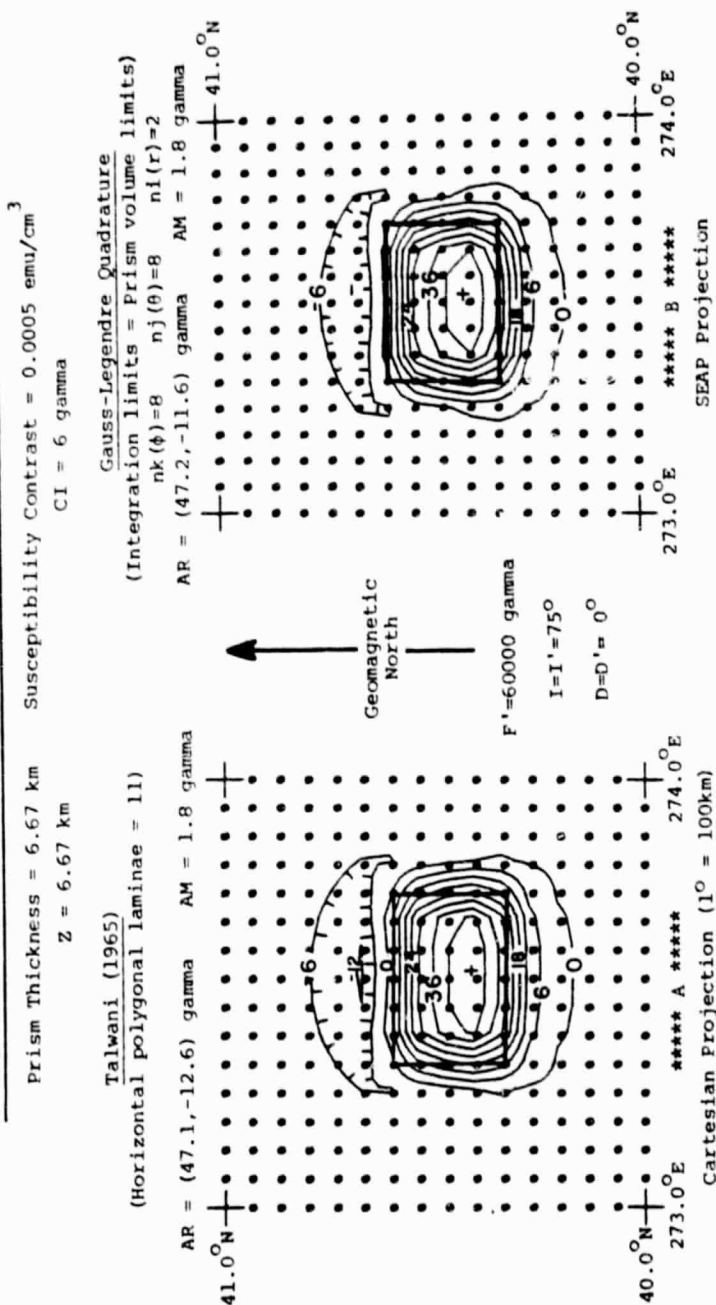


Figure V.3 Magnetic anomaly comparisons for a spherical prism.

PRISMATIC MODEL TOTAL MAGNETIC ANOMALY FIELDS

Prism Thickness = 6.67 km Susceptibility Contrast = 0.0005 emu/cm³

Z = 6.67 km

CI = 6 gamma

Andreasen and Zietz (1969)
(adapted from Plate 153A)

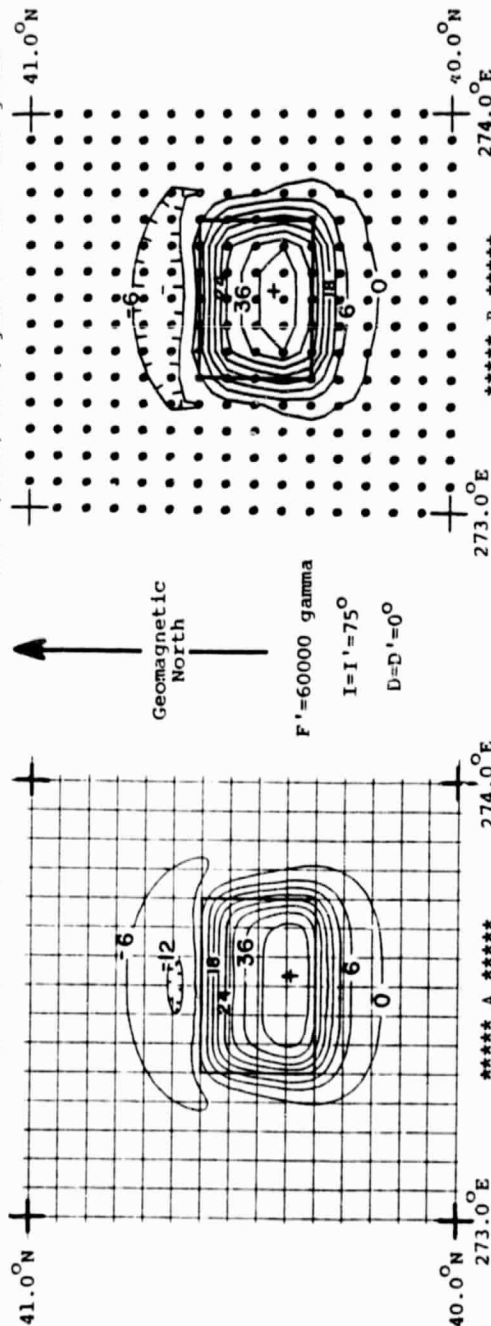
AR = (47.1, -12.6) gamma

Gauss-Legendre Quadrature

(Integration limits = Interpolated Prism volume limits)

$n_k(\phi) = 8$ $n_j(\theta) = 8$ $n_i(r) = 2$

AR = (47.1, -11.7) gamma AM = 1.9 gamma

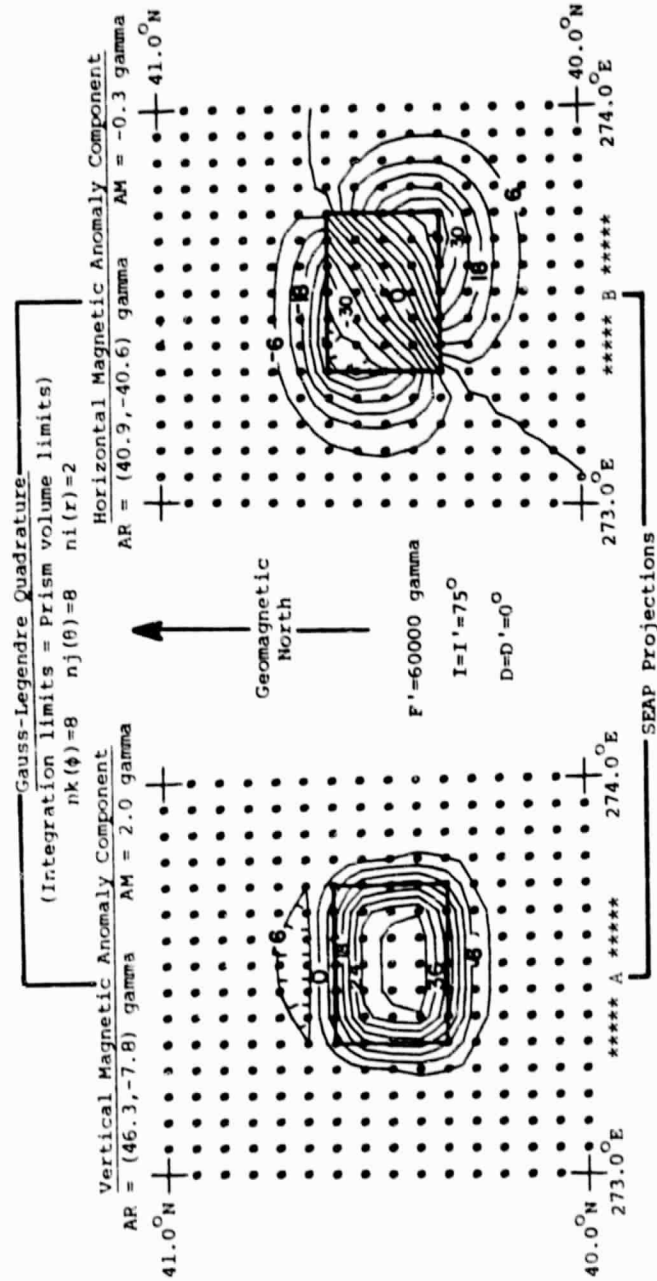


SEAP Projection

Figure V.4 Magnetic anomaly comparisons for a spherical prism where the Gauss-Legendre quadrature solution (B) is developed from interpolated limits of integration.

PRISMATIC MODEL TOTAL MAGNETIC ANOMALY FIELDS

Prism Thickness = 6.67 km Susceptibility contrast = 0.0005 emu/cm^3
 $Z = 6.67 \text{ km}$ $CI = 6 \text{ gamma}$



Some of the versatility of potential field modeling by the Gauss-Legendre quadrature formulation is illustrated in the next two figures. In Figure V.5, the radial and horizontal components of the magnetic anomaly are shown due to the spherical prism model. These anomaly components were obtained by evaluating and summing at each observation point the vertical and horizontal components of the point dipole anomalies (i.e., equation (V.2)) due to the 128 equivalent point sources used in the quadrature formula. Other geophysically interesting characteristics of the prism's anomalous gravity and magnetic potentials can be determined in this fashion as well, including the associated geoidal anomaly, vector anomaly components and spatial derivatives of any order.

In Figure V.6, the effect of including a remanent component in the polarization of the prismatic model is demonstrated. The polarization of a source represents the vector sum of its remanent magnetization field and the inducing geomagnetic field. For the case considered here, the effect of remanence yields a uniform polarization field with inclination $I' = 30^\circ$ and declination $D' = N30^\circ E$ in contrast to the attitude of the geomagnetic field over the observation grid which is $I = 90^\circ$ and $D = 0^\circ$. The anomaly for this case in Cartesian coordinates according to the closed form solution given by Andreasen and Zietz (1969) is illustrated in Figure V.6.A. Comparing this result with the spherical coordinate solution given by Gauss-Legendre quadrature in Figure V.6.B again demonstrates good correspondence with respect to the small spatial scale being considered.

The foregoing examples show that the formulation of the quadrature solution in spherical coordinates for bodies of arbitrary shape and physical properties gives results which reduce to well studied solutions under relevant modeling circumstances. Accordingly, these examples help provide useful practical incentives for implementing potential anomaly field modeling of regional geologic sources by Gauss-Legendre quadrature integration. Ku (1977) also presents a number of comparisons, although in Cartesian coordinates, which further illustrate the excellent agreement between the quadrature formulation and other published solutions for such idealized sources as the step model, rectangular prism, sphere, and vertical and inclined dykes.

PRISMATIC MODEL TOTAL MAGNETIC ANOMALY FIELDS

Prism Thickness = 6.67 km Susceptibility Contrast = 0.0005 emu/cm^3
 $Z = 6.67 \text{ km}$ $CI = 6 \text{ gamma}$

Andreasen and Zietz (1969)
 (adapted from Plate 162D)

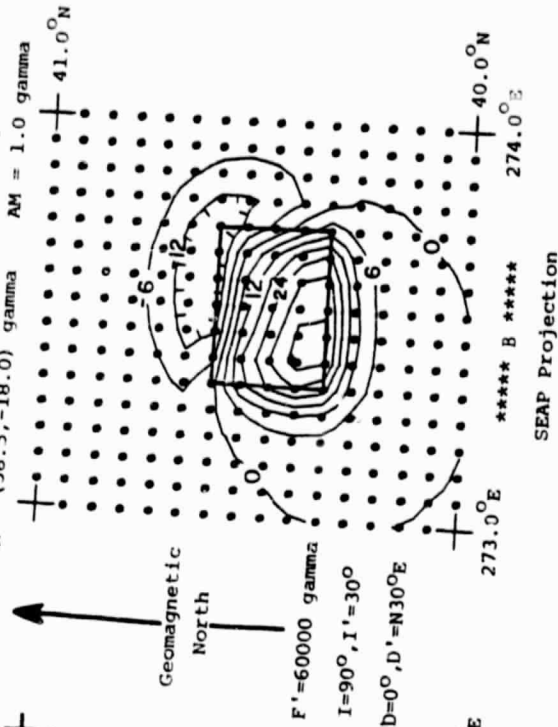
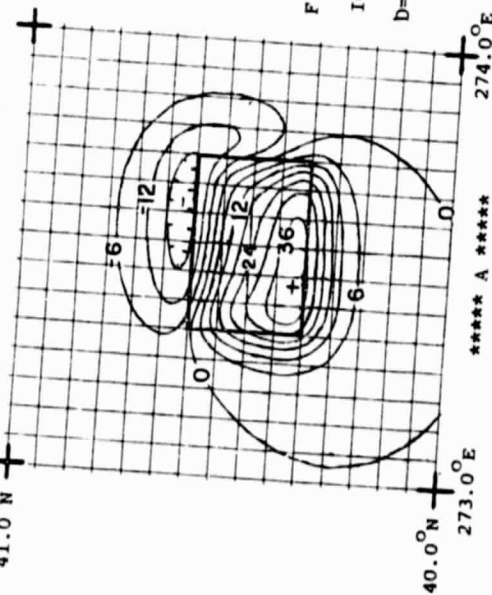
AR = (41.1, -21.0) gamma

Gauss-Legendre Quadrature
 (Integration limits = Prism volume limits)

$nk(\phi) = 8$ $nj(\theta) = 8$ $ni(r) = 2$

AR = (38.5, -18.0) gamma AM = 1.0 gamma

41.0°N
 40.0°N
 273.0°E
 274.0°E



$F' = 60000 \text{ gamma}$
 $I = 90^\circ, I' = 30^\circ$
 $D = 0^\circ, D' = N30^\circ E$

Figure V.6 Remanent magnetic anomaly comparisons for a spherical prism.

As a more regional-scale example, consider the application of Gauss-Legendre quadrature integration for modeling gravity and magnetic anomaly signatures at the satellite elevation of 450 km due to the crustal thickness anomaly which is gridded in Figure V.7.A. This zone of enhanced crustal thickness, extending from the Texas panhandle northeastward into Kansas, is portrayed by seismic evidence (Warren and Healy, 1973) as roughly 10 km of lighter crustal material displacing denser (mantle) material to a depth of 50 km. To illustrate the gravity modeling procedure, a density contrast of -0.3 gm/cm^3 was assumed for this feature.

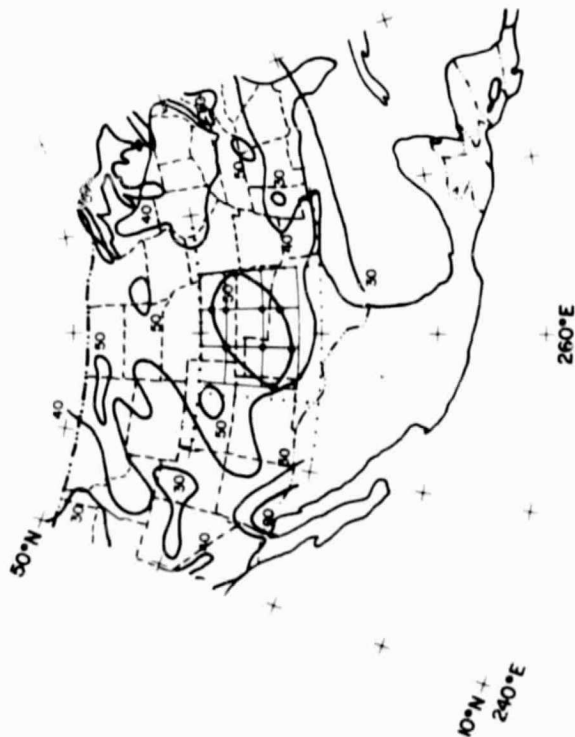
Magnetic considerations, on the other hand, suggest that the crustal thickness anomaly also may represent a zone of positive magnetization contrast due to downward deflection of the Curie isotherm in the region of thick, cooler crustal material or thicker magnetic crust extending into non-magnetic mantle material. For the purposes of this example, a volume susceptibility contrast of $10 \times 10^{-3} \text{ emu/cm}^3$ was assumed for the zone of enhanced crustal thickness which is representative of the general magnetization reported for the lower crust (e.g., Hall, 1974; Shuey *et al.*, 1973).

To determine the variable limits of integration for the evaluation of the quadrature formula, the crustal thickness anomaly was referenced to the body point grid shown in Figure V.7.A. For each Gauss-Legendre node in the ϕ -longitude coordinates of the body, the θ -latitude limits of the body were interpolated from the 6 points describing the body's boundary. The radial limits, in turn, were interpolated from the 6 boundary points and 3 interior points of the body for each Gauss-Legendre node with horizontal (ϕ, θ) -coordinates. For the particular model considered here, of course, the radial coordinates of the 9 body points used to approximate the subsurface configuration of the body were specified to represent a uniform thickness of 10 km.

The resultant gravity anomaly at 450 km elevation due to this feature is illustrated in Figure V.7.B. The gravity effect was calculated by evaluating an $n_k \cdot n_j \cdot n_i = 16 \cdot 16 \cdot 2 = 512$ point Gauss-Legendre quadrature formula over the (41,41) grid of observations. The magnetic effect of the crustal thickness anomaly also was computed in this manner at 450 km elevation. The resultant total magnetic intensity anomaly in the IGRF-1965 updated to 1968 is demonstrated in Figure V.8.A. To remove anomaly distortion due to regional variability of the

ENHANCED CRUSTAL THICKNESS MODEL MODEL GEOMETRY

Ci=10 km

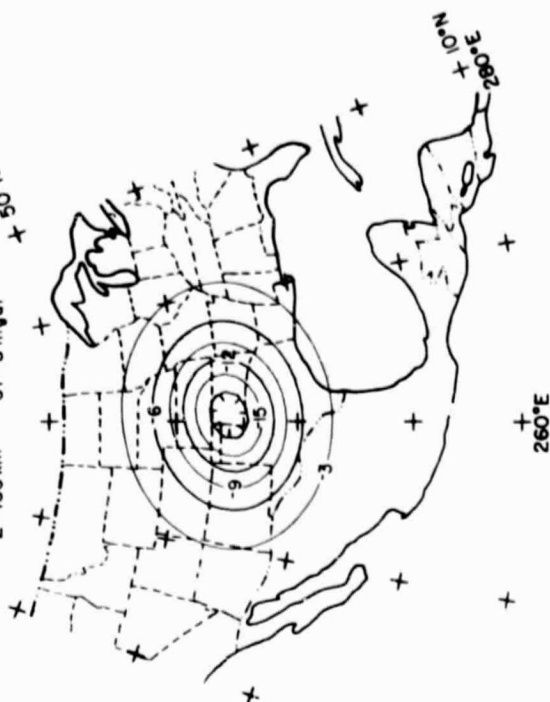


***** A *****

ENHANCED CRUSTAL THICKNESS MODEL

GRAVITY ANOMALY

$\eta(\theta)=16$ $\eta(r)=2$ $\Delta m=-0.3 \text{ gm/cm}^3$
 $AR=(-0.2, -196) \text{ mgal}$ $AM=-2.046 \text{ mgal}$
 $Z=450 \text{ km}$ $C1=3 \text{ mgal}$ 50°N



***** B *****

Figure V.7 A) SEAP projection of crustal thickness anomaly model geometry adapted from Warren and Healy (1973). The model is referenced to a body point grid which gives latitude, longitude, and top and bottom radial coordinates for the 9 points of the model's surface envelope used to interpolate the variable volume limits of integration. The shape of the thickened crust (10 km) is indicated by the 50 km depth contour on which the grid is superimposed. B) SEAP projection of the gravity anomaly for the crustal thickness model calculated at 450 km elevation by Gauss-Legendre quadrature integration.

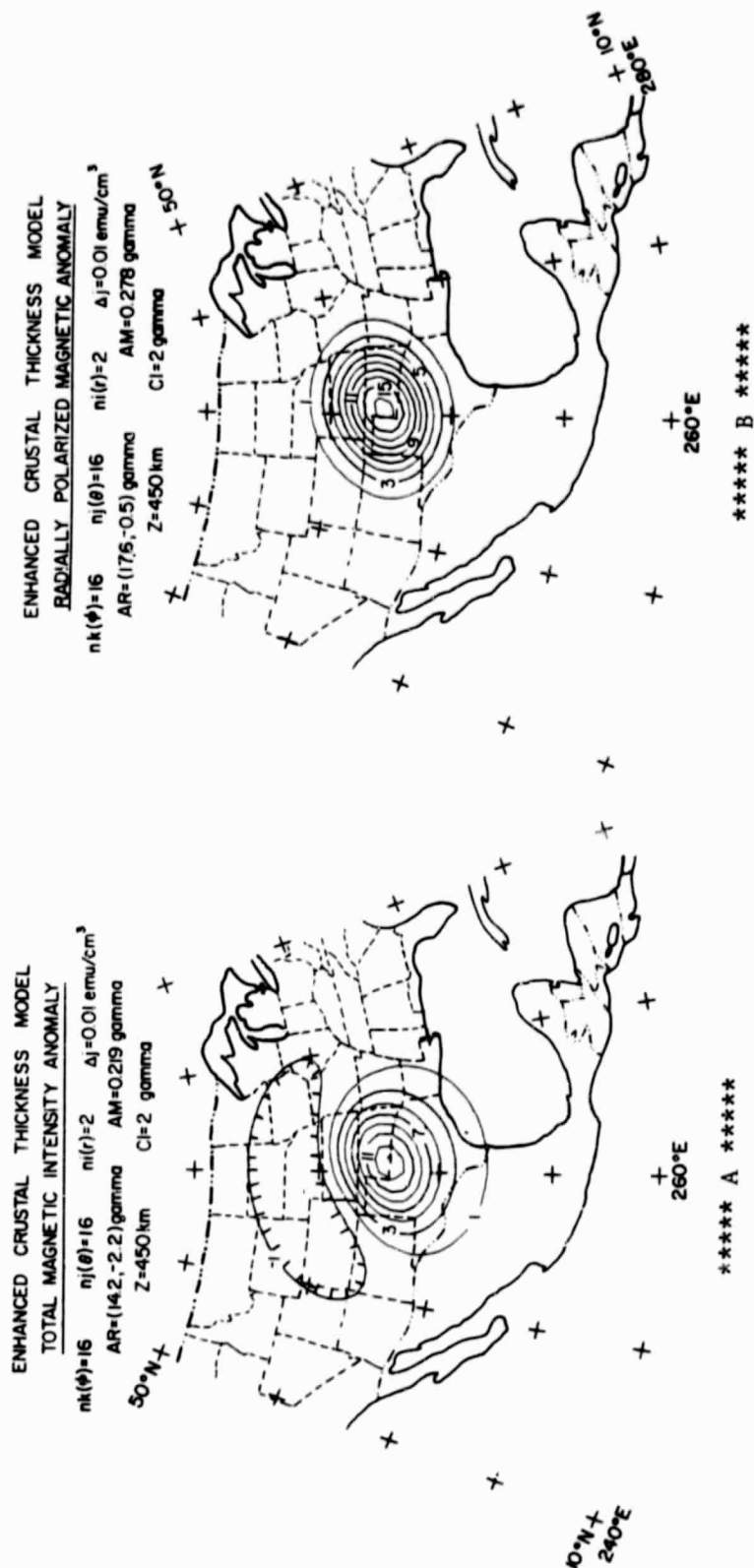


Figure V.8 A) SEAP projection of total magnetic intensity anomaly for the crustal thickness model computed in the IGRF-1965 updated to 1968 by Gauss-Legendre quadrature integration. B) SEAP projection of reduced to the pole magnetic anomaly for the crustal thickness model by Gauss-Legendre quadrature integration using a normalized polarizing amplitude of 60,000 gamma.

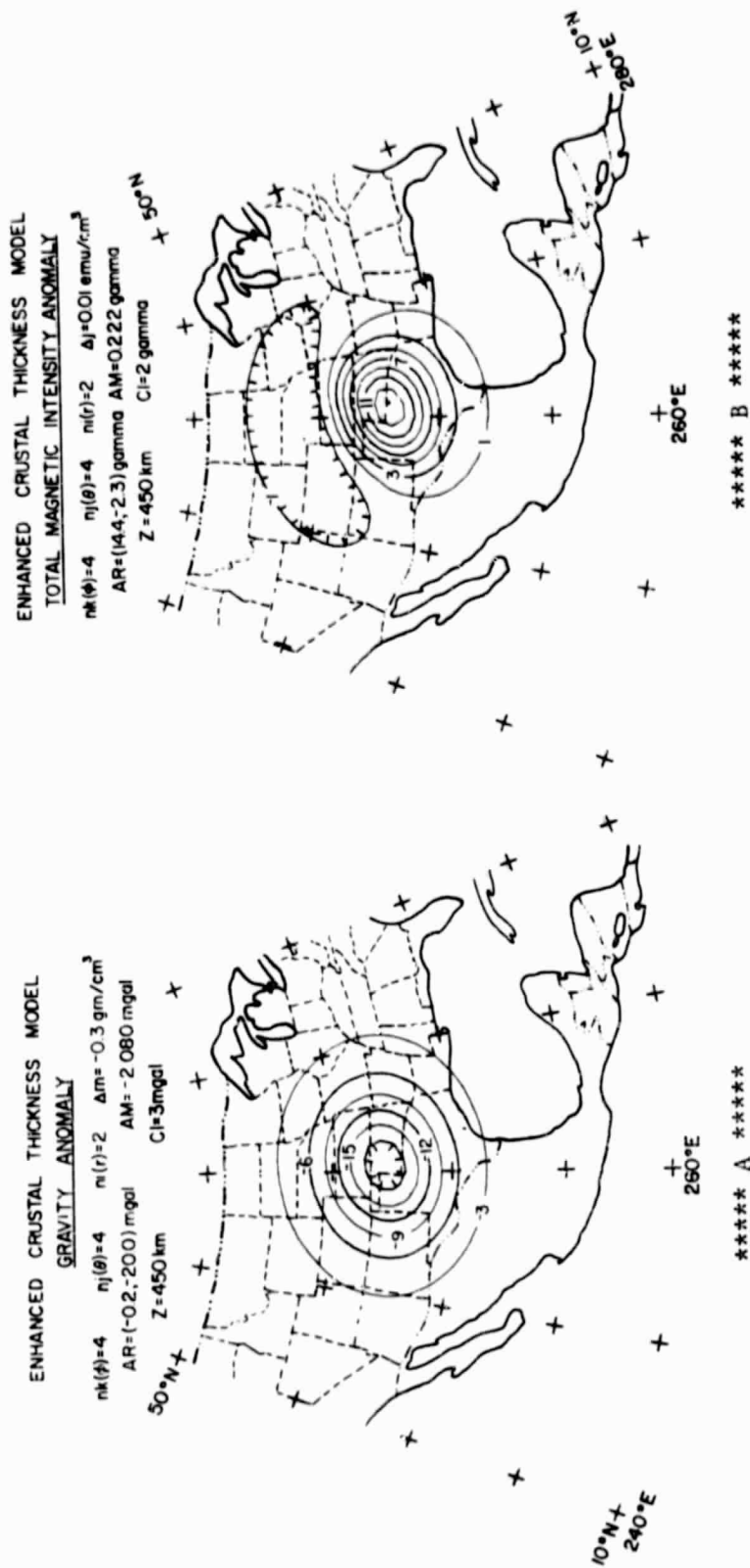


Figure V.9 Relative precision of the gravity anomaly (A) and total magnetic intensity anomaly (B) calculations is essentially unchanged at 450 km elevation by a 93.75% reduction in the number of Gauss-Legendre nodes.

reference field, the magnetic effect was computed next assuming a uniform polarizing field intensity of 60,000 gamma and radial geomagnetic field inclination at both source and observation points. Accordingly, Figure V.8.B illustrates the resultant magnetic anomaly field reduced to radial polarization at 450 km elevation for the crustal thickness model.

Finally, Ku (1977) noted that for accurate implementation of the method the distance between the equivalent source points and the observation point must be greater than the equivalent source point spacing within the body. This limitation can be minimized in practice by either subdividing the body into an appropriate number of smaller bodies, or increasing the number of equivalent point sources, or increasing the distance between the observation point and the body. The latter consideration suggests that the Gauss-Legendre quadrature formulation is especially well suited for modeling satellite level gravity and magnetic anomalies because of the large elevations involved with these measurements.

The principle is demonstrated in Figure V.9 where the gravity anomaly and total magnetic intensity anomaly due to the crustal thickness model are computed at 450 km elevation using an $n_k \times n_j \times n_i = 4 \times 4 \times 2 = 32$ point quadrature formula rather than the 512 point formula. The comparison of the mean gravity anomaly amplitudes of Figures V.7.B and 9.A shows accordingly that a 93.75% reduction in the number of equivalent point sources results in only a 1.67% reduction in the relative precision of the gravity anomaly calculation. A slightly smaller reduction of 1.37% is evident for the relative precision of the magnetic anomaly calculations illustrated in Figures V.8.A and 9.B.

E. Conclusions

Regional gravity and magnetic anomaly modeling for arbitrarily shaped lithospheric sources with variable physical properties can be achieved accurately and efficiently in spherical coordinates using Gauss-Legendre quadrature integration. The procedure involves representation of the anomalous source as a distribution of equivalent point gravity poles or point magnetic dipoles which contribute incremental

anomaly values that are evaluated and summed at each observation point to obtain the total anomaly. The distribution of equivalent point sources is determined directly from the volume limits of the anomalous body. For an arbitrarily shaped body, the variable limits of integration can be obtained from interpolations performed on a set of body points which approximate the surface envelope of the anomalous source.

A chief practical advantage of the method is its considerable versatility. The physical properties of the equivalent point sources, for example, can be individually varied to reflect physical property variations of the body that is being modeled. The method also can be extended readily to model the geoidal anomaly, vector components, and spatial derivatives to any order of the body's anomalous gravitational and magnetic potentials. Finally, the accuracy of the method can be controlled by adjusting the number of equivalent point sources or the distance between the source and observation point. In this regard, the method is particularly well suited for satellite gravity and magnetic anomaly modeling because the efficiency and accuracy of the application increases with increasing distance between source and observation points.

In consideration of the foregoing results, it is concluded that Gauss-Legendre quadrature integration facilitates a powerful and efficient approach to spherical earth modeling of regional-scale lithospheric gravity and magnetic anomaly sources. Accordingly, the method has widespread application in the analysis and design of regional-scale gravity and magnetic surveys for lithospheric investigation.

F. References

- Andreasen, G.E., and I. Zietz, Magnetic fields for a 4x6 prismatic model, U.S.G.S. Professional Paper 666, 1969.
- Bhattacharyya, B.K., Computer modeling in gravity and magnetic interpretation, *Geophysics*, 43, 912-929, 1978.
- Cain, T.C., S.J. Hendricks, R.A. Langel, W.V. Hudson, A proposed model for the International Geomagnetic Reference Field, 1965, *J. Geomag. Geoelectr.*, 19, 335-355, 1967.

- Carnahan, B., Applied Numerical Methods, J. Wiley and Sons, Inc., New York, 1969.
- Hall, D.H., Long-wavelength aeromagnetic anomalies and deep crustal magnetization in Manitoba and Northwestern Ontario, Canada, Pageoph., 40, 403-430, 1974.
- Heiskanen, W.A., and H. Mortiz, Physical Geodesy, W.H. Freeman and Co. San Francisco, 1967.
- Ku, C.C., A direct computation of gravity and magnetic anomalies caused by 2- and 3-dimensional bodies of arbitrary shape and arbitrary magnetic polarization by equivalent point method and a simplified cubic spline, Geophysics, 42, 610-622, 1977.
- Shuey, R.T., D.K. Schellinger, E.H. Johnson, and L.B. Alley, Aero-magnetics and the transition between the Colorado Plateau and the Basin and Range Provinces, Geology, 1, 107-110, 1973.
- Stroud, A.H., and D. Secrest, Gaussian Quadrature Formulas, Prentice-Hall, New Jersey, 1966.
- Talwani, M., and M. Ewing, Rapid computation of gravitational attraction of three-dimensional bodies of arbitrary shape, Geophysics, 25, 203-225, 1960.
- Talwani, M., Computation with the help of a digital computer of magnetic anomalies caused by bodies of arbitrary shape, Geophysics, 30, 797-817, 1965.
- von Frese, R.R.B., W.J. Hinze, L.W. Braile, and A.J. Luca, Spherical earth gravity and magnetic anomaly modeling by Gauss-Legendre quadrature integration, NASA-GSFC TM(in press), 1980.
- Warren, D.H., and J.H. Healy, Structure of the crust in the conterminous United States, Tectonophysics, 20, 203-213, 1973.

VI. GRAVITY AND MAGNETIC ANOMALY MODELING OF MISSISSIPPI EMBAYMENT CRUSTAL STRUCTURE AT SATELLITE ELEVATIONS

A. Abstract

A model for the three-dimensional crustal structure of the northern Mississippi Embayment is generalized from published surface wave dispersion, seismic refraction, and gravity studies of the region. The gravity and magnetic anomaly signatures due to this model are computed at 450 km elevation by Gauss-Legendre quadrature integration for comparison with observed anomalies at satellite elevations. The computed positive gravity anomaly compares well with upward continued free-air gravity data suggesting that the generalized model is representative of the crustal structure of the Embayment. Magnetic anomaly calculations show that the pronounced minimum observed over the Embayment in the POGO satellite magnetometer data can be accounted for by a decrease in the magnetization of the lower crust which corresponds to the major gravity source of the region. The results of this investigation support the failed-rift hypothesis for the origin of the Mississippi Embayment. Accordingly, these results suggest that observable gravity and magnetic anomalies characterize failed rifts (aulacogens) at satellite elevations, where the primary source of both anomalies is a high density rift component of non-magnetic lower crustal material.

B. Introduction

Satellite-level magnetic and gravity anomaly interpretational methods largely have been limited to visual spatial correlation of anomalies with known geological features and simple flat earth modeling approximations. However, the full importance of satellite-level anomalies, which map the anomalies of large scale geologic features that are difficult

to recognize and isolate in low-level data, will not be achieved until direct modeling of large-scale structural features is accomplished utilizing the spherical earth condition. Modeling of geologic features incorporating available geologic and geophysical data as constraints can be employed as an interpretive technique by altering the model until the computed anomalies match the observed anomalies. Furthermore, spectral analysis of the calculated satellite-level magnetic and gravity anomalies of geologic models provides critical information for designing filters to isolate the observed anomalies of these features.

In the previous discussion a technique was described and demonstrated for numerically modeling potential field characteristics due to regional-scale geologic sources by Gauss-Legendre quadrature integration. Herein, the method is used to obtain a preliminary view of the gravity and magnetic anomaly characteristics for the Mississippi Embayment at 450 km elevation. This information, in turn, is pertinent to evaluating the feasibility of using satellite gravity and magnetic surveys for detecting anomaly signatures due to failed rifts. The Mississippi Embayment is particularly suited for this application because a number of geophysical constraints are available for developing a first-order model of its crustal structure.

C. Model Description

The Mississippi Embayment represents a broad, spoon-shaped reentrant of Mesozoic and Cenozoic sedimentary rocks which extends into the Paleozoic terrane of the North American craton from the south. As shown in Figure VI.1, the axis of this feature roughly parallels the Mississippi River tapering northward into the tectonically active region of the New Madrid seismic zone.

Based on the regional geology, Burke and Dewey (1973) suggested the embayment is a Mesozoic aulacogen developed from a triple junction located in the vicinity of Jackson, Mississippi. However, an integrated analysis of gravity, seismic, stratigraphic and petrologic data by Ervin and McGinnis (1975) suggests the embayment is a late Precambrian aulacogen which was reactivated most recently in the late Cretaceous by tensional forces initiated during the formation of the present Atlantic Ocean basin by subsidence of the Gulf Coastal Plain.

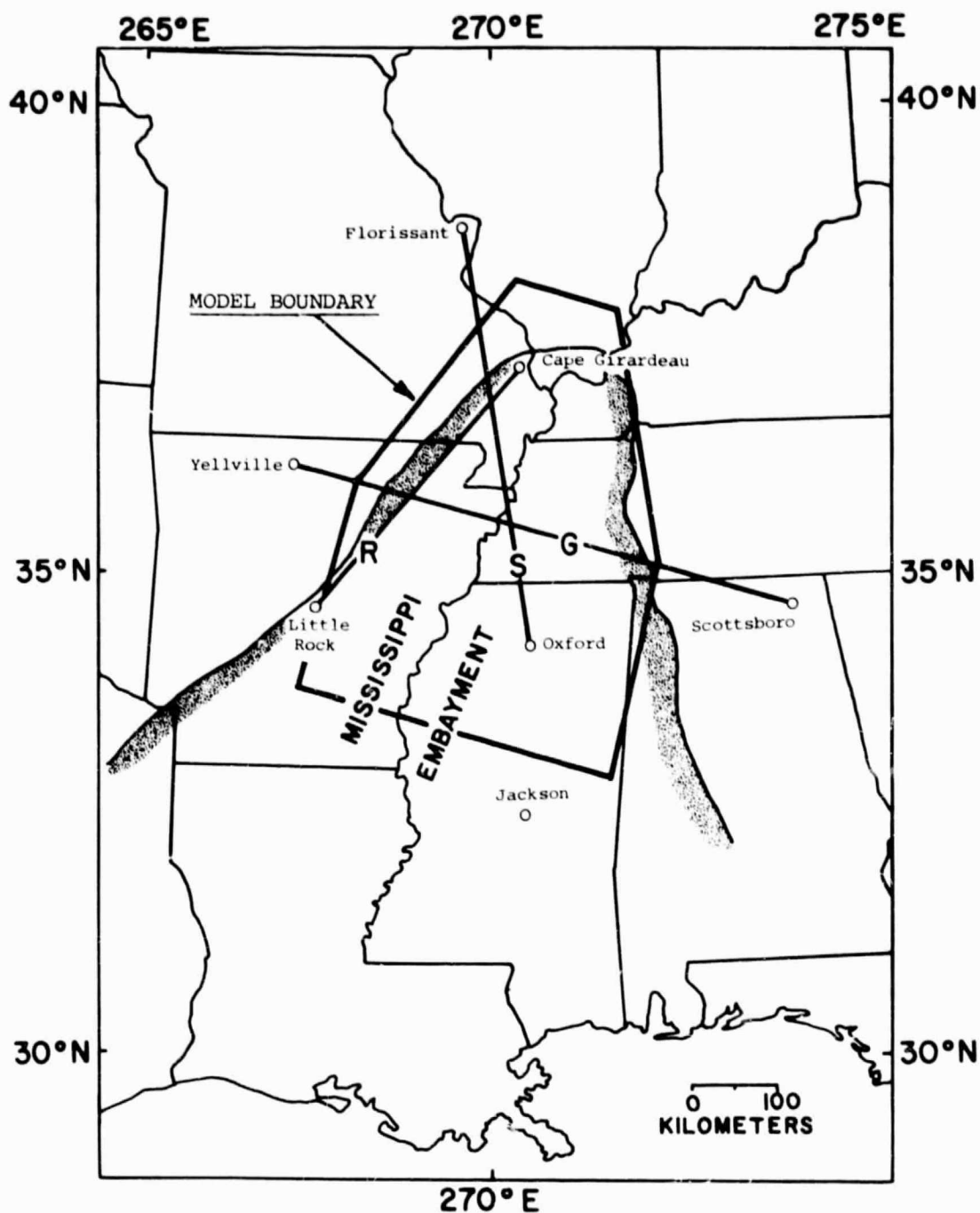


Figure VI.1 Index map of the Mississippi Embayment (shaded contour) region where G is the gravity profile studied by Ervin and McGinnis (1975), R is the seismic refraction line studied by McCamy and Meyer (1966), and S is the surface wave propagation path studied by Austin and Keller (1979). The lateral subsurface boundary of the model generalized in Figure VI.2.C for this study also is indicated.

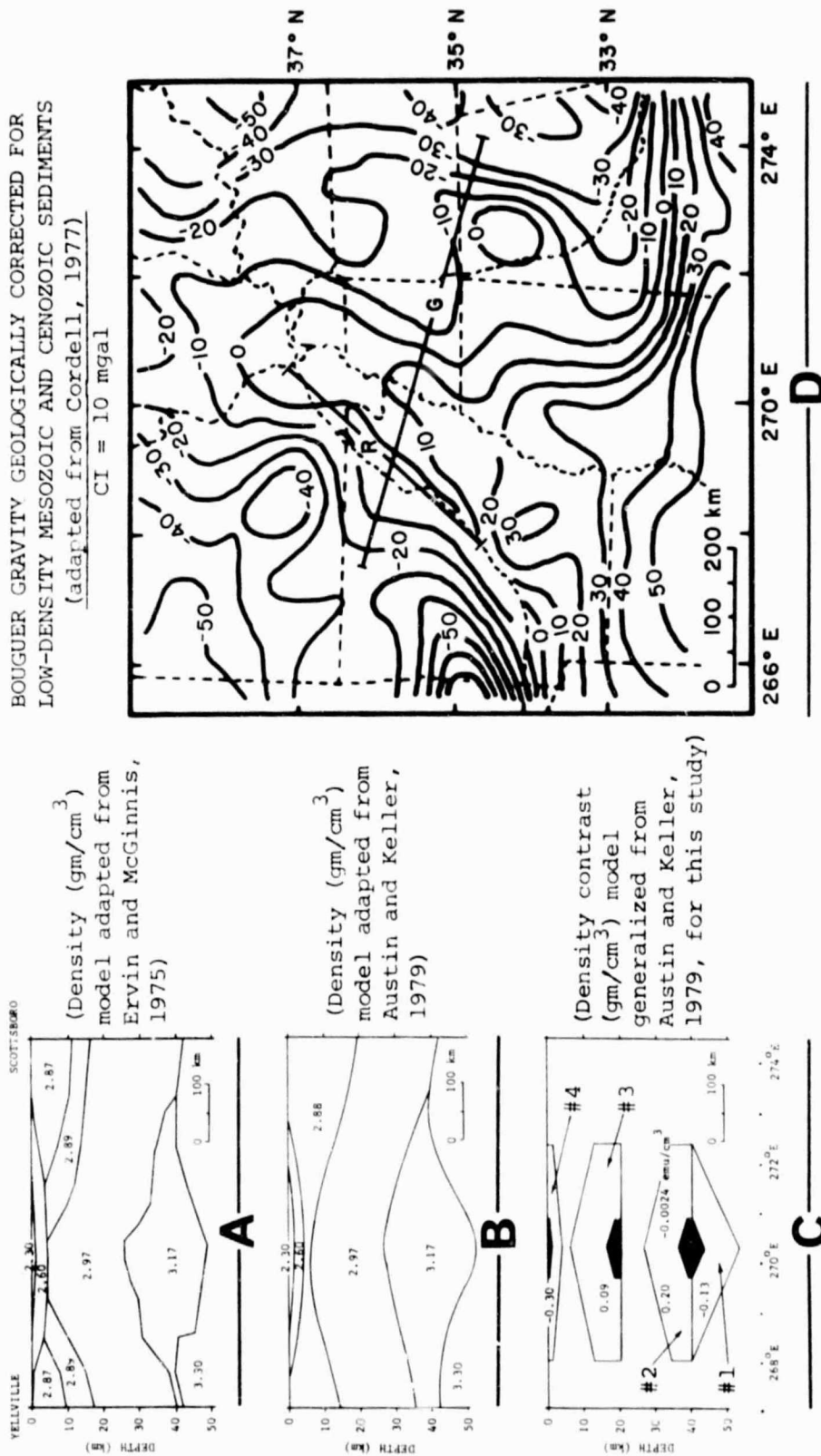


Figure VI.2 Mississippi Embayment density models adapted from A) Ervin and McGinnis (1975) and B) Austin and Keller (1979). C) The density contrast model generalized for this study from Austin and Keller (1979). Body #2 with magnetization contrast -0.0024 emu/cm^3 also was used to model POGO satellite magnetometer data over the Embayment. D) The gravity data of Cordell (1977) used to develop the lateral subsurface configuration outlined in Figure VI.1 of the density contrast model generalized in C.

Figure VI.2.A is a cross-section of the density structure of the Mississippi Embayment given by Ervin and McGinnis (1975) along a profile between Yellville, Arkansas and Scottsboro, Alabama (hereafter called Y-S profile). This density model was synthesized from regional gravity data derived from the U.S. Bouguer gravity anomaly map of Woollard and Joesting (1964) and the results of a reversed seismic refraction profile between Little Rock, Arkansas and Cape Girardeau, Missouri as described by McCamy and Meyer (1966). Austin and Keller (1979) integrated the work of McCamy and Meyer (1966) with an analysis of Rayleigh wave dispersion along a propagation path between Oxford, Mississippi and Florissant, Missouri to obtain a similar density model for the Y-S profile which is illustrated in Figure VI.2.B. An index map for locating these various studies is given in Figure VI.1. In general, the crustal cross-sections shown in Figures VI.2.A and B support the failed-rift model for the origin of the Mississippi Embayment.

The agreement of surface wave, seismic refraction, and gravity data in the region of the Embayment suggests that the crustal cross-section given in Figure VI.2.B can be useful for developing a reasonably valid three-dimensional model of the Embayment. Accordingly, the crustal cross-section that was generalized from Figure VI.2.B for the purposes of this study is given as the 4-body model shown in Figure VI.2.C. The gravity analysis due to Cordell (1977) was used to project the characteristics of this generalized crustal cross-section north and south of the Y-S profile.

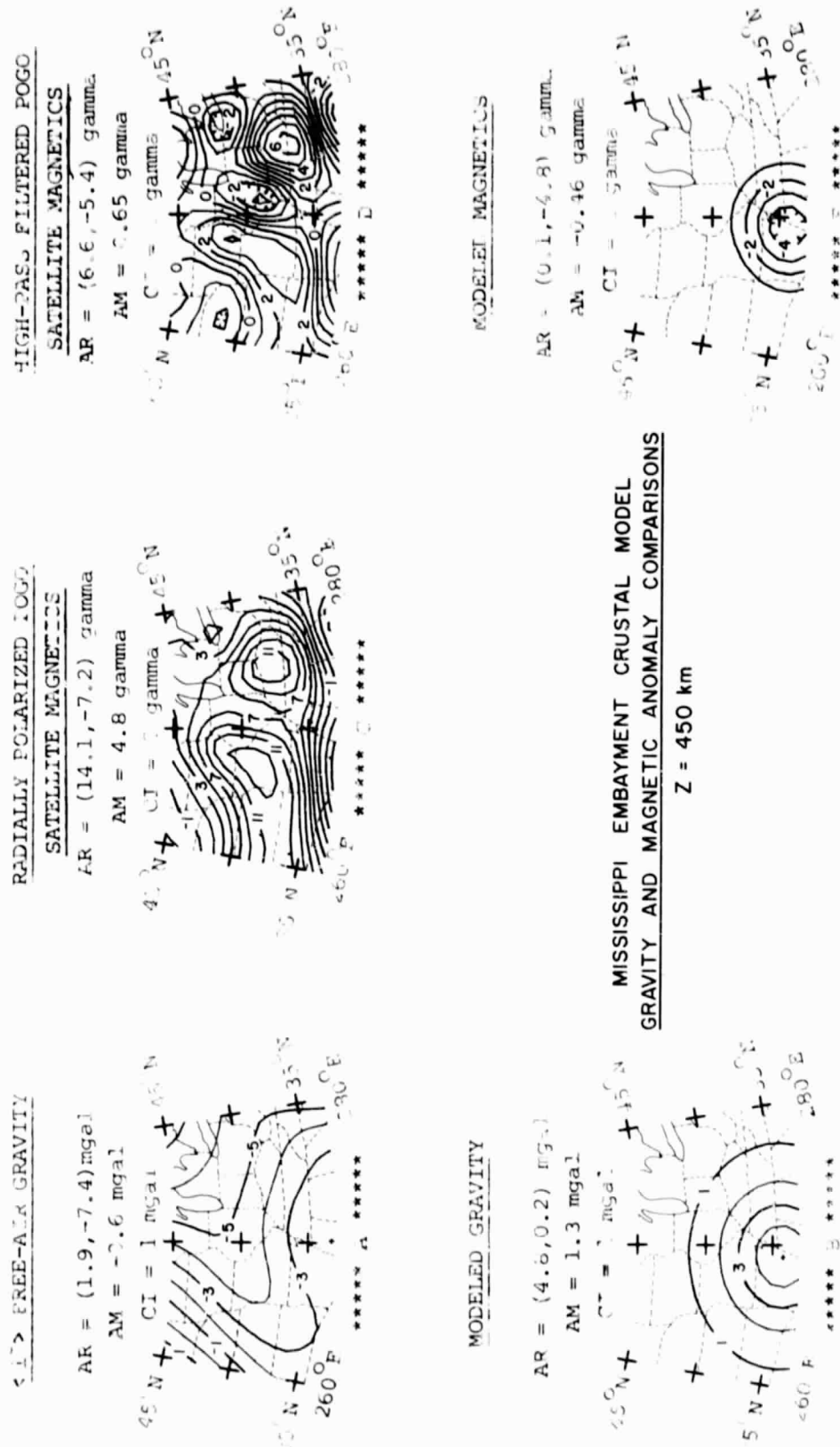
Cordell (1977) corrected the smoothed positive Bouguer anomaly of the Embayment for the low-density sediments and observed the long continuous positive anomaly with an amplitude of 15 to 45 mgal increasing southward that is illustrated in Figure VI.2.D. The axis of this anomaly follows closely the Mississippi River northward beyond its confluence with the Ohio River into southern Illinois. The anomaly exhibits fairly uniform behavior south of the Y-S profile until about 33°N where it increases sharply, thus, suggesting that the crustal cross-section may be uniformly projected southward along the Mississippi River to approximately 33°N . Northward decreasing gravity anomaly values in conjunction

with the northward tapering surface configuration of the Embayment suggest a commensurate northward tapering projection of the crustal cross-section along the Mississippi River into southern Illinois. Hence, to obtain the first-order, three-dimensional generalization of the crustal structure of the Embayment used in this investigation, the crustal cross-section of Figure VI.2.C was projected uniformly south of the Y-S profile and tapered uniformly northward as indicated in Figure VI.1. The northern ends of the 4 bodies of this generalized model as projected onto the cross-section along the Y-S profile are given by the shaded regions of Figure VI.2.C.

To compute the potential field anomalies at 450 km elevation, each of the 4 bodies of this generalized model was represented by a Gauss-Legendre quadrature formula consisting of 128 equivalent point sources. The latitude and longitude limits of each body were represented each by 8 point sources and the radial limits by 2 point sources. Pertinent body volume limits were interpolated from a set of body points that sampled the coordinates of the surface envelope for each body. The quadrature formulae were next evaluated and summed over a (21,13) observation grid spanning the region $(260-280)^{\circ}\text{E}$, $(33-45)^{\circ}\text{N}$ and compared to observed gravity and magnetic anomaly data at 450 km elevation.

D. Results and Discussion

Free-air gravity anomaly values upward continued from the surface of the earth to an elevation (Z) of 450 km by equivalent point source inversion are illustrated for the study area in the stereographic equal-area polar (SEAP) projection in Figure VI.3.A. The amplitude range (AR) of the data set is between 1.9 and -7.4 mgal and the amplitude mean (AM) is -3.6 mgal. These data exhibit a pronounced relative positive anomaly with slightly greater than 3 mgal of relative amplitude in the region of the Embayment. The gravity effect (Figure VI.3.B) of the generalized 4-body model described above is roughly a 4 mgal anomaly that, in general, corresponds to the observed data. The general degree of this correspondence for profiles along 35°N and 37°N is illustrated in Figures VI.4 and 5, respectively. Here,



MISSISSIPPI EMBAYMENT CRUSTAL MODEL
GRAVITY ANOMALY PROFILE COMPARISONS ALONG 35° N

Z = 450 km

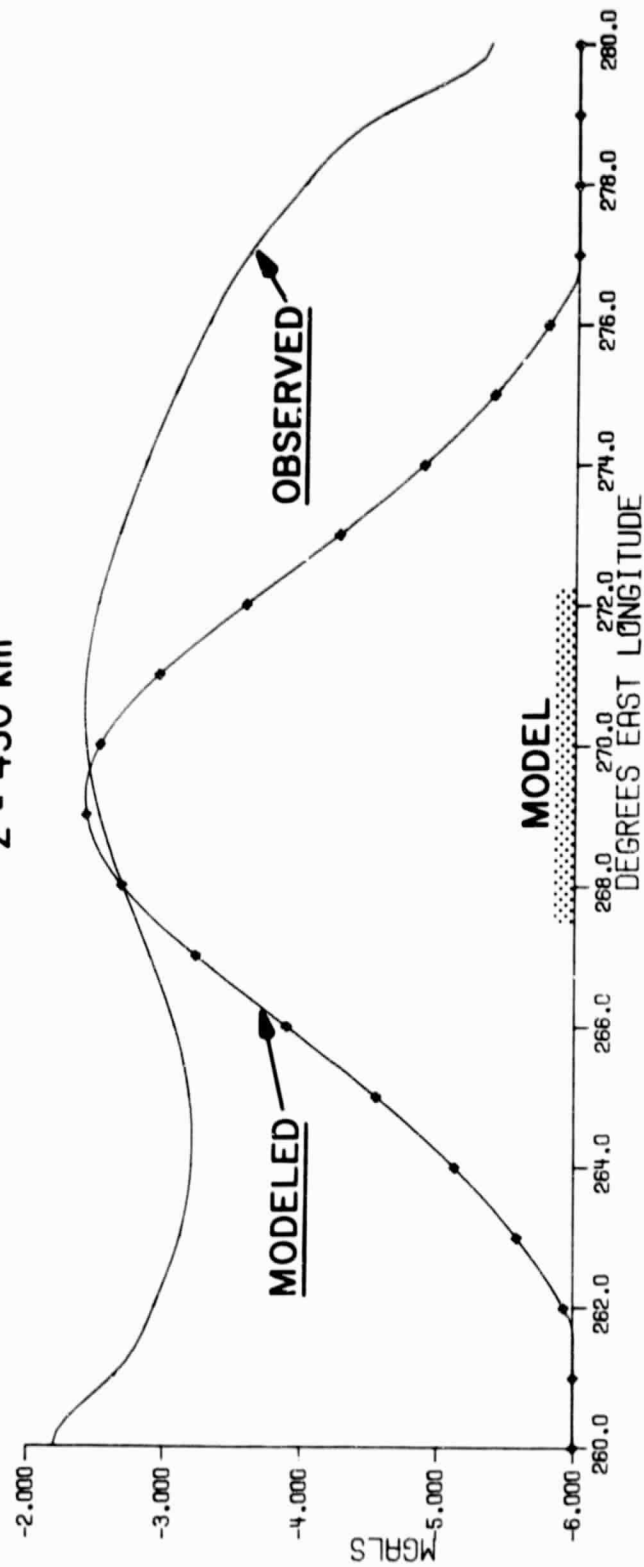


Figure VI.4 Mississippi Embayment satellite-level profile comparisons between Gauss-Legendre quadrature modeled gravity anomaly and observed upward continued 1°-averaged free-air gravity anomaly data along 35°N latitude. The shaded region indicates the location of the generalized Mississippi Embayment crustal model along the profile.

MISSISSIPPI EMBAYMENT CRUSTAL MODEL
GRAVITY ANOMALY PROFILE COMPARISONS ALONG 37° N

Z = 450 km

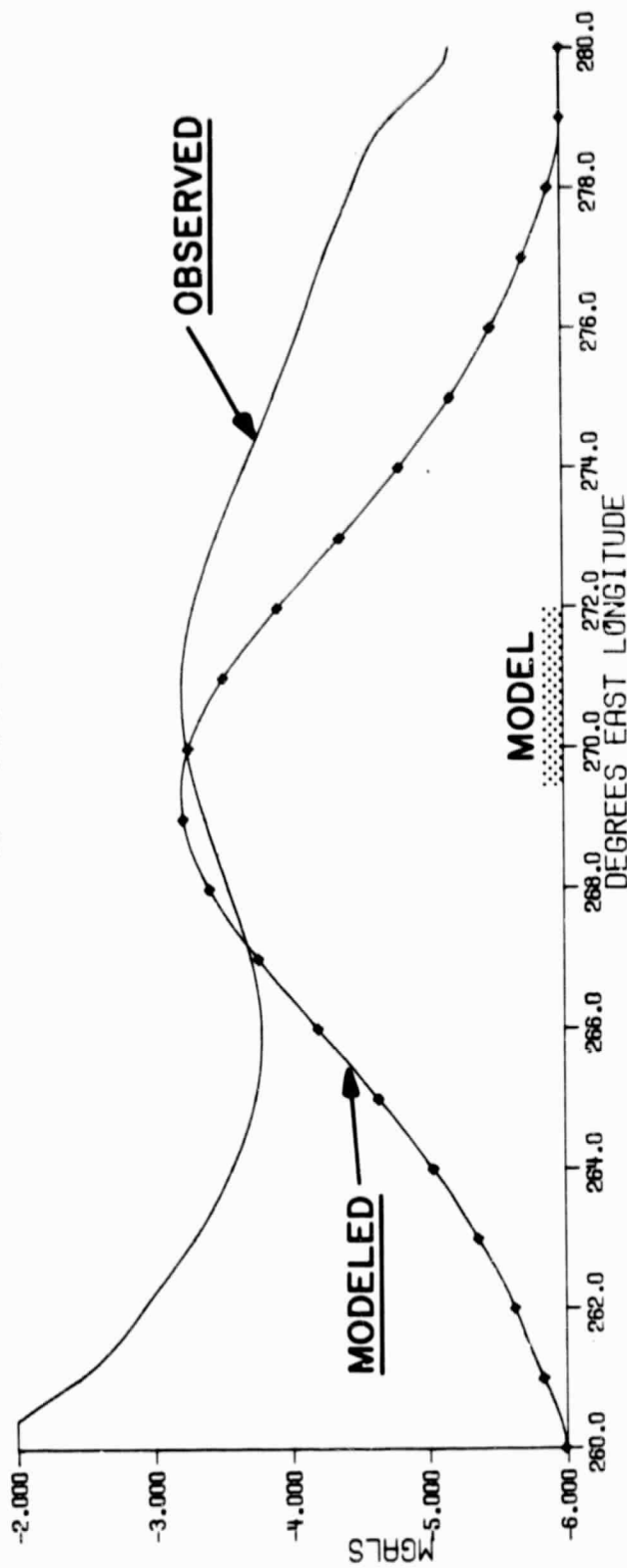


Figure VI.5 Mississippi Embayment satellite-level profile comparisons between Gauss-Legendre quadrature modeled gravity anomaly and observed upward continued 1°-averaged free-air gravity anomaly data along 37°N latitude. The shaded region indicates the location of the generalized Mississippi Embayment crustal model along the profile.

the profile peaks of the modeled gravity anomaly have been adjusted to the respective peak values of the observed profiles over the Embayment model to facilitate the comparison.

A study of the profile comparisons shows increasing disparity between the modeled and observed data along the anomaly flanks away from the model. This may reflect contributions to the observed data from sources outside the study area that have not been modeled. Nonetheless, the general agreement between the modeled and observed data over the Embayment suggests that the observed gravity anomaly can be accounted for reasonably well at 450 km elevation by the 4-body model generalized in the previous section.

POGO satellite magnetometer observations reduced to radial polarization using a normalization amplitude of 60,000 gamma by equivalent point source inversion are given for the study area in Figure VI.3.C. These data show a prominent east-west magnetic high that is breached in the vicinity of the Embayment by a magnetic low. Inverse correlations of positive gravity and negative magnetic anomalies that characterize the Embayment also have been observed at satellite elevations for features such as the Yellowstone geothermal area where it is proposed that the net negative magnetization may be due to upward deflection of the Curie isotherm (von Frese et al., 1979). In this regard, Mitchell et al., (1977) using travel time residuals of teleseismic P-waves also have speculated that the New Madrid seismic zone may be underlain by a mantle hot spot such as suggested for the Yellowstone region.

To better resolve the characteristics of the magnetic anomaly for the Embayment region, the radially polarized data were high-pass filtered for anomaly wavelengths smaller than about 10^0 . The high-pass filtered data are illustrated in Figure VI.3.D and show a negative anomaly of roughly -3 gamma over the Embayment. Wasilewski et al., (1979) found that all of the information from analysis of medium to long-wavelength magnetic anomalies indicates that the sources probably are contained in the lower crust which, in general, may be substantially more magnetic than the upper crust. Typical estimates of deep crustal magnetization are on the order of 5×10^{-3} emu/cm³ (e.g., Hall, 1974;

Shuey et al., 1973). Wasilewski et al., (1979) propose that conditions for coherent regional magnetization are enhanced as crustal depth increases. Remanence and thermal overprints are diminished, and viscous magnetization and initial susceptibility are enhanced with increasing temperature especially within 100°C - 150°C of the Curie point. The thickness of the crust within this thermal regime of the Curie point may be 5 to 20 km depending on the steepness of the geothermal gradient. Accordingly, they suggest that deep crustal magnetic sources probably are related to lateral variations of petrologic factors or Curie isotherm topography.

Consideration of the foregoing remarks indicates that the most obvious deep crustal source for the observed magnetic anomaly is body #2 which also represents the major gravity source of the Embayment model. Austin and Keller (1979) propose that the combination of bodies #1 and #2 was formed as a manifestation of a mantle upwarp beneath the Embayment comprising of a mixture of crust and upper mantle material that cooled subsequently to form a block of high density material. Magnetic hypotheses which are consistent with this view include body #2 as a zone of negative magnetization contrast with respect to the lower crust due to depletion of magnetic minerals. Negative magnetization for body #2 also can result from temperatures which exceed the Curie point, although present heat flow data (Sass et al., 1976) do not appear to warrant this hypothesis for the Embayment.

Body #3 may represent an additional magnetic source for the Embayment assuming crustal magnetization increases with depth. However, the positive magnetic contribution of body #3 will be relatively weak if the Curie isotherm depth is about 40 km or more. Arguments for including bodies #1 and #4 in a magnetic model of the Embayment appear to be lacking, so that body #2 probably represents the primary source for the observed magnetic anomaly data if the Curie isotherm is at about 40 km of depth in the region of the Embayment.

Accordingly, the magnetic anomaly due to body #2 was calculated in Figure VI.3.E using a magnetization contrast of $-2.4 \times 10^{-3} \text{ emu/cm}^3$. These results show that the anomaly amplitude observed for the region of the

MISSISSIPPI EMBAYMENT CRUSTAL MODEL
MAGNETIC ANOMALY PROFILE COMPARISONS ALONG 35° N
Z = 450 km

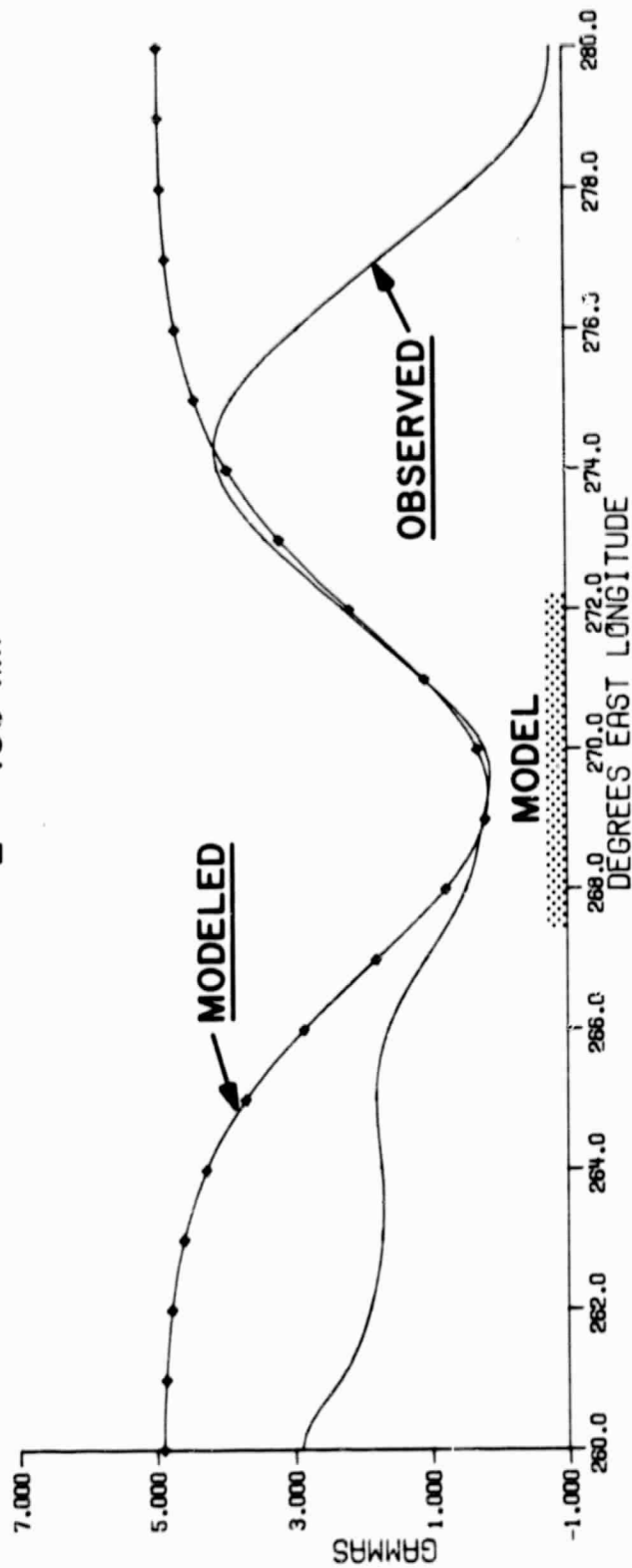


Figure VI.6 Mississippi Embayment satellite-level profile comparisons between Gauss-Legendre quadrature modeled magnetic anomaly and high-pass ($\lambda \leq 10^\circ$) filtered reduced to the pole POGO satellite observed magnetic anomaly data along 35°N latitude. The shaded region indicates the location of the generalized Mississippi Embayment crustal model along the profile.

MISSISSIPPI EMBAYMENT CRUSTAL MODEL
MAGNETIC ANOMALY PROFILE COMPARISONS ALONG 37° N

Z = 450 km

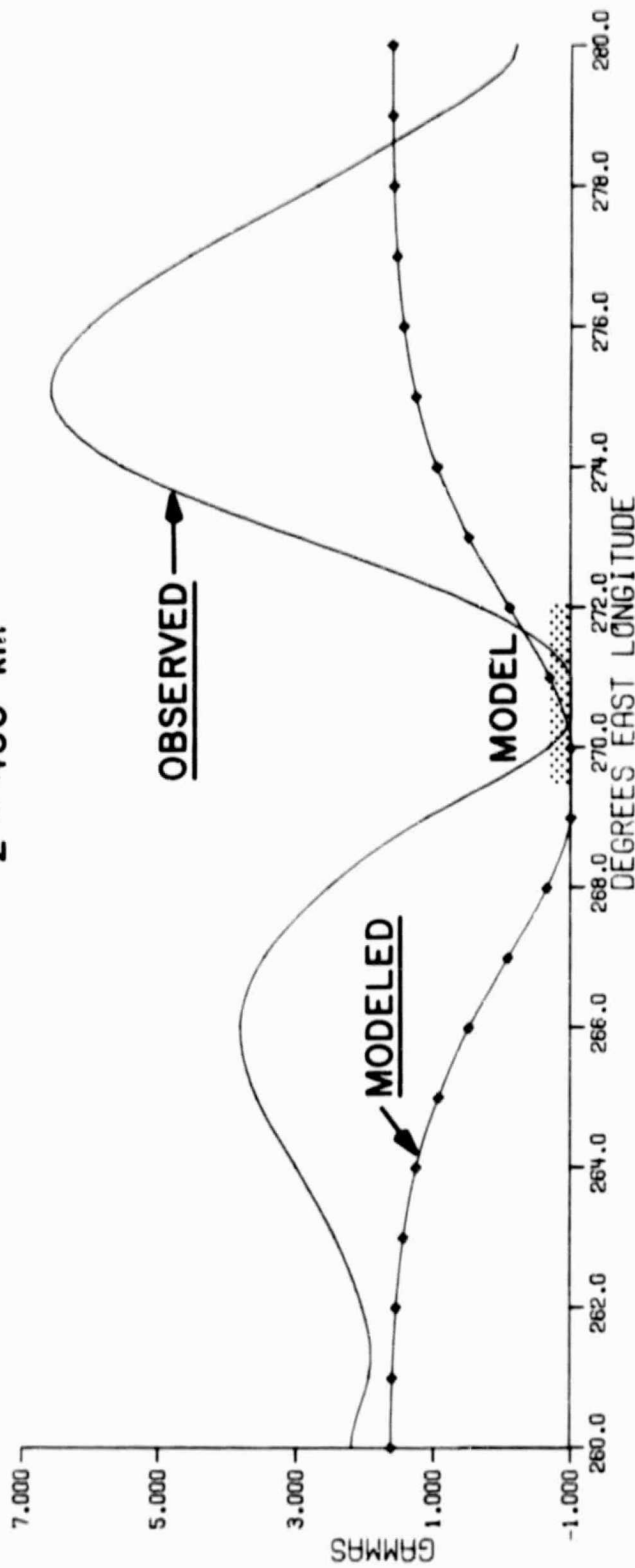


Figure VI.7 Mississippi Embayment satellite-level profile comparisons between Gauss-Legendre quadrature modeled magnetic anomaly and high-pass ($\lambda \leq 10^\circ$) filtered reduced to the pole POGO satellite observed magnetic anomaly data along 37°N latitude. The shaded region indicates the location of the generalized Mississippi Embayment crustal model along the profile.

the Embayment at 450 km elevation can be well matched by a source such as body #2 located near the base of the crust with magnetic properties which correspond with the magnetization characteristics anticipated for the lower crust. Hence, body #2 as determined for gravity modeling considerations represents at least a preliminary magnetic model for the Embayment.

Substantial differences are apparent, however, between the spatial characteristics of the observed and modeled magnetic anomalies. Profile comparisons between Figures VI.3.D and 3.E along 35°N and 37°N are given in Figures VI.5 and 7, respectively, which illustrate this disparity. Here again, the modeled profile peaks are adjusted to the observed anomaly peaks over the Embayment model to facilitate comparison. In general, these comparisons indicate that body #2 is magnetically more extensive to the north and more restricted in longitude than it is gravitationally, although care must be taken with this interpretation because the observed data obviously contain the magnetic effects from sources outside the Embayment. Further refinements of the magnetic model are necessary and will be particularly warranted when the data are available from the current Magsat program (Langel, 1979) to verify and further upgrade the POGO satellite magnetic anomalies for lithospheric applications.

E. Conclusions

A preliminary three-dimensional model of crustal structure for the Mississippi Embayment was generalized from analyses of surface wave dispersion (Austin and Keller, 1979), seismic refraction data (McCamy and Meyer, 1966) and gravity data (Ervin and McGinnis, 1975; Cordell, 1977). The agreement between the gravity anomaly calculated for the 4-body model and the gravity data observed at 450 km elevation suggests that this model represents a reasonably valid generalization of the crustal density structure of the Embayment. The magnetic anomaly calculations show that the magnetic data observed at 450 km elevation can be modeled by a non-magnetic portion of the lower crust located along the axis of the Embayment that also corresponds to the major gravity source of the region. These results are consistent with the failed-rift hypothesis for the origin of the Mississippi Embayment.

This investigation further indicates that an aulacogen may be characterized at satellite elevations by observable positive gravity and negative magnetic anomalies. The primary source of both anomalies is the portion of the rift that defines a lateral variation in the physical properties of the lower crust. Finally, these results demonstrate the basic difficulty of separating pertinent anomalies at satellite elevations which perhaps is a major limitation to interpretation of satellite observed gravity and magnetic anomaly data. However, the application of the modeling capacity demonstrated in this investigation will help to alleviate this problem.

F. References

- Austin, C.B., and G.R. Keller, A crustal structure study of the Mississippi Embayment; in Braile, L.W., W.J. Hinze, J.L. Sexton, G.R. Keller, and E.G. Lidiak, eds., An integrated geophysical and geological study of the tectonic framework of the 38th parallel lineament in the vicinity of its intersection with the extension of the New Madrid fault zone, NUREG/CR-1014, 101-133, 1979.
- Burke, K., and J.F. Dewey, Plume-generated triple junctions: Key indicators in applying plate tectonics to old rocks, *Jour. Geology*, 81, 406-433, 1973.
- Cordell, L., Regional positive gravity anomaly over the Mississippi Embayment, *Geophys. Res. Letters*, 4, 285-287, 1977.
- Ervin, C.P., and L.D. McGinnis, Reelfoot rift: Reactivated precursor to the Mississippi Embayment, *Geol. Soc. Am. Bull.*, 86, 1287-1295, 1977.
- Hall, D.H., Long-wavelength aeromagnetic anomalies and deep crustal magnetization in Manitoba and Northwestern Ontario, Canada, *Pageoph.*, 40, 403-430, 1974.
- Langel, R.A., Near-earth satellite magnetic field measurements: A prelude to Magsat, *EOS (Am. Geophys. Union Trans.)*, 60, 667-668, 1979.
- McCamy, K., and R.P. Meyer, Crustal results of fixed multiple shots in the Mississippi Embayment; in Steinhart, J.S., and T.J. Smith, eds., *The Earth Beneath the Continents*, *Am. Geophys. Union Geophys. Mon.*, 19, 370-381, 1966.
- Mitchell, B.J., and C.C. Cheng, and W. Stauder, A three-dimensional velocity model of the lithosphere beneath the New Madrid Seismic Zone, *Seis. Soc. Am. Bull.*, 67, 1061-1074, 1977.

- Sass, J.H., W.H. Diment, A.H. Lachenbruch, B.V. Marshall, R.J. Munroe, T.H. Moses, Jr., and T.C. Urban, A new heat-flow contour map of the conterminous United States, U.S.G.S. Open-file Rpt. 76-756, 1976.
- Shuey, R.T., D.K. Schellinger, E.H. Johnson, and L.B. Alley, Aeromagnetics and the transition between the Colorado Plateau and the Basin and Range Provinces, *Geology*, 1, 107-110, 1973.
- von Frese, R.R.B., L.W. Braile, and W.J. Hinze, Correlation of long-wavelength gravity and magnetic anomalies of North America (abst.), *IAGA Bulletin*, 43, 166, 1979.
- Wasilewski, P.J., H.H. Thomas, and M.A. Mayhew, The Moho as a magnetic boundary, NASA-GSFC TM80245, 1979.
- Woollard, G.P., and H.R. Joesting, Bouguer gravity anomaly map of the United States, *Am. Geophys. Union and U.S. Geological Survey*, scale 1:2,500,000, 1964.

VII. SUMMARY AND CONCLUSIONS

Artificial, earth-orbiting satellites are making increasingly available consistent, regional-scale gravity and magnetic anomaly data which are largely free from the effects of near-surface geologic sources that otherwise tend to distort the signatures of deep, broad lithospheric variations. Accordingly, satellite potential field observations facilitate a unique characterization of the attributes of geologically significant regions measured in hundreds or even thousands of kilometers. These zones identified and characterized on a global basis can provide useful information for deciphering earth history including paleo and contemporary geodynamics, delineation of segments of the lithosphere into resource provinces, and for numerical modeling of lithospheric processes.

To realize this promise, however, procedures are required to accurately and efficiently analyze potential field anomalies for lithospheric information directly in spherical coordinates. As demonstrated by this investigation, an especially powerful and efficient approach to generalized spherical earth processing of satellite potential field observations is to relate the gravity or magnetic anomalies to spherical distributions of equivalent point sources by methods of least squares matrix inversion. Linear transformations of the resultant equivalent source field permit generalized processing of the potential field anomalies in the spherical domain that is analogous to conventional geophysical processing methods routinely employed in the Cartesian plane.

For example, spherical earth processing of gravity anomalies by equivalent point source inversion can yield corresponding geoidal deflections, vector anomaly components, anomaly continuations and differentiations at any point in source-free space. Similar elements for magnetic anomalies can be obtained in the spherical domain by equivalent point source inversion as well. In addition, equivalent

point source inversion can be used to differentially reduce regional magnetic anomalies to the radial pole. In general, the precision of these generalized spherical earth processing procedures is equivalent to the accuracy of the least squares fit achieved by the matrix inversion between the equivalent source field and the observed anomalies.

Equivalent point source inversion was used to investigate regional correlations of surface free-air gravity and POGO satellite magnetic anomalies and regional heat flow and tectonic data for North America and adjacent marine areas. The combined analysis of these different classes of geophysical data is useful for improving the quality and uniqueness of their geologic interpretation, particularly in consideration of the general absence of regional ground-truth information.

The qualitative analysis by visual spatial correlation indicates that regional gravity anomalies reflect the prevailing structural trends of both oceanic and continental terranes. When upward continued to 450 km elevation, the gravity anomalies show strikingly direct correspondences to the regional heat flow pattern, whereas magnetic anomalies demonstrate limited correlation.

Over continental terrane gravity and magnetic anomalies exhibit basically an inverse correlation at satellite elevations. One type of inverse correspondence is exemplified by the transcontinental magnetic maxima and gravity minima that span the midcontinental region between the Anadarko Basin and Cincinnati Arch. Seismic evidence shows this region is characterized by enhanced crustal thickness, thus, suggesting that the regional combination of negative gravity and positive magnetic anomalies may reflect displacement of denser and less magnetic mantle material by an anomalously thick crust.

The second type of inverse correlation is typified by the magnetic minimum and gravity maximum observed for the Yellowstone geothermal region. Here the regional inverse correspondence of positive gravity and negative magnetic anomalies may be related to increased heat flow which is likely to produce a region of relative net negative magnetization by deflecting the Curie isotherm to a shallower depth, as well as a thinned crust and inflated elevation that may not be isostatically compensated.

A more quantitative investigation of these regional correlations was developed utilizing Poisson's theorem in a moving-window linear regression analysis performed between suitable derivatives of the anomalous gravity and magnetic potentials at satellite elevations. These results are useful for establishing patterns of anomaly correlation and provide initial physical property constraints to facilitate further investigation of correlating anomalies.

Over continental terrane, for example, the previously described inverse correlation of regional gravity and magnetic anomalies is well delineated by the regional patterns of the statistical correlation coefficients derived from the moving-window Poisson's analysis. In addition, these results indicate surprisingly large magnetizations ($\approx 1.8 \times 10^{-2} \text{ emu/cm}^3$) for the transcontinental magnetic sources.

Over the oceans, regional correlations of gravity and magnetic anomalies appear limited and poorly developed. The results of the moving-window Poisson's analysis suggest this observation may reflect decreased magnetic polarization of the oceanic crust relative to continental crust due to the influence of temperature and time on the remanent moments of crustal extrusive rocks. Statistically, however, oceanic regions are characterized primarily by direct regional anomaly correlations. This correspondence perhaps is best exemplified by the higher order gravity and magnetic anomaly derivatives of the Caribbean, eastern Gulf of Mexico and Atlantic Ocean.

In general, the broad conclusions suggested by the correlation analyses developed during the course of this investigation indicate that long-wavelength magnetic anomalies as mapped by the POGO and more recently the Magsat programs provide a valuable complementary data set to gravity and other classes of geophysical data for investigating the megatectonic features of continents and oceans.

The capacity to directly model potential field anomalies observed in spherical coordinates was investigated as an essential element to complement the spherical earth processing and correlation procedures described above. Accordingly, a technique was developed and demonstrated which employs Gauss-Legendre quadrature integration to numerically model gravity and magnetic anomaly potentials and their derivatives in the spherical domain due to arbitrarily shaped geological bodies with arbitrary physical properties.

The modeling procedure involves representing the anomalous body by a distribution of equivalent point sources which is determined directly from the volume limits of the body. Calculating and summing at each observation point the effects of the equivalent point sources located at these selected coordinates within the body's volume gives an accurate estimate for the potential field anomaly of the arbitrary body. The method is especially well suited for satellite gravity and magnetic anomaly modeling because the efficiency and accuracy of the application increases with increasing distance between source and observation points.

The Gauss-Legendre quadrature modeling procedure was used to investigate a 4-body model of northern Mississippi Embayment crustal structure that was generalized from analyses of surface wave dispersion, seismic refraction and surface Bouguer gravity anomaly data. The modeled gravity anomaly signature compares favorably to the relative positive free-air gravity anomalies upward continued to 450 km elevation, thus, suggesting that the 4-body model is a geologically reasonable representation of the density structure of the Embayment.

Magnetic modeling shows that the pronounced minimum observed in the POGO satellite magnetic anomaly data differentially reduced to radial polarization can be accounted for by a block of non-magnetic material located at the base of the crust along the axis of the Embayment. This particular block of lower crust also corresponds to the primary gravity source for the region according to the gravity modeling considerations.

The results of the modeling application are consistent with the failed-rift (aulacogen) hypothesis for the origin of the Mississippi Embayment. More generally, these results suggest that an aulacogen may be characterized at satellite elevations by observable positive gravity and negative magnetic anomalies, due principally to the rift component which defines a non-magnetic block of high-density material within the lower crust.

In contrast to the widespread use of potential field anomalies referenced in the Cartesian plane for geologic analysis, there has been in the past a general inability to routinely analyze gravity

and magnetic anomalies in spherical coordinates for subsurface information that has limited the utility of satellite potential field observations in lithospheric studies. During the course of this investigation, however, procedures have been developed and verified for generalized processing, correlation analysis and modeling of potential field anomalies in the spherical domain that are analogous to the essential geophysical methods of interpretation commonly employed in conventional flat earth applications.

In general, then, these spherical earth techniques can be used to routinely perform on spherically registered potential field anomalies nearly any type of geophysical analysis that finds widespread use in the flat earth domain. Accordingly, it is concluded that the ultimate utility of satellite potential field observations for lithospheric analysis now is basically a technological question of how accurately lithospheric potential field signals can be measured and reduced by satellite programs. Clearly, the results and procedures of this investigation can play a significant role in helping to resolve this survey design problem.

In summation, the results and procedures developed during the course of this investigation have been shown to represent a powerful and efficient approach to the geological analysis of gravity and magnetic anomalies in the spherical domain. Accordingly, it is concluded that the methods and results of this study have widespread application in the analysis and design of regional-scale gravity and magnetic surveys for lithospheric investigation.

BIBLIOGRAPHY

BIBLIOGRAPHY

- Allredge, L.R., G.D. Van Voorhis and T.M. Davis, A magnetic profile around the world, *Jour. Geophys. Res.*, 68, 3679-3692, 1963.
- Andreasen, G.E., and I. Zietz, Magnetic fields for a 4x6 prismatic model, U.S.G.S. Professional Paper 666, 1969.
- Austin, C.B., and G.R. Keller, A crustal structure study of the Mississippi Embayment; in Braile, L.W., W.J. Hinze, J.L. Sexton, G.R. Keller, and E.G. Lidiak, eds., An integrated geophysical and geological study of the tectonic framework of the 38th parallel lineament in the vicinity of its intersection with the extension of the New Madrid fault zone, NUREG/CR-1014, 101-133, 1979.
- Bhattacharyya, B.K., Computer modeling in gravity and magnetic interpretation, *Geophysics*, 43, 912-929, 1978.
- Bowman, P.L., L.W. Braile, V.W. Chandler, W.J. Hinze, A.J. Luca and R.R.B. von Frese, Magnetic and gravity anomaly correlation and its application to satellite data, NASA-GSFC TM 79702, 1979.
- Burke, K., and J.F. Dewey, Plume-generated triple junctions: Key indicators in applying plate tectonics to old rocks, *Jour. Geology*, 81, 406-433, 1973.
- Cain, T.C., S.J. Hendricks, R.A. Langel, W.V. Hudson, A proposed model for the International Geomagnetic Reference Field-1965, *J. Geomag. Geoelectr.*, 19, 335-355, 1967.
- Carnahan, B., *Applied Numerical Methods*, J. Wiley and Sons, Inc. New York, 1969.
- Chandler, V.W., J.S. Koski, W.J. Hinze and L.W. Braile, Combined analysis of multi-source gravity and magnetic anomaly data sets, *Geophysics* (in press), 1980.
- Chapman, D.S., and H.N. Pollack, Global heat flow: A new look, *Earth and Planetary Science Lett.*, 28, 23-32, 1975.
- Chapman, M.E., and M. Talwani, Comparison of gravimetric geoids with Geos 3 altimetric geoid, *Jour. Geophys. Res.*, 84, 3803-3816, 1979.
- Cordell, L., Regional positive gravity anomaly over the Mississippi Embayment, *Geophys. Res. Letters*, 4, 285-287, 1977.
- Dampney, C.N.G., The equivalent source technique, *Geophysics*, 34, 39-53, 1969.

- Ervin, C.P. and L.B. McGinnis, Reelfoot rift: Reactivated precursor to the Mississippi Embayment, *Geol. Soc. Am. Bull.*, 86, 1287-1295, 1975.
- Hall, D.H., Long-wavelength aeromagnetic anomalies and deep crustal magnetization in Manitoba and Northwestern Ontario, Canada, *Pageoph.*, 40, 403-430, 1974.
- Hamilton, W., and W.B. Myers, Cenozoic tectonics of the western United States, *Rev. Geophysics*, 4, 509-549, 1966.
- Heiskanen, W.A., and H. Moritz, *Physical Geodesy*, W.H. Freeman and Co., San Francisco, 1967.
- Hinze, W.J., L.W. Braile, V.W. Chandler, and F.E. Mazzella, Combined magnetic and gravity analysis, U.S.G.S. Final Rpt., NASA Contract No. S-500 29A Modification No. 8, 1975.
- Innes, M.J.S., A.K. Goodacre, A.A. Weston, and J.R. Weber, Gravity and isostasy in the Hudson Bay region, *Science, History and Hudson Bay*, 2, 703-728, 1968.
- Jackson, D.D., Interpretation of inaccurate, insufficient and inconsistent data, *Geophys. J.R. Astro. Soc.*, 28, 97-109, 1972.
- Jefferys, H., The Fenno-Scandian uplift, *Roy. Geol. Soc. Lond.*, 131, 323-325, 1975.
- Kaula, W.M., Theory of statistical analysis of data distributed over a sphere, *Reviews of Geophysics*, 5, 83-107, 1967.
- Keller, G.R., L.W. Braile and P. Morgan, Crustal structure, geophysical models and contemporary tectonism of the Colorado Plateau, *Tectonophysics*, 61, 131-147, 1979.
- Kellogg, O.D., *Foundations of Potential Theory*, Dover Publications, Inc., New York, 1953.
- Kontis, A.L. and G.A. Young, Approximation of residual total-magnetic intensity anomalies, *Geophysics*, 29, 623-627, 1964.
- Ku, C.C., A direct computation of gravity and magnetic anomalies caused by 2- and 3-dimensional bodies of arbitrary shape and arbitrary magnetic polarization by equivalent point method and a simplified cubic spline, *Geophysics*, 42, 610-622, 1977.
- Lanczos, C., 1961, *Linear Differential Operators*, D. Van Nostrand Co., London, 1961.
- Langel, R.A., Near-earth satellite magnetic field measurements: A prelude to Magsat, *EOS (Am. Geophys. Union Trans.)*, 60, 667-668, 1979.
- Lawson, C.L. and R.J. Hanson, *Solving Least Squares Problems*, Prentice-Hall, Inc., New Jersey, 1974.

- Lyubimov, A.A. and G.A. Lyubimov, The use of Poisson's ratio for geologic interpretation of gravity and magnetic anomaly analogs, *Razvedka i Okhrana Nedr*, 34, 38-42, 1968.
- Mayhew, M.A., Magnetic anomaly map of North America south of 50°N from POGO data, GSFC-NASA Doc. X-922-76-201, 1976.
- Mayhew, M.A., Large scale variations in crustal magnetization in central U.S. based on satellite data, *EOS Trans., AGU*, 59, 228, 1977.
- Mayhew, M.A. Inversion of satellite magnetic anomaly data, *J. Geophys.*, 45, 119-128, 1979.
- McCamy, K. and R.P. Meyer, Crustal results of fixed multiple shots in the Mississippi Embayment; in Steinhart, J.S., and T.J. Smith, eds., *The Earth Beneath the Continents*, *Am. Geophys. Union Geophys. Mon.*, 19, 370-381, 1966.
- Mitchell, B.J., and C.C. Cheng, and W. Stauder, A three-dimensional velocity model of the lithosphere beneath the New Madrid Seismic Zone, *Seis. Soc. Am. Bull.*, 67, 1061-1074, 1977.
- Nettleton, L.L., Gravity and magnetic calculations, *Geophysics*, 7, 293-310, 1942.
- Nettleton, L.L. and T.A. Elkins, Association of magnetic and density contrasts with igneous rock classifications, *Geophysics*, 9, 60-78, 1944.
- Poisson, S.D., Memoire sur la theorie du magnetisme, *Memories de l'Academie royale des sciences de l'Institut de France*, 247-348, 1826.
- Pollack, H.N., and D.S. Chapman, On the regional variation of heat flow, geotherms, and lithospheric thickness, *Tectonophysics*, 38, 279-296, 1977.
- Ramsey, A.S., *An Introduction to the Theory of Newtonian Attraction*, Cambridge Univ. Press, New York, 1940.
- Sass, J.H., W.H. Diment, A.H. Lachenbruch, B.V. Marshall, R.J. Munroe, T.H. Moses, Jr., and T.C. Urban, A new heat-flow contour map of the conterminous United States, *U.S.G.S. Open-file Rpt.* 76-756, 1976.
- Shuey, T.R., D.K. Schellinger, E.H. Johnson and L.B. Alley, Aeromagnetics and the transition between the Colorado Plateau and the Basin and Range Provinces, *Geology*, 1, 107-110, 1973.
- Smellie, D.W., Elementary approximations in aeromagnetic interpretation, *Geophysics*, 21, 1021-1040, 1956.

- Strange, W.E. and G.P. Woollard, The use of geologic and geophysical parameters in the evaluation, interpolation and prediction of gravity, Hawaii Inst. of Geophys., Doc. HIG-64-17, 1964.
- Stroud, A.H., and D. Secrest, Gaussian Quadrature Formulas, Prentice-Hall, New Jersey, 1966.
- Talwani, M., and M. Ewing, Rapid Computation of gravitational attraction of three-dimensional bodies of arbitrary shape, *Geophysics*, 25, 203-225, 1960.
- Talwani, M., Computation with the help of a digital computer of magnetic anomalies caused by bodies of arbitrary shape, *Geophysics*, 30, 797-817, 1965.
- Talwani, M., and X. LePichon, Gravity field over the Atlantic Ocean; in Hart, P.J., ed., *The Earth's Crust and Upper Mantle*, Am. Geophys. Union Geophys. Mon., 13, 341-351, 1969.
- Vening Meinesz, F.A., *Developments in Solid Earth Geophysics-1-The Earth's Crust and Mantle*, Elsevier, New York, 1964.
- Vigneresses, J.L., Damped and constrained least squares method with application to gravity interpretation, *J. Geophys.*, 45, 17-28, 1978.
- von Frese, R.R.B., L.W. Braile, and W.J. Hinze, Correlation of long-wavelength gravity and magnetic anomalies of North America (abst.), *IAGA Bulletin*, 43, 166, 1979.
- von Frese, R.R.B., W.J. Hinze, L.W. Braile and A.J. Luca, Spherical earth gravity and magnetic anomaly modeling by Gauss-Legendre quadrature integration, NASA-GSFC TM(in press), 1980.
- Warren, D.H. and J.H. Healy, Structure of the crust in the conterminous United States, *Tectonophysics*, 20, 203-213, 1973.
- Wasilewski, P.J., H.H. Thomas and M.A. Mayhew, The Moho as a magnetic boundary, NASA-GSFC TM80245, 1979.
- Woollard, G.P., The relationship of gravity anomalies to surface elevation, crustal structure and geology, Univ. of Wis. Geophys. Polar Res. Center. Res. Rept. SER. 62-9, 1962.
- Woollard, G.P. and H.R. Joesting, Bouguer gravity anomaly map of the United States, Am. Geophys. Union and U.S.G.S., scale 1:2,500,000, 1964.
- Worzel, J.L., Gravity investigations of the subduction zone; in Sutton, G.H., M.H. Manghnani, and R. Moberly, eds., *The Geophysics of the Pacific Ocean Basin and its Margin*, Am. Geophys. Union Geophys. Mon., 19, 1-15, 1976.